



HAL
open science

New oxamate-based architectures and their properties

Ang Li

► **To cite this version:**

Ang Li. New oxamate-based architectures and their properties. Inorganic chemistry. Sorbonne Université, 2019. English. NNT : 2019SORUS205 . tel-03030124

HAL Id: tel-03030124

<https://theses.hal.science/tel-03030124v1>

Submitted on 29 Nov 2020

HAL is a multi-disciplinary open access archive for the deposit and dissemination of scientific research documents, whether they are published or not. The documents may come from teaching and research institutions in France or abroad, or from public or private research centers.

L'archive ouverte pluridisciplinaire **HAL**, est destinée au dépôt et à la diffusion de documents scientifiques de niveau recherche, publiés ou non, émanant des établissements d'enseignement et de recherche français ou étrangers, des laboratoires publics ou privés.



Sorbonne Université

École Doctorale de Chimie Moléculaire de Paris Centre –ED 406

*Institut Parisien de Chimie Moléculaire (IPCM) / Equipe de Recherche en Matériaux Moléculaires
et Spectroscopies (ERMMES)*

New oxamate based architectures and their properties

Par Ang Li

Thèse de doctorat de Chimie Inorganique

Présentée et soutenue publiquement le 25 Septembre 2019

Devant un jury composé de :

Mme Carole DAIGUEBONNE, Maître de Conférences (INSA Rennes)	Rapporteur
M Guillaume ROGEZ, Directeur de Recherche (IPCMS Strasbourg)	Rapporteur
Mme Anne DOLBECQ, Directeur de Recherche (ILV Versailles)	Examinatrice
M Guillaume VIVES, Maître de Conférences (IPCM Paris)	Examineur
M Yves JOURNAUX, Directeur de Recherche (IPCM Paris)	Directeur de thèse
M Laurent LISNARD, Chargé de Recherche (IPCM Paris)	Invité

Acknowledgement

Firstly, I would like to deeply thank my thesis director, Pr. Yves Journaux and supervisor of thesis, Dr Laurent Lisnard for accepting me to do my PhD research and guiding me in the lab work and physical characterization. I am very appreciated for their continuous support, assistance, patience, motivation, humor and encouragement during my PhD research. In the four years study I really get countless scientific wealth from them. Also, they helped me a lot in writing this thesis, which could not go smoothly without their careful revision. Not only in science, they also cared about my daily life and provide their best to support me. As a foreign student, I am very appreciated for their enthusiasm and kindness.

Secondly, I would like to thank my committee members of defense: Mme. Carole Daiguebonne; M. Guillaume Rogez; Mme. Anne Dolbecq and M. Guillaume Vives for being as my committee members. I want to thank you for examining my thesis and providing your insightful comments and suggestions in my defense. Thank you very much.

In addition, I would like to thank all the professors and engineers including in my work: Mme YanLing Li who guides me in the area of SQUID measurement and data fitting and especially thanks for your help and guides to my PhD study and daily life ; Mme. Lise-Marie Chamoreau for her persistent efforts for XRD and instruction of diffractometer and Olex software; M. Geoffrey Gontard and M. Jérémy Forté for their helping in crystal structure resolution; M. Benoit Baptiste for his great job in the XPRD measurement and characterization. And very thanks to every teacher, professor and engineer who guide and help me in experiment.

Meanwhile, my PhD thesis work would never be possible without the support from our great ERMES team. I would like to say thanks to our great leader Prof. Rodrigue Lescouëzec and Dr. Benoit Fleury for their scientific instruction, valuable suggestion and countless help in the lab work. And all my former and current group members: Dr. Amina Benchora; Dr. Rémi Plamont; Dr. Jessica Flores; Dr. Juan Ramón Jiménez; Dr. Qui Pham; Jana Glatz and Maxime Fuchs. Thank you for all your help and It is really a happy time to work with you such nice colleagues.

I also would like to thank my two tutors of comité de suivi, M. Guillaume Vives and Mme. Marvaud Valérie for their advices, guidance and concern. Also, I would like to thank Prof. Miguel Julve and Prof. Francese Floret who come from Valencia University. I am very appreciated for your

warm hospitality and I really learned a lot both in chemistry and magnetism from you.

I would like to also thank all the French and Chinese friends I met. Thank you very much for being so nice and helpful to me and the unique friendship in France. Of course, I would like to thank the China Scholarship Council (CSC) for funding my PhD scholarship.

A special thanks to my friend SuMeng for always supporting and helping me with her kindness and care. It is my great fortune to meet you in Paris and it is a memorable time to be with you.

Last but not the least, I would to thank my family in China. My dear mother and father give their endless love, care, faith, support and understanding to me throughout my life. I would like to dedicate this thesis to my Family.

Ang Li

July 2019 in Paris

Contents

Chapter 1. Introduction	9
1.1 Molecular Magnetism	9
1.2 Magnetic Coordination Polymers	11
1.3 Metalloligand	12
1.4 Oxamate ligands	15
1.4.1 1D chains	17
1.4.2 2D networks	20
1.4.3 3D networks	22
1.4.4 Amino acid-based 3D networks	25
1.5 Aim of the work	28
References	32
Chapter 2. Bench reactivity screening, 0D complexes and 1D chain compound structural characterization and magnetic properties	43
2.1 General Introduction	43
2.2 Reactivity screening in aqueous and non-aqueous solutions	43
2.3 Structural and magnetic characterizations	45
2.3.1 Structure of $\text{Li}_2[\text{Cu}(\text{ohpma})(\text{OH})]\cdot 5\text{H}_2\text{O}$	45
2.3.2 Structure characterization of $\text{Li}_4[\text{Cu}(\text{paba})_2(\text{H}_2\text{O})]\cdot 9\text{H}_2\text{O}$	47
2.3.3 Structure and magnetic characterization of $\{(\text{HNEt}_3)[\text{Cu}(\text{ohpma})]\}$	48
2.3.4 Structure and magnetic characterization of $(\text{TMA})_3[\{\text{Co}^{\text{III}}(\text{ohpma})_2\text{Co}^{\text{II}}(\text{MeOH})_2\}_3]\cdot 10\text{H}_2\text{O}\cdot 5\text{MeOH}$	53
2.4 Conclusion	60
References	62
Chapter 3. Reactivity screening in solvothermal conditions and 1D chain compounds structural characterization and magnetic properties.	67
3.1 Reactivity screening	67
3.2 1D chain compound	70
3.2.1 Structure of $[\text{Cu}_4\text{Co}_3(\text{oaba})_4(\text{OH})_2(\text{DMF})_4]\cdot 3(\text{DMF})\cdot 2\text{H}_2\text{O}$	70
3.2.2 Magnetism of $\{\text{CuCo-oaba}\}$ chain	73
3.2.3 Structure of $[\text{Cu}(\text{ohpma})\text{M}(\text{OAc})(\text{DMF})_2]$ ($\text{M} = \text{Co}^{\text{II}}; \text{Mn}^{\text{II}}$)	74
3.2.4 $[\text{Cu}(\text{ohpma})\text{Co}_x\text{M}_y(\text{OAc})(\text{DMF})_2]$ ($\text{M} = \text{Mn}^{\text{II}}; \text{Ni}^{\text{II}}$)	76

3.2.5	Magnetism of {ohpma}-based chains	78
3.3	Conclusions	82
	Reference	83
Chapter 4. Synthesis, characterization and magnetic properties of an oxamato bridged		
	hetero-metallic 2D compound.	87
4.1	2D anionic compound.....	87
4.1.1	Synthesis and structural characterization of (TMA) ₃ [CuMn(paba) ₂ (OAc)]·7H ₂ O	87
4.1.2	Thermal studies of (TMA) ₃ [CuMn(paba) ₂ (OAc)]·7H ₂ O	91
4.1.3	Structural characterization of (TMA) ₃ [CuMn(paba) ₂ (OAc)].....	92
4.1.4	Magnetic Property.....	94
4.2	Conclusion.....	100
	References.....	101
Chapter 5. Synthesis, characterization and magnetic properties of oxamato bridged homo-		
	and hetero-metallic 3D compounds.	105
5.1	Homometallic 3D compound, [Mn(H ₂ O)(Hpaba)]	105
5.1.1	Synthesis and structural characterization of [Mn(H ₂ O)(Hpaba)].....	105
5.1.2	Magnetic Property of [Mn(H ₂ O)(Hpaba)]	110
5.2	Homometallic 3D compound, (TMA)[Cu(paba)]·1.5H ₂ O	112
5.2.2	Thermal Property of (TMA)[Cu(paba)]·1.5H ₂ O.....	116
5.2.3	Magnetic Property of (TMA)[Cu(paba)]·1.5H ₂ O	117
5.3	Heterometallic 3D compound, (TMA) ₂ [CuMn ₂ (ox)(paba) ₂](DMF)·3H ₂ O	119
5.3.1	Synthesis and structural characterization of (TMA) ₂ [CuMn ₂ (ox)(paba) ₂](DMF)·3H ₂ O	119
5.3.2	Thermal property of (TMA) ₂ [CuMn ₂ (ox)(paba) ₂](DMF)·3H ₂ O	122
5.4	Conclusion.....	126
	References.....	127
Conclusions and Perspectives		131
Appendix.....		135
	Content	135
	1. Ligands synthesis and characterisation.....	136
	2. Chapter 2 Bench reactivity screening, 0D complexes and 1D chain compound structural characterization and magnetic properties.....	149

3. Chapter 3 Reactivity screening in solvothermal conditions and 1D chain compounds structural characterization and magnetic properties.....	153
4. Chapter 4 Synthesis, characterization and magnetic properties of an oxamato bridged hetero-metallic 2D compound.....	158
5. Chapter 5 Synthesis, characterization and magnetic properties of oxamato bridged homo- and hetero-metallic 3D compounds.....	160
6. Instruments	166
7. BVS calculations	169
8. Crystallographic tables	172
References.....	186

Chapter 1:

Introduction

Chapter 1. Introduction

1.1 Molecular Magnetism

Molecular magnetism lies in the interdisciplinary crossing point between chemistry, physics and material science. It attracts quite a large number of chemists and physicists due to the potential applications in nanoscience¹. Over the past years, intense research efforts have been focus on molecule-based magnets (MBMs) for fundamental scientific studies as well as technological applications such as molecular spintronics, high-density data storage and quantum computing²⁻⁴. The first study of the magnetic property of a molecular complex can be dated back to 1952, and was done by Bleaney and Browsers. In their work they postulate the dimetallic structure of copper acetate due to the presence of a triplet EPR spectrum resulting from the interaction between the single electrons of the two copper ions⁵. Then Oliver Kahn, with its pioneer work, developed the theoretical model which emphasized the importance of overlap between magnetic orbitals. In the case of an interaction between two magnetic centers each containing one single electron, the coupling constant, J , can be expressed by $J = 2K + 4\beta S$; with K the exchange integral between the two electron ($K > 0$), S the overlap integral ($S > 0$) and β the transfer integral ($\beta < 0$) with

$$K = \langle A(1)B(2) | r_{12}^{-1} | A(2)B(1) \rangle$$

$$\beta = \langle A(i) | h(i) | B(i) \rangle$$

$$S = \langle A(i) | B(i) \rangle$$

Where $h(i)$ is the one electron Hamiltonian for electron i and r_{12} is the interelectronic distance. When the orbitals are orthogonal, $J > 0$ and the interaction is ferromagnetic; when the orbitals overlap, $J < 0$, the interaction is antiferromagnetic⁶⁻⁸.

The discovery of single molecule magnets (SMM) gave another major boost to the molecular magnetism scientific area. A single molecule magnet is a molecule that can retain its magnetisation in the absence of magnetic field under a blocking temperature (T_B), resulting in magnetic hysteresis loops and slow relaxation of the magnetization. The first SMM was reported by Sessoli R^{9,10} with the $[\text{Mn}_{12}\text{O}_{12}(\text{O}_2\text{CMe})_{16}\text{H}_2\text{O}_4]$ complex, known as $\{\text{Mn}_{12}\}$, shown in figure 1.1(a). A ferromagnetic interaction between the four central paramagnetic Mn^{IV} ions ($S = 3/2$) was observed, as well as between the eight peripheral Mn^{III} ions ($S = 2$). However, the central Mn^{IV} interact anti-ferromagnetically with the peripheral Mn^{III} . Consequently, its total ground state spin S is 10. Hysteresis loop and frequency-dependent out-of phase (χ'') signal in alternating current (AC) susceptibility were observed. This discovery prompted intense work on 3d transition metal based SMM as well as 4f lanthanide-based SMM because of their large magnetic moment and

anisotropy^{11,12}. Furthermore, SMMs illustrate well the many advantages molecular chemistry offers in a “bottom-up” approach to the preparation of nanoscale magnetic materials. Recently, a novel dysprosium metallocene cation SMM $[(\eta^5\text{-Cp}^*)\text{Dy}(\eta^5\text{-Cp}^{i\text{Pr}5})][\text{B}(\text{C}_6\text{F}_5)_4]$ ($\text{Cp}^{i\text{Pr}5}$ = penta-isopropylcyclopentadienyl, Cp^* = pentamethylcyclopentadienyl) was reported with a blocking temperature near 80 K. It is the first example of an SMM working above the liquid nitrogen temperature (Figure 1.2)¹³.

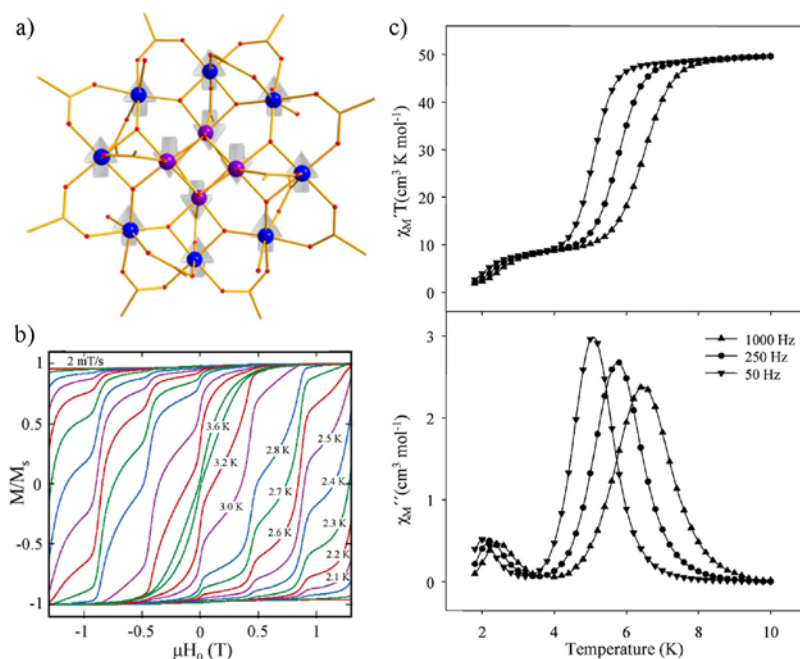


Figure 1.1 (a) The structure of $[\text{Mn}_{12}\text{O}_{12}(\text{O}_2\text{CMe})_{16}\text{H}_2\text{O}_4]$. (b) Hysteresis of Mn_{12} -BrAC complex. (c) AC susceptibility of Mn_{12} -BrAC complex, Reproduced from Ref^{9,11,12}.

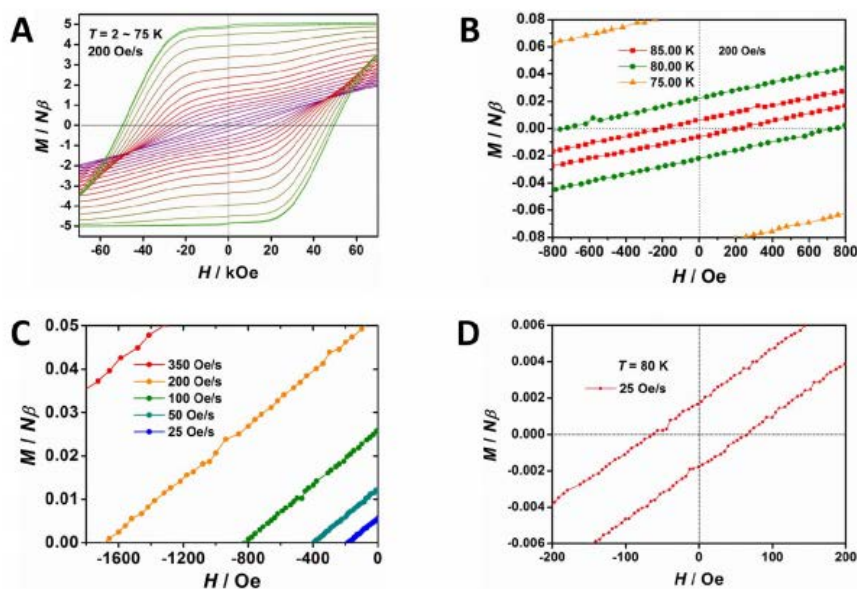


Figure 1.2 Hysteresis loop of $[(\eta^5\text{-Cp}^*)\text{Dy}(\eta^5\text{-Cp}^{i\text{Pr}5})][\text{B}(\text{C}_6\text{F}_5)_4]$ at different temperatures and various field sweep rate, Reproduced from Ref¹³.

1.2 Magnetic Coordination Polymers

With the exception of the very recent and specific example presented above, magnetic coordination polymers (MCPs) have the advantage of displaying appealing magnetic properties at higher temperatures. Whether it is a blocking temperature for one-dimension (1D) compounds, or the occurrence of spontaneous magnetization in two-dimension (2D) and three-dimension (3D) systems.

Besides, when looking at CPs chemistry, porous CPs (ie. metal-organic framework, MOF¹⁴) have been the focus of intensive research, and have largely proved their appeal for the diverse properties and applications they offer¹⁵⁻¹⁹. The preparation of porous MCPs represents therefore an attractive target as a class of multifunctional molecular materials. And more generally, the association of magnetic properties to one or more additional properties, such as conductivity, luminescence, chirality or photoactivity is intensively looked at²⁰⁻²⁶.

Synthetically, MCPs rely on the adequate choice of both organic linkers and metal ions, so that sufficient control over dimensionality is reached, while fulfilling the necessary requirements for the occurrence of the targeted magnetic properties. In 1D systems behaving as single-chain magnets (SCMs), a blocking of the magnetization requires the presence of anisotropic magnetic ions^{27,28}, while the occurrence of long-range ordering implies non-isolated 1D systems with cooperative interchain interaction. Magnetic ordering will occur only in 2D systems with easy axis magnetic anisotropy (Ising model). In 3D MCPs, both isotropic (Heisenberg model) and anisotropic (easy axis or easy plane) systems can display magnetic ordering^{29,30}. In all cases, the ligands must efficiently promote interaction between magnetic centers.

In 1D polymers, researchers made use of transition metal ions and lanthanide ions with strong anisotropy as paramagnetic centers, bridged through small organic linkers such as azide^{31,32}, carboxylate^{31,33}, oxalate³⁴, cyanide³⁵ or organic radicals³⁶⁻³⁹. Then homo- or hetero-metallic SCM were synthesized with blocking temperature just below 20K. The same small polyatomic linkers have been used to prepare 2D and 3D MCPs, where a higher ordering temperature is expected. In terms of coordinating ability, these ligands afford multiple binding directions and cyanide (including its derivatives, dicyanamide and tricyanomethanide), azide, oxalate or carboxylate ligands have successfully led to 2D or 3D MCPs (Figure 1.3)^{31,40-49}. These bridges are excellent magnetic couplers and can promote moderate to strong ferro- and antiferromagnetic magnetic interactions. Their bridging modes to transition metal centers are very rich, which lead to various structures with interesting magnetic properties^{31,42,44-46}. However, diversity in coordination modes can also bring some obstacles to a well-controlled design over the structure and the magnetic behavior. Typical synthesis routes rely mostly on serendipity and usually suffer from unplanned architectures and/or

compositions. For example, the construction of heterometallic CPs can be uncertain, especially when metal ions have to be introduced simultaneously^{20,50,51}.

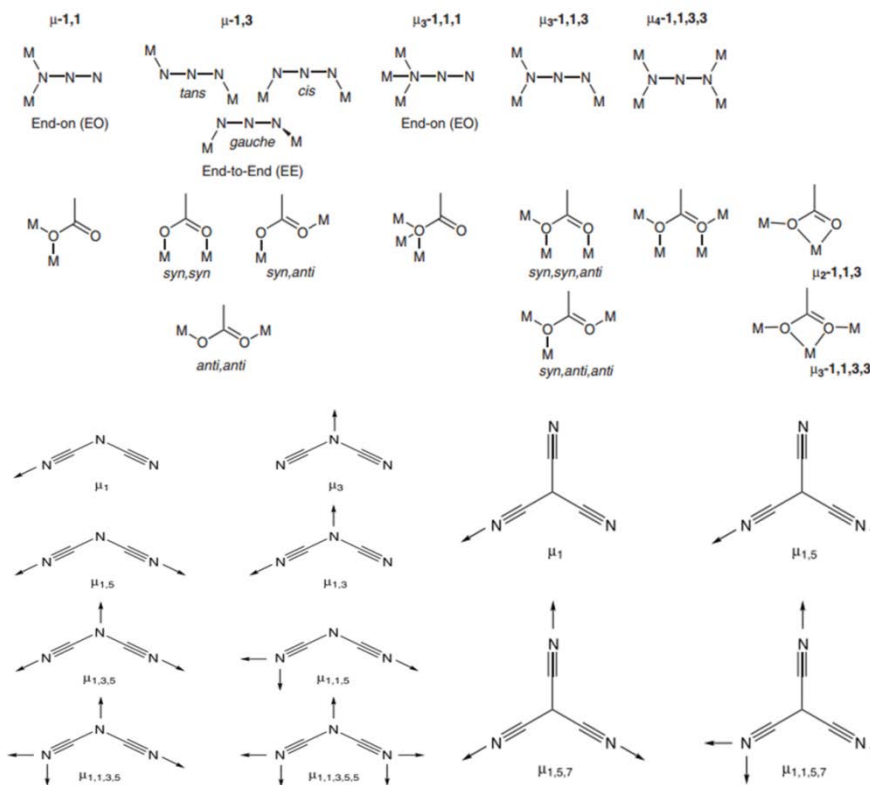


Figure 1.3 Coordination modes of selected groups (azide, carboxylic acid, dicyanamide, tricyanomethanide) which are commonly used in nD multidimensional CPs (n = 0, 1, 2) Reproduced from Ref^{31,46}

In order to overcome some of the drawbacks presented above, a more rational design and synthesis strategy, known as “complex-as ligand”, in which a metalloligand is prepared and used in a multi-step approach, can be applied for MCPs preparation.

1.3 Metalloligand

A metalloligand can be defined as a metallic complex capable of making further coordination bonds with secondary metal ions^{26,52–54}. Besides the available coordination sites, the directionality of the additional bonds, the relative conformational rigidity, the stability to withstand subsequent synthetic manipulations, and the potential for further structural modulation are ideal features for a metalloligand^{52,53}. By playing with the metal ion geometry, the nature of the coordination group, and the nature of the additional metal ion (solvated, partially blocked), this molecular ‘programmed self-assembly’ strategy could lead the target compounds to desired dimensionality, from 0D to 3D^{55–58}.

Overall, the ‘complex-as-ligand’ strategy is efficient for the rational design of multi-dimensional networks which are structurally controlled. It is also an especially favorable method to construct

heterometallic systems, which are attractive when investigating MCPs. When two interacting magnetic centres are not identical, whatever the nature of the interaction is ferro or antiferromagnetic coupling, a leftover magnetic moment at low temperature is obtained.

For instance, the oxalate-based metalloligand $[M^{III}(ox)_3]^{3-}$, is able to afford both 2D and 3D networks when associated with a divalent metal ions: $(Cat)[M^II M^{III}(ox)_3]$ ($Cat = cation$). In these MCPs the oxalato ion plays a double role: first it acts as structuring agent and second, it transmit efficiently the electronic interaction^{59–61}. Noticeably, the counter-ion here acts not only in keeping electroneutrality but also as a templating guide that determines the final network's dimensionality. Using tetrabutylammonium, the 2D honeycomb-like structure was obtained for the $[NBu_4][M^II Cr(ox)_3]$ compounds ($M^{II} = Mn, Fe, Co, Ni, Cu, Zn$). They present a ferromagnetic ordering from 6 to 12K. In contrast, with chiral tris or bis-bipyridyl complexes as counter-cations, 3D oxalate-based enantiopure families have been successfully synthesized. Regularly alternating chirality ($\Delta\Lambda$) of the two octahedral coordinated metal ions comprises the 2D honeycomb network (Fig 1.4 a), while the 3D MCPs are composed of homochiral metal ions. The increase in dimensionality is caused by the asymmetric nature of the counter-ion and the existence of only one diastereoisomeric building block. The templating complexes set the $[M^{III}(ox)_3]^{3-}$ metalloligands into one configuration, preventing thus the growing into 2D planes and leading to the 3D network, with a homochiral configuration ($\Delta\Delta$ or $\Lambda\Lambda$, Figure 1.4 b)^{61–63}.

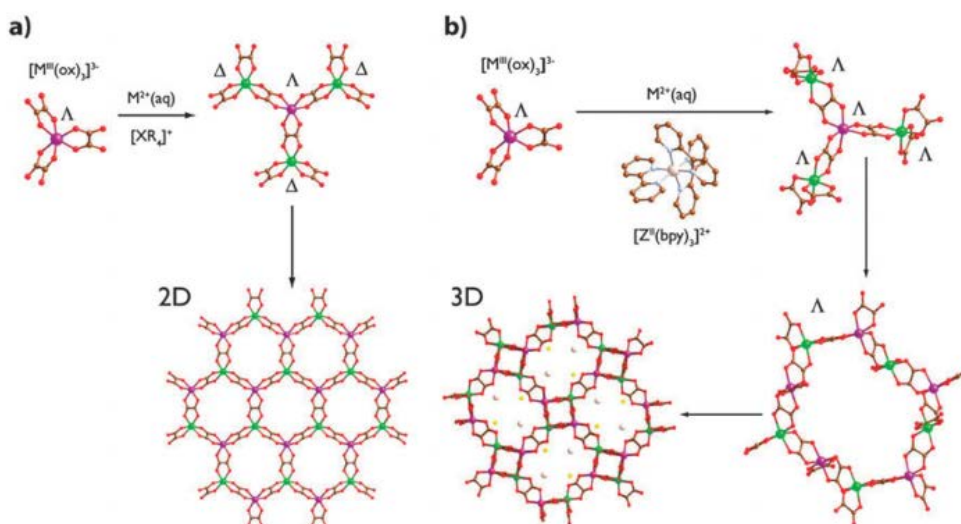


Figure 1.4 2D heterochiral (a) and 3D homochiral (b) oxalate-based architectures depending on the nature of the cation used to template their assembly from $[M^{III}(ox)_3]^{3-}$ metalloligand. Reproduced from Ref⁶¹.

Another widely researched family of metalloligands used to build heterometallic MCPs is that of cyanidometallates. As a bridging ligand, cyanide plays a crucial role for the preparation of

switchable magnets due to its electron transfer property. In MCPs built from hexa- or octa-cyanidometallaes, $(\text{Cat})_x\text{A}^{\text{II}}[\text{B}^{\text{III}}(\text{CN})_6]_y$ and $\text{A}^{\text{II}}_2[\text{B}^{\text{IV}}(\text{CN})_8]$ (Cat: alkali ion), it can mediate the electron transfer from $(\text{A}^{\text{n}}\text{-NC-B}^{\text{m}}\text{-CN-})$ to $(\text{A}^{\text{n-1}}\text{-NC-B}^{\text{m+1}}\text{-CN-})$ under external stimuli such as irradiation, heat or pressure, named metal to metal charge transfer (MMCT) effect (Figure 1.5)^{21,64–68}.

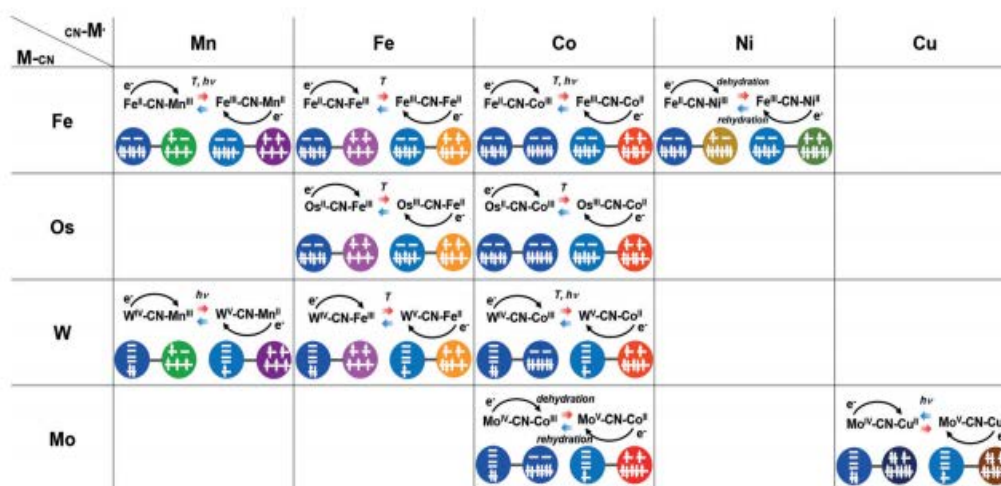


Figure 1.5 Illustration of various external stimuli-tuned MMCT and MMCT-coupled spin transition with $\text{A}^{\text{n}}\text{-NC-B}^{\text{m}}$ linkages. Reproduced from Ref⁶⁸

Furthermore, investigations on the first reported photomagnetic Prussian blue analogue, $\{\text{CoFe}\}^{69}$, have shown that the photomagnetic property of the Prussian blue analogue network family strongly depends on the nature and amount of the inserted alkali cation (Figure 1.6)^{70–72}.

Cyanidometallate-based MCPs of lower dimensionality are also known^{73–76} and some of them display photomagnetic properties. For example, photomagnetism was observed in the 2D compound $\text{Cs}[\{\text{Co}(3\text{-cyanopyridine})_2\}-\{\text{W}(\text{CN})_8\}]\cdot\text{H}_2\text{O}$ with a bistable phase transition from $\{\text{Co}^{\text{III}}_{\text{LS}}\text{W}^{\text{IV}}\}$ ($S = 0$) to $\{\text{Co}^{\text{II}}_{\text{HS}}\text{W}^{\text{V}}\}$ (Fig 1.6)⁷⁷ (Fig 1.6) ($S = 2$). O. Sato *et al.* also reported in a 1D double zig-zag chain a photoinduced transformation from diamagnetic $\text{Fe}^{\text{II}}_{\text{LS}}(\mu\text{-CN})\text{Co}^{\text{III}}_{\text{LS}}$ to metastable paramagnetic $\text{Fe}^{\text{III}}_{\text{LS}}(\mu\text{-CN})\text{Co}^{\text{II}}_{\text{HS}}$ under irradiation at 10K. The paramagnetic phase showed a SCM behavior and the reverse MMCT transformation can be thermally switched (Figure 1.6)⁷⁸.

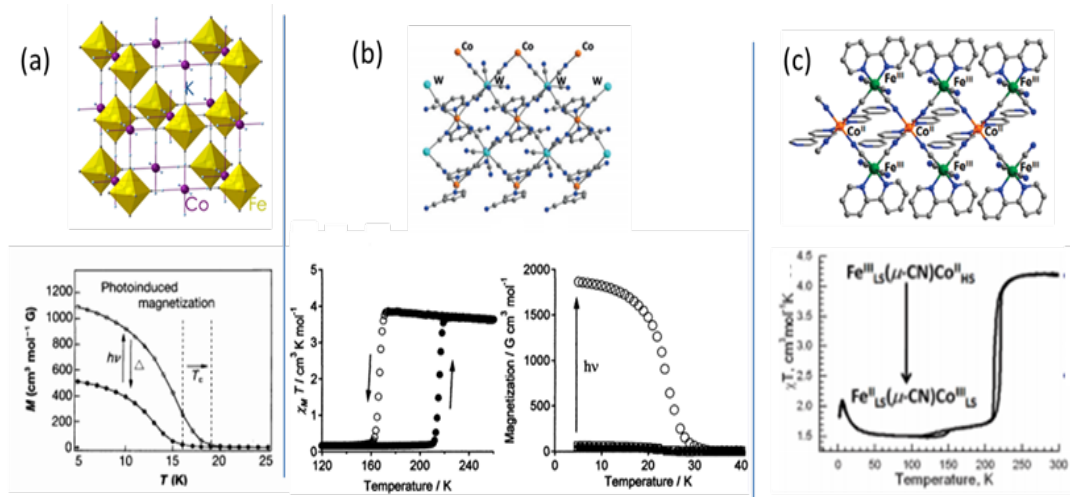


Figure 1.6 (a) Scheme of a Fe/Co Prussian blue analogue and photomagnetic effect shown by temperature dependence of magnetization. (b) Structure of $\text{Cs}[\{\text{Co}(3\text{-cyanopyridine})_2\}-\{\text{W}(\text{CN})_8\}]\cdot\text{H}_2\text{O}$ and its Temperature dependence of $\chi_M T$ value and field-cooled magnetization curve before irradiating with light and after thermal treating. (c) Structure of $\{[\text{Fe}(2,2'\text{-bipyridine})(\text{CN})_4]_2\text{Co}(4,4'\text{-bipyridine})\} \cdot 4\text{H}_2\text{O}$ and its temperature dependence of $\chi_M T$. Reproduced from Ref^{68,77,78}

1.4 Oxamate ligands

Oxamate based N-substituted ligands are known as excellent candidates for the synthesis of heterometallic MCPs. From the point view of coordination chemistry, the planar oxamate group has amide nitrogen and carboxylic oxygen atoms on one side and two carbonyl oxygen atoms on the other side, which is suitable for the 'complex-as-ligand' strategy. To date, the bis-bidentate $[\text{CuL}_2]^{2-}$ and tetrakis-bidentate $[\text{Cu}_2\text{L}_2]^{4-}$ moieties are the most commonly used metalloligand in oxamate chemistry^{79–82}. The amide nitrogen and carbonyl oxygen atoms show excellent coordination affinity to 3d transition metal ions, especially for the divalent ions (Cu^{2+} , Co^{2+} , Mn^{2+} , Ni^{2+} ...), forming robust building blocks. The reaction of additional metal ions to the free carbonyl oxygen atoms completes what constitutes an efficient multi-step synthesis process for heterometallic coordination polymers. The wide choice of possible substituents on the nitrogen atom of the oxamate group represents a valuable synthetic tool (Figure 1.7 and Table 1.2). It facilitates structural modifications, such as the introduction of bulky groups or the preparation of polymetallic metalloligands with different connectivities. It also greatly favors the introduction of additional physical properties, such as chirality⁸³, luminescence⁸⁴, photo- and redox-activity^{85–87} or pH-triggered switches⁸⁸.

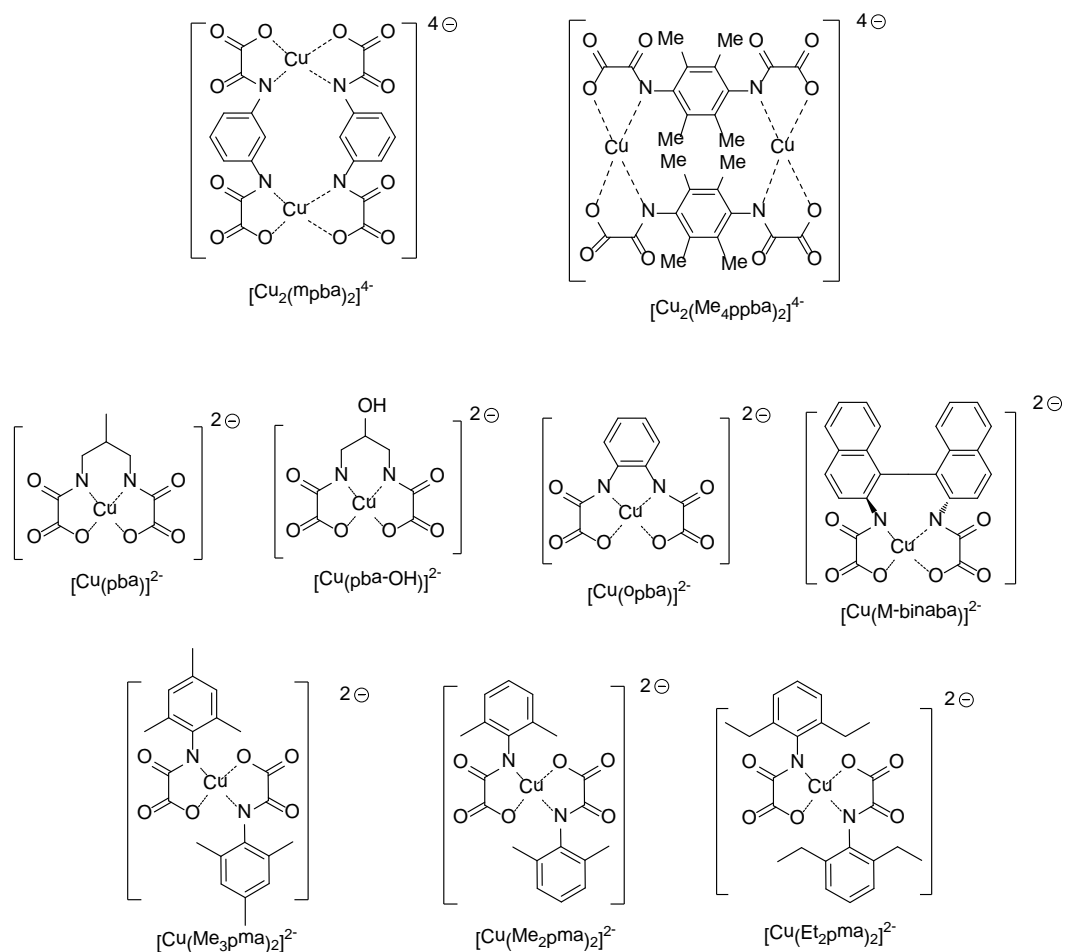


Figure 1.7 Scheme of the oxamato-bridged metalloligands involved in preparation of multi-dimensional MCPs

<i>Abbreviation</i>	<i>Chemical name</i>
H ₄ .mpba	m-phenylenebis(oxamato)
H ₄ .Me ₄ ppba	2,3,5,6-tetramethyl-N,N'-1,4-phenylenebis(oxamate);
H ₂ .Me ₂ pma	N-2,6-dimethylphenyloxamate
H ₂ .Me ₃ pma	N-2,4,6-trimethylphenyloxamate
H ₂ .Et ₂ pma	N-2,6-diethylphenyloxamate
(M)H ₄ .binaba	(M)-1,1'-binaphthalene-2,2'-bis(oxamate)
H ₄ -opba	orthophenylenebis(oxamato)
H ₄ -pba	1,3-propylenebis(oxamato)
H ₄ -pba-OH	2-hydroxy-1,3-propylenebis(oxamato)

Table 1.2 Abbreviation codes and their corresponding chemical name of oxamate ligands precursors used in preparing metalloligands.

In terms of magnetism, the bidentate oxamate bridging group can mediate a strong magnetic coupling between paramagnetic ions. The homometallic antiferromagnetic coupling constant J ranges from -400cm^{-1} to -20 , for Cu^{II} and Ni^{II} respectively^{7,89}. For heterobimetallic systems, J values

are found between -80 and -120 cm^{-1} for $\text{Cu}^{\text{II}}/\text{Ni}^{\text{II}}$ ^{90,91}, -23 and -37 cm^{-1} for $\text{Cu}^{\text{II}}/\text{Mn}^{\text{II}}$ ^{90,92} and range from -35 to -48 cm^{-1} for $\text{Cu}^{\text{II}}/\text{Co}^{\text{II}}$ ⁸⁰. In case of polyoxamate ligands linked by substituted benzene scaffold with different oxamate position pattern, the copper ions are coupled by spin polarisation mechanism. A ferromagnetic coupling between the two far placed metal center can be observed if number of atoms between these two center is odd ($2n+1$), shown in Figure 1.8. This configuration leads to an alternation of the sign of the spin density on the unpaired electrons^{93–95}.

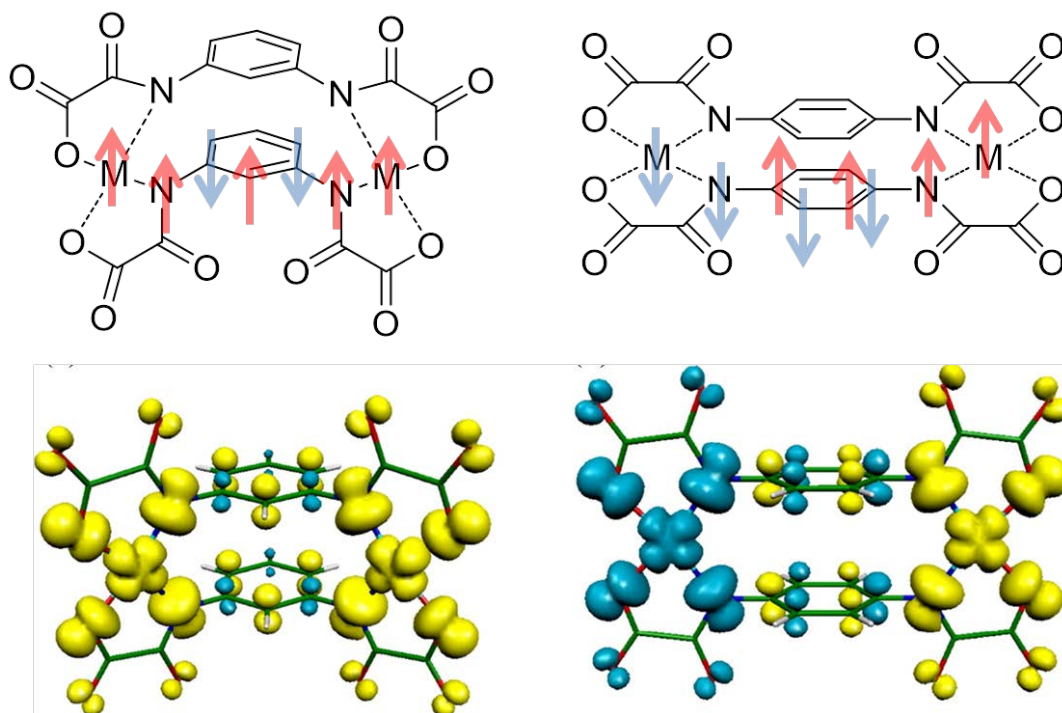


Figure 1.8 Up: structures of the meta and para cyclophane-type anionic dinuclear units and their alternating spin polarization. Down: Spin density distributions and spin states of meta and para anionic dinuclear units. Yellow and blue contours represent positive and negative spin densities, respectively.

In the following part, we will introduce briefly the oxamate-based MCPs.

1.4.1 1D chains

From the existing results in the literature, all oxamate-based 1D chains have so far been obtained with Cu^{II} metalloligand coordinating Mn^{II} or Co^{II} metal ions. In the heterometallic chains, the Cu^{II} metal ions are four-coordinate in square planar geometry to the amide nitrogen and carboxylate oxygen from the two adjacent oxamate ligands, or five-coordinate with an additional solvent molecule (DMSO, H_2O , DMF) in the apical position. The Co^{II} or Mn^{II} ions adopt an octahedral geometry. They are coordinated to four carbonyl oxygen atoms from two oxamate ligands and two solvent molecules complete the coordination sphere. Two shapes of chains are observed: linear and zigzag. This is related to the configuration adopted by the octahedral metal ion configuration, *trans*

or *cis*, most probably to primarily accommodate any steric hindrance caused by the ligand. The linear chain is observed for metal ions in *trans* geometry, zigzag chain for the *cis* one.

The first examples of 1D oxamate-based chains were obtained with the ligands {pba} and {pbaOH} (see Figure 1.9) as {Cu-Mn} bimetallic zigzag chains. The two analogues, $[\text{MnCu}(\text{pba})(\text{H}_2\text{O})_3] \cdot 2\text{H}_2\text{O}$ and $[\text{MnCu}(\text{pbaOH})(\text{H}_2\text{O})_3]$ ^{57,96}, have very similar chain structures but are slightly different as to the relative position of the chains within the lattice due to hydroxyl group and co-crystallized water molecules. In the high temperature range, both compounds show typical ferrimagnetic chain behaviour due to the intra-chain antiferromagnetic coupling between copper and manganese ions. However, in the low temperature range, antiferromagnetic ordering was observed for compound $[\text{MnCu}(\text{pba})(\text{H}_2\text{O})_3] \cdot 2\text{H}_2\text{O}$ due to the interchain antiferromagnetic coupling, while ferromagnetic interchain ordering was seen for $[\text{MnCu}(\text{pbaOH})(\text{H}_2\text{O})_3]$, with T_c at 4.7 K due to the interchain ferromagnetic coupling (T_c is the Curie temperature where magnetic ordering happens). This is due to the different spatial disposition in the lattice, highlighting the role of intermolecular interactions. Indeed, a partially desolvated phase, $[\text{MnCu}(\text{pbaOH})(\text{H}_2\text{O})_2]$ ⁹⁷ where the Cu^{II} loses its H_2O molecule, shows an important increase of T_c to 30K, while introduction of additional H_2O molecules, $[\text{MnCu}(\text{pbaOH})(\text{H}_2\text{O})_3] \cdot 2\text{H}_2\text{O}$ ⁹⁸, gave an antiferromagnetic ordering with $T_N = 2.4\text{K}$, as well as metamagnetic behavior. With applied fields larger than 0.9 KOe, the antiferromagnetic interchain interaction is overcome, and the compound moved to a ferromagnetic phase.

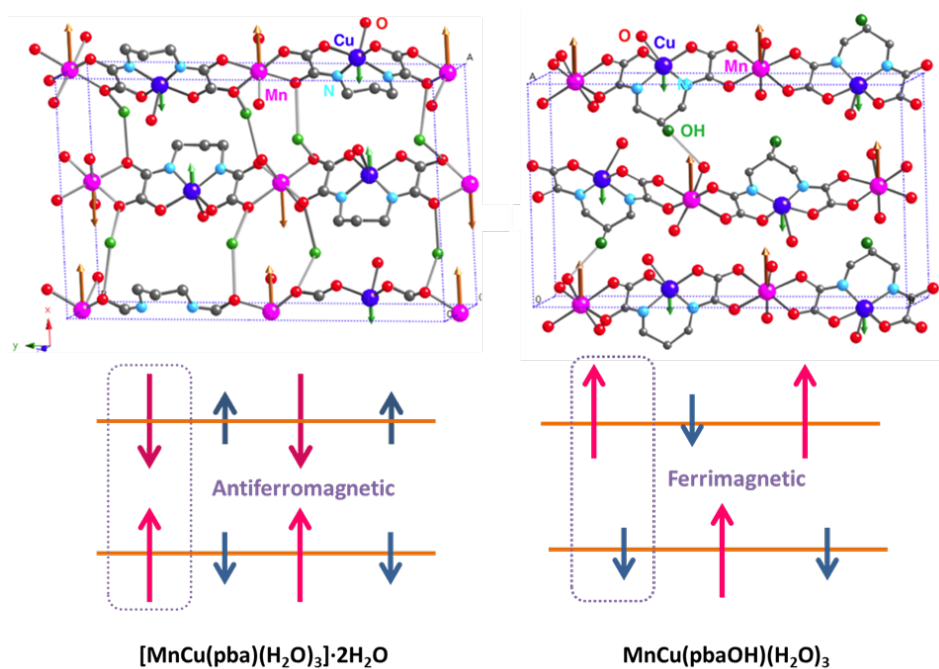


Figure 1.9 Perspective views of the two 1D CPs $[\text{MnCu}(\text{pba})(\text{H}_2\text{O})_3] \cdot 2\text{H}_2\text{O}$ and $[\text{MnCu}(\text{pbaOH})(\text{H}_2\text{O})_3]$ in the lattice and magnetic scheme of their corresponding interchain action.

Following the ‘complex as ligand’ strategy, opba, Me₂pma, Me₃pma, and binaba aromatic oxamate ligands were successfully used to prepare the [CuL]²⁻ or [CuL₂]²⁻ metalloligands and synthesize chains^{80,83,99} (Figure 1.10). The heterometallic chains [CoCu(Me₃pma)₂(H₂O)₂] \cdot 4H₂O and [CoCu(binaba)(DMF)₂] \cdot DMF both show SCM properties with $T_B = 3.5$ K and 1.8 K.

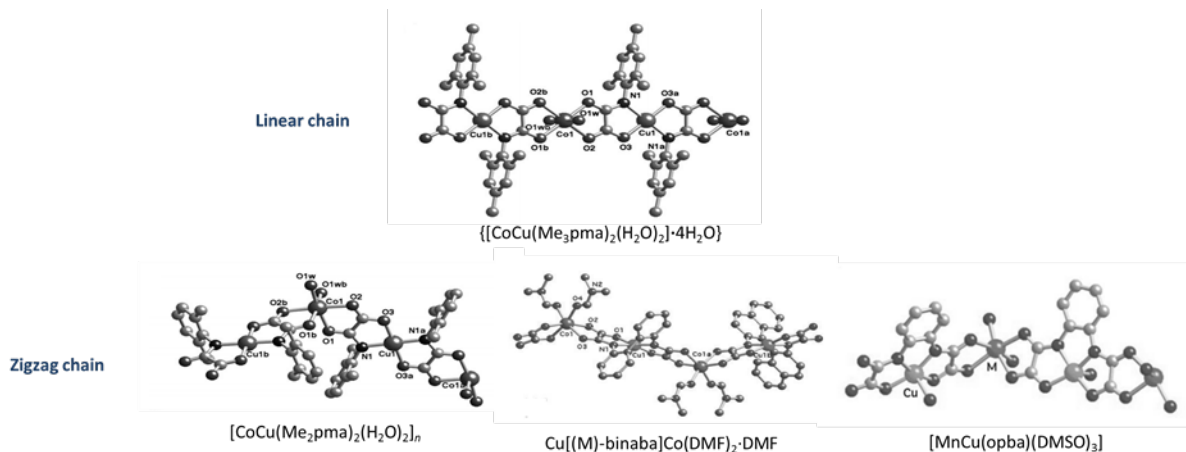


Figure 1.10. Views of fragments of aromatic oxamate-based chains sorted by the shape of chain^{80,83,99}.

In most zigzag chains, octahedral metal ions alternate Δ and Λ configurations leading to achiral chains. However, the use of the chiral H₂Et₂binaba ligand has led to the formation of chiral zigzag chains where the configuration of the octahedral metal ion does not alternate: [Co(Λ)Cu(M)-(binaba)(DMF)₂] \cdot DMF and [Co(Δ)Cu(P)-(binaba)(DMF)₂] \cdot DMF. Theoretically, the formation of helicoidal chiral chains should be possible with achiral ligands, if the configuration of the octahedral metal ions remain fixed (Figure 1.11). So far, there is however no example of such an heterometallic chain with oxamate ligands.

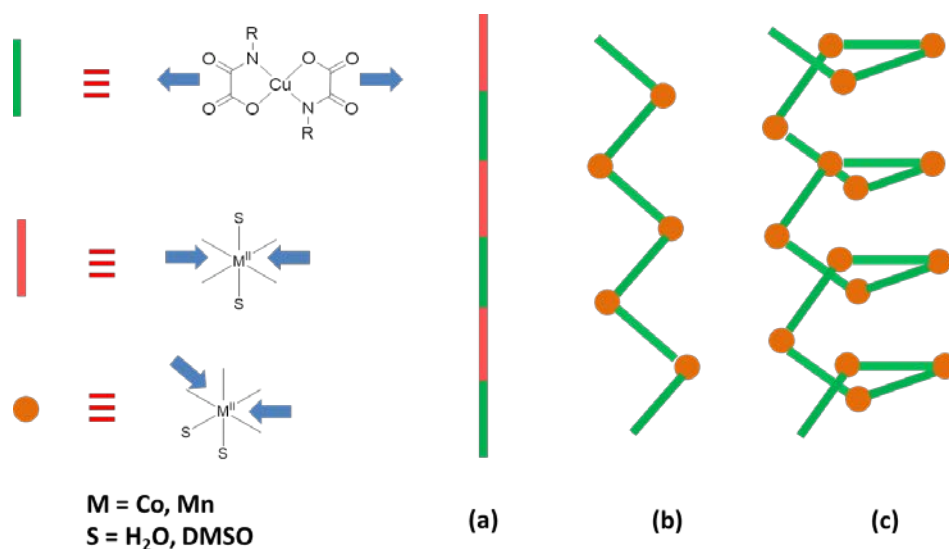


Fig 1.11 Proposed structure of oxamate heterobimetallic chain (a) linear chain (b) zigzag chain (c) helical chain.

1.4.2 2D networks

We summarized that there are mainly two different kinds of 2D planes based on oxamate metalloligand, brick-wall and honeycomb, and one derivative form, an interlocked honeycomb plane. Both mono- and bisoxamate ligands can lead to 2D structures (see Figure 1.12).

All brick-wall neutral structures come from phenylenebisoxamate ligands and their corresponding bimetallic metalloligands $[\text{Cu}_2(\text{L})_2]^{4+}$ ($\text{L} = \text{mpba}$ and Me_4ppba). The coordination geometries of Cu^{II} and M^{II} ($\text{M} = \text{Mn}, \text{Co}$) are similar to that of the geometries in the 1D chain, and the 2D structure can be interpreted as 1D linear or zigzag neutral $\{\text{Cu-oxamate-M}\}$ chains linked by the phenylene groups. The brick-wall structure affords an oxamate-phenyl-oxamate scaffold that is suitable for spin polarization mechanism, making its magnetic properties tunable.

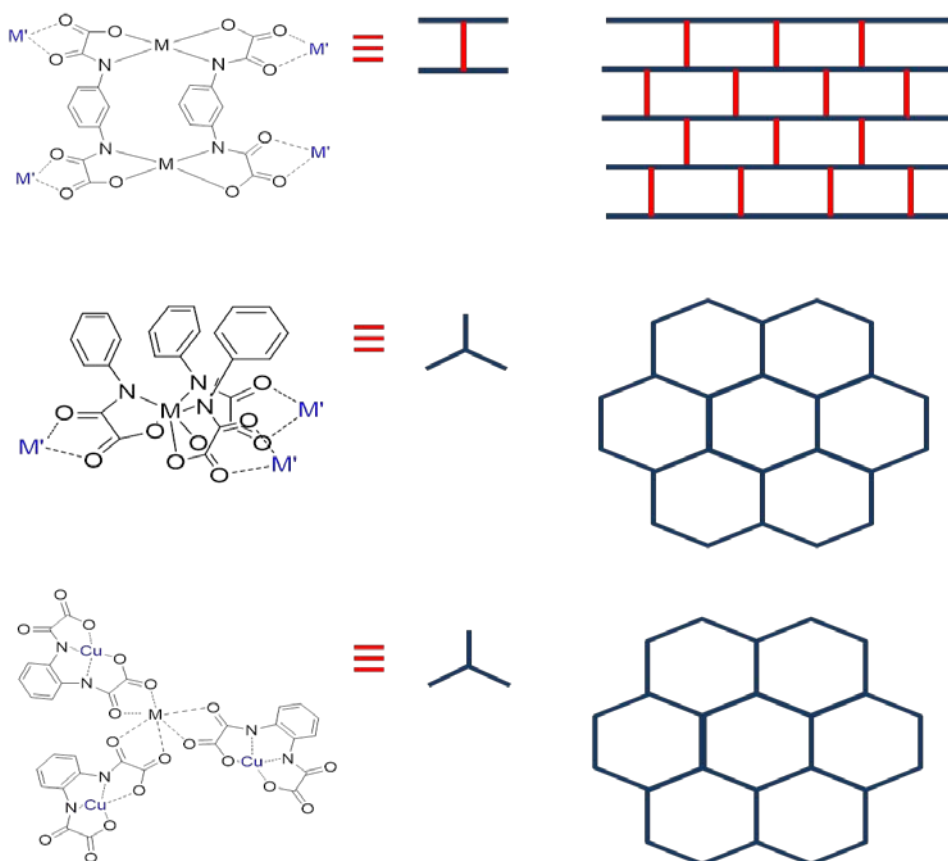


Figure 1.12 Oxamate-bridged bimetallic coordination polymers from metal-mediated self-assembly, brick-wall and honeycomb planes¹⁰⁰.

The first oxamate-based brick-wall compound was $[\text{Co}_2\text{Cu}_2(\text{mpba})_2(\text{H}_2\text{O})_6] \cdot 6\text{H}_2\text{O}$, with water molecules coordinated to Co^{II} ion in *trans* configuration. It behaves as a metamagnet, and a 1.2 KOe applied field is necessary to overcome antiferromagnetic interactions between the ferrimagnetic planes¹⁰¹. Another 2D MCP, $[\text{Mn}_2\text{Cu}_2(\text{Me}_4\text{ppba})_2(\text{H}_2\text{O})_6] \cdot 8\text{H}_2\text{O}$, shows at low temperature a strong

antiferromagnetic interaction that results from the Cu^{II} ions across the double *p*-phenylene spacers through the spin polarization mechanism¹⁰² (Figure 1.13).

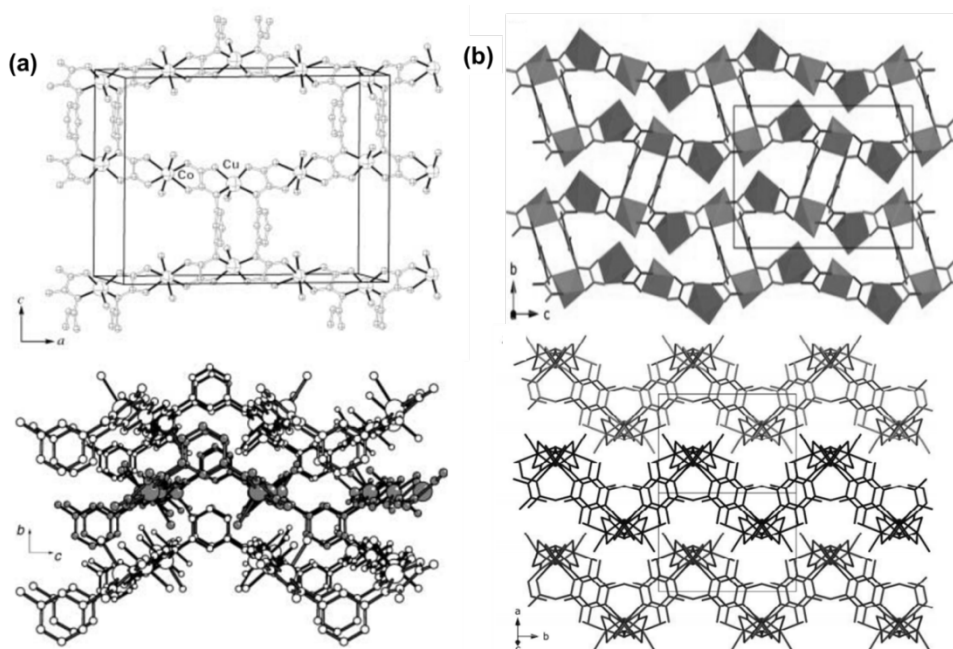


Figure 1.13 Projection view of the 2D neutral network of $[\text{Co}_2\text{Cu}_2(\text{mpba})_2(\text{H}_2\text{O})_6]$ (a), and $[\text{Mn}_2\text{Cu}_2(\text{Me}_4\text{ppba})_2(\text{H}_2\text{O})_6]$ (b) along the *y* and *x* axis and view of the packing of corrugated 2D sheets^{101,102}.

Considering the *cis* configuration of the octahedral metal ions in the zig-zag chains, the two solvent molecules could be replaced by another oxamate group. This corresponds to an anionic $\{[\text{Cu}^{\text{II}}(\text{oxamate})_2]_{3/2}\text{M}^{\text{II}}\}^-$ honeycomb network, and where counter-cations are needed to keep the electroneutrality. An typical example is $(n\text{-Bu}_4\text{N})_4[\text{Mn}_4\text{Cu}_6(\text{Me}_2\text{pma})_{12}(\text{DMSO})_2] \cdot 8\text{DMSO} \cdot 2\text{H}_2\text{O}$, which consists of $\{\text{Mn}^{\text{II}}_6\text{Cu}^{\text{II}}_6\}$ hexagonal units, with triple oxamate-coordinated Mn^{II} ions extending in three direction to afford the network. As in the 1D zigzag chain, Δ and Λ Mn isomers alternate regularly in this topology. Noticeably, to avoid the formation of its 1D analogue chain, a large excess of Mn (Mn:Cu = 5:1) has been used instead of the 1:1 stoichiometry for the chain¹⁰³.

Historically however, the first reported oxamate-based honeycomb 2D network display a more complex structure. The compound was obtained with methylpyridinium-nitronylnitroxide radicals as cations, which connect interpenetrated hexagonal networks, $(\text{Me-rad})_2[\text{Mn}_2(\text{Cu}(\text{opba})_3(\text{DMSO})_2) \cdot 2\text{H}_2\text{O}]^{104}$. Other derivatives of the polycatenated network were later obtained using ethylpyridinium-nitronylnitroxide radicals as well as Ni^{II} or Co^{II} ions besides Mn^{II} , increasing the magnetic ordering temperature from 22.5 to 37 K¹⁰⁵ (Figure 1.14).

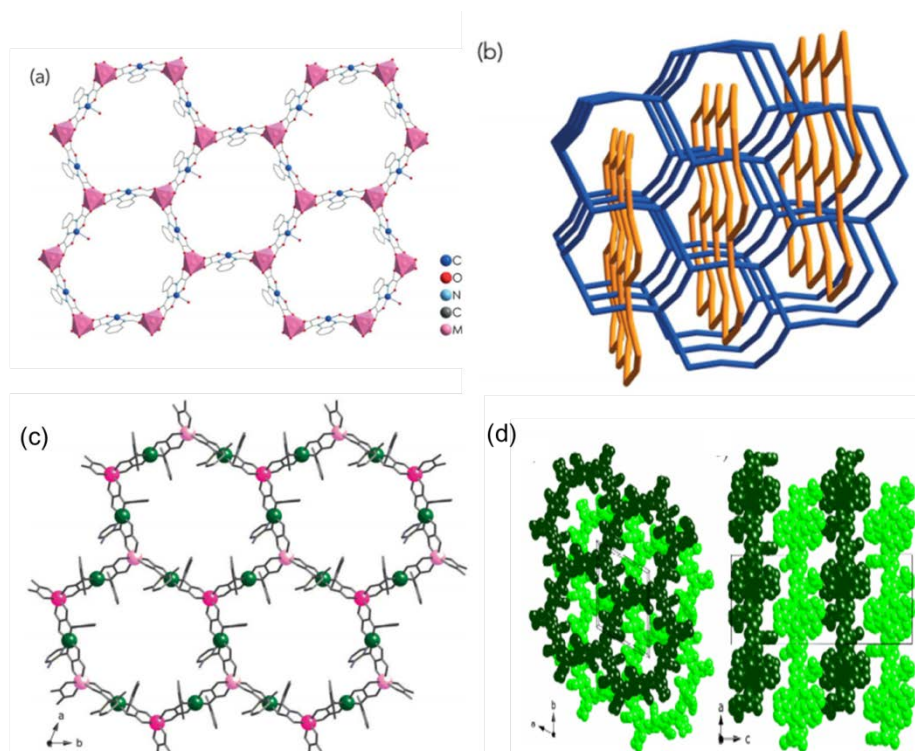


Figure 1.14 (a) View of the 2D honeycomb layer $\{\text{Mn}_2(\text{Cu}(\text{opba})_3(\text{DMSO})_2)\}$, (b) and its polycatenated structure. (c) View of the $\{\text{Mn}_4\text{Cu}_6(\text{Me}_2\text{pma})_{12}(\text{DMSO})_2\}$ honeycomb network, with Mn^{II} ion isomers ($\Delta\Lambda$) represented by purple and pink respectively. (d) Perspective view of the packing of the adjacent layers in $\{\text{Mn}_4\text{Cu}_6(\text{Me}_2\text{pma})_{12}(\text{DMSO})_2\}$ ^{104,106}

1.4.3 3D networks

In terms of design, the hexakis(bidentate), triple-stranded dinuclear metalloligand $[\text{M}^{\text{II}}_2(\text{mpba})_3]^{8-}$ ($\text{M}=\text{Ni}^{\text{II}}, \text{Co}^{\text{II}}, \text{Mn}^{\text{II}}$) is appealing for the preparation of 3D MCPs. In this meso-helicate-type complex, two octahedral metal-tris(oxamate) moiety with different chirality ($\Delta\Lambda$) are connected by three *meta* substituted phenylene spacers. The latter would act as pillars, ferromagnetically coupling the oxamato-bridged $\{\text{M}'_{3/2}\text{M}\}$ hexagonal layers through the spin polarization mechanism. Unfortunately, attempts to crystallize the network have only succeeded with monovalent lithium cations for M' (Figure 1.15).

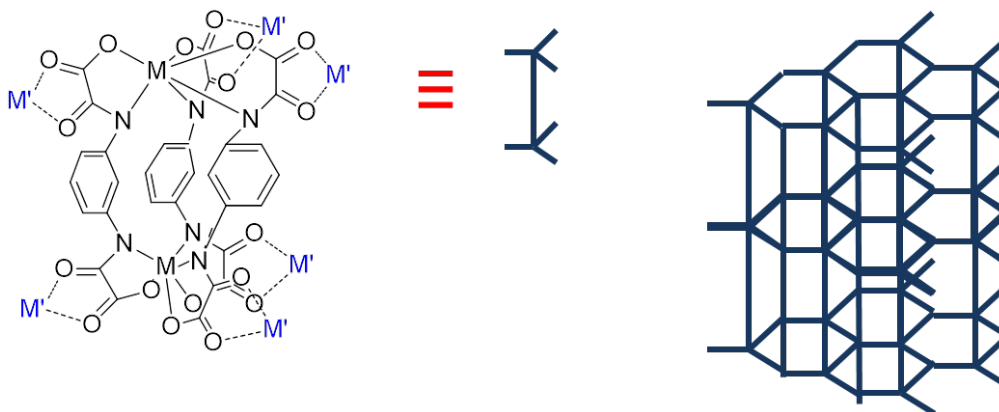


Figure 1.15 Proposed 3D MCP from the $[\text{M}^{\text{II}}_2\text{mpba}_3]^{8-}$ metalloligand

If the bimetallic hexakis(bidentate) $[M^{II}_2(mpba)_3]^{8-}$ metalloligand failed to yield 3D MCPs so far, it is important to realize that the mpba ligand remains attractive. Owing to the *meta*-substituted configuration, this ligand and its derivatives are able to act as efficient ferromagnetic coupling units, favoring long-range magnetic ordering. Indeed, the rung-like tetrakis(bidentate) binuclear $[Cu_2(L)_2]^{4-}$ ($L = mpba$ and Me_3paba) metalloligand, which has afforded the 2D ‘brick-wall’ topology, is also capable of yielding 3D $\{Mn_{4/3}Cu_2\}$ MCPs. In this case the mpba ligands serve as pillars between the planes but unlike the 2D compounds, the planes do not have a honeycomb-shaped arrangement but a semi regular paving of octagon and squares (Figure 1.16).

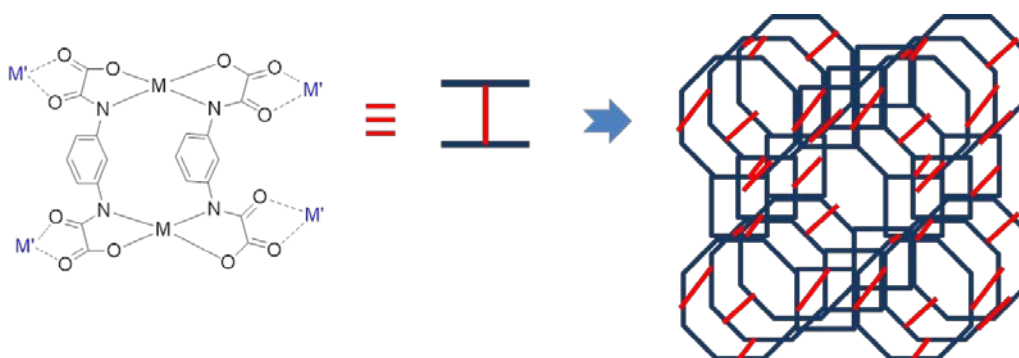


Figure 1.16 3D network based on semi-regular tiling of octagons and squares plans linked by pillars

The two 3D MCPs obtained from the tetrakis(bidentate) metalloligands, $Na_4[Mn_4(Cu_2(mpba)_2(H_2O)_4)_3] \cdot 72.5H_2O$ ¹⁰⁷ and $Na_4[Mn_4(Cu_2(Me_3mpba)_2(H_2O)_{3.33})_3] \cdot 50H_2O$ ¹⁰⁸, are topologically identical but show differences in their arrangement, due to the different steric hindrances from the ligands. $Na_4[Mn_4(Cu_2(Me_3mpba)_2(H_2O)_{3.33})_3] \cdot 50H_2O$ exhibits selective gas and vapor absorption (CH_4 , H_2O , CH_3OH , CO_2), which is accompanied by a variation of the long-range magnetic properties as a function of the absorbed guest molecule. $Na_4[Mn_4(Cu_2(mpba)_2(H_2O)_4)_3] \cdot 72.5H_2O$ behaves as a magnetic sponge. The anhydrous phase is amorphous but its crystallinity is recovered upon rehydration. Morphous to amorphous phase transition under heating causes a slight color change of the crystal with size shrinking. The T_c of the hydrated phase is 22.5 K whereas it is only 2.3 K for the anhydrous one. To date, they represent the best examples of porous MCPs prepared with oxamate ligands (Figure 1.17).

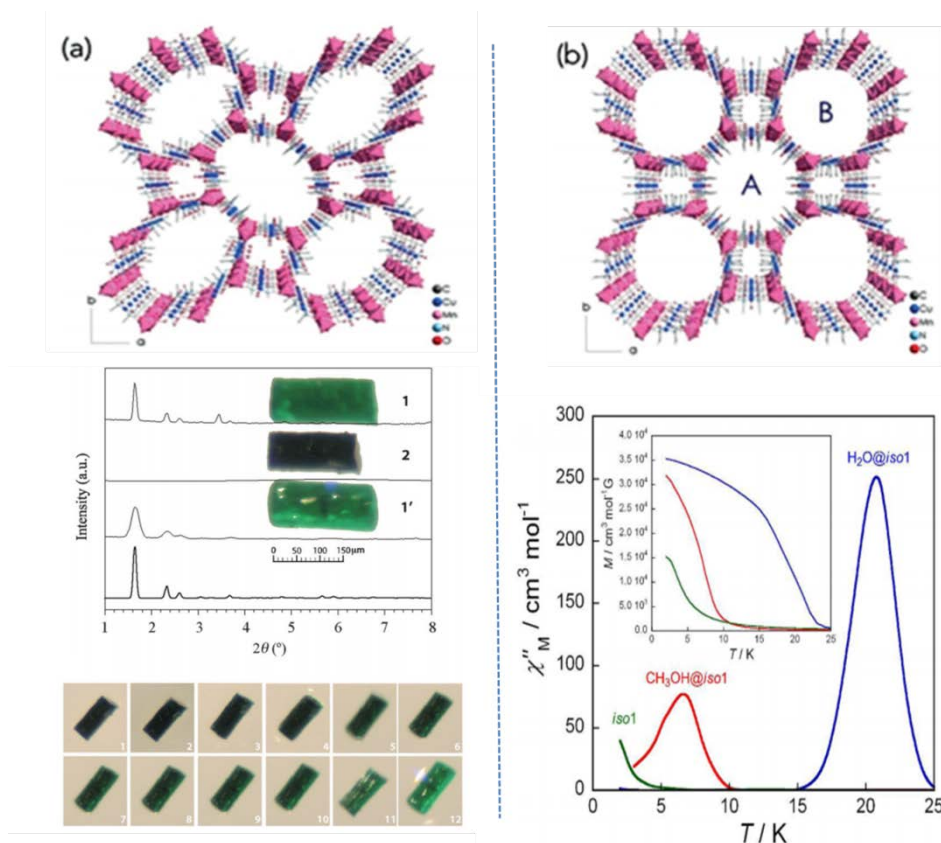


Figure 1.17 Left: Perspective view of $\{\text{Mn}_4(\text{Cu}_2(\text{mpba})_2(\text{H}_2\text{O})_4)_3\}$; PXRD pattern of the hydrated (1), anhydrous (2) and rehydrated phases (1'); Images of the rehydration of a single crystal immersed into water. Right: Perspective view of $\{\text{Mn}_4(\text{Cu}_2(\text{Me}_3\text{mpba})_2(\text{H}_2\text{O})_{3.33})_3\}$; Temperature dependence of the out-of-phase χ''_M for the anhydrous network (green), $\text{Na}_4[\text{Mn}_4(\text{Cu}_2(\text{Me}_3\text{mpba})_2) \cdot 37\text{CH}_3\text{OH}]$ (red), and $\text{Na}_4[\text{Mn}_4(\text{Cu}_2(\text{Me}_3\text{mpba})_2(\text{H}_2\text{O})_{3.33})_3] \cdot 50\text{H}_2\text{O}$ (blue). Inset shows the corresponding M v. T curves^{107,108}.

Steric hindrance from the ligand can, not only change the porous nature of a 3D network, but also its dimensionality. In the 2D MCPs section, we have mentioned $(n\text{-Bu}_4\text{N})_4[\text{Mn}_4\text{Cu}_6(\text{Me}_2\text{pma})_{12}(\text{DMSO})_2]$. The use ethyl groups on the pma ligand instead of methyl, and using the same synthesis (stoichiometry, counter-ion and solvents) has led to a 3D network, $(n\text{-Bu}_4\text{N})_4[\text{Mn}_4\text{Cu}_6(\text{Et}_2\text{pma})_{12}] \cdot \text{DMSO} \cdot 10\text{H}_2\text{O}$ ¹⁰⁶. This structure can be interpreted as infinite parallel array of oxamato-bridged chain in a sequence of Cu-Mn(Δ)-Cu-Mn(Δ)-Cu-Mn(Λ)-Cu-Mn(Λ) sequence, further connected by additional $[\text{Cu}(\text{Et}_2\text{pma})_2]^{2-}$ metalloligands. This network has a higher T_c (20 K) than its 2D cousin (10 K). The variation of the counter-ions will also affect the network topology.

Another 3D compound, $[(S)\text{-}(1\text{-PhEt})\text{Me}_3\text{N}]_4[\text{Mn}_4\text{Cu}_6(\text{Et}_2\text{pma})_{12}(\text{DMSO})_3] \cdot 3\text{DMSO} \cdot 5\text{H}_2\text{O}$ ¹⁰⁹, was synthesized with a chiral counter-ion. It consists of two interpenetrated oxamato-bridged $\{\text{Mn}^{\text{II}}_2\text{Cu}^{\text{II}}_3\}$ anionic networks of opposite chirality and it shows a magnetic ordering $T_c = 15$ K (Figure 1.18).

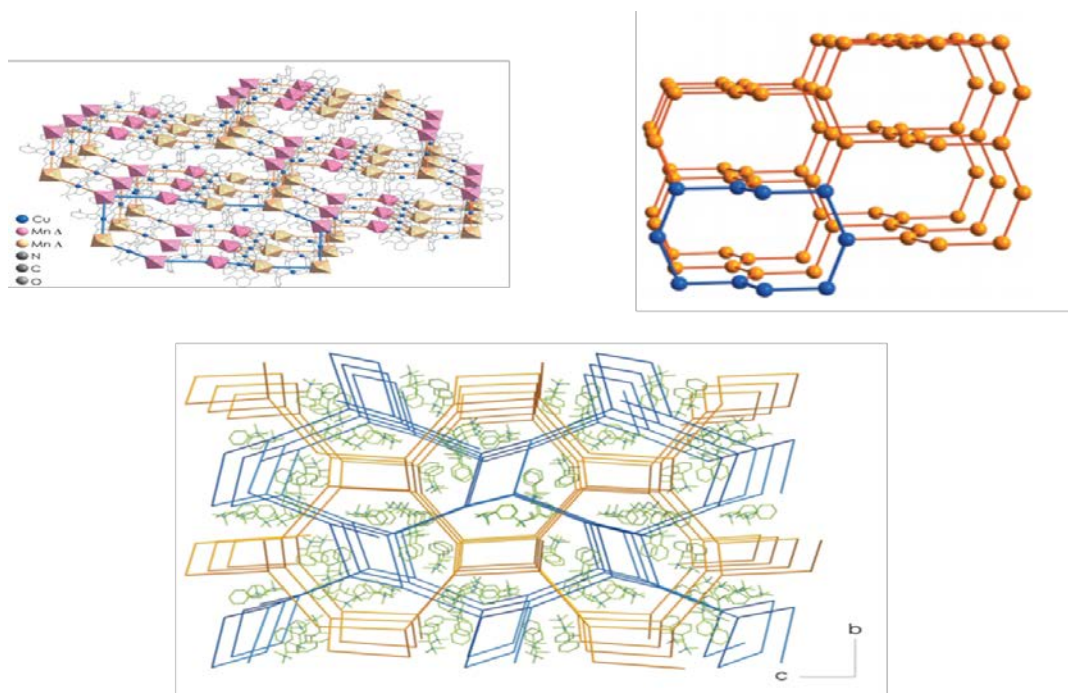


Figure 1.18 Upper: Perspective view of $(n\text{-Bu}_4\text{N})_4[\text{Mn}_4\text{Cu}_6(\text{Et}_2\text{pma})_{12}]$ and scheme of the network. Down: Perspective views of the two interpenetrated networks in $[(S)\text{-}(1\text{-PhEt})\text{Me}_3\text{N}]_4[\text{Mn}_4\text{Cu}_6(\text{Et}_2\text{pma})_{12}(\text{DMSO})_3]^{100,106,109}$

1.4.4 Amino acid-based 3D networks

Recently, Emilio Pardo and co-workers have explored a series of new chiral oxamate and oxamide ligands derived from amino acids (AA). In comparison to classical oxamate ligand, AA-based oxamate ligands provide more coordination sites, more flexible coordination modes and more “growing” directions (Figure 1.19). Indeed, with this family of ligand, a series of multifunctional porous metal-organic-frameworks (MOF) were successfully synthesized with applications in various areas: drug delivery¹¹⁰, ferroelectricity¹¹¹, selective gas and light hydrocarbons sorption^{112,113}, mercury removal¹¹⁴, selective gold and platinum recovery and catalysis^{115,116}.

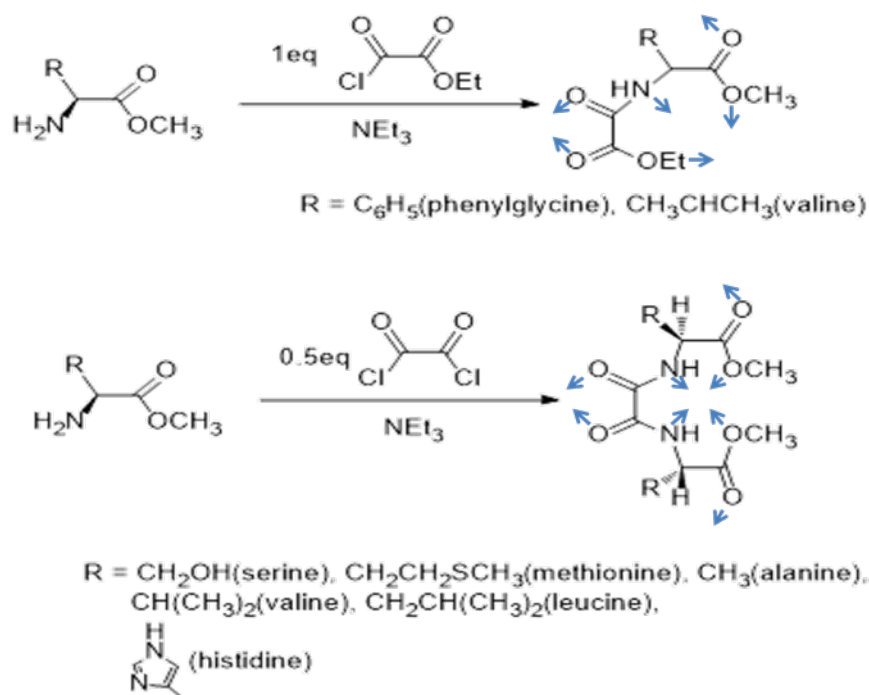


Figure 1.19 Synthetic scheme AA-based oxamate and oxamide ligands: HMeEt-(R)-N-(ethyl oxoacetate) amino acid ligands and bis(amino acid)oxalamide ligands. Blue arrows represent the possible coordination sites.

It is interesting to look at their structural features to broaden our vision of the oxamate ligands coordination chemistry. For AA-based oxamate ligands, the chiral helicoidal homometallic chain $(\text{Me}_4\text{N})[\text{Cu}^{\text{II}}(\text{R})\text{-pegma}] \cdot 2\text{H}_2\text{O}$ ((R)-pegma = (R)-N-(ethyl oxoacetate)phenylglycine), was used as a ‘metalloligand’. Square planar $[\text{Ni}(\text{cyclam})]^{2+}$ cations (cyclam = 1,4,8,11-tetraazacyclotetradecane) linked to the chiral chains through the free carbonyl groups from the phenyl-glycine amino acid residues, produced a 3D chiral porous network, $[\text{Ni}(\text{cyclam})][\text{Cu}^{\text{II}}((\text{R})\text{-pegma})_2] \cdot 6\text{H}_2\text{O} \cdot 2\text{iPrOH}$ ¹¹². Using *D*-valine, the enantiopure hexanuclear wheel $(\text{Me}_4\text{N})_6[\text{Cu}^{\text{II}}_6((\text{R})\text{-valma})_6] \cdot 7\text{H}_2\text{O}$ where (R)-valma = (R)-N-(ethyl oxoacetate)valine was obtained and use also as a metalloligand. Coordination of $[\text{Ni}(\text{cyclam})]^{2+}$ to the free carbonyl groups and reorganization of the metalloligand into 1D homochiral chain has yielded another homochiral 3D MOF, $[\text{Ni}(\text{cyclam})][\text{Cu}^{\text{II}}((\text{R})\text{-valma})_2] \cdot 15\text{H}_2\text{O}$ (Figure 1.20). In these two MOFs, the Cu^{II} atoms have different coordination modes, resulting in 1D chiral secondary building units with different structural topologies^{117,118}.

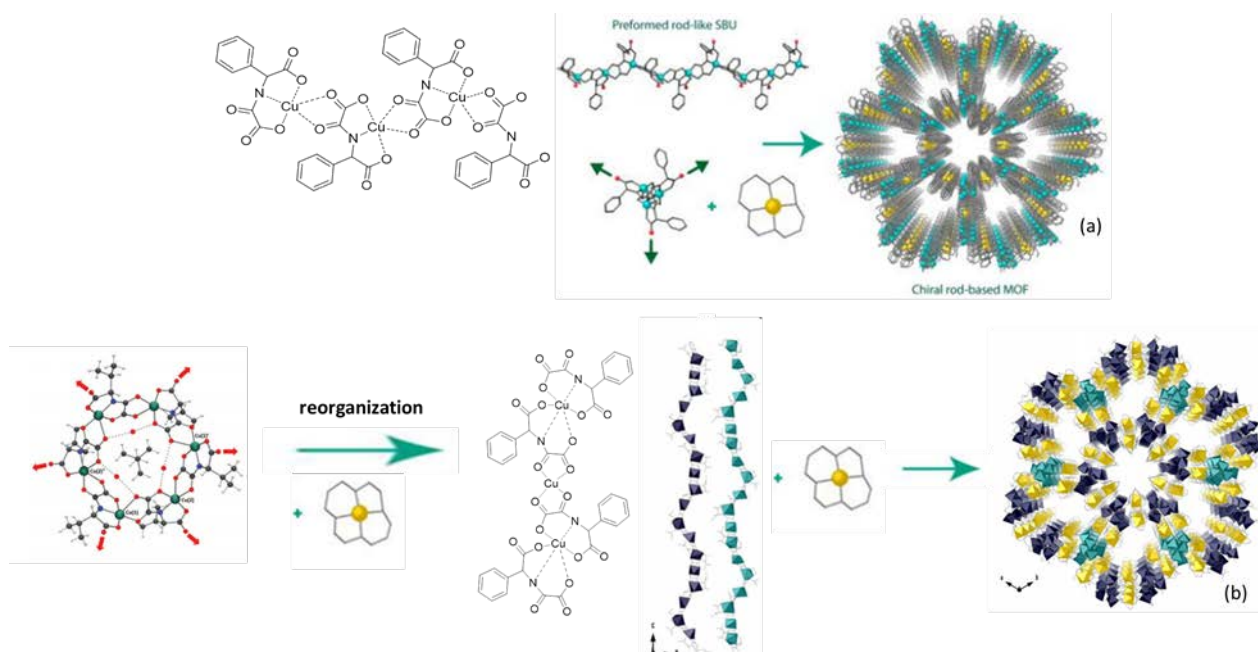


Figure 1.20 (a) Cu^{II} coordination modes in the 1D metalloligand and structure of [Ni(cyclam)][Cu^{II}((R)-pegma)]₂¹¹². (b) Structure of the hexanuclear metalloligand, coordination modes and perspective view of chains in the structure of [Ni(cyclam)][Cu^{II}((R)-valma)]₂^{117,118}.

Regarding AA-based oxamide ligands, all the MOFs have been obtained from the bimetallic Cu^{II}-based metalloligands (Me₄N)₂[Cu₂(AA-oxamate)(OH)₂] (AA: serine, histidine, methionine, alanine, valine, leucine). For example, addition of Ca²⁺ cations yields the robust, water-stable hexagonal framework [CaCu₆((S,S)-methox)₃(OH)₂(H₂O)]·16H₂O (AA: methionine) that proved efficient for mercury removal¹¹⁴. A parent MOF also efficient for mercury removal with a square structure, [Cu₄((S,S)-methox)₂]·5H₂O, was obtained by acidification of the metalloligand¹¹⁹. The MOF obtained from the histidine-based metalloligand shows a more complex hexagonal structure, [Ca₆Cu₂₄((S,S)-hismox)₁₂(H₂O)₃]·212H₂O, and it can undergo post-synthetic cation exchange and yield the ferroelectric MOF, (CH₃NH₃)₁₂[Cu₂₄((S,S)-hismox)₁₂(H₂O)₃]·178H₂O¹¹¹ (Figure 1.21).

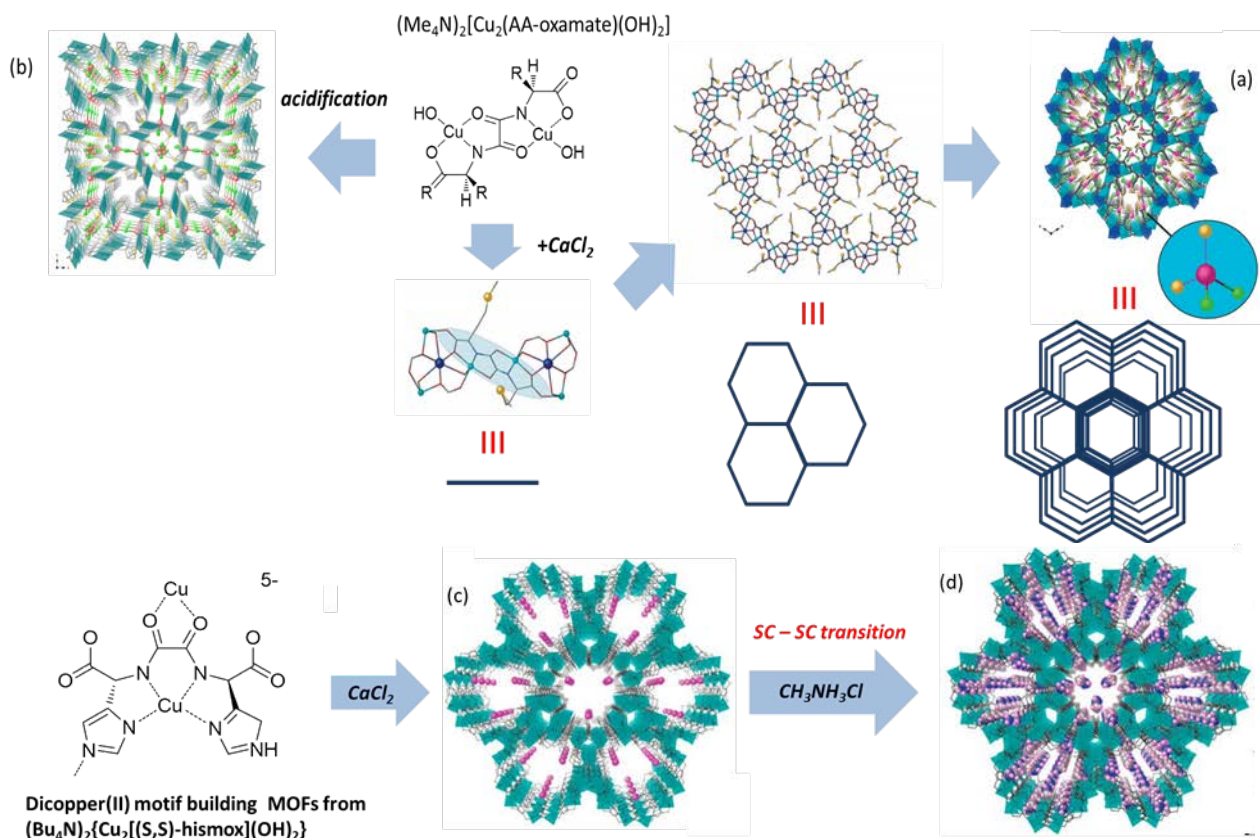


Figure 1.21 Up: the route from (Me₄N)₂[Cu₂(AA-oxamate)(OH)₂] to synthesize [CaCu₆((S,S)-methoxy)₃(OH)₂(H₂O)]·16H₂O@3HgCl₂ (AA: methionine) (a) and [Cu₄((S,S)-methoxy)₂]·5H₂O (b) which are efficient to remove mercury. Down: Synthesis route of [Ca₆Cu₂₄((S,S)-hismox)₁₂(H₂O)₃]·212H₂O (c) and (CH₃NH₃)₁₂[Cu₂₄((S,S)-hismox)₁₂(H₂O)₃]·178H₂O (d)^{111,114,119}.

1.5 Aim of the work

In this PhD project, we have explored the reactivity of heterotopic oxamate-based ligands that were chosen for the preparation of magnetic multidimensional architectures. More specifically, our goal is the preparation of porous MCPs, ie. magnetic MOFs.

Looking at the oxamate-based MCPs examples we have mentioned, crystals obtained from aromatic oxamate ligands are mainly grown in highly polar solvents and using H-tubes or non-stoichiometric reactions. And considering the number of morphologies that have been reported over 30 years, it would seem that crystal growth is a considerable limitation. Yet, MOFs synthesized from AA-based oxamate ligands suffer the crystal growth issue but the large amount of new morphologies reported over a relative short period of time would indicate that the use of heterotopic ligands with higher coordinating ability is a relevant strategy. However, exclusive antiferromagnetic coupling in

these homometallic systems makes them less appealing for MCPs. Besides, the lack of aromatic spacer prevents the occurrence of spin polarization.

To address these issues, we have decided to use phenyl-based oxamate ligands bearing additional coordinating groups. We hope such heterotopic ligands will provide the supplementary connectivity (albeit serendipitous) leading to multidimensional structures, while retaining magnetic coupling abilities.

Generally, substituted anilines are reacted with either ethyl oxalyl chloride to synthesize the oxamate ester proligands and or with diethyl oxalate to prepare the oxamide ligands. The oxamate ester proligands can undergo saponification, followed by acidification to form the oxamic acid (Figure 1.22).

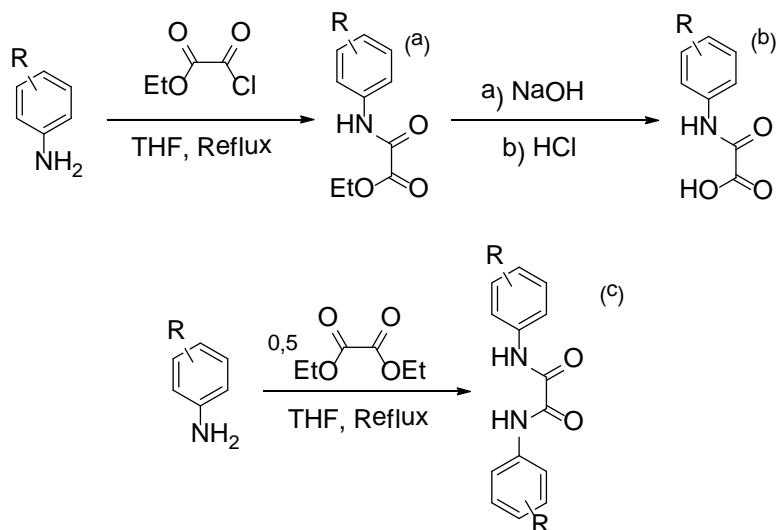


Figure. 1.22 schematic route for the synthesis of the ester oxamate proligand (a), the oxamic acid (b), and the oxamide ligand (c).

Ortho- and para-substituted aromatic ligands were explored and used as starting material to build the nD coordination polymers, with hydroxy and carboxylic groups introduced into the phenyloxamate ligand. The ester proligands and acidic ligands were both employed to prepare the MCPs (Figure 1.23 and Table 1.3).

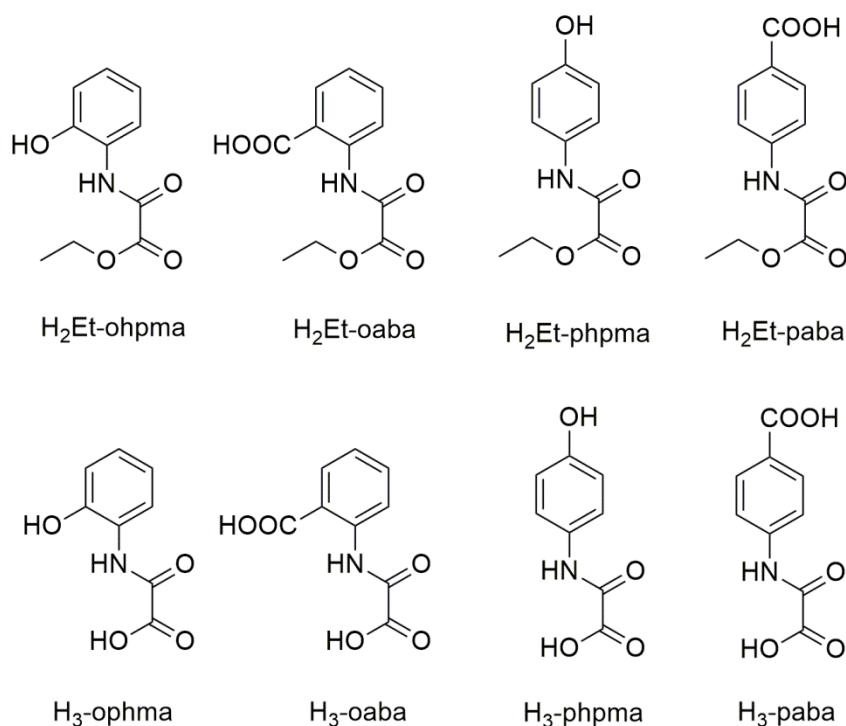


Figure.1.23 Heterotopic oxamate-based ligands used in this thesis.

<i>Abbreviation</i>	<i>Chemical name</i>
H ₂ Et-ohpma	Ethyl N-(2-hydroxyphenyl)oxamate
H ₃ -ohpma	N-(2-hydroxyphenyl)oxamic acid
H ₂ Et-oaba	2-(ethyloxamate)benzoic acid
H ₃ -oaba	2-(oxamate)benzoic acid
H ₂ Et-phpma	Ethyl N-(4-hydroxyphenyl)oxamate
H ₃ -phpma	N-(4-hydroxyphenyl)oxamic acid
H ₂ Et-paba	4-(ethyloxamate)benzoic acid
H ₃ -paba	4-(oxamate)benzoic acid

Table 1.3 Abbreviation codes and their corresponding chemical name of heterotopic oxamate ligands used in this thesis.

More precisely, Chapter 2 will discuss of the reactivity in bench condition of the ligands with transition metal ions ($M = \text{Cu}, \text{Co}, \text{Mn}, \text{Ni}, \text{Fe},$) in aqueous or non-aqueous solvents, for the characterization of the metalloligands. In a serendipity approach, reactivity with preformed coordination clusters has also been explored.

Chapter 3 to 5 will be devoted to the investigation of the ligands reactivity in solvothermal conditions. Indeed, solvothermal synthesis is widely used in MOF chemistry. This method imposes strong constrains both in temperatures and pressure to the reaction media, often beyond the solvent's boiling point. Such conditions result in the increase of solubility and mobility of the reactants. In oxamate chemistry, the solvothermal method is rarely used. Reported attempts showed important

drawbacks, such as (de)protonation issues of the amide nitrogen atom that prevent coordination and weaken the magnetic interaction^{120,121}. Besides, oxamate ligands are sensitive to hydrolysis, and decomposition into oxalate is a liability in these conditions. Nevertheless, we have carefully screened several synthetic parameters, hoping that the implementation of the method would overall improve crystal growth and favor robust nD systems. Fortunately, a series of novel oxamate-based homo- and hetero-metallic 1D, 2D and 3D MCPs were successfully synthesized and characterized. Chapters **3** to **5** will present these results, sorted by dimensionality.

Finally, we will conclude this work and give some prospects on this new family of heterotopic oxamate-based ligands for the preparation of MCPs.

We hope this work will be appreciated by those who are engaged in coordination chemistry, and provide the reader with useful insights on the research on oxamate-based MCPs.

References

- 1 M. Mannini, F. Pineider, C. Danieli, F. Totti, L. Sorace, P. Sainctavit, M.-A. Arrio, E. Otero, L. Joly, J. C. Cezar, A. Cornia and R. Sessoli, *Nature*, 2010, **468**, 417–421.
- 2 S. J. Bartolome, F. Luis and J. F. Fernández, Eds., *Molecular Magnets: Physics and Applications*, Springer-Verlag, Berlin Heidelberg, 2014.
- 3 L. Bogani and W. Wernsdorfer, *Nat. Mater.*, 2008, **7**, 179–186.
- 4 M. N. Leuenberger and D. Loss, *Nature*, 2001, **410**, 789.
- 5 Bleaney B. and Bowers K. D., *Proc. R. Soc. London, Ser. A*, 1952, **214**, 451–465.
- 6 O. Kahn and B. Briat, *J. Chem. Soc., Faraday Trans. 2*, 1976, **72**, 1441–1446.
- 7 O. Kahn, *Molecular Magnetism*, VCH Publishers Inc, New York, 1993.
- 8 O. Kahn, *Angew. Chem. Int. Ed.*, 1985, **24**, 834–850.
- 9 A. Caneschi, D. Gatteschi, R. Sessoli, A. L. Barra, L. C. Brunel and M. Guillot, *J. Am. Chem. Soc.*, 1991, **113**, 5873–5874.
- 10 R. Sessoli, H.-L. Tsai, A. R. Schake, S. Wang, J. B. Vincent, K. Folting, D. Gatteschi, G. Christou and D. N. Hendrickson, *J. Am. Chem. Soc.*, 1993, **115**, 1804–1816.
- 11 M. Murugesu, J. Raftery, W. Wernsdorfer, G. Christou and E. K. Brechin, *Inorg. Chem.*, 2004, **43**, 4203–4209.
- 12 J.-H. Jia, Q.-W. Li, Y.-C. Chen, J.-L. Liu and M.-L. Tong, *Coord. Chem. Rev.*, 2019, **378**, 365–381.
- 13 F.-S. Guo, B. M. Day, Y.-C. Chen, M.-L. Tong, A. Mansikkamäki and R. A. Layfield, *Science*, 2018, **362**, 1400–1403.
- 14 S. R. Batten, N. R. Champness, X.-M. Chen, J. Garcia-Martinez, S. Kitagawa, L. Öhrström, M. O’Keeffe, M. Paik Suh and J. Reedijk, *Pure Appl. Chem.*, 2013, **85**, 1715–1724.
- 15 P. Horcajada, R. Gref, T. Baati, P. K. Allan, G. Maurin, P. Couvreur, G. Férey, R. E. Morris and C. Serre, *Chem. Rev.*, 2012, **112**, 1232–1268.
- 16 H. Furukawa, K. E. Cordova, M. O’Keeffe and O. M. Yaghi, *Science*, 2013, **341**, 1230444.
- 17 S. Wuttke, *Angew. Chem. Int. Ed.*, , DOI:10.1002/ange.201906230.
- 18 H.-C. “Joe” Zhou and S. Kitagawa, *Chem. Soc. Rev.*, 2014, **43**, 5415–5418.

- 19 G. Maurin, C. Serre, A. Cooper and G. Férey, *Chem. Soc. Rev.*, 2017, **46**, 3104–3107.
- 20 T. R. Cook and P. J. Stang, *Chem. Rev.*, 2015, **115**, 7001–7045.
- 21 D. N. Woodruff, R. E. P. Winpenny and R. A. Layfield, *Chem. Rev.*, 2013, **113**, 5110–5148.
- 22 C. Train, R. Gheorghe, V. Krstic, L.-M. Chamoreau, N. S. Ovanesyan, G. L. J. A. Rikken, M. Gruselle and M. Verdaguer, *Nat. Mater.*, 2008, **7**, 729–734.
- 23 W.-H. Zhu, Z.-M. Wang and S. Gao, *Inorg. Chem.*, 2007, **46**, 1337–1342.
- 24 Y. Cui, Y. Yue, G. Qian and B. Chen, *Chem. Rev.*, 2012, **112**, 1126–1162.
- 25 E. Coronado, C. J. Gómez-García, A. Nuez, F. M. Romero, E. Rusanov and H. Stoeckli-Evans, *Inorg. Chem.*, 2002, **41**, 4615–4617.
- 26 E. Pardo, C. Train, G. Gontard, K. Boubekur, O. Fabelo, H. Liu, B. Dkhil, F. Lloret, K. Nakagawa, H. Tokoro, S. Ohkoshi and M. Verdaguer, *J. Am. Chem. Soc.*, 2011, **133**, 15328–15331.
- 27 R. J. Glauber, *J. Math. Phys.*, 1963, 294–307.
- 28 A. Caneschi, D. Gatteschi, N. Lalioti, C. Sangregorio, R. Sessoli, G. Venturi, A. Vindigni, A. Rettori, M. G. Pini and M. A. Novak, *Angew. Chem. Int. Ed.*, 2001, **40**, 1760–1763.
- 29 F. Palacio, in *Magnetic Molecular Materials*, D. Gatteschi, O. Kahn, J. Miller, F. Palacio, Dordrecht Boston London, Kluwer Academic Publishers., 1991, vol. 198, pp. 1–34.
- 30 Y. Journaux, J. Ferrando-Soria, E. Pardo, R. Ruiz-Garcia, M. Julve, F. Lloret, J. Cano, Y. Li, L. Lisnard, P. Yu, H. Stumpf and C. L. M. Pereira, *Eur. J. Inorg. Chem.*, 2018, **2018**, 228–247.
- 31 Q. Yue and E.-Q. Gao, *Coord. Chem. Rev.*, 2019, **382**, 1–31.
- 32 G.-M. Zhuang, X.-B. Li, Y.-Q. Wen, C.-Y. Tian and E.-Q. Gao, *Eur. J. Inorg. Chem.*, 2014, **2014**, 3488–3498.
- 33 Y.-F. Deng, T. Han, W. Xue, N. Hayashi, H. Kageyama and Y.-Z. Zheng, *Dalton Trans.*, 2017, **46**, 1449–1454.
- 34 P. Bhatt, M. D. Mukadam, S. S. Meena, S. K. Mishra, R. Mittal, P. U. Sastry, B. P. Mandal and S. M. Yusuf, *Appl. Phys. Lett.*, 2017, **110**, 102901.
- 35 W. Jiang, C. Jiao, Y. Meng, L. Zhao, Q. Liu and T. Liu, *Chem. Sci.*, 2018, **9**, 617–622.
- 36 A. Caneschi, D. Gatteschi, J. P. Renard, P. Rey and R. Sessoli, *Inorg. Chem.*, 1989, **28**, 3314–3319.

- 37 K. Bernot, L. Bogani, R. Sessoli and D. Gatteschi, *Inorg. Chim. Acta*, 2007, **360**, 3807–3812.
- 38 X. Meng, W. Shi and P. Cheng, *Coord. Chem. Rev.*, 2019, **378**, 134–150.
- 39 K. Bernot, L. Bogani, A. Caneschi, D. Gatteschi and R. Sessoli, *J. Am. Chem. Soc.*, 2006, **128**, 7947–7956.
- 40 A. Cornia, A. Caneschi, P. Dapporto, A. C. Fabretti, D. Gatteschi, W. Malavasi, C. Sangregorio and R. Sessoli, *Angew. Chem. Int. Ed.*, 1999, **38**, 1780–1782.
- 41 X.-Y. Wang, Z.-M. Wang and S. Gao, *Chem. Commun.*, 2008, 281–294.
- 42 M. Trivedi, G. Singh, A. Kumar and N. P. Rath, *RCS Adv.*, 2014, **4**, 34110–34116.
- 43 Y.-T. Yang, F.-H. Zhao, Y.-X. Che and J.-M. Zheng, *Inorg. Chem. Commun.*, 2011, **14**, 1802–1806.
- 44 X.-M. Zhang, Y.-Q. Wang, Y. Song and E.-Q. Gao, *Inorg. Chem.*, 2011, **50**, 7284–7294.
- 45 L. Shi, D. Shao, F.-Y. Shen, X.-Q. Wei and X.-Y. Wang, *Chin. J. Chem.*, 2019, **37**, 19–24.
- 46 S. R. Batten and K. S. Murray, *Coord. Chem. Rev.*, 2003, **246**, 103–130.
- 47 P. Gütllich, Y. Garcia and T. Woike, *Coordination Chemistry Reviews*, 2001, **219–221**, 839–879.
- 48 C. N. R. Rao, S. Natarajan and R. Vaidhyanathan, *Angewandte Chemie International Edition*, 2004, **43**, 1466–1496.
- 49 J. S. Miller and J. L. Manson, *Acc. Chem. Res.*, 2001, **34**, 563–570.
- 50 M. Kurmoo, *Chem. Soc. Rev.*, 2009, **38**, 1353–1379.
- 51 R. Chakrabarty, P. S. Mukherjee and P. J. Stang, *Chem. Rev.*, 2011, **111**, 6810–6918.
- 52 G. Kumar and R. Gupta, *Chem. Soc. Rev.*, 2013, **42**, 9403–9453.
- 53 S. Srivastava and R. Gupta, *CrystEngComm*, 2016, **18**, 9185–9208.
- 54 E. Coronado, J. R. Galán-Mascarós, C. J. Gómez-García and J. M. Martínez-Agudo, *Inorg. Chem.*, 2001, **40**, 113–120.
- 55 K. A. Leslie, R. S. Drago, G. D. Stucky, D. J. Kitko and J. A. Breese, *Inorg. Chem.*, 1979, **18**, 1885–1891.
- 56 Olivier. Kahn, Yu. Pei, Michel. Verdaguer, J. Pierre. Renard and Jorunn. Sletten, *J. Am. Chem. Soc.*, 1988, **110**, 782–789.
- 57 Yu. Pei, Michel. Verdaguer, Olivier. Kahn, Jorunn. Sletten and J. Pierre. Renard, *J. Am. Chem.*

- Soc.*, 1986, **108**, 7428–7430.
- 58 S. Turner, O. Kahn and L. Rabardel, *J. Am. Chem. Soc.*, 1996, **118**, 6428–6432.
- 59 R. Pellaux, H. W. Schmalle, R. Huber, P. Fischer, T. Hauss, B. Ouladdiaf and S. Decurtins, *Inorg. Chem.*, 1997, **36**, 2301–2308.
- 60 H. Tamaki, Z. J. Zhong, N. Matsumoto, S. Kida, M. Koikawa, N. Achiwa, Y. Hashimoto and H. Okawa, *J. Am. Chem. Soc.*, 1992, **114**, 6974–6979.
- 61 M. Clemente-León, E. Coronado, C. Martí-Gastaldo and F. M. Romero, *Chem. Soc. Rev.*, 2011, **40**, 473–497.
- 62 S. A. Sahadevan, A. Abhervé, N. Monni, C. Sáenz de Pipaón, J. R. Galán-Mascarós, J. C. Waerenborgh, B. J. C. Vieira, P. Auban-Senzier, S. Pillet, E.-E. Bendeif, P. Alemany, E. Canadell, M. L. Mercuri and N. Avarvari, *J. Am. Chem. Soc.*, 2018, **140**, 12611–12621.
- 63 H. Ōkawa, A. Mishima, H. Yoshino and M. Ohba, *Chem. Lett.*, 2018, **47**, 444–446.
- 64 D. Gatteschi, R. Sessoli and J. Villain, *Molecular Nanomagnets*, Oxford University Press, 2006.
- 65 S. T. Liddle and J. van Slageren, *Chem. Soc. Rev.*, 2015, **44**, 6655–6669.
- 66 K. Liu, X. Zhang, X. Meng, W. Shi, P. Cheng and A. K. Powell, *Chem. Soc. Rev.*, 2016, **45**, 2423–2439.
- 67 C. A. P. Goodwin, F. Ortu, D. Reta, N. F. Chilton and D. P. Mills, *Nature*, 2017, **548**, 439–442.
- 68 Y.-S. Meng, O. Sato and T. Liu, *Angew. Chem. Int. Ed.*, 2018, **57**, 12216–12226.
- 69 O. Sato, T. Iyoda, A. Fujishima and K. Hashimoto, *Science*, 1996, **272**, 704–705.
- 70 A. Bleuzen, C. Lomenech, V. Escax, F. Villain, F. Varret, C. Cartier dit Moulin and M. Verdaguer, *J. Am. Chem. Soc.*, 2000, **122**, 6648–6652.
- 71 V. Escax, A. Bleuzen, C. Cartier dit Moulin, F. Villain, A. Goujon, F. Varret and M. Verdaguer, *J. Am. Chem. Soc.*, 2001, **123**, 12536–12543.
- 72 O. Sato, *Acc. Chem. Res.*, 2003, **36**, 692–700.
- 73 R. Lescouëzec, J. Vaissermann, C. Ruiz - Pérez, F. Lloret, R. Carrasco, M. Julve, M. Verdaguer, Y. Dromzee, D. Gatteschi and W. Wernsdorfer, *Angew. Chem. Int. Ed.*, 2003, **42**, 1483–1486.
- 74 L. M. Toma, R. Lescouëzec, F. Lloret, M. Julve, J. Vaissermann and M. Verdaguer, *Chem. Commun.*, 2003, 1850–1851.

- 75 S. Ferlay, T. Mallah, J. Vaissermann, F. Bartolomé, P. Veillet and M. Verdaguer, *Chem. Commun.*, 1996, 2481–2482.
- 76 M. Ohba, N. Maruono, H. Okawa, T. Enoki and J.-M. Latour, *J. Am. Chem. Soc.*, 1994, **116**, 11566–11567.
- 77 Y. Arimoto, S. Ohkoshi, Z. J. Zhong, H. Seino, Y. Mizobe and K. Hashimoto, *J. Am. Chem. Soc.*, 2003, **125**, 9240–9241.
- 78 T. Liu, Y.-J. Zhang, S. Kanegawa and O. Sato, *J. Am. Chem. Soc.*, 2010, **132**, 8250–8251.
- 79 E. Pardo, R. Ruiz-García, J. Cano, X. Ottenwaelder, R. Lescouëzec, Y. Journaux, F. Lloret and M. Julve, *Dalton Trans.*, 2008, 2780–2805.
- 80 E. Pardo, R. Ruiz-García, F. Lloret, J. Faus, M. Julve, Y. Journaux, M. A. Novak, F. S. Delgado and C. Ruiz-Pérez, *Chem. - Eur. J.*, 2007, **13**, 2054–2066.
- 81 C. L. M. Pereira, A. C. Doriguetto, C. Konzen, L. C. Meira - Belo, U. A. Leitão, N. G. Fernandes, Y. P. Mascarenhas, J. Ellena, A. L. Brandl, M. Knobel and H. O. Stumpf, *Eur. J. Inorg. Chem.*, 2005, 5018–5025.
- 82 E. Pardo, C. Train, R. Lescouëzec, Y. Journaux, J. Pasán, C. Ruiz-Pérez, F. S. Delgado, R. Ruiz-García, F. Lloret and C. Paulsen, *Chem. Commun.*, 2010, **46**, 2322.
- 83 J. Ferrando-Soria, D. Cangussu, M. Eslava, Y. Journaux, R. Lescouëzec, M. Julve, F. Lloret, J. Pasán, C. Ruiz-Pérez, E. Lhotel, C. Paulsen and E. Pardo, *Chem. Eur. J.*, 2011, **17**, 12482–12494.
- 84 J. Ferrando-Soria, H. Khajavi, P. Serra-Crespo, J. Gascon, F. Kapteijn, M. Julve, F. Lloret, J. Pasan, C. Ruiz-Perez, Y. Journaux and E. Pardo, *Adv. Mater.*, 2012, **24**, 5625–5629.
- 85 M.-C. Dul, E. Pardo, R. Lescouëzec, L.-M. Chamoreau, F. Villain, Y. Journaux, R. Ruiz-García, J. Cano, M. Julve, F. Lloret, J. Pasán and C. Ruiz-Pérez, *J. Am. Chem. Soc.*, 2009, **131**, 14614–14615.
- 86 M. Castellano, R. Ruiz-García, J. Cano, J. Ferrando-Soria, E. Pardo, F. R. Fortea-Pérez, S.-E. Stiriba, M. Julve and F. Lloret, *Acc. Chem. Res.*, 2015, **48**, 510–520.
- 87 M. Castellano, R. Ruiz-García, J. Cano, J. Ferrando-Soria, E. Pardo, F. R. Fortea-Pérez, S.-E. Stiriba, W. P. Barros, H. O. Stumpf, L. Cañadillas-Delgado, J. Pasán, C. Ruiz-Pérez, G. de Munno, D. Armentano, Y. Journaux, F. Lloret and M. Julve, *Coord. Chem. Rev.*, 2015, **303**, 110–138.
- 88 W. D. do Pim, W. X. C. Oliveira, M. A. Ribeiro, É. N. de Faria, I. F. Teixeira, H. O. Stumpf, R. M. Lago, C. L. M. Pereira, C. B. Pinheiro, J. C. D. Figueiredo-Júnior, W. C. Nunes, P. P. de Souza, E. F. Pedroso, M. Castellano, J. Cano and M. Julve, *Chem. Commun.*, 2013, **49**, 10778–10780.

- 89 E. Pardo, K. Bernot, M. Julve, F. Lloret, J. Cano, R. Ruiz Garcia, J. Pasan, C. Ruiz Perez, X. Ottenwaelder and Y. Journaux, *Chem. Commun.*, 2004, **(8)**, 920–921.
- 90 Y. Pei, Y. Journaux and O. Kahn, *Inorg. Chem.*, 1988, **27**, 399–404.
- 91 P. J. Van Koningsbruggen, O. Kahn, K. Nakatani, Y. Pei, J. P. Renard, M. Drillon and P. Legoll, *Inorg. Chem.*, 1990, **29**, 3325–3331.
- 92 Y. Pei, Y. Journaux and O. Kahn, *Chem. Commun.*, 1986, 1300–13001.
- 93 P. Karafiloglou, *J. Chem. Educ.*, 1989, **66**, 816.
- 94 I. Fernandez, R. Ruiz, J. Faus, M. Julve, F. Lloret, J. Cano, X. Ottenwaelder, Y. Journaux and M. C. Munoz, *Angew. Chem. Int. Ed.*, 2001, **40**, 3039–3042.
- 95 E. Pardo, J. Faus, M. Julve, F. Lloret, M. C. Muñoz, J. Cano, X. Ottenwaelder, Y. Journaux, R. Carrasco, G. Blay, I. Fernández and R. Ruiz-García, *J. Am. Chem. Soc.*, 2003, **125**, 10770–10771.
- 96 Y. Pei, M. Verdaguer, O. Kahn, J. Sletten and J. P. Renard, *Inorg. Chem.*, 1987, **26**, 138–143.
- 97 Keitaro. Nakatani, Pierre. Bergerat, Epiphane. Codjovi, Corine. Mathoniere, Yu. Pei and Olivier. Kahn, *Inorg. Chem.*, 1991, **30**, 3977–3978.
- 98 V. Baron, B. Gillon, J. Sletten, C. Mathoniere, E. Codjovi and O. Kahn, *Inorg. Chim. Acta*, 1995, **235**, 69–76.
- 99 H. O. Stumpf, Y. Pei, L. Ouahab, F. Le Berre, E. Codjovi and O. Kahn, *Inorg. Chem.*, 1993, **32**, 5687–5691.
- 100 Y. Journaux, J. Ferrando-Soria, E. Pardo, R. Ruiz-Garcia, M. Julve, F. Lloret, J. Cano, Y. Li, L. Lisnard, P. Yu, H. Stumpf and C. L. M. Pereira, *Eur. J. Inorg. Chem.*, 2018, **2018**, 228–247.
- 101 C. L. M. Pereira, E. F. Pedroso, H. O. Stumpf, M. A. Novak, L. Ricard, R. Ruiz-García, E. Rivière and Y. Journaux, *Angew. Chem. Int. Ed.*, 2004, **43**, 956–958.
- 102 J. Ferrando-Soria, J. Pasán, C. Ruiz-Pérez, Y. Journaux, M. Julve, F. Lloret, J. Cano and E. Pardo, *Inorg. Chem.*, 2011, **50**, 8694–8696.
- 103 J. Ferrando-Soria, T. Grancha, M. Julve, J. Cano, F. Lloret, Y. Journaux, J. Pasán, C. Ruiz-Pérez and E. Pardo, *Chem. Commun.*, 2012, **48**, 3539–3541.
- 104 H. O. Stumpf, Y. Pei, O. Kahn, L. Ouahab and D. Grandjean, *Science*, 1993, **261**, 447–449.
- 105 O. Cador, M. G. F. Vaz, H. O. Stumpf, C. Mathonière and O. Kahn, *Synthetic Metals*, 2001, **122**, 559–567.

- 106 J. Ferrando-Soria, T. Grancha, M. Julve, J. Cano, F. Lloret, Y. Journaux, J. Pasán, C. Ruiz-Pérez and E. Pardo, *Chem. Commun.*, 2012, **48**, 3539–3541.
- 107 J. Ferrando - Soria, R. Ruiz - García, J. Cano, S.-E. Stiriba, J. Vallejo, I. Castro, M. Julve, F. Lloret, P. Amorós, J. Pasán, C. Ruiz - Pérez, Y. Journaux and E. Pardo, *Chem. Eur. J.*, 2012, **18**, 1608–1617.
- 108 J. Ferrando-Soria, P. Serra-Crespo, M. de Lange, J. Gascon, F. Kapteijn, M. Julve, J. Cano, F. Lloret, J. Pasán, C. Ruiz-Pérez, Y. Journaux and E. Pardo, *J. Am. Chem. Soc.*, 2012, **134**, 15301–15304.
- 109 T. Grancha, M. Mon, F. Lloret, J. Ferrando-Soria, Y. Journaux, J. Pasán and E. Pardo, *Inorg. Chem.*, 2015, **54**, 8890–8892.
- 110 M. Mon, R. Bruno, J. Ferrando-Soria, L. Bartella, L. D. Donna, M. Talia, R. Lappano, M. Maggiolini, D. Armentano and E. Pardo, *Mater. Horiz.*, 2018, **5**, 683–690.
- 111 M. Mon, J. Ferrando-Soria, M. Verdaguer, C. Train, C. Paillard, B. Dkhil, C. Versace, R. Bruno, D. Armentano and E. Pardo, *J. Am. Chem. Soc.*, 2017, **139**, 8098–8101.
- 112 T. Grancha, X. Qu, M. Julve, J. Ferrando-Soria, D. Armentano and E. Pardo, *Inorg. Chem.*, 2017, **56**, 6551–6557.
- 113 T. Grancha, M. Mon, J. Ferrando-Soria, J. Gascon, B. Seoane, E. V. Ramos-Fernandez, D. Armentano and E. Pardo, *J. Mater. Chem. A*, 2017, **5**, 11032–11039.
- 114 M. Mon, F. Lloret, J. Ferrando - Soria, C. Martí - Gastaldo, D. Armentano and E. Pardo, *Angew. Chem. Int. Ed.*, 2016, **55**, 11167–11172.
- 115 M. Mon, M. A. Rivero - Crespo, J. Ferrando - Soria, A. Vidal - Moya, M. Boronat, A. Leyva - Pérez, A. Corma, J. C. Hernández - Garrido, M. López - Haro, J. J. Calvino, G. Ragazzon, A. Credi, D. Armentano and E. Pardo, *Angew. Chem. Int. Ed.*, 2018, **57**, 6186–6191.
- 116 M. Mon, J. Ferrando-Soria, T. Grancha, F. R. Fortea-Pérez, J. Gascon, A. Leyva-Pérez, D. Armentano and E. Pardo, *J. Am. Chem. Soc.*, 2016, **138**, 7864–7867.
- 117 T. Grancha, J. Ferrando-Soria, D. M. Proserpio, D. Armentano and E. Pardo, *Inorg. Chem.*, 2018, **57**, 12869–12875.
- 118 T. Grancha, J. Ferrando-Soria, J. Cano, F. Lloret, M. Julve, G. D. Munno, D. Armentano and E. Pardo, *Chem. Commun.*, 2013, **49**, 5942–5944.

119 M. Mon, X. Qu, J. Ferrando-Soria, I. Pellicer-Carreño, A. Sepúlveda-Escribano, E. V. Ramos-Fernandez, J. C. Jansen, D. Armentano and E. Pardo, *J. Mater. Chem. A*, 2017, **5**, 20120–20125.

120 F. R. Fortea-Pérez, J. Vallejo, M. Julve, F. Lloret, G. De Munno, D. Armentano and E. Pardo, *Inorg. Chem.*, 2013, **52**, 4777–4779.

121 L.-N. Ma, X.-Y. Li, W.-J. Shi, Y.-Z. Li, G. Liu, L. Hou and Y.-Y. Wang, *ChemPlusChem*, 2019, **84**, 62–68.

Chapter 2:

Bench reactivity screening, 0D complexes and 1D chain compound, structural characterization and magnetic properties

Chapter 2. Bench reactivity screening, 0D complexes and 1D chain compound structural characterization and magnetic properties.

2.1 General Introduction

If the main goal of this thesis is the investigation of the reactivity of new oxamate ligands in solvothermal conditions, we have also studied their reactivity in bench conditions, following the synthetic strategies applied for classical oxamate ligands.

In this chapter, Cu^{II} ions were used in aqueous or non-aqueous media to obtain and characterize metalloligands, with two main methods for crystallization, diffusion and slow evaporation. The diffusion method is routinely used for the preparation of oxamate-based metalloligands in aqueous solutions. Slow Evaporation was preferred for non-aqueous reactions. As an alternative to the metal salts used traditionally in coordination chemistry, we have also employed coordination clusters as metal ion sources for the reactions in non-aqueous media.

The heterotopic oxamate ligands targeted in this project were not widely researched before. The few known results are: {Cu[Cu(oaba)(H₂O)(py)]₂} and {Cu[Cu(oaba)(MeOH)]₂}.2H₂O chains¹; the [Co(Hpaba)(H₂O)₃].1.5H₂O chain and the [Cu₂(MeHpaba)₄(MeOH)₂].1.5H₂O.3.68MeOH complex, both of which contain protonated amide groups².

2.2 Reactivity screening in aqueous and non-aqueous solutions

In aqueous solution the ester form of the ligand was used to react Cu^{II} metal ions (CuCl₂ and Cu(OAc)₂) in the presence of alkali bases (LiOH, NaOH) or of NH₃ for complete deprotonation, and leave to crystallize using diffusion.

In non-aqueous solution, the two forms of the ligands were used in MeOH or MeCN. Cu^{II} salts or coordination clusters, [Co₂(μ-OH₂)(O₂(CMe₃)₄(HO₂(CMe₃)₄)] (Co₂Piv) and [Ni₂(μ-OH₂)(O₂(O₂(CMe₃)₄(HO₂(CMe₃)₄)] (Ni₂Piv)^{3,4}, were reacted in the presence of tetramethylammonium hydroxide (TMAOH), tetrabutylammonium hydroxide (TBAOH), triethylamine (NEt₃) or sodium methoxide (NaOMe).

In aqueous solution, all the ligands but H₂Et-phpma give clear solutions, the results are more mixed in non-aqueous media (see Table 2.1). As could have been feared, reaction with para-substituted phenyloxamate ligands, especially phpma, yields poorly soluble products, which could be insoluble {Cu-phpma} polymers.

Method Ligand	Reaction in water with Cu ^{II}	Reaction with Cu ^{II}		Reaction with coordination clusters	
		MeOH	MeCN	MeOH	MeCN
H ₂ Li-paba·H ₂ O; H ₂ Et-paba	Clear green solution	Clear green solution	Suspension	Suspension	Suspension
H _{2.5} Na _{0.5} -oaba·0.5(H ₂ O); H ₂ Et-oaba	Clear green solution	Clear green solution with precipitate	Clear green solution with precipitate	Clear solution	Suspension
H ₂ Na-phpma·0.5H ₂ O; H ₂ Et-phpma	Suspension	Suspension	Suspension	Suspension	Suspension
H _{2.5} Na _{0.5} -ohpma·0.5H ₂ O; H ₂ Et-ohpma	Clear green solution	Clear green solution	Clear green solution	Clear solution	Suspension

Table 2.1 Results of the screening

Despite our best efforts in varying stoichiometry, concentration or temperature in the synthetic conditions, crystal growth has failed in a majority of cases. Nevertheless, suitable single-crystals have been obtained for four new compounds: three molecules and one polymer. Complex **2.1** Li₂[Cu(ohpma)(OH)]·5H₂O and complex **2.2** Li₄[Cu(paba)₂(H₂O)]·9H₂O were obtained by diffusion of acetone in aqueous solutions, compound **2.3** (HNEt₃)[Cu(ohpma)] was obtained by slow evaporation of a MeOH solution, and complex **2.4** (TMA)₃[{Co^{III}(ohpma)₂Co^{II}(MeOH)₂}₃]·10H₂O·5MeOH was obtained from the reaction between the H₃-ohpma ligand and Co₂Piv in MeOH.

As mentioned earlier, the reactions of the phpma ligand with Cu^{II} give insoluble products, green precipitates are obtained almost immediately after addition of the metal ion and final solutions are colourless. We assume that such a ligand is more inclined to afford polymers, rather than a classical 0D [Cu(L)₂]⁴⁺ complex. Nevertheless, the coordination of the oxamate groups of the ligands occurs, as attested with IR spectroscopy in the case of a reaction in MeOH and using TMAOH (Figure 2.1).

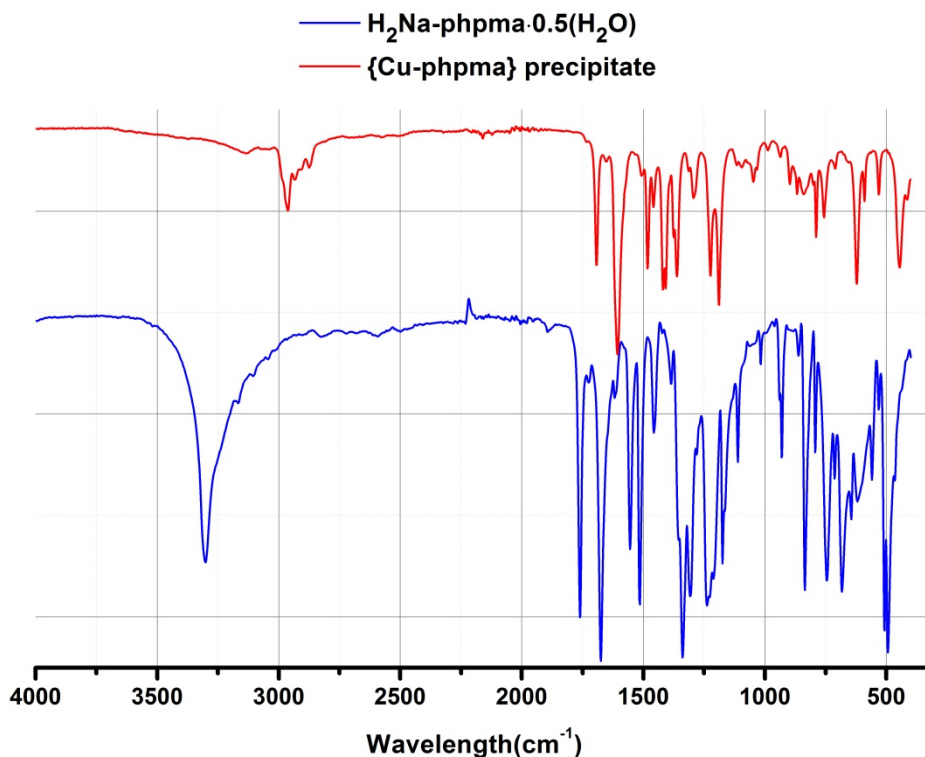


Figure 2.1 IR spectra of a {Cu-phpma} precipitate and of the H₂Na-phpma ligand.

Distinct absorption bands between 3000 cm⁻¹ to 2800 cm⁻¹ corresponds to the C-H stretching vibration of the counter-ion, TMA⁺, and the C=O stretching vibration in the 1700-1600 cm⁻¹ region are characteristic of coordinated oxamate moieties.

2.3 Structural and magnetic characterizations

2.3.1 Structure of Li₂[Cu(ohpma)(OH)]·5H₂O

Complex **2.1** crystallizes in the *P2(1)2(1)2(1)* space group and consists of an anionic [Cu(ohpma)]⁻ unit, a coordinated hydroxide anion, lithium cations, and water molecules. The Cu^{II} atom is coordinated to the tridentate (ohpma)³⁻ ligand via the oxygen and nitrogen atoms of the oxamate group, and the oxygen atom of the deprotonated hydroxy substituent (See Figure 2.2). An hydroxide anion complete the square planar coordination sphere of the Cu^{II} ions. This hydroxide anion is stabilized by coordinated Li⁺ cations that can also be found bis-chelated by the oxamate function. One water molecule can also be found in what would be the apical position of the Cu^{II} complex, at 2.597(1) Å. The Cu-N(amide) and Cu-O(carboxylate) bond lengths are 1.926(1) and 2.012(2) Å, respectively. For the Cu-N distance, it is relatively short and resembles that of more constrained oxamate complexes, such as those obtained with bis-oxamate ligand (from 1.887 Å to 1.931 Å)⁵⁻¹⁰, in opposition to bis(mono-oxamate) Cu^{II} complexes¹¹⁻¹³. The O-Cu-O angle from the phenolato group to the oxamate group is a good indicator of the constraint coming from the tridentate side of

the ligand, with a value here of 165° .

In the crystal lattice, the lithium cation coordinated to the oxamato group of the metalloligand is also bound to phenolato group and an hydroxide anion coming from two distinct adjacent complexes. This generates a 2D arrangement in the crystallographic (*ab*) plane. H-bonds involving two water molecules, a Li^+ cation and the hydroxy substituent of the ligand ($\text{O}\cdots\text{O}$: 2.77 and 2.86 Å) complete the structuration in the solid and connect the planes along *c* (Figure 2.3).

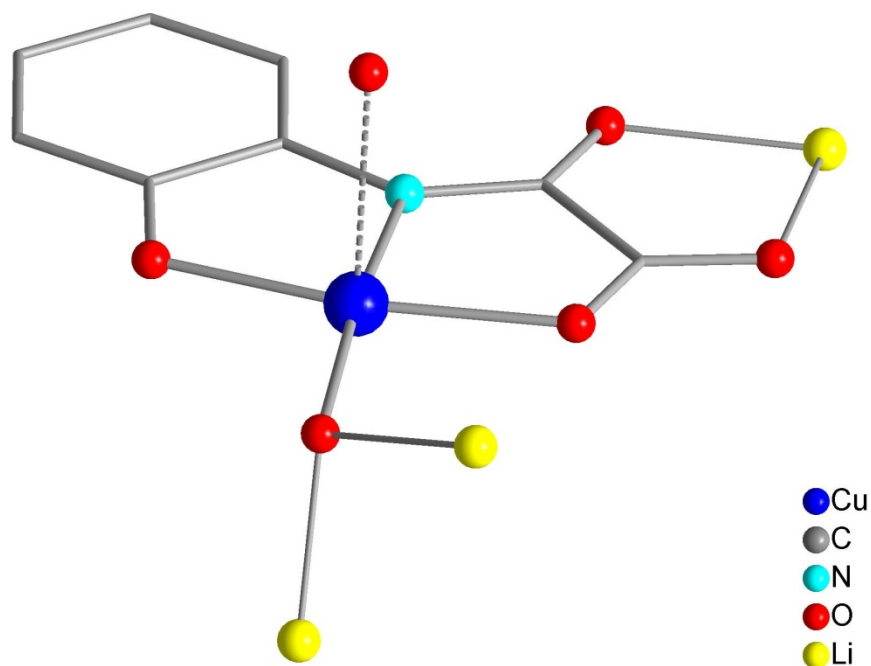


Figure 2.2 View of the $[\text{Cu}(\text{ohpma})(\text{OH})]^{2-}$ complex, H atoms have been omitted for clarity.

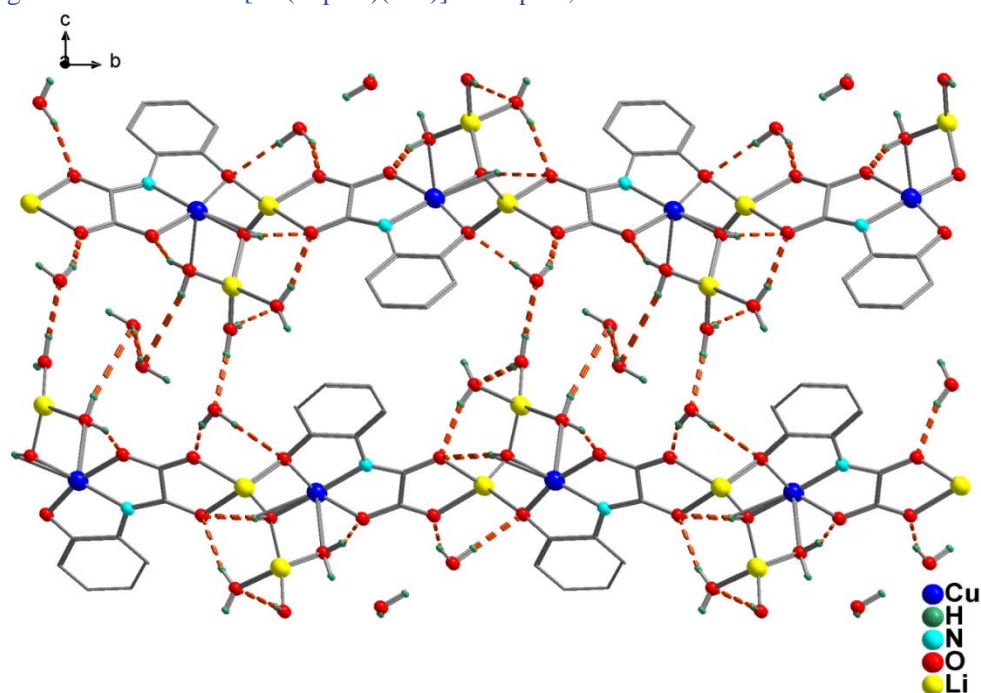


Figure 2.3 Crystal packing of complex 2.1 along *a*.

2.3.2 Structure characterization of $\text{Li}_4[\text{Cu}(\text{paba})_2(\text{H}_2\text{O})]\cdot 9\text{H}_2\text{O}$

Complex **2.2** crystallizes in the $P2(1)/c$ space group and consists of an anionic $[\text{Cu}(\text{paba})_2]^{4-}$ complex, lithium counter-cations and water molecules. The central Cu atom is five-coordinate in a square-based pyramid geometry. In the pyramid base, the metal ion is bis-chelated by nitrogen and oxygen atoms from two oxamato groups, with Cu-N (1.954(1), 1.973 (1) Å) and Cu-O (1,979(1), 1.993(1) Å) distances in accordance with reported bis(mono-oxamate) copper(II) metalloligand^{11,12} (Figure 2.4). A coordinated water molecule occupies the apical position at 2.360(6) Å. The coordination sphere of the Cu^{II} ions is slightly distorted. The Cu atom is situated just above the plane defined by the N/O atoms of the oxamate groups (0.184 Å), which form a dihedral angle of 19° . In the complex, the phenylcarboxylato groups point in the same direction, with phenyl rings almost parallel to each other (6° dihedral angle, φ - φ distance= 3.38 Å).

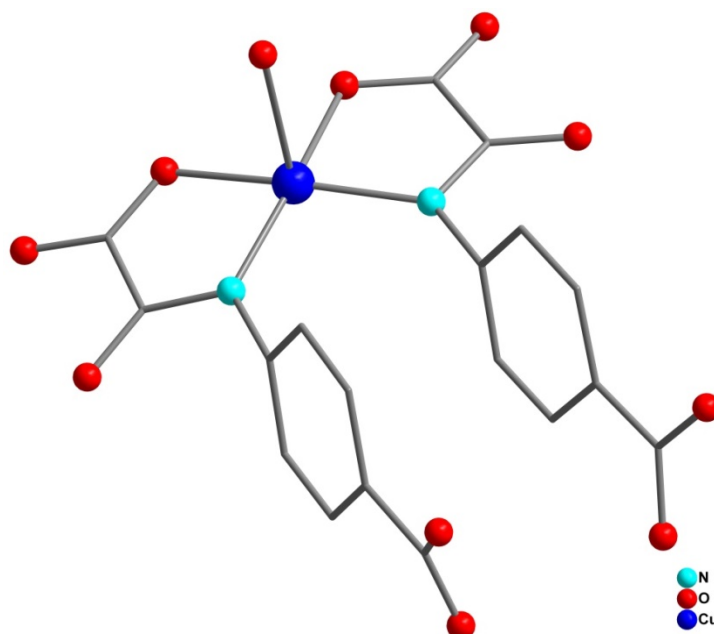


Figure 2.4 view of the anionic $[\text{Cu}(\text{paba})_2(\text{H}_2\text{O})]^{4-}$ unit of complex 2.2, H atom was omitted for clarity.

In the solid, two $[\text{Cu}(\text{paba})_2(\text{H}_2\text{O})]^{4-}$ complexes are connected to each other via the coordination of two lithium cations to the carboxylate groups (Figure 2.5). These dimers are aligned along the crystallographic b axis, and stacked along a via a network of H-bonds (Figure 2.6). The lithium ion coordinated to the ligand is the only one that has been found by crystallography.

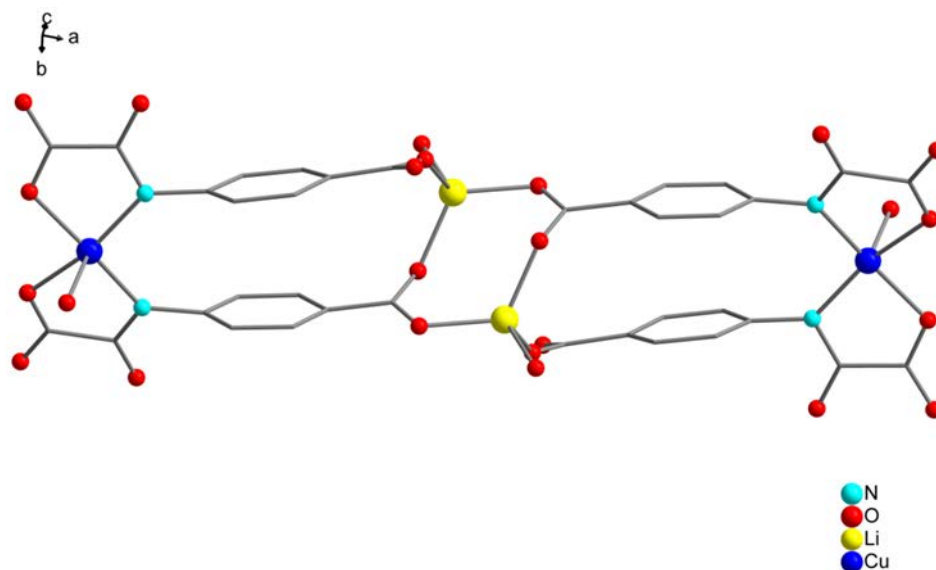


Figure 2.5 View of metalloligand dimer linked through Li^+ .

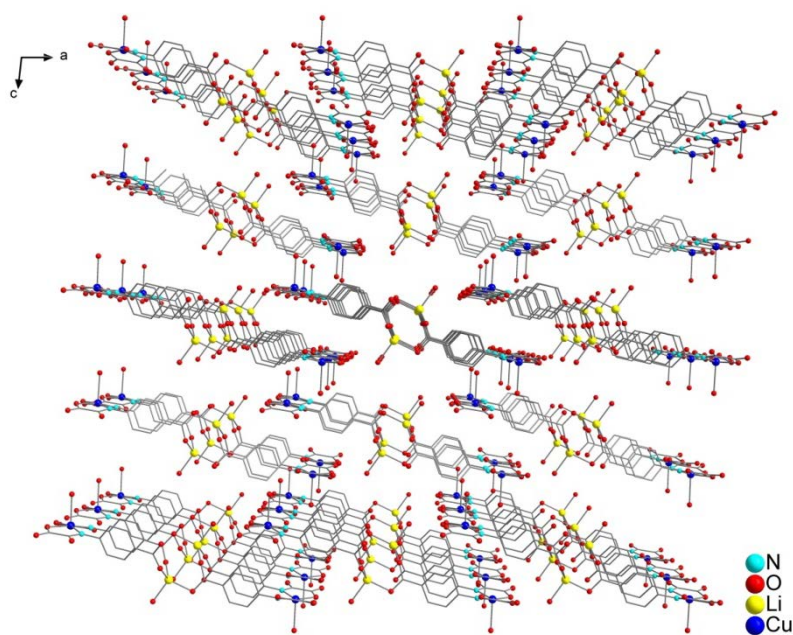


Figure 2.6 Crystal packing of 2.2. H atoms have been omitted for clarity.

2.3.3 Structure and magnetic characterization of $\{(\text{HNEt}_3)[\text{Cu}(\text{ohpma})]\}$

2.3.3.1 Structure

Compound **2.3** consists of an anionic oxamato-bridged Cu^{II} helicoidal chain with triethylammonium counter-cations. It crystallizes in the trigonal $P3_2$ space group.

The Cu^{II} ion is five-coordinate and adopts a square-based pyramid geometry. The base is defined by one nitrogen and two oxygen atoms coming from phenolato group and oxamato groups of the ligand (N1, O1, O4), and one oxygen atom (O3) from a second oxamate function belonging to an

adjacent metalloligand. The latter is coordinated in a *cis* fashion and has its remaining carbonyl oxygen atom (O2) occupying the apical position of the Cu^{II} complex (Figure 2.7). The bond lengths around the Cu atom (in Å: Cu-N1 = 1.914(2), Cu-O3 = 1.965(2), Cu-O4 = 1.969(1), Cu1-O1 = 1.983(1), Cu1-O2 = 2.243(1)) are similar to the metalloligand we have discussed above. The constraint of the ligand's tridentate coordination mode is also similar, with an O-Cu-O angle of 162°.

Interestingly, this 1D chain has a helicoidal configuration, which is rarely observed in oxamate chemistry^{14,15}. Indeed, the only two other examples of helical chains have been observed with an amino-acid-based oxamate ligand, (R)-N-(ethyloxoacetate)phenylglycine, or the 2-dimethylaminoethyl(oxamate). Indeed, these ligands have very similar tridentate coordination modes with donor atoms on the β-carbon of the N-substituted oxamato group.

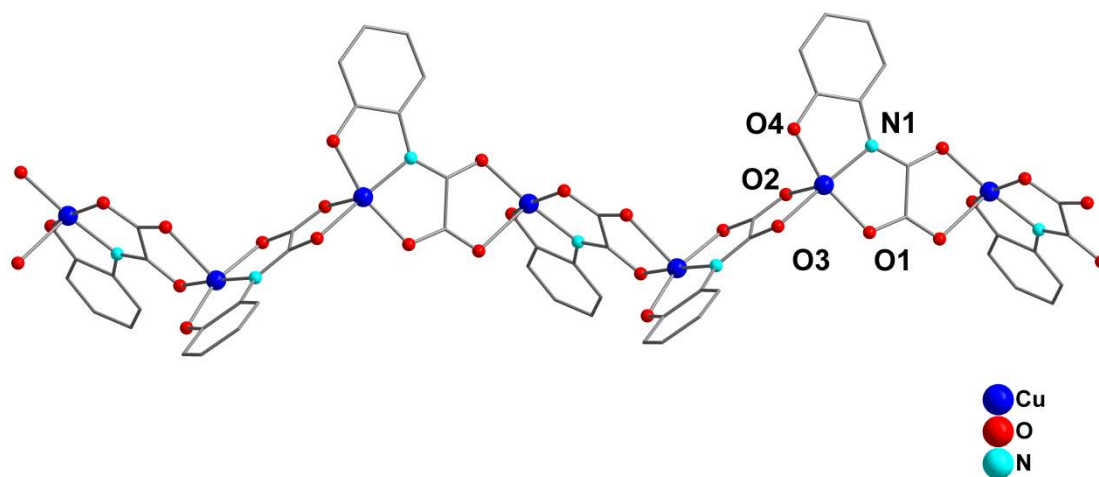


Figure 2.7 View of the chain compound 2.3. HNEt₃⁺ and H atom have been omitted for clarity.

Compound **2.3** grows parallel to the crystallographic *c* axis and the chains are rather well separated from each other (Figure 2.8 and Figure 2.9). The helicoidal configuration along with the peripheral phenyl groups from the ligands and the bulky triethylammonium cations afford an effective spacing between the metal ions of neighboring chains. The shortest interchain Cu...Cu distance is 9.66 Å.

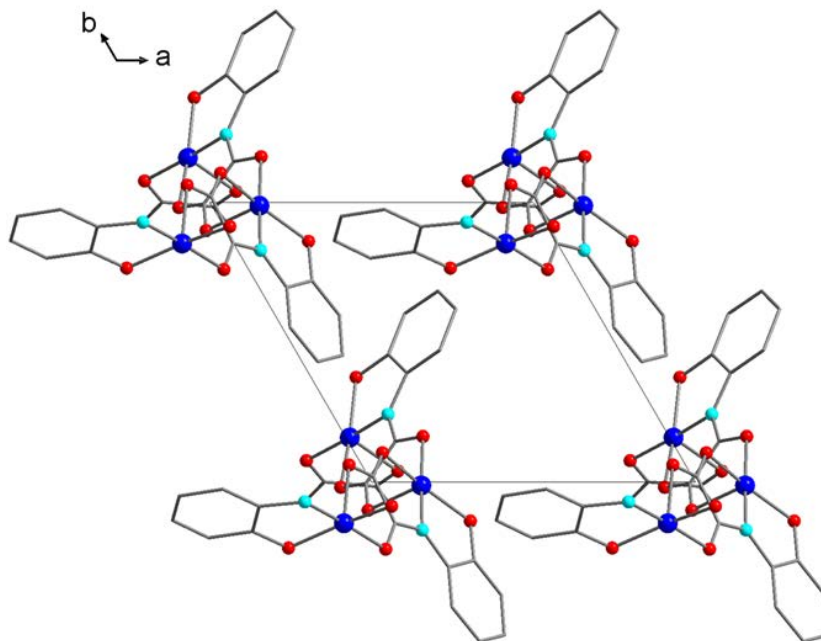


Figure 2.8 Crystal packing of compound 2.3, (*ab*) plane

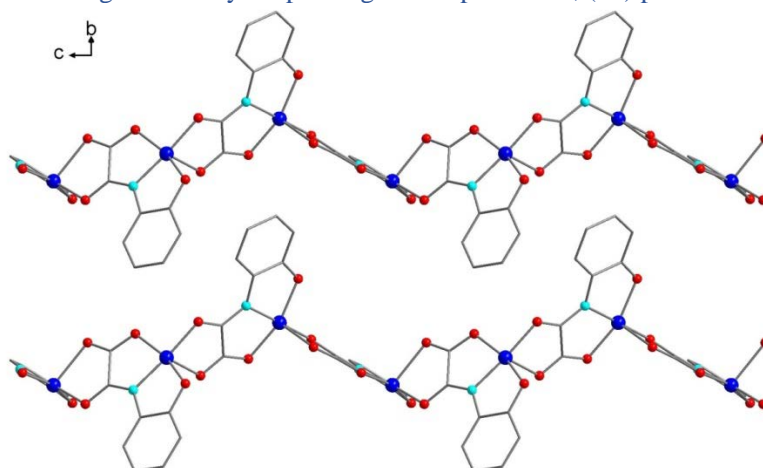


Figure 2.9 Crystal packing of compound 2.3, (*bc*) plane.

2.3.3.2 Magnetic characterization

The magnetic properties of grinded single crystals of compound **2.3** were investigated in the 2.0–300 K range. Two applied field, 1000 Oe and 1T, were used in low temperature and high temperature, respectively. Its $\chi_M T$ vs. T plot (χ_M being the magnetic susceptibility per Cu^{II} ion) is shown in Figure 2.10. At room temperature, $\chi_M T$ is equal to $0.376 \text{ cm}^3 \text{ mol}^{-1} \text{ K}$, a smaller value than the calculated one for an isolated Cu^{II} ion ($S_{\text{Cu}^{\text{II}}} = 1/2$, $\chi_M T = 0.413 \text{ cm}^3 \text{ mol}^{-1} \text{ K}$ with $g_{\text{Cu}} = 2.1$) using the following formula:

$$\chi_M T(\text{Cu}^{\text{II}}) \approx \frac{1}{8} S(S+1) g_{\text{Cu}}^2$$

Upon cooling, $\chi_M T$ steadily decreases to reach a value of $0.007 \text{ cm}^3 \text{ mol}^{-1} \text{ K}$ at 2 K. These features are typical of an antiferromagnetic behavior arising from an antiferromagnetic interaction between

two adjacent Cu^{II} ions through the oxamato bridge. In the case of an antiferromagnetically coupled homometallic chain, a more sensible representation is the χ_M versus T plot which is depicted in Figure 2.10 (bottom). A broad maximum of χ_M was observed at 70 K in the χ_M vs. T curve followed by a minimum and a sharp increase at low temperature. This last feature is due to a small amount of Cu^{II} uncoupled impurity.

To model the magnetic data of **2.3** the Bonner Fisher's empirical law for a $S = 1/2$ 1D regular chain has been used¹⁶ to which we added the TIP contribution (temperature independent paramagnetism) of $60 \cdot 10^{-6} \text{ cm}^3 \text{ mol}^{-1}$ per Cu^{II} ion. Furthermore, to take into account the small amount of impurity a Curie law term was added

$$\chi_M = \frac{Ng^2\beta^2}{kT} \frac{0.25+0.074975x+0.075235x^2}{1.0+0.9931x+0.172135x^2+0.757825x^3} (1 - \rho) + \left(\frac{N\beta^2g^2}{4kT}\right)\rho + TIP \quad (1)$$

with

$$x = |J|/kT;$$

N being Avogadro's number, β being the electronic Bohr magneton, k is the Boltzmann constant, J is the magnetic coupling constant and g is the gyromagnetic Lande factor. ρ is the mass proportion of uncoupled impurity. The best fit parameters obtained from the eq. (1) are $J = -84.1 \text{ cm}^{-1}$, $g = 2.176$, $\rho = 0.0033$ (Figure 2.10), with $R = 9.14 \times 10^{-8}$ (R is the agreement factor defined as $\sum[(\chi_M T)_{exp} - (\chi_M T)_{calcd}]^2 / \sum[(\chi_M T)_{exp}]^2$).

In comparison to other oxamate-bridged Cu^{II} homometallic compounds, the result shows a weaker antiferromagnetic interaction in **2.3**^{17,18}. This is due to the particular coordination of the copper ion inside this chain that presents the so-called orbital reversal phenomenon¹⁹⁻²¹. Because of to the helical structure and the 4+1 copper coordination, the Cu-O2 bond length is the largest. This means that the delocalized spin density onto the O2 oxygen atom is very weak. In fact, the high spin densities are localized on the O1, O3, O4 and N1 atoms to which the orbital $d_{x^2-y^2}$ that contains the single electron of the Cu^{II} ion points to. In comparison to the examples in the literature where the magnetic $d_{x^2-y^2}$ orbitals of neighboring copper ions share the same plane with the oxamato bridge, the interaction with the oxamate bridge is much weaker because it only occurs on the amide function side. This considerably reduces the overlap between the magnetic orbitals of the neighboring magnetic centers. The interaction being proportional to the overlap between magnetic orbitals, a lower overlap results in a lower interaction as observed in compound **2.3** (Figure 2.11). A copper chain with the 2-dimethylaminoethyl(oxamato) ligand that presents the same helical structure was already published and the interaction is equal to $J = -74.1 \text{ cm}^{-1}$, a value close to the one observed in **2.3**¹⁴.

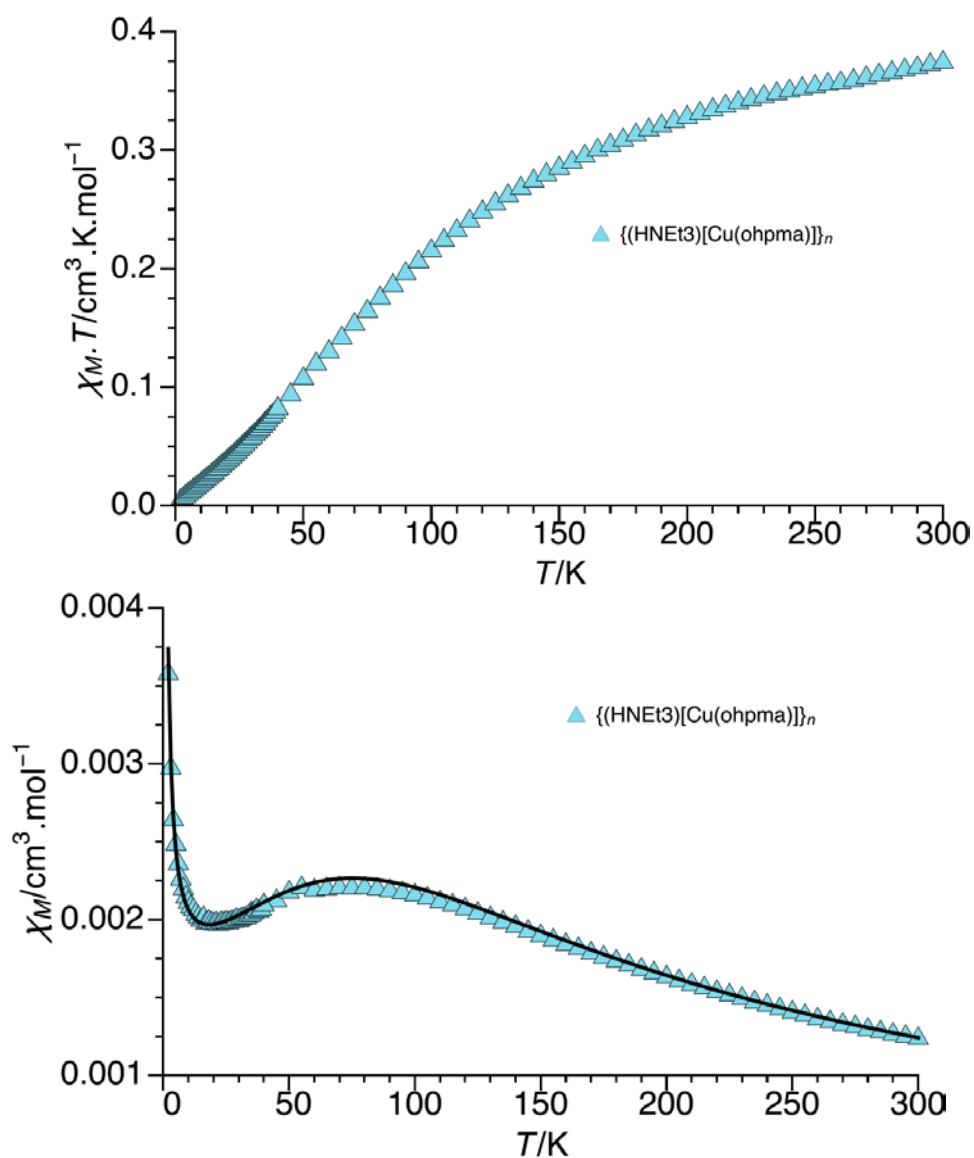


Figure 2.10 Top: Temperature dependence of $\chi_M T$ for compound 2.3 under an applied field magnetic field of 1 T ($T \geq 40$ K) and 1000 Oe ($T < 40$ K). bottom Experimental and best fit curve of χ_M v. T for 2.3.

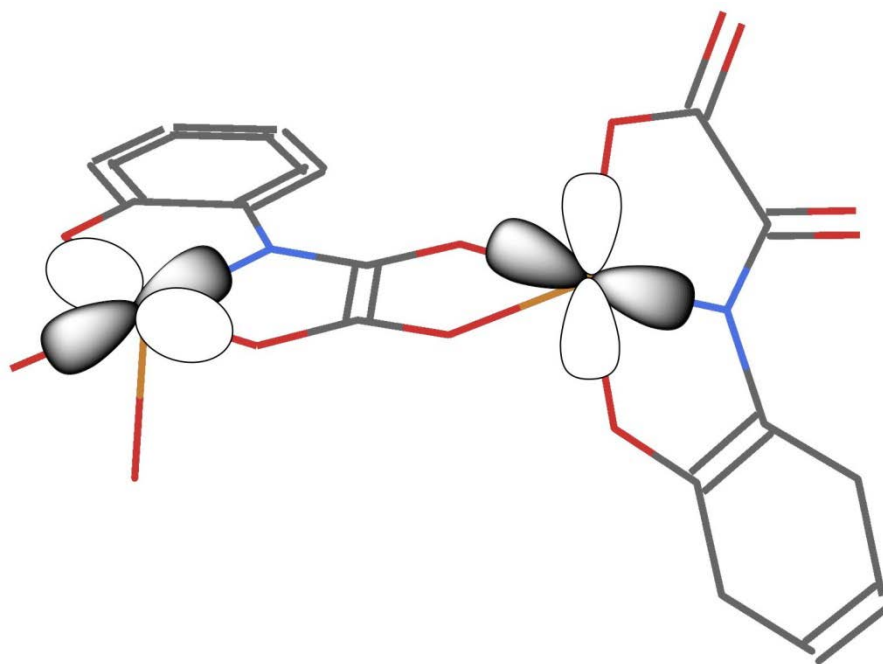


Figure 2.11 Magnetic orbitals orientation of compound 2.3 .

2.3.4 Structure and magnetic characterization of $(\text{TMA})_3\{\{\text{Co}^{\text{III}}(\text{ohpma})_2\text{Co}^{\text{II}}(\text{MeOH})_2\}_3\}\cdot 10\text{H}_2\text{O}\cdot 5\text{MeOH}$

2.3.4.1 Structure

Complex **2.4** crystallizes in the monoclinic $P21/c$ space group and consists of an anionic hexametallc mixed-valent $\{\text{Co}^{\text{III}}_3\text{Co}^{\text{II}}_3\}$ complex (Figure 2.12). In the ring, three Co^{II} ions are bridged by three bis-bidentate $[\text{Co}^{\text{III}}(\text{ohpma})_2]^{3-}$ metalloligands. In the metalloligand, the Co^{III} ion is coordinated to two tridentate $(\text{ohpma})^{3-}$ ligands, via the nitrogen and oxygen atoms of the oxamato groups, and the oxygen atoms of the deprotonated hydroxy substituents. The Co^{III} ion is thus six-coordinate in an octahedral geometry. $\text{Co}^{\text{III}}\text{-N/O}$ bond lengths vary from 1.871(6) to 1.968(4) Å (*av.* 1.907 Å). Angles in the octahedral geometry around the metal center vary from 83 to 98° (average deviation to orthogonality of 4°) and the O-Co-O angles indicative of the ligands' constraint vary from 169 to 171°. The Co^{II} ions are six-coordinate in distorted octahedral environment. Each ion is coordinated to two metalloligands via their remaining carbonyl oxygen atoms, and to two methanol solvent molecules. $\text{Co}^{\text{II}}\text{-O}$ distances vary from 2.031(6) to 2.168(5) Å (*av.* 2.095 Å), and the O-Co-O angles from 80 to 100° (*av.* deviation 5°). BVS calculations support the presence of both Co^{II} and Co^{III} ions. The oxidation of the cobalt ions must result from the coordination by two $(\text{ohpma})^{3-}$ ligand.

In the solid, the TMA^+ cations are located between the rings, and relatively strong H-bonds ($\text{O}\cdots\text{O} < 2.6$ Å) between coordinated methanol molecules and oxygen atoms from the deprotonated hydroxy

substituents generate chains of rings along the crystallographic b axis. The shortest intermolecular metal-metal distance is actually situated along the H-bond between Co^{II} and Co^{III} ions, and is of 5.72 Å. Considering paramagnetic ions, the shortest intermolecular distance is also found between two adjacent rings in the chain, and it is equal to 6.74 Å.

Complex **2.4** is only the third example of oxamate-based coordination ring. The other two examples being a Cu^{II} hexametallc wheel, which is based on an amino-acid-based oxamate ligand²² and a decametallc $\{\text{Mn}^{\text{II}}_5\text{Cu}^{\text{II}}_5\}$ wheel obtained from bis-oxamate ligand²³.

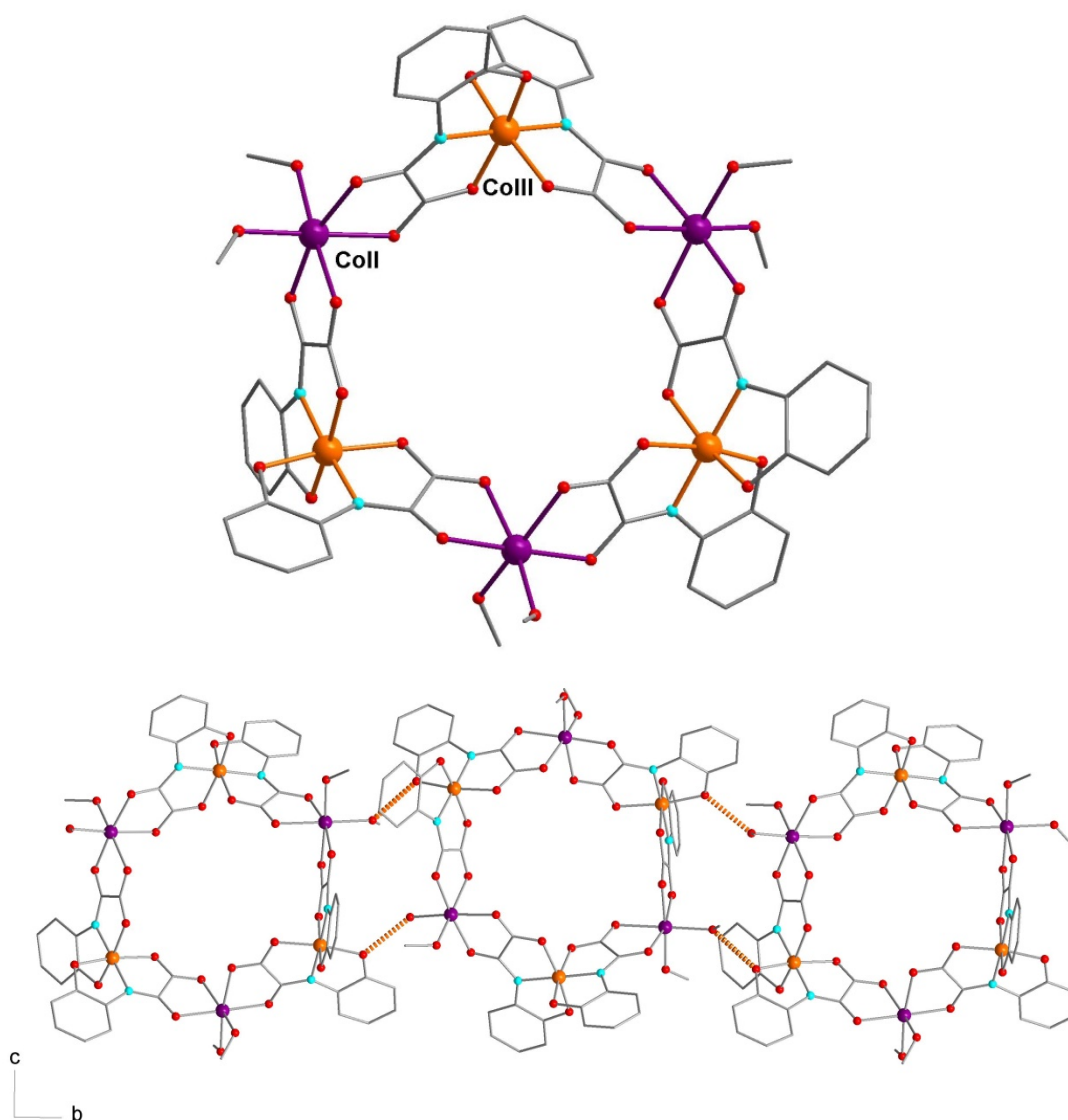


Figure 2.12 View of complex **2.4**, and of the H-bonded ring chains. TMA^+ and H atom have been omitted for clarity.

2.3.4.2 Magnetic property

The magnetic properties of complex **2.4** were studied under a field of 500 Oe and in a 3-200 K temperature range, shown by the χ_{MT} versus T plot in Figure 2.13. At 200 K, the χ_{MT} value is 9.71

$\text{cm}^3 \text{mol}^{-1} \text{K}$ and it fits in the expected range for three isolated Co^{II} ions ($2.7 < \chi_M T < 3.4 \text{ cm}^3 \text{mol}^{-1} \text{K}$ for one $\text{Co}(\text{II})$ ^{24,25,29}, so $8.1 < \chi_M T < 10.2$). Upon cooling, $\chi_M T$ steadily decreases to reach a value of $6.37 \text{ cm}^3 \text{mol}^{-1} \text{K}$ at 14 K. The product then goes up before finally decreasing to $5.82 \text{ cm}^3 \text{mol}^{-1} \text{K}$ at 3 K. Up to 14 K, this behavior is typical of $\text{Co}(\text{II})$ ions in octahedral environment with a $^4\text{T}_{1g}$ ground state and first order spin-orbit coupling. The bump in the $\chi_M T$ curve around 12K is caused by the non stoichiometric $\text{Co}(\text{OH})_{2-x}(\text{Y})(\text{H}_2\text{O})_n$ impurities which is commonly seen around 10–15 K in Co^{II} complex²⁶ (Figure 2.13).

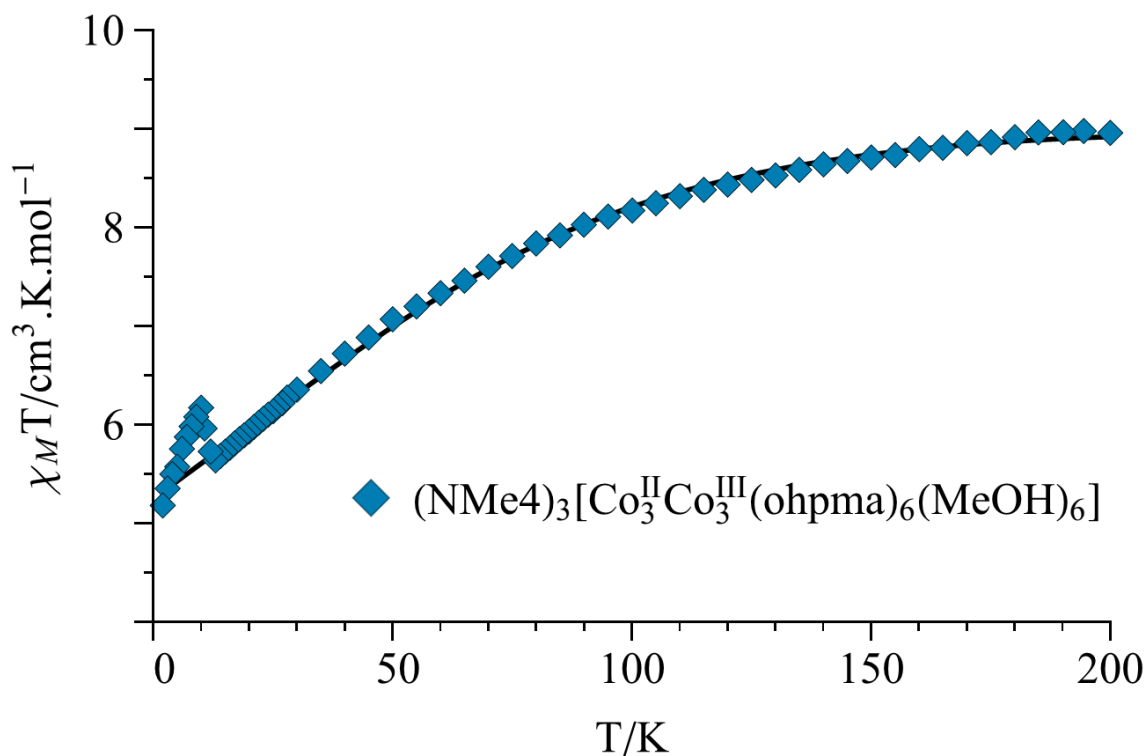


Figure 2.13 Temperature dependence of $\chi_M T$ of complex 2.4 under an applied field magnetic field of 500Oe from 3K to 200K. The solid black line is the best fit curve.

The interaction between the Co^{II} ions through the diamagnetic Co^{III} ions within the ring is expected to be very small and the magnetic data can be modeled as three isolated Co^{II} ions using the following Hamiltonian and the $\text{T} \equiv \text{P}$ isomorphism²⁷⁻²⁹ :

$$\mathcal{H}^v = \sum_{i=1}^3 \left[-\frac{3}{2} \alpha \lambda L_{\text{Co}i} S_{\text{Co}i} + \Delta \left(L_z^2_{\text{Co}i} - \frac{1}{3} L^2_{\text{Co}i} \right) + \left(-\frac{3\alpha}{2} L_v_{\text{Co}i} + g_e S_v_{\text{Co}i} \right) \beta \cdot H \right] \quad \text{with } v = x, y, z \quad (2)$$

λ is the spin-orbit coupling constant, α the orbital reduction factor and Δ the axial distortion parameter. L and S are respectively the orbital and spin operators with $L = 1$ in the T-P isomorphism approach and $S = 3/2$. The least square fit of the magnetic data gave $\lambda = -132 \text{ cm}^{-1}$, $\alpha = 0.84$, $\Delta = -378 \text{ cm}^{-1}$, with an agreement factor $F = 2.6 \cdot 10^{-5}$.

The dynamic properties of **2.4** were explored by alternating-current measurements (AC). At zero DC magnetic field, there was neither frequency-dependent χ_M' nor χ_M'' signal observed. This is due to the fast quantum tunneling effect which is reported in other SIMs or SMMs^{30,31}. However when a

1800 Oe DC magnetic field is applied, both the χ_M' and χ_M'' gave strong frequency dependent signals typical of SMMs as shown in Figure 2.14. However the blocking temperature is quite low and the maxima of χ_M' and χ_M'' are only visible at high frequency.

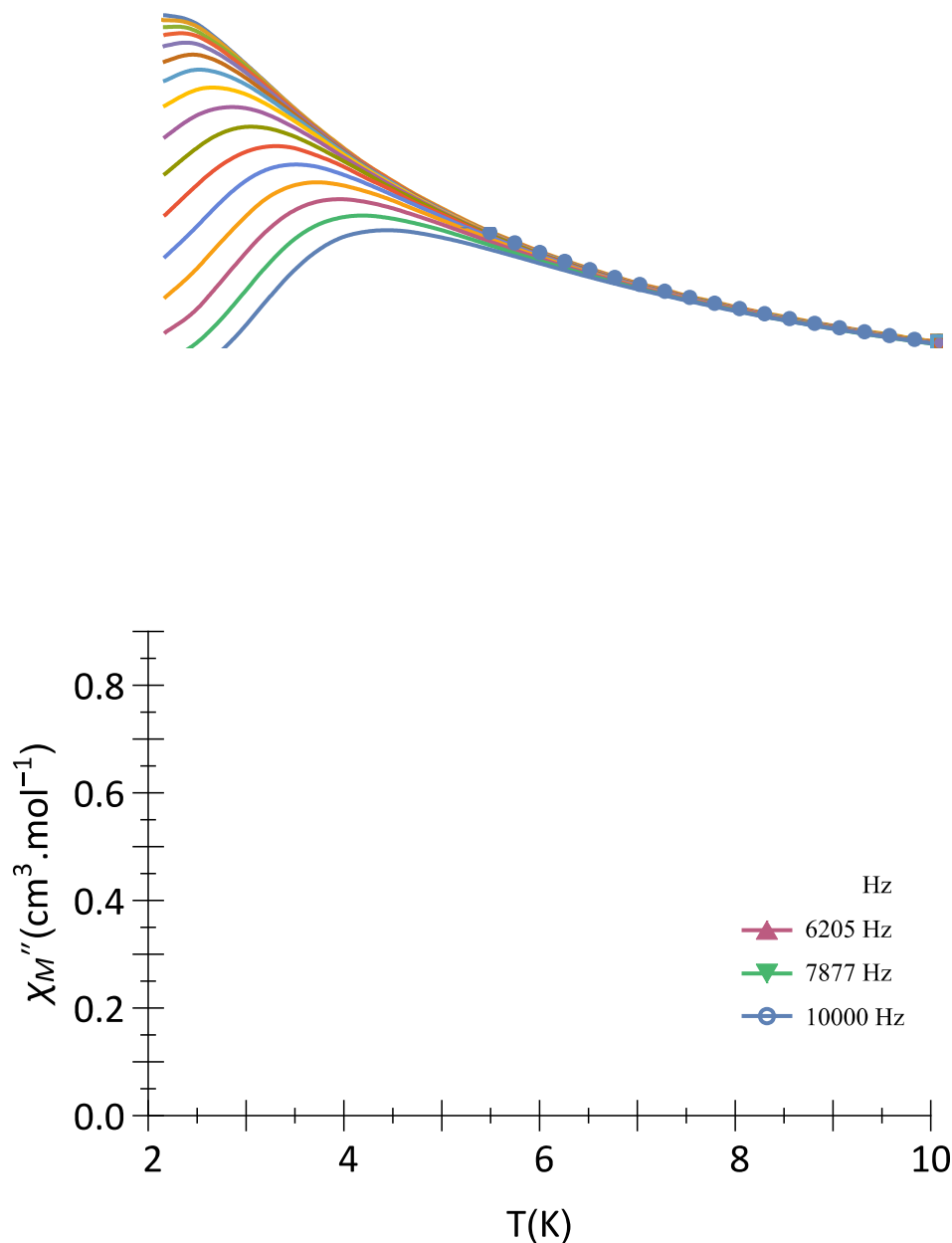


Figure 2.14 Temperature dependence of χ_M' (a) and χ_M'' (b) of complex 2.4 under an applied DC field of 1800 Oe in the frequency range of 10–10000Hz. The solid lines are only eye-guides.

To extract the relaxation times, the generalized Debye model, which considers a distribution of relaxation time, has been used³².

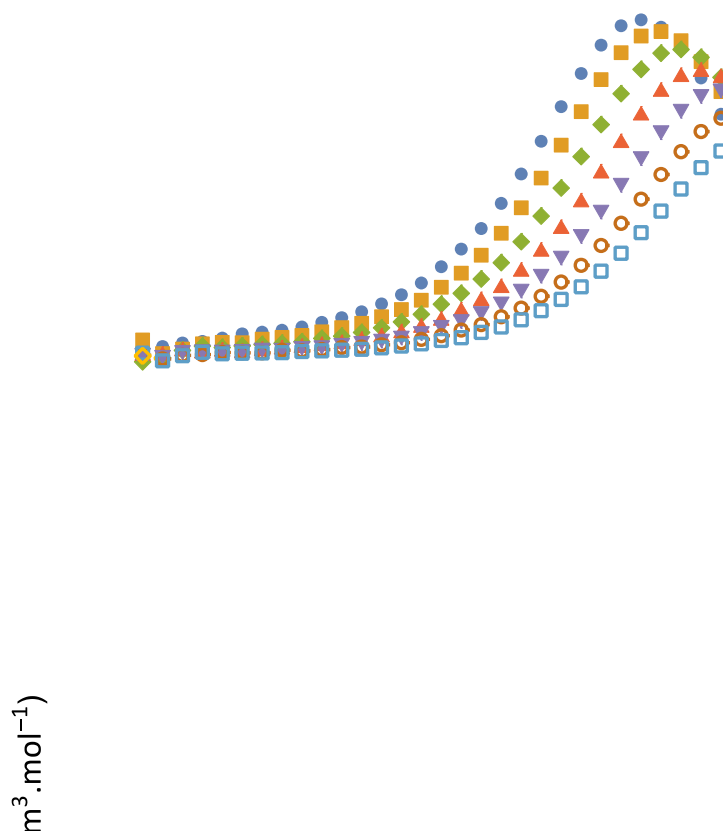


Figure 2.15 (top) Out-of-phase component, χ_M'' , of the magnetic susceptibility of 2.4 under a 1.8 kOe magnetic field and for frequencies between 10 Hz and 10 kHz. (bottom) Cole–Cole plot of 2.4 measured from 2.5 to 5 K under 1.8 kOe. The solid lines are the least-squares fitting of the data using a generalized Debye model

The frequency dependence of χ_M'' and Cole-Cole plot of **2.4** are shown in Figure 2.15. As suggested by Dekker *et al.*,³³ a two steps procedure was used to extract the relaxation time τ at each temperature. First a fit to the locus of χ of the Cole-Cole plot was performed to extract the values of χ_{adia} , χ_{iso} and η using equation (3), independent of τ and of the frequency.

$$\chi'' = \frac{1}{4\cos^2(\frac{\pi\eta}{2})} (\sqrt{2} \sqrt{\cos^2(\frac{\pi\eta}{2}) (-\cos(\pi\eta)(\chi_{\text{adia}} + \chi_{\text{iso}} - 2\chi')^2 + 4\chi'(\chi_{\text{adia}} + \chi_{\text{iso}}) - 6\chi_{\text{adia}}\chi_{\text{iso}} + \chi_{\text{adia}}^2 + \chi_{\text{iso}}^2 - 4(\chi')^2) + \sin(\pi\eta)(\chi_{\text{adia}} - \chi_{\text{iso}})}) \quad (3)$$

Where χ_{adia} and χ_{iso} stand for adiabatic and isothermal susceptibilities respectively and η characterizes the spreading of the relaxation time. In a second step τ is obtained by the fit of χ' and χ'' using the values of χ_{adia} , χ_{iso} and η determined in the first step:

$$\chi' = \frac{(\chi_{\text{iso}} - \chi_{\text{adia}}) \left((2\pi)^{1-\eta} \sin\left(\frac{\pi\eta}{2}\right) (v\tau)^{1-\eta} + 1 \right)}{(2\pi)^{2-2\eta} (v\tau)^{2-2\eta} + 2^{2-\eta} \pi^{1-\eta} \sin\left(\frac{\pi\eta}{2}\right) (v\tau)^{1-\eta} + 1} + \chi_{\text{adia}} \quad (4)$$

$$\chi'' = \frac{(2\pi)^{1-\eta} \cos(\frac{\pi\eta}{2}) (\chi_{iso} - \chi_{adia}) (\nu\tau)^{1-\eta}}{(2\pi)^{2-2\eta} (\nu\tau)^{2-2\eta} + 2^{2-\eta} \pi^{1-\eta} \sin(\frac{\pi\eta}{2}) (\nu\tau)^{1-\eta} + 1} \quad (5)$$

The values of τ , η , χ_{iso} and χ_{adia} at the studied temperatures are given in Table 2.2. The small η values ($\eta = 0.07-0.13$), with respect to that expected for a Debye model ($\eta = 0$), indicate a small dispersion of relaxation times³⁴.

Temperature K	χ_{adia}	χ_{iso}	η	$\tau \times 10^6$ from χ'	$\tau \times 10^6$ from χ''
2.5	0.138	2.24	0.1160	41.2	41.3
2.8	0.160	2.14	0.0934	33.7	33.5
3.0	0.173	2.03	0.0860	26.7	26.4
3.3	0.168	1.92	0.0924	20.5	20.1
3.5	0.191	1.80	0.0913	15.9	15.8
3.8	0.211	1.70	0.0964	12.5	12.3
4.0	0.289	1.60	0.0849	10.5	10.4
4.3	0.349	1.52	0.0768	8.92	8.90
4.5	0.306	1.44	0.1020	6.81	6.71
4.8	0.348	1.37	0.0990	5.88	5.80
5	0.422	1.31	0.0863	5.50	5.44

Table 2.2 Best values of χ_{adia} , χ_{iso} , η and τ extracted from the fit of the Cole-Cole plot, χ_M' and χ_M'' .

The spin relaxation can occur by several mechanisms^{35,36}, namely quantum tunneling, direct, Raman and Orbach processes. The thermal and magnetic field variation of these mechanisms are given in equation 6.

$$\tau^{-1} = AH^2T + \frac{B_1}{1+B_2H^2} + CT^n + \tau_0^{-1} \exp(-U_{eff}/kT) \quad (6)$$

where n is the Raman exponent, τ_0 is the pre-exponential factor and U_{eff} is the effective energy barrier to reverse the magnetization³⁶. For Kramer's doublet the theoretical n exponent is equal to 9³⁷.

Obviously, the determination of 6 parameters with a single data set is extremely delicate and almost meaningless due to over-parameterization. In favorable cases, it is possible to determine the three parameters for magnetic field-dependent relaxation mechanisms at low temperatures by measuring the relaxation time as a function of the magnetic field. For this to happen, the Raman and Orbach mechanisms must be negligible at these temperatures. This is the case for the Raman mechanism, which varies according to the power of 9 of the temperature, but for the Orbach one, the energy barrier must be large to fulfill this condition. In the case of compound **2.4**, these favorable conditions are not met due to the low blocking temperature which implies a probable small energy

barrier. The determination of the parameters by modeling the $1/\tau$ curve as a function of temperature is therefore rather unreliable. Nevertheless, considering that the $\text{Log}(\tau)$ curve as a function of $1/T$ is almost linear, we have assumed that the Orbach mechanism is dominant and equation (7) has been used to fit the data.

$$\tau^{-1} = \tau_0^{-1} \exp\left(-\frac{U_{eff}}{KT}\right) \quad (7)$$

The best fit parameters are $U_{eff} = 8.5 \text{ cm}^{-1}$ and $\tau_0 = 4.6 \cdot 10^{-7}$ (Figure 2.14), with $R = 2.5 \times 10^{-3}$. The deviation from linearity at low temperature for experimental points on the curve of $\text{Log}(\tau)$ versus $1/T$ is probably due to the effect of relaxation mechanisms not considered in the modeling (Figure 2.16 bottom). The U_{eff} and τ_0 values are in the expected range for SMM compound. However, these values should be taken with caution because only the Orbach relaxation mechanism has been taken into account. Moreover, the least square fits that take into account the other possible mechanisms allow a perfect model of the curve but with multiple different parameter sets. Most of them are physically acceptable, which confirms that in the case of **2.4** it is impossible to determine the respective weights of the different relaxation mechanisms.

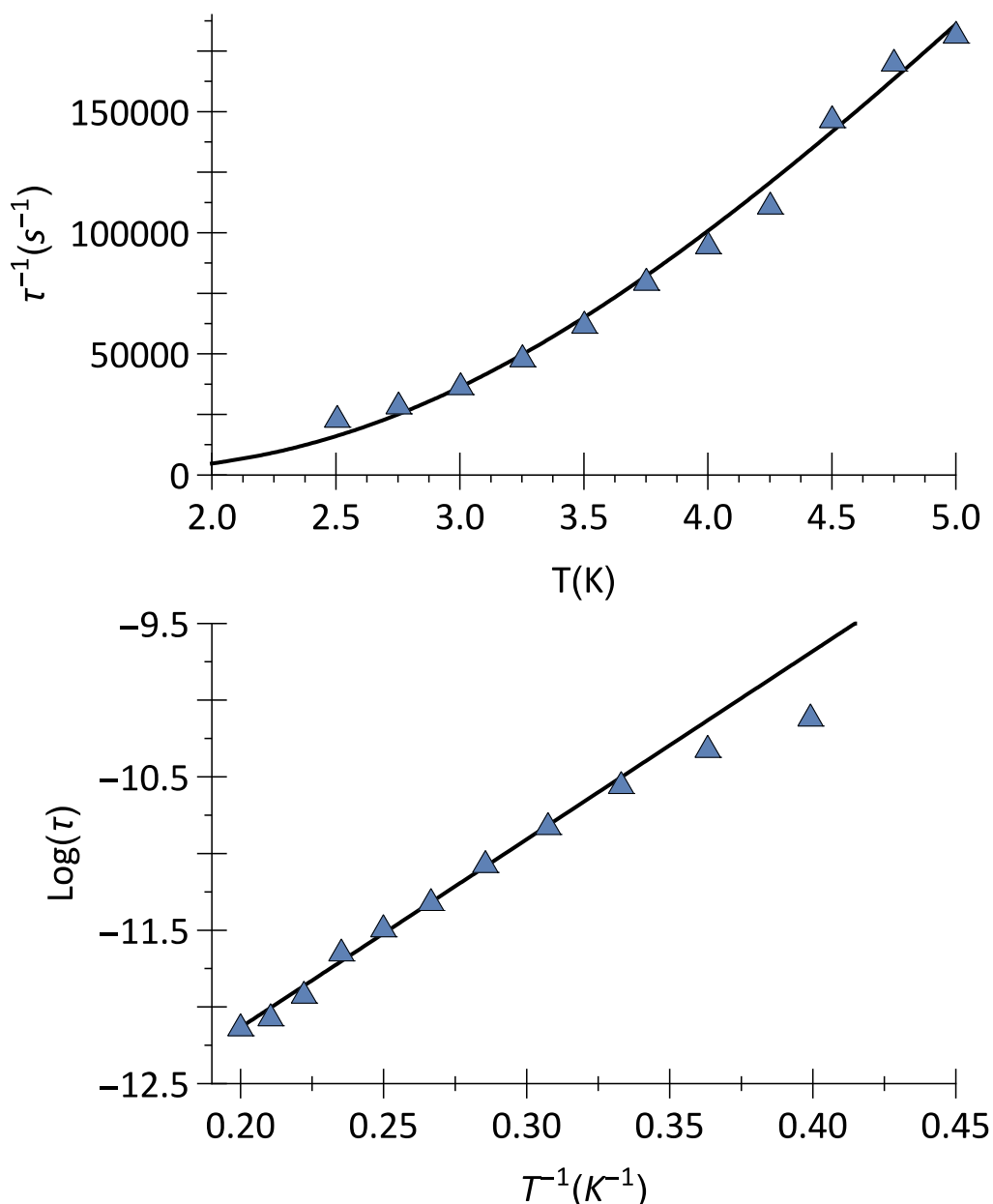


Figure 2.16 Top Relaxation Time τ^{-1} vs T for complex 2.4, Bottom $\text{Log}(\tau)$ vs $1/T$ for compound 2.4. The solid black line are the best fit curves..

2.4 Conclusion

In this chapter, four heterotopic oxamate-based ligands had their reactivity screened in bench conditions. Both ester pro-ligands and acidic ligands were used in aqueous or non-aqueous solution. Most of our syntheses have failed at yielding crystalline solids, the usual synthetic strategies employed for classical phenyl-based oxamate ligands show some limits for more complex and less predictable ligands.

Nevertheless, two anionic Cu-based metalloligands, $\text{Li}_2[\text{Cu}(\text{ohpma})(\text{OH})]$ and $\text{Li}_4[\text{Cu}(\text{paba})_2(\text{H}_2\text{O})] \cdot 9\text{H}_2\text{O}$, were synthesized in water, while non-aqueous reactions gave a 1D

helical compound, $(\text{HNEt}_3)[\text{Cu}(\text{ohpma})]$ and a coordination ring, $(\text{TMA})_3[\{\text{Co}^{\text{III}}(\text{ohpma})_2\text{Co}^{\text{II}}(\text{MeOH})_2\}_3] \cdot 10\text{H}_2\text{O} \cdot 5\text{MeOH}$.

Although bench reactions with heterotopic oxamate ligands in a less rational and more serendipitous approach have proven difficult, the ring compound actually shows why there could be an appeal with it. It is structurally uncommon for oxamate ligands, it displays field-induced SMM properties, and finally the presence of labile MeOH molecules makes it a candidate for further coordination chemistry.

References

- 1 K. Yoneda, Y. Hori, M. Ohba and S. Kitagawa, *Chemistry Letters*, 2008, **37**, 64–65.
- 2 T. L. Oliveira, L. H. G. Kalinke, E. J. Mascarenhas, R. Castro, F. T. Martins, J. R. Sabino, H. O. Stumpf, J. Ferrando, M. Julve, F. Lloret and D. Cangussu, *Polyhedron*, 2014, **81**, 105–114.
- 3 G. Aromí, A. S. Batsanov, P. Christian, M. Helliwell, A. Parkin, S. Parsons, A. A. Smith, G. A. Timco and R. E. P. Winpenny, *Chemistry – A European Journal*, 2003, **9**, 5142–5161.
- 4 G. Chaboussant, R. Basler, H.-U. Güdel, S. Ochsenbein, A. Parkin, S. Parsons, G. Rajaraman, A. Sieber, A. A. Smith, G. A. Timco and R. E. P. Winpenny, *Dalton Trans.*, 2004, 2758–2766.
- 5 S. Turner, O. Kahn and L. Rabardel, *J. Am. Chem. Soc.*, 1996, **118**, 6428–6432.
- 6 L. Cui, J. Ge, C. F. Leong, D. M. D’Alessandro and J.-L. Zuo, *Dalton Trans.*, 2017, **46**, 3980–3988.
- 7 T. Rüffer, B. Bräuer, A. K. Powell, I. Hewitt and G. Salvan, *Inorganica chimica acta*, 2007, **360**, 3475–3483.
- 8 E.-Q. Gao, J.-K. Tang, D.-Z. Liao, Z.-H. Jiang, S.-P. Yan and G.-L. Wang, *Inorganic Chemistry*, 2001, **40**, 3134–3140.
- 9 M. V. Marinho, T. R. G. Simões, M. A. Ribeiro, C. L. M. Pereira, F. C. Machado, C. B. Pinheiro, H. O. Stumpf, J. Cano, F. Lloret and M. Julve, *Inorg. Chem.*, 2013, **52**, 8812–8819.
- 10 H. O. Stumpf, Y. Pei, O. Kahn, L. Ouahab and D. Grandjean, *Science*, 1993, **261**, 447–449.
- 11 E. Pardo, R. Ruiz - García, F. Lloret, J. Faus, M. Julve, Y. Journaux, F. Delgado and C. Ruiz - Pérez, *Advanced Materials*, 2004, **16**, 1597–1600.
- 12 J. Ferrando-Soria, T. Grancha, M. Julve, J. Cano, F. Lloret, Y. Journaux, J. Pasán, C. Ruiz-Pérez and E. Pardo, *Chem. Commun.*, 2012, **48**, 3539–3541.
- 13 E. Pardo, C. Train, R. Lescouëzec, Y. Journaux, J. Pasán, C. Ruiz-Pérez, F. S. Delgado, R. Ruiz-García, F. Lloret and C. Paulsen, *Chem. Commun.*, 2010, **46**, 2322.
- 14 C. Kachi-Terajima, M. Ishii, T. Saito, C. Kanadani, T. Harada and R. Kuroda, *Inorg. Chem.*, 2012, **51**, 7502–7507.
- 15 T. Grancha, X. Qu, M. Julve, J. Ferrando-Soria, D. Armentano and E. Pardo, *Inorg. Chem.*, 2017, **56**, 6551–6557.
- 16 J. C. Bonner and M. E. Fisher, *Phys. Rev.*, 1964, **135**, A640–A658.
- 17 J. Parreiras, E. N. Faria, W. X. C. Oliveira, W. D. D. Pim, R. V. Mambrini, E. F. Pedroso, M. Julve, C. L. M. Pereira and H. O. Stumpf, *J. Coord. Chem.*, 2018, **71**, 797–812.
- 18 E.-Q. Gao, Q.-H. Zhao, J.-K. Tang, D.-Z. Liao, Z.-H. Jiang and S.-P. Yan, *J. Chem. Soc., Dalton Trans.*, 2001, 1537–1540.

- 19 J. J. Girerd, O. Kahn and M. Verdagner, *Inorg. Chem.*, 1980, **19**, 274–276.
- 20 H. Tamaki, Z. J. Zhong, N. Matsumoto, S. Kida, M. Koikawa, N. Achiwa, Y. Hashimoto and H. Okawa, *J. Am. Chem. Soc.*, 1992, **114**, 6974–6979.
- 21 Y. Journaux, J. Sletten and O. Kahn, *Inorg. Chem.*, 1985, **24**, 4063–4069.
- 22 T. Grancha, J. Ferrando-Soria, J. Cano, F. Lloret, M. Julve, G. D. Munno, D. Armentano and E. Pardo, *Chem. Commun.*, 2013, **49**, 5942–5944.
- 23 W. D. do Pim, É. N. de Faria, W. X. C. Oliveira, C. B. Pinheiro, W. C. Nunes, J. Cano, F. Lloret, M. Julve, H. O. Stumpf and C. L. M. Pereira, *Dalton Transactions*, 2015, **44**, 10939–10942.
- 24 J. M. Herrera, A. Bleuzen, Y. Dromzée, M. Julve, F. Lloret and M. Verdagner, *Inorg. Chem.*, 2003, **42**, 7052–7059.
- 25 D. Maspoch, N. Domingo, D. Ruiz-Molina, K. Wurst, J.-M. Hernández, G. Vaughan, C. Rovira, F. Lloret, J. Tejada and J. Veciana, *Chem. Commun.*, 2005, 5035–5037.
- 26 J. R. Neilson, D. E. Morse, B. C. Melot, D. P. Shoemaker, J. A. Kurzman and R. Seshadri, *Phys. Rev. B*, 2011, **83**, 094418.
- 27 J. S. Griffith, *The Theory of Transition-Metal Ions*, Cambridge University Press, 1971.
- 28 M. E. Lines, *Journal of Chemical Physics*, 1971, **55**, 2977–2984.
- 29 F. Lloret, M. Julve, J. Cano, R. Ruiz-García and E. Pardo, *Inorganica Chimica Acta*, 2008, **361**, 3432–3445.
- 30 N. Ishikawa, M. Sugita, T. Ishikawa, S. Koshihara and Y. Kaizu, *J. Am. Chem. Soc.*, 2003, **125**, 8694–8695.
- 31 M. Jeletic, P.-H. Lin, J. J. Le Roy, I. Korobkov, S. I. Gorelsky and M. Murugesu, *J. Am. Chem. Soc.*, 2011, **133**, 19286–19289.
- 32 K. S. Cole and R. H. Cole, *The Journal of Chemical Physics*, 1941, **9**, 341–351.
- 33 C. Dekker, A. F. M. Arts, H. W. de Wijn, A. J. van Duyneveldt and J. A. Mydosh, *Phys. Rev. B*, 1989, **40**, 11243–11251.
- 34 J. A. Mydosh, *Spin Glasses : An Experimental Introduction*, CRC Press, 1993.
- 35 K. N. Shrivastava, *phys. stat. sol. (b)*, 1983, **117**, 437–458.
- 36 J. M. Zadrozny, M. Atanasov, A. M. Bryan, C.-Y. Lin, B. D. Reinken, P. P. Power, F. Neese and J. R. Long, *Chem. Sci.*, 2013, **4**, 125–138.
- 37 L. T. A. Ho and L. F. Chibotaru, *Phys. Rev. B*, 2018, **97**, 024427.

Chapter 3:

*Reactivity screening in solvothermal conditions and
1D chain compounds structural characterization and
magnetic properties*

Chapter 3. Reactivity screening in solvothermal conditions and 1D chain compounds structural characterization and magnetic properties.

3.1 Reactivity screening

This chapter and the following two will present the preparation of oxamate-based MCPs under solvothermal conditions. Firstly, we have performed a reactivity screening with the aforementioned four oxamic acid ligands. They were used to coordinate Cu^{II} , Mn^{II} and Co^{II} ions (chloride or acetate salts) in pure DMF (4 mL), water or alcohol (4 mL) or mixture solution (4mL, DMF/ H_2O = 7:1). Water or alcohol as the sole solvent was rapidly abandoned for decomposition issues. Besides chloride anions, acetates were also chosen for their ability to act as a weak base to favor the deprotonation of the amide in solvothermal condition. To provide a stronger base, tetramethylammonium hydroxide (TMAOH) or triethylamine (NEt_3) were used in the reactivity screening. The solvothermal technique is an easy-operated one that consists in mixing all the starting materials and solvent into a Teflon-lined autoclave, perform a thermal treatment with a preset heating and cooling procedure (Figure 3.1). If successful, crystals form during the solvothermal synthesis cycle.

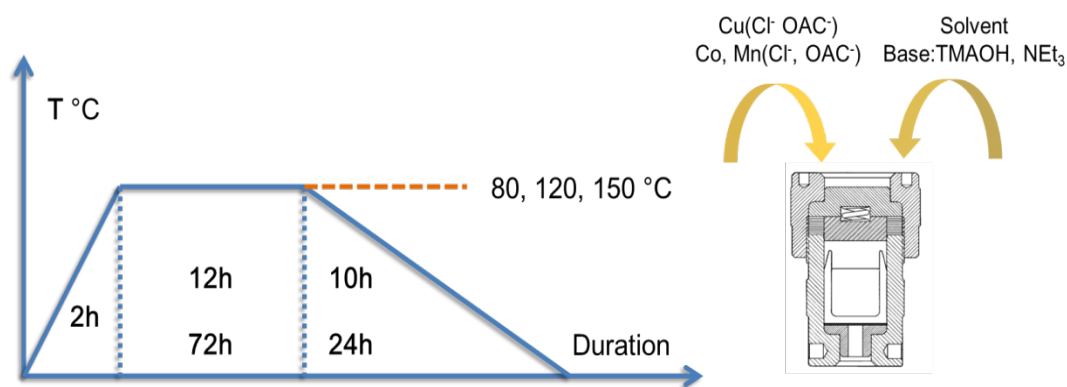


Figure 3.1 Strategy applied on solvothermal reactions in this thesis

Two reaction times for three different temperatures were used for the compounds presented in this manuscript. Each procedure consisted of three stages: 1). Heating up from room temperature to 25 °C in 10 minutes, and from 25 °C to the set temperature ($T = 80, 120$ or 150 °C) in 2h. 2). Keeping the temperature during 12 hr (short cycle) or 72 hr (long cycle). 3). Cooling down to 25 °C

in 10 hr (short cycle) or 24 hr (long cycle).

Table 3.1 below sums up the screening done on all four oxamic acid ligands for each reaction time (long v. short) at 80, 120 or 150 °C.

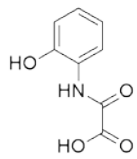
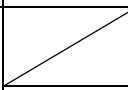
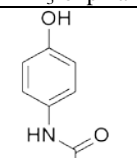
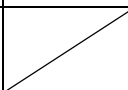
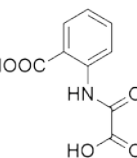
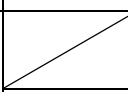
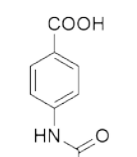
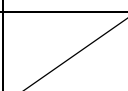
Ligand	Cu(OAc) ₂ CuCl ₂	Mn(OAc) ₂ ;MnCl ₂	Base	Solvents (4 mL)	Warming-Cooling procedure
		Co(OAc) ₂ ;CoCl ₂			
 H ₃ -ohpma	0.5 mmol	0.5 mmol	 TMAOH NEt ₃	DMF DMF+H ₂ O	Long and short cycle
 H ₃ -phpma	0.5 mmol	0.5 mmol	 TMAOH NEt ₃	DMF DMF+H ₂ O	Long and short cycle
 H ₃ -oaba	0.5 mmol	0.5 mmol	 TMAOH NEt ₃	DMF DMF+H ₂ O	Long and short cycle
 H ₃ -paba	0.5 mmol	0.5 mmol	 TMAOH NEt ₃	DMF DMF+H ₂ O	Long and short cycle

Table 3.1 Scheme of reactivity screening of the four acidic ligands

Considering the relatively high number of factors, drawing definitive conclusions from this screening would be unreliable. Nevertheless some general trends have been observed, and combinations that almost systematically fail have been identified.

Theoretically higher temperature should accelerate and promote the coordination reaction, however, for all four candidate ligands, reaction at 150 °C (in some cases at 120 °C) gave dark

brown solution with dark brown powders or green solution with red/brown powders, especially in the presence of base. While it clearly indicates oxidations issues for the metal ions, it also points to decomposition problems. Although bases are necessary for the deprotonation of the ligand and the full participation of the oxamate to the building of the CP, their use also favors side products, and it seems that the more base is used, the more decomposition and/or side-products occur. It is also clear that the presence of hydroxide is an aggravating factor, yet, most of our results were obtained with TMA^+ as counterions. This is confirmed by the use of TMA^+ salts of the ligands that seem to improve the yields. Last but not least, DMF was found to be the most appropriate solvent for the solvothermal reactions. H_2O , MeOH and EtOH gave poor results. DMF and DMF/ H_2O mixture were tested to influence the final compounds solubility.

Purple solution and homogenous purple powders sometimes appeared in the base-involved reaction screening of paba ligand with Cu^{II} and Co^{II} . However, the powders were not crystalline and sometimes happen to be {oxalate-Co} complexes. In basic condition, mixture of green crystalline and brown powders was always observed in Cu^{II} and Mn^{II} -involved synthesis. For oaba series, reaction without base very often gave a clear solution, with no solids appearing while standing at room temperature during at least several weeks. Base induced decomposition was both observed from reactivity study in ohpma and oaba –OH series ligand.

Specifically, for phpma ligands, whatever the metal, bases stoichiometry or temperature, the resulting solution was always brown/red with brown/black powders. It seems that decomposition was always on this kind of ligands. Whatever the metal source, the base or the temperature, the final solutions were always found to be brownish-red, with eventually some brown/black solid residues. This would point to unexpected reactions (redox and/or organic) with a probable decomposition of the ligand and the formation of metal oxides.

Fortunately, a series of multi-dimensional MCPs from oaba, paba and ohpma ligands were successfully synthesized and isolated as single crystals and we will start in the present chapter with the 1D systems obtained from the oaba and ohpma ligands.

3.2 1D chain compound

3.2.1 Structure of $[\text{Cu}_4\text{Co}_3(\text{oaba})_4(\text{OH})_2(\text{DMF})_4]\cdot 3(\text{DMF})\cdot 2\text{H}_2\text{O}$

The neutral 1D compound ($\{\text{CuCo-oaba}\}$; compound **3.1**; Figure 3.2) was synthesized at 80 °C with a 1:1:1 stoichiometry (ligand: $\text{Cu}(\text{OAc})_2$: $\text{Co}(\text{OAc})_2$) and without additional base. The DMF and H_2O solvent content was determined by elemental analysis and TGA.

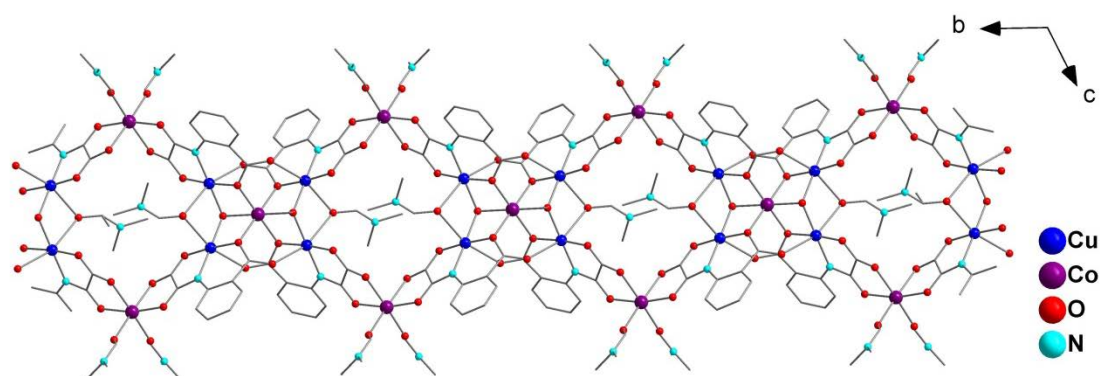


Figure 3.2 View of a fragment of the bimetallic chain of $\{\text{CuCo-oaba 1D}\}$ compound. H atoms have been omitted for clarity.

The dark purple product crystallizes in the $P-1$ triclinic space group. The asymmetric unit is made of two oaba ligands, two copper atoms, two cobalt atoms, one bridging hydroxide and DMF molecules (Figure 3.3).

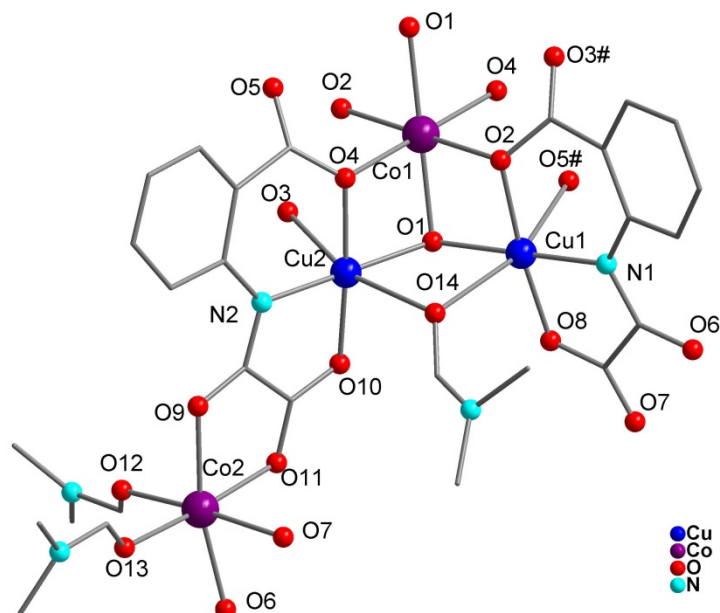


Figure 3.3 Perspective view of the asymmetric unit of compound 3.1. H atoms have been omitted for clarity.

Cu1 and Cu2 are structurally identical. Each copper ion is coordinated in a 4 + 2 geometry. The equatorial plane is formed by the tridentate oaba ligand using the nitrogen and oxygen atoms of the

chelating oxamate groups (N1, O8 and N2, O10 for Cu1 and Cu2 respectively) and one oxygen atom of the carboxylate group (O2,O4). The plane is completed by an oxygen atom of a μ_3 -hydroxide group (O1) that bridges Cu1, Cu2 and Co1. The remaining oxygen atom of the carboxylate group from adjacent oaba ligands (O5#, O3#), as well as a bridging DMF molecule (O14) complete the coordination spheres of the Cu^{II} ions, resulting in distorted octahedral geometries (O/N_{eq}-Cu-O/N_{eq} from 84 to 97°; O5-Cu1-O14=161°; O3-Cu2-O14 = 163°). Cu-O and Cu-N bond length are similar to the previously reported [Cu{Cu(oaba)(H₂O)(py)}₂] and [Cu{Cu(oaba)(MeOH)}₂] 2D compounds¹. They range from 1.946(7) to 1.976(7) Å for the equatorial positions and from 2.500(9) to 2.529(5) Å for the apical ones. Co1 and Co2 are both six-coordinate with an octahedral geometry. Co1 lies on the inversion center and binds the two {Cu(oaba)} metalloligands of the asymmetric unit in a facial manner via the μ_3 -hydroxide group and two carboxylate oxygen atoms (O2, O4). Co2 is *cis*-coordinated to the remaining carbonyl groups of two adjacent metalloligands (O6, O7, O9 and O11) and has two DMF molecules to complete its coordination sphere. The Co-O distances are quite narrow, and range from 2.081(6) to 2.135(9) Å. Some distortion is however apparent looking at O-Co-O angles that go from 78 to 102°, and deviate on average from orthogonality by 6°. The *cis* coordination of Co2 to two adjacent {Co(Cu(oaba))₂(OH)(DMF)} sub-units generates a zig-zag “half” chain, fusing to its symmetry equivalent on Co1, yielding the 1D compound (Figure 3.4). Alternatively, the chain can also be seen as [Co{Cu(oaba)}₄(OH)₂(DMF)₂]⁴⁺ pentametallic tetrakis-bidentate units connected by two cobalt ions into the 1D arrangement. In the crystal, the chain are aligned with each other along the crystallographic *b* axis, and are stacked along *a*. There are no obvious supramolecular interactions in the solid. The chains are well isolated within the crystal. The shortest interchain metal-metal distance is between two Co2 atoms and is equal to 8.884(3) Å

Charge balance, BVS calculations and geometric considerations support the presence of Co^{II} and of a hydroxido group.

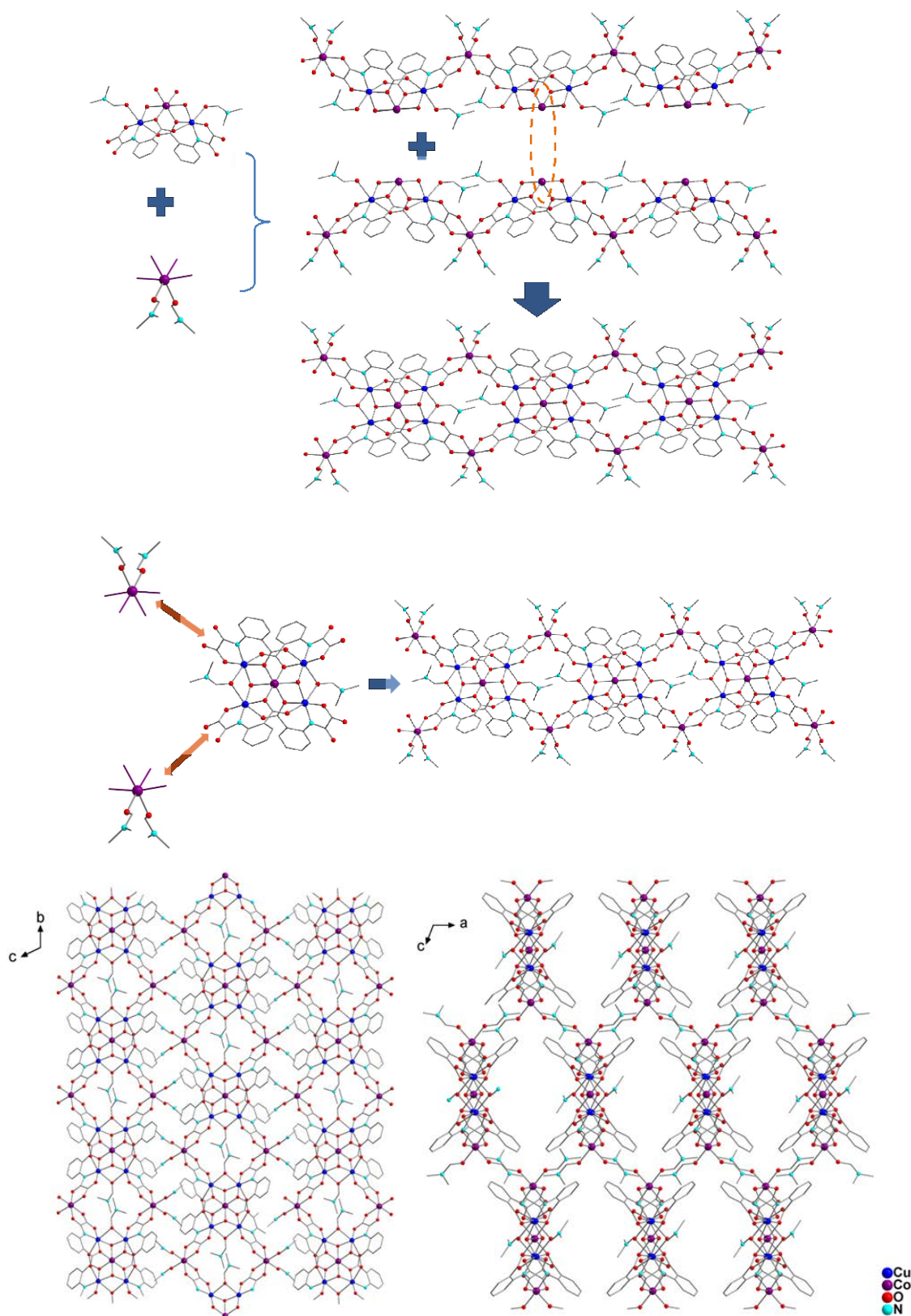


Figure 3.4 Scheme of the self-assembly in compound 3.1 by oxamate groups with Co^{II} ions (upper), and crystal packing of 3.1 in the *bc* and *ac* planes. H atoms have been omitted for clarity.

3.2.2 Magnetism of {CuCo-oaba} chain

The magnetic properties of compound **3.1** in the form of the $\chi_M T$ versus T plot [χ_M is the magnetic susceptibility per {Cu₄Co₃} unit] is shown in Figure 3.5, as well as the magnetic behavior of a hypothetical uncoupled {Cu₄Co₃} system. The value of $\chi_M T$ at room temperature is of 9.0 cm³mol⁻¹K, a value which is lower than the smallest value expected for the sum of four Cu^{II} and three Co^{II} non-interacting ions (≈ 10.1 cm³mol⁻¹K; $S_{Cu} = 1/2$ with $g = 2.12$, $\chi_M T(\text{Cu}^{\text{II}}) = 0.421$ cm³mol⁻¹K; octahedral Co^{II} with orbitally degenerate ⁴T_{1g} ground state, $2.7 < \chi_M T(\text{Co}^{\text{II}}) < 3.4$ cm³mol⁻¹K²⁻⁴), indicating a strong antiferromagnetic coupling between the ions. Upon cooling, the $\chi_M T$ product smoothly decreases until 170 K and then more sharply, down to 2.12 cm³mol⁻¹K at 2 K. The shape of this curve is typical of the combination of an antiferromagnetic interaction between the magnetic centers with the effect of spin-orbit coupling on the Co^{II} ions. No maximum of χ_M was observed in the temperature range investigated, showing that there is no magnetic ordering with the well isolated chains in the crystal. The M versus H plots for compound **3.1** at 2.0 K (M is the magnetization per {Cu₃Co₄} unit and H is the applied magnetic field) shows a slow saturation process in the applied field range.

Modeling the magnetic properties of this compound is extremely difficult. The size of the matrix in the {Cu₄Co₃} unit is already 27648 x 27648 and in an idealized symmetry it is necessary to take into account seven parameters. Besides this, the repetition of this unit in a chain structure must also be taken into account. This is clearly beyond the actual possibility of modelization technics.

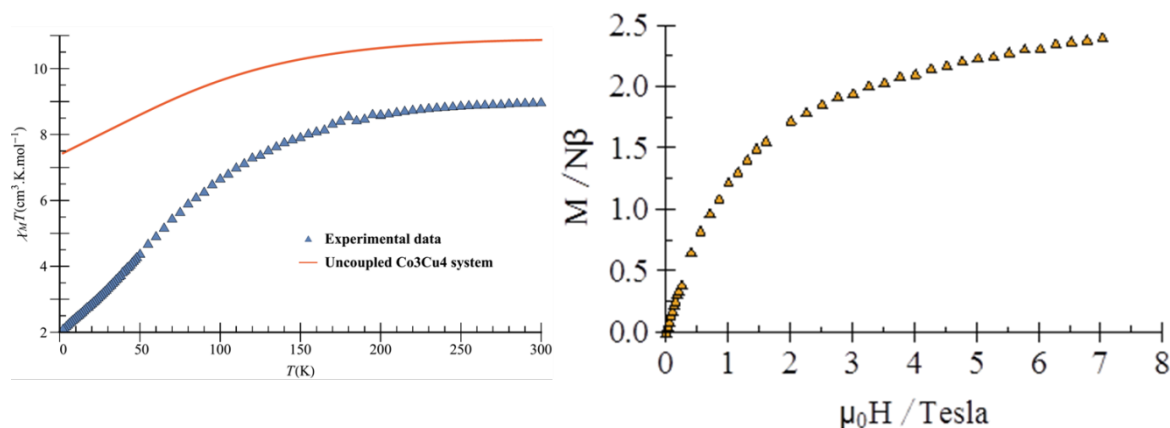


Figure 3.5 On the left thermal dependence of $\chi_M T$ for compound 3.1 in an applied field of 1 T ($T \geq 200\text{K}$) and 250 Oe ($T < 200\text{K}$). The uncoupled $\{\text{Cu}_4\text{Co}_3\}$ system is calculated taking into account the spin-orbit coupling on the cobalt ions with $\lambda = -180\text{ cm}^{-1}$, $\alpha = 0.9$, $\Delta = -800\text{ cm}^{-1}$ (λ , α and Δ being respectively the spin orbit coupling constant, the orbital reduction factor and the distortion) and for copper ions an average g factor of 2.12 and a TIP contribution of $60 \cdot 10^{-6}\text{ cm}^3\text{ mol}^{-1}$ per copper. On the right, magnetization of compound 3.1 versus magnetic field at 2 K

3.2.3 Structure of $[\text{Cu}(\text{ohpma})\text{M}(\text{OAc})(\text{DMF})_2]$ ($\text{M} = \text{Co}^{\text{II}}$; Mn^{II})

Ohpma-based chain compounds $[\text{Cu}(\text{ohpma})\text{M}(\text{OAc})(\text{DMF})_2]$ ($\text{M} = \text{Co}^{\text{II}}$; Mn^{II} ; compound 3.2 and compound 3.3) were also successfully synthesized from acetate salts at $80\text{ }^\circ\text{C}$ and in the absence of base. The two chains are isostructural.

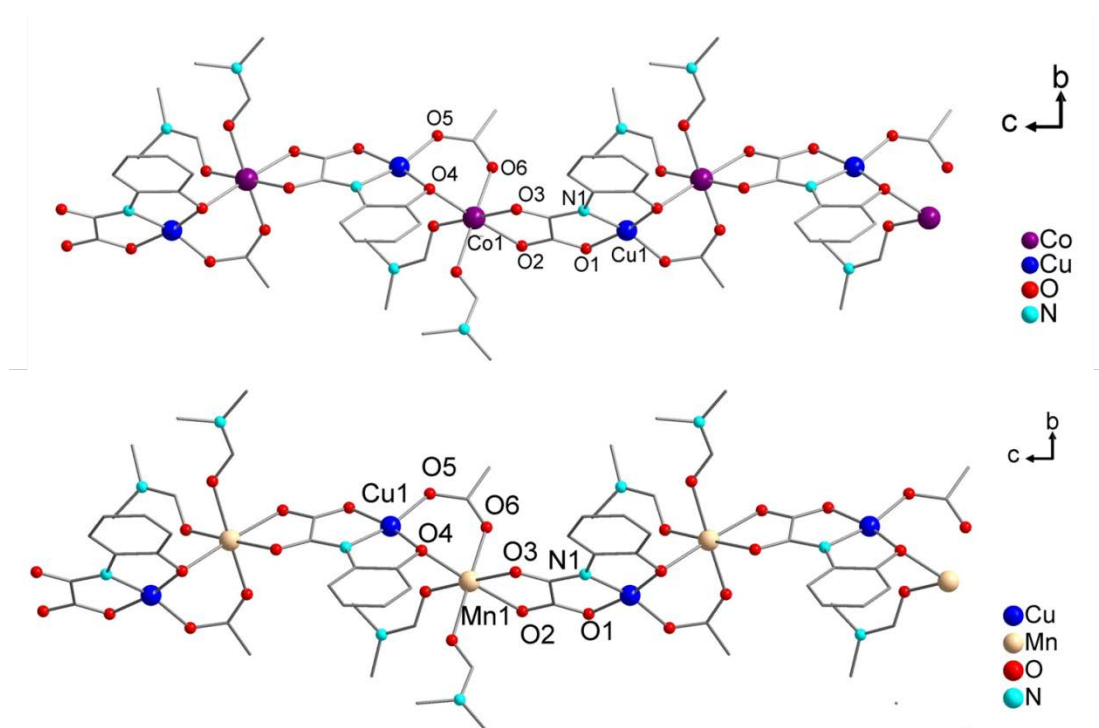


Figure 3.6 View of the bimetallic chains $\{\text{CuM-ohpma 1D}\}$ 3.2 and 3.3, H atoms have been omitted for clarity.

Compounds **3.2** and **3.3** consist of a neutral hetero-bimetallic oxamato-, and acetato-bridged chain (Figure 3.6) that crystallizes in the $P2_1/c$ monoclinic space group. The chain is made of $[\text{Cu}(\text{ohpma})]^-$ metalloligands where the Cu^{II} is coordinated to one nitrogen atom (N1) and one oxygen atom (O1) of the oxamate group, and the oxygen atom (O4) of the ligand's phenolato group. The metalloligands then bridge the additional M^{II} ions via the remaining chelating carbonyl groups of the oxamate function (O2, O3), as well as the phenolato group of the ligand (O4), and via an additional μ -acetato bridge (O5, O6). The copper ions are four-coordinate in a square-planar environment with, in comparison to the metalloligand (see Chapter 2), comparable Cu-O distances (1.956 Å [1.902(1)-2.006(1)]), and slightly shorter Cu-N bond length (1.902(2) and 1.905(1) Å). The distortion of the square planar geometry is barely more pronounced than in the metalloligand alone, with Cu-O/N angles ranging from 83 to 102°, and a dihedral angle between the N1-Cu-O1 and the O4-Cu-O5 plane of 13 and 12°, for the Co^{II} and the Mn^{II} respectively. The M^{II} ions are six-coordinate, with two DMF molecules completing the coordination sphere. They have fairly regular octahedral environments, with homogeneous M-O distances ranging from 2.061(1) to 2.133(2) Å for Co^{II} , and from 2.131(2) to 2.206(2) Å for Mn^{II} . These distances are similar to previously reported oxamate-based 1D polymers with *cis*-coordinated Co^{II} or Mn^{II} ions⁵⁻⁷. The O-Co-O angles vary from 79 to 98°, and deviate on average by 4° from orthogonality. For Mn^{II} ions, these angles range from 76 to 100°, with an average deviation of 5°.

The chains are parallel to each other and aligned along the crystallographic *c* axis (Figure 3.7). The shortest interchain metal-metal distances were found at 7.12 Å (Cu-Co) and 7.15 Å (Cu-Mn).

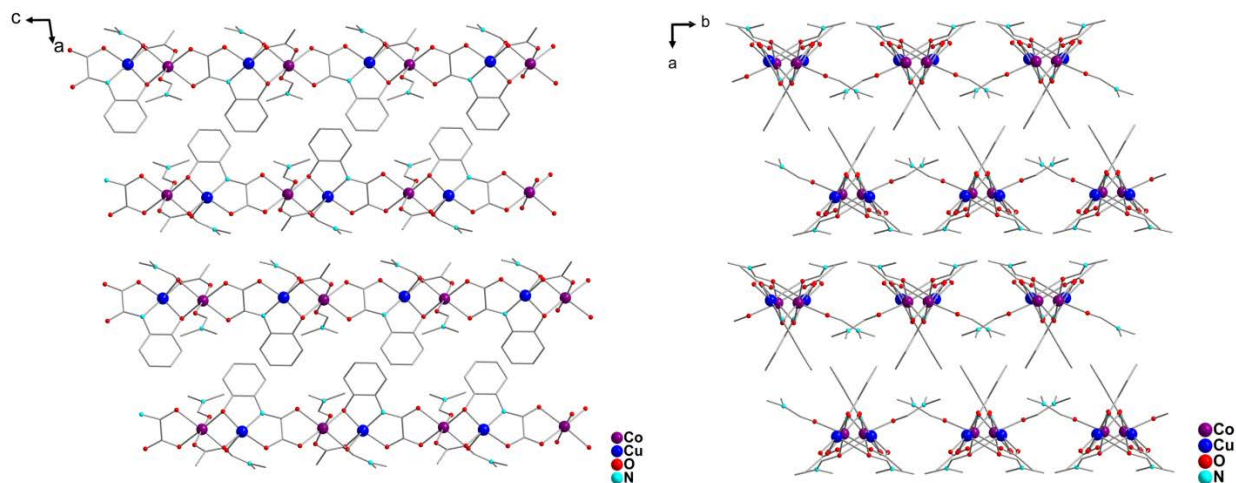


Figure 3.7 Crystal packing of compound 3.2 along c-axis and b-axis direction.

3.2.4 $[\text{Cu}(\text{ohpma})\text{Co}_x\text{M}_y(\text{OAc})(\text{DMF})_2]$ ($\text{M} = \text{Mn}^{\text{II}}$; Ni^{II})

To further investigate the magnetic properties, we have introduced a third metal into in the synthesis of the $[\text{Cu}(\text{ohpma})\text{Co}(\text{OAc})(\text{DMF})_2]$ chain. This has led us to the following heterotrimetallic compounds: $[\text{Cu}(\text{ohpma})\text{Co}_{0.57}\text{Mn}_{0.43}(\text{OAc})(\text{DMF})_2]$ and $[\text{Cu}(\text{ohpma})\text{Co}_{0.59}\text{Ni}_{0.41}(\text{OAc})(\text{DMF})_2]$ (**3.4** and **3.5**, respectively). Single-crystal (see Appendix) and powder X-ray diffraction (Figure 3.8) confirms that all four chains are isostructural. To explain the differences that were observed between the experimental X-ray powder diffraction diagrams, or between the diagrams calculated from single-crystal X-ray diffraction data and the experimental ones, we have performed Le Bail refinements (Table 3.2). They indicate mainly a slight increase of the unit cell parameter a . The metal content in the formulae of compounds **3.4** and **3.5** was taken from ICP-AES results and differ from the single-crystal X-Ray data. In the latter, site occupancies for the Co, Mn and Ni atoms were refined and gave on the measured crystals $\{\text{Co}_{0.78}\text{Mn}_{0.22}\}$ and $\{\text{Co}_{0.28}\text{Ni}_{0.72}\}$ for **3.4** and **3.5**. A second set of ICP-AES titrations confirmed the ratios given in the formulae and were $\{\text{Co}_{0.56}\text{Mn}_{0.44}\}$ and $\{\text{Co}_{0.54}\text{Ni}_{0.46}\}$.

		a (Å)	b (Å)	c (Å)	β (°)
3.2	SC-XRD	15.31(4)	8.38(2)	15.90(4)	98.20(1)
	Lebail	15.49	8.40	15.89	98.00
3.3	SC-XRD	15.17 (7)	8.48(4)	16.17 (7)	98.44 (3)
	Lebail	15.33	8.52	16.19	98.39
3.4	SC-XRD	15.26 (4)	8.43 (2)	16.00 (4)	98.27(1)
	Lebail	15.47	8.43	15.98	98.11
3.5	SC-XRD	15.38(4)	8.37 (2)	15.84(4)	98.09 (5)
	Lebail	15.58	8.38	15.83	97.88

Table 3.2 Unit cell parameters for 3.2-3.5 obtained by single-crystal X-Ray diffractions (SC-XRD) and after Lebail refinements of the powder patterns.

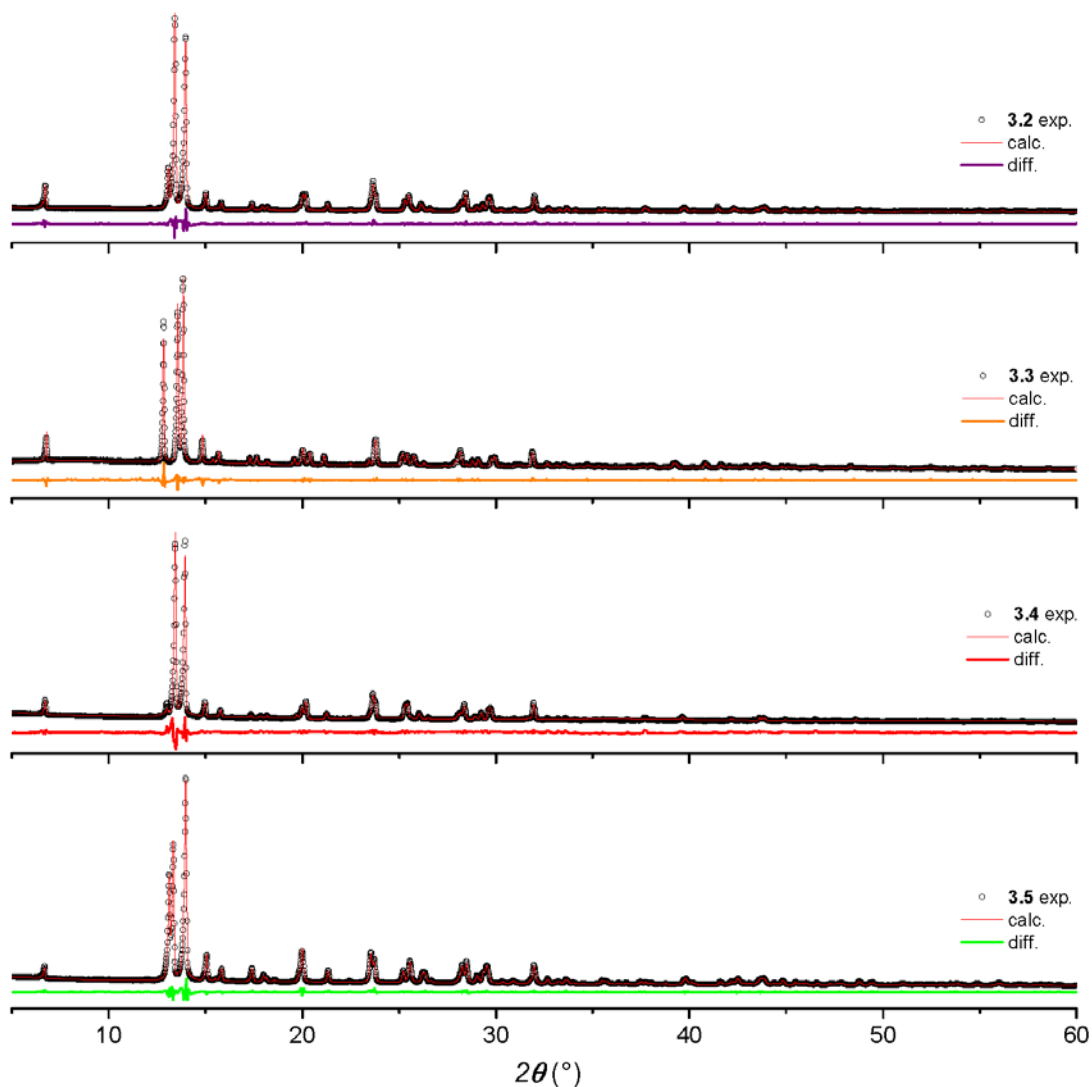


Figure 3.8 Calculated and experimental PXRD patterns for the chains 3.2-3.5.

3.2.5 Magnetism of {ohpma}-based chains

The DC magnetic properties of compounds **3.2-3.5** in the form of $\chi_M T$ versus T plots are shown in Figure 3.9. The value of $\chi_M T$ for compounds **3.2** and **3.5** at 300 K ({CuCo} and {CuCoNi}) are within the theoretical range, assuming non-interacting ions (see Table. 3.3). In the presence of Mn^{II} however, these values are below the theoretical limit, pointing at the existence of a strong antiferromagnetic interaction in **3.3** and **3.4** ({CuMn} and {CuCoMn}), or at least, stronger than in **3.2** and **3.5**.

		Exp.	Theoretical	
3.2	{CuCo}	3.41	$3.11 < \chi_M T < 3.81$	<ul style="list-style-type: none"> • $S_{Cu} = 1/2$; $g_{Cu} = 2.1$; $\chi_M T(\text{Cu}^{\text{II}}) = 0.41$; • $2.7 < \chi_M T(\text{Co}^{\text{II}}) < 3.4$; • $S_{Mn} = 5/2$; $g_{Mn} = 2.0$; $\chi_M T(\text{Mn}^{\text{II}}) = 4.37$; • $S_{Ni} = 1$; $g_{Ni} = 2.2$; $\chi_M T(\text{Ni}^{\text{II}}) = 1.21$.
3.3	{CuMn}	4.50	4.78	
3.4	{CuCo _{0.57} Mn _{0.43} }	3.81	$3.83 < \chi_M T < 4.23$	
3.5	{CuCo _{0.59} Ni _{0.41} }	2.77	$2.50 < \chi_M T < 2.91$	

Table 3.3 Experimental and theoretical $\chi_M T$ values at 300 K ($\text{cm}^3 \text{mol}^{-1} \text{K}$)

The existence of antiferromagnetic interactions is supported by the temperature dependence of the $\chi_M T$ products, which, in all four cases, continuously decrease from 300 to 60 K. In the case of **3.3**, $\chi_M T$ reaches a plateau at 60 K, with a value of $3.88 \text{ cm}^3 \text{mol}^{-1} \text{K}$, before increasing sharply up to $16.85 \text{ cm}^3 \text{mol}^{-1} \text{K}$ at 2 K. For **3.4**, the decrease of $\chi_M T$ continues from 60 K to 18 K where a plateau at $2.05 \text{ cm}^3 \text{mol}^{-1} \text{K}$ is reached. The $\chi_M T$ product then slightly increases to $2.20 \text{ cm}^3 \text{mol}^{-1} \text{K}$ at 4.5 K before reaching 2.11 at 2 K. The $\chi_M T$ products of **3.2** and **3.5** keep decreasing below 60 K, down to $0 \text{ cm}^3 \text{mol}^{-1} \text{K}$ at 2K. A small field-dependent contribution was observed at 15 K in the heterobimetallic chain **3.2**. This was confirmed with the occurrence of an opening of the zero-field-cooled and field-cooled (ZFC/FC) susceptibility measurements and attributed to trace amount of cobalt hydroxide.

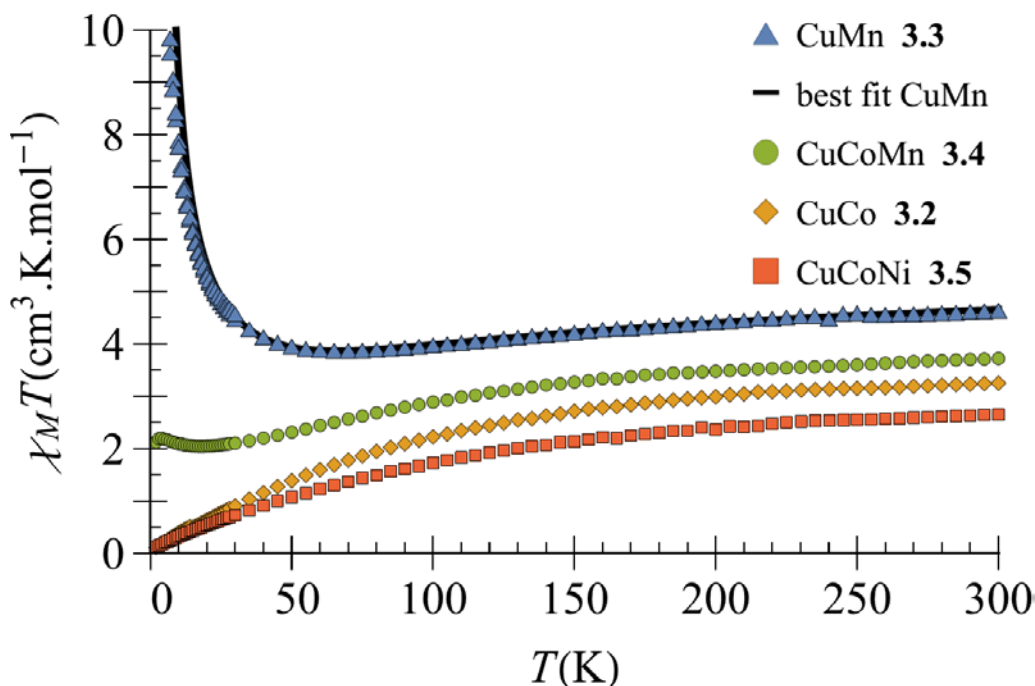


Figure 3.9 Temperature dependence of $\chi_M T$ for compound 3.2-3.5 (Applied field for compound 3.2: 5000 Oe ($T \geq 200$ K) and 200 Oe ($T < 200$ K); compound 3.3: 5000 Oe ($250 \text{ K} \leq T \leq 300 \text{ K}$), 1000 Oe ($30 \text{ K} \leq T < 250 \text{ K}$) and 200 Oe ($2 \text{ K} \leq T < 30 \text{ K}$); compound 3.4: 5000 Oe ($T \geq 200 \text{ K}$) and 200 Oe ($T < 200 \text{ K}$); compound 3.5: 5000 Oe ($T \geq 200 \text{ K}$) and 250 Oe ($T < 200 \text{ K}$).

The presence of a minimum is characteristic of ferrimagnetic $\{\text{Mn}^{\text{II}}-\text{Cu}^{\text{II}}\}$ chain compounds⁸⁻¹⁰. However, there is no minimum and increase of the $\chi_M T$ product at low temperature for the $\{\text{CuCo}\}$ chain. This is in contrast with the other bimetallic $\{\text{CuCo}\}$ chains with oxamato bridges published in the literature¹¹⁻¹⁴. For the trimetallic chains, the $\chi_M T$ value of the $\{\text{CuCoMn}\}$ chain steadily decreases but reaches a minimum around 20 K, before going up. We assume that it is due to the presence of Mn^{II} ions with a larger magnetic moment that reinforce the ferrimagnetic character of the chain. Finally, for the $\{\text{CuCoNi}\}$ chain, $\chi_M T$ decreases constantly. In this case, the low magnetic moment of the Ni ions does not change the behavior of the parent $\{\text{CuCo}\}$ chain.

Unfortunately, it is only possible to simulate the magnetic properties of the $\{\text{CuMn}\}$ chain for which a theoretical alternating chain model has been developed using the following Hamiltonian for the interaction^{15,16}:

$$\mathcal{H} = -J \sum_i S_{Bi} [(1 + \alpha)S_{Ai} + (1 - \alpha)S_{Ai+1}]$$

The least square fitting of the experimental data were done in the 22-300 K temperature range to avoid the effect of interchain interactions. The best fitted parameters are equal to $J = -22.0 \text{ cm}^{-1}$, $\alpha =$

0.59 and $g_{Cu} = 2.14$, with an agreement factor of $\left(F = \frac{\sum_j(\chi_{M.T_j^{exp}} - \chi_{M.T_j^{calc}})^2}{\sum_j(\chi_{M.T_j^{exp}})^2}\right) = 4.7 \cdot 10^{-5}$. This corresponds to $J_{ox} = -35 \text{ cm}^{-1}$ and $J_{hydro} = -9.0 \text{ cm}^{-1}$. The interaction between the Cu^{II} and Mn^{II} ions are in the expected range for the oxamato bridge.

There is no model for a {CuCo} alternating chain. However, Drillon *et al* have developed a model for a regular chain that takes into account spin-orbit coupling¹⁷. In this model, even for small values of the Cu^{II} - Co^{II} interaction, a minimum of $\chi_{M}T$ is expected, and at this stage there is no satisfactory explanation to the absence of a minimum. The only possible explanation would be strong antiferromagnetic interchain interaction that seems unlikely owing to the crystal structure with well isolated chains (shortest interchain metal-metal distances were found at 7.12 Å (Cu-Co) and 7.15 Å (Cu-Mn)).

The M versus H plots for compounds **3.2-3.5** at 2.0 K are shown in Figure 3.10. For compound **3.3** the saturated magnetization value at 7 T is $3.9 \text{ N}\mu_{\text{B}}$, which is consistent for an $S = 2$ ground state for the basic {CuMn} unit resulting from antiferromagnetic coupling between the Mn^{II} and Cu^{II} ions. The M versus H curve of **3.2** is more puzzling. Even at 7 T the M value is only $0.38 \text{ N}\beta$ and the variation of M with the magnetic field is almost linear. It resembles the variation of an antiferromagnetic phase. For compound **3.2**, the presence of a magnetic order is consistent with the evolution of the $\chi_{M}T$ product with the temperature, which tends towards zero at low temperature. However this seems incompatible with the structure of the compound with well-isolated chains within the crystal. Moreover, since this compound is isostructural with **3.3**, it is difficult to understand why compound **3.3** behaves as an isolated ferrimagnetic chain while **3.2** would present an antiferromagnetic order. One possible explanation would be that the interchain interactions develop only in two dimensions. This excludes a magnetic order for compound **3.3** containing isotropic Mn^{II} ions while the presence of Ising type Co^{II} ions in **3.2** could lead to an antiferromagnetic order. If this is the case, the antiferromagnetic interchain interaction for compound **3.3** should nevertheless be seen at low temperature. To check this hypothesis, the fit of $\chi_{M}T$ versus temperature for **3.3** was redone on the whole range of temperature, but in including a Curie-Weiss law in the model to take into account the interchain interaction. The best fitted parameters are equal to $J = -23 \text{ cm}^{-1}$, $\alpha = 0.37$,

$g_{Cu} = 2.10$ and $\theta = -5.9$ K, with an agreement factor $F = 1.56 \cdot 10^{-3}$. The very high θ value for compound **3.3** makes the hypothesis of an interchain interaction in two dimensions plausible. Furthermore, this is coherent with the observed magnetization curves for **3.4** and **3.5**. For the {CuCoMn} compound **3.4**, the introduction of an isotropic ion suppresses the crossover toward an Ising type behavior for the chain and prevents the magnetic ordering. In contrast, the introduction of Ni^{II} ions does not suppress the magnetic ordering, probably because Ni^{II} ions are sufficiently anisotropic to maintain Ising type anisotropy in the chain.

The last point to address is, why is a maximum of χ_M –i.e. a signature of antiferromagnetic ordering– not seen for **3.2** (see Figure 3.11). The ZFC/FC curves depicted in Figure 3.11 bring the answer. The two curves diverge at 15 K and there is another anomaly at 5.5 K. This indicates the presence of a small amount of ferromagnetic impurity. Unfortunately, it is often the case with Co^{II} complexes. Despite all best efforts and cautiousness, most synthesis involving cobalt(II) lead to in this temperature range¹⁸. The presence of this impurity most likely masks the occurrence of a maximum of χ_M .

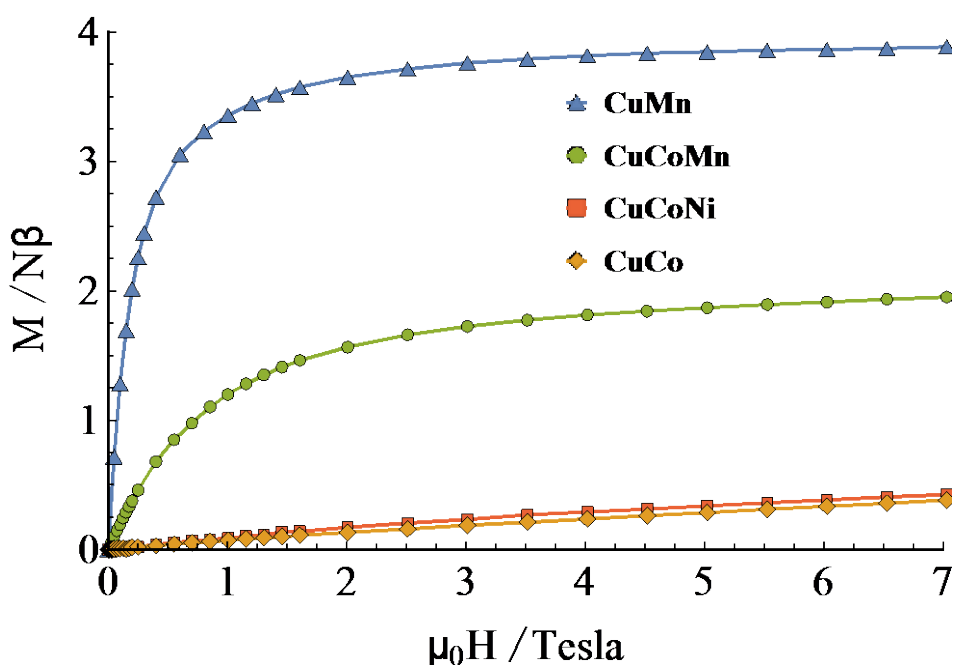


Figure 3.10 Field dependence of magnetization of compound 3.2-3.5 at 2.0 K. The solid lines are guides to the eye.

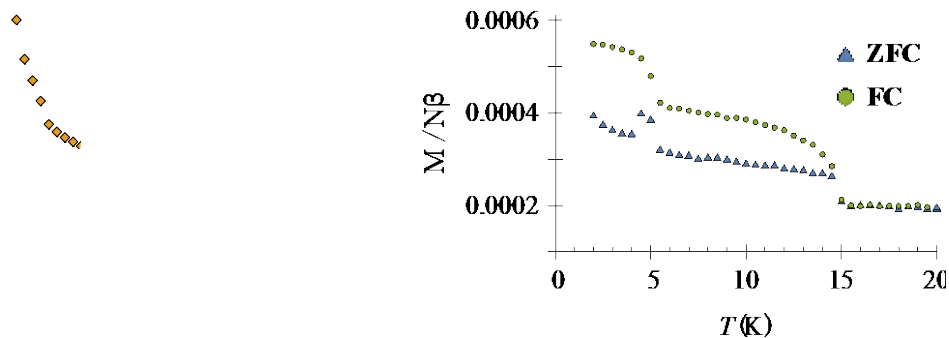


Figure 3.11 Temperature dependence of χ_M for compound 3.2 in an 200G applied field (left), Temperature dependence of ZFC and FC for 3.2 in an 30G applied field.

3.3 Conclusions

New neutral heterometallic oxamate-based 1D compounds have been successfully synthesized from *ortho*-substituted phenyloxamate ligands, with carboxylato (oaba) and hydroxido groups (ohpma). They represent the first examples of 1D oxamate-based polymers obtained solvothermally. The location of the additional coordinating groups in *ortho* position can be seen as the limitation for the preparation of higher dimensionality networks. Indeed, even the monometallic bis-tridentate $\{M(\text{ohpma})_2\}$ metalloligand would not, in theory, lead to higher dimensionality. Nevertheless, the more serendipitous nature of the oaba ligand leaves it as a viable candidate.

In comparison to the multi-step approach traditionally used for oxamate chemistry, the one-pot method used here solvothermally has not been an issue for the preparation of heterobimetallic compounds. It has even been possible to prepare heterotrimetallic chains in the case of the ohpma ligand. This is made possible by the strong affinity of copper ions for the oxamate ligands. However, the preparation of heterometallic chains, and especially the chains based on cobalt(II), has not led to SCM. Indeed, if the additional coordinating groups successfully yield novel morphologies, even for 1D compounds, it comes at a cost over the predictability of the magnetic interactions.

Reference

- 1 K. Yoneda, Y. Hori, M. Ohba and S. Kitagawa, *Chemistry Letters*, 2008, **37**, 64–65.
- 2 J. M. Herrera, A. Bleuzen, Y. Dromzée, M. Julve, F. Lloret and M. Verdaguer, *Inorg. Chem.*, 2003, **42**, 7052–7059.
- 3 D. Maspoch, N. Domingo, D. Ruiz-Molina, K. Wurst, J.-M. Hernández, G. Vaughan, C. Rovira, F. Lloret, J. Tejada and J. Veciana, *Chem. Commun.*, 2005, 5035–5037.
- 4 F. Lloret, M. Julve, J. Cano, R. Ruiz-Garcia and Emilio. Pardo, *Inorg. Chim. Acta*, 2008, **361**, 3432–3445.
- 5 E. Pardo, C. Train, R. Lescouëzec, Y. Journaux, J. Pasán, C. Ruiz-Pérez, F. S. Delgado, R. Ruiz-Garcia, F. Lloret and C. Paulsen, *Chem. Commun.*, 2010, **46**, 2322.
- 6 E. Pardo, R. Ruiz-García, F. Lloret, J. Faus, M. Julve, Y. Journaux, M. A. Novak, F. S. Delgado and C. Ruiz-Pérez, *Chem. - Eur. J.*, 2007, **13**, 2054–2066.
- 7 Y. Pei, M. Verdaguer, O. Kahn, J. Sletten and J. P. Renard, *Inorg. Chem.*, 1987, **26**, 138–143.
- 8 Olivier. Kahn, Yu. Pei, Michel. Verdaguer, J. Pierre. Renard and Jorunn. Sletten, *Journal of the American Chemical Society*, 1988, **110**, 782–789.
- 9 H. O. Stumpf, Y. Pei, L. Ouahab, F. Le Berre, E. Codjovi and O. Kahn, *Inorganic Chemistry*, 1993, **32**, 5687–5691.
- 10 H. O. Stumpf, Y. Pei, O. Kahn, J. Sletten and J. P. Renard, *J. Am. Chem. Soc.*, 1993, **115**, 6738–6745.
- 11 P. J. Van Koningsbruggen, O. Kahn, K. Nakatani, Y. Pei, J. P. Renard, M. Drillon and P. Legoll, *Inorg. Chem.*, 1990, **29**, 3325–3331.
- 12 C. L. M. Pereira, A. C. Doriguetto, C. Konzen, L. C. Meira - Belo, U. A. Leitão, N. G. Fernandes, Y. P. Mascarenhas, J. Ellena, A. L. Brandl, M. Knobel and H. O. Stumpf, *European Journal of Inorganic Chemistry*, 2005, **2005**, 5018–5025.
- 13 E. Pardo, R. Ruiz-García, F. Lloret, J. Faus, M. Julve, Y. Journaux, F. Delgado and C. Ruiz-

Pérez, *Adv. Mater.*, 2004, **16**, 1597–1600.

14 J. Ferrando-Soria, D. Cangussu, M. Eslava, Y. Journaux, R. Lescouëzec, M. Julve, F. Lloret, J. Pasán, C. Ruiz-Pérez, E. Lhotel, C. Paulsen and E. Pardo, *Chem. Eur. J.*, 2011, **17**, 12482–12494.

15 R. Georges, J. Curély, J. C. Gianduzzo, X. Qiang, O. Kahn and Y. Pei, *Physica B: Condensed Matter*, 1988, **153**, 77–84.

16 Y. Pei, O. Kahn, J. Sletten, J. P. Renard, R. Georges, J. C. Gianduzzo, J. Curely and Q. Xu, *Inorg. Chem.*, 1988, **27**, 47–53.

17 P. J. Van Koningsbruggen, O. Kahn, K. Nakatani, Y. Pei, J. P. Renard, M. Drillon and P. Legoll, *Inorg. Chem.*, 1990, **29**, 3325–3331.

18 J. R. Neilson, D. E. Morse, B. C. Melot, D. P. Shoemaker, J. A. Kurzman and R. Seshadri, *Phys. Rev. B*, 2011, **83**, 094418.

Chapter 4:

Synthesis, characterization and magnetic properties of an oxamato bridged heterometallic 2D compound.

Chapter 4. Synthesis, characterization and magnetic properties of an oxamate bridged hetero-metallic 2D compound.

Chapter 4 presents the structural characterization and magnetic study of a 2D anionic heterometallic architecture: $(\text{TMA})_3[\text{CuMn}(\text{paba})_2(\text{OAc})] \cdot 7\text{H}_2\text{O}$ (compound **4.1**). Its desolvated phase, $(\text{TMA})_3[\text{CuMn}(\text{paba})_2(\text{OAc})]$ (compound **4.2**), obtained by heating up compound **4.1** at 90 °C, was also characterized. Novel coordination modes and arrangements were found in this 2D brick-wall structure.

4.1 2D anionic compound

4.1.1 Synthesis and structural characterization of $(\text{TMA})_3[\text{CuMn}(\text{paba})_2(\text{OAc})] \cdot 7\text{H}_2\text{O}$

Compound **4.1** was synthesized solvothermally from the tetramethylammonium salt of the paba ligand, $\text{H}(\text{TMA})_2\text{-paba} \cdot 1.5\text{H}_2\text{O}$ ligand, with metal ion acetate salts, in DMF and in the presence of one equivalent of TMAOH. Small green crystals were obtained, and the X-Ray data collection was performed on the CRISTAL beamline in Soleil.

Compound **4.1** crystallizes in the monoclinic $\text{P2}_1/\text{n}$ space group. The structure of **4.1** consists of an anionic $\{\text{Mn}^{\text{II}}\text{-Cu}^{\text{II}}\}$ 2D network $[\text{CuMn}(\text{paba})_2(\text{OAc})]^{3-}$, water crystallization molecules and three tetramethylammonium $(\text{TMA})^+$ counter-cations. The Cu^{II} ion (Cu1) is five-coordinate in a square pyramidal environment. Two paba ligands bind the copper center in a *cis* fashion, each via one nitrogen atom and one oxygen atom from the oxamate group (N1,O7; N2,O8). One oxygen atom (O4) coming from a mono-coordinated acetate anion completes the coordination sphere of the copper ion. Two nitrogen atoms and one oxygen atom (O7) from the ligands, as well as the oxygen atom from the acetate group define the square base of the pyramidal environment (See Figure 4.1). The bond lengths in this plan range from 1.965(8) to 2.033(6) Å, with the shortest distances found for the Cu-N bonds. The apical position is defined by one oxamate oxygen atom (O8), at 2.187(7) Å. The geometry of the Cu^{II} ion is distorted, with N/O-Cu-N/O angles varying from 80 to 100° (av. deviation of 6°), and a twisted square base (N1-Cu1-O7/N2-Cu1-O4 dihedral angle: 15°). As a result, and despite the *cis* coordination of the ligands, the position of the carboxylate arms is closer to 180° than to 90°. Indeed, the (OO)C-Cu-C(OO) angle is 144°. The two ligands also show different

conformations. The dihedral angles between the phenyl rings and the oxamate groups planes are found at 88 and 30° (around N1 and N2 respectively). However, with the *cis* coordination of the ligands and the distortion of the Cu^{II} geometry, the dihedral angles between the phenyl rings and the square base of the metal ion are similar, 86 and 88°.

The Mn^{II} ion is six-coordinate with a distorted octahedral surrounding. The metallic center is cis-coordinated by the remaining four carbonyl groups of two oxamate ligands (O5, O6, O9, O10) and by two mono-coordinated carboxylate groups (O2, O11) coming from another two paba ligands. The Mn-O distances range from 2.118(6) to 2.224(5) and average 2.167 Å. The O-Mn-O angles vary from 75 to 102° with an averaged deviation to orthogonality of 5°. BVS calculations support the presence of Mn^{II} ions.

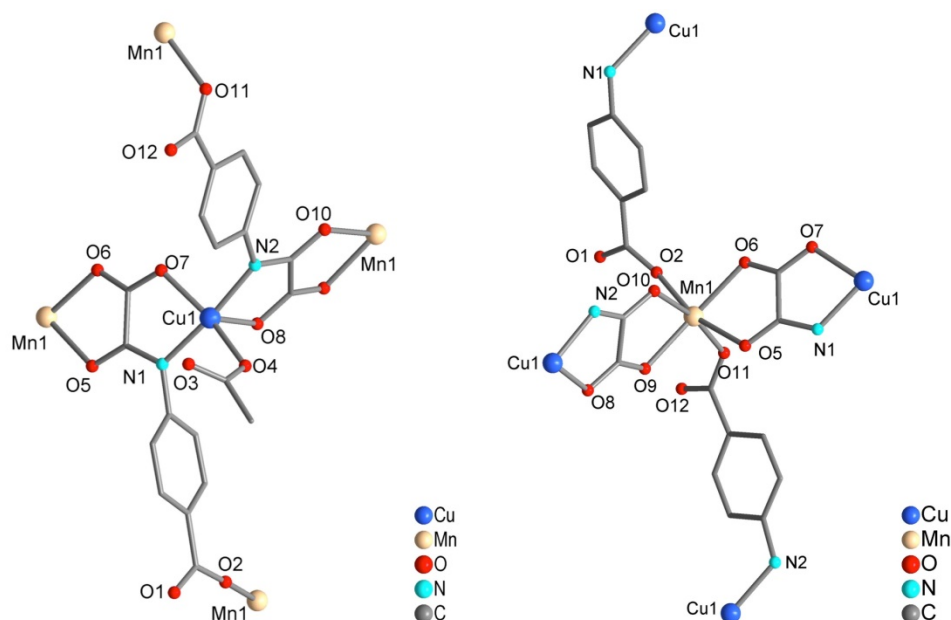


Figure 4.1 Perspective view of the asymmetric unit in compound 4.1 which shows the coordination environments of the Cu^{II} and Mn^{II} ions together with atom labels.

Considering the [Cu(paba)₂]⁴⁻ metalloligand, its coordination via the oxamate bridges to Mn^{II} ions gives a zig-zag chain (Mn-Cu-Mn = 118°) along the crystallographic *a* axis, with the pendant *para*-substituted phenyl carboxylate groups roughly aligned along *c* (see Figure 4.2). These carboxylate groups then bind manganese ions from adjacent chains to yield the corrugated 2D brick-wall structure (Figure 4.3).

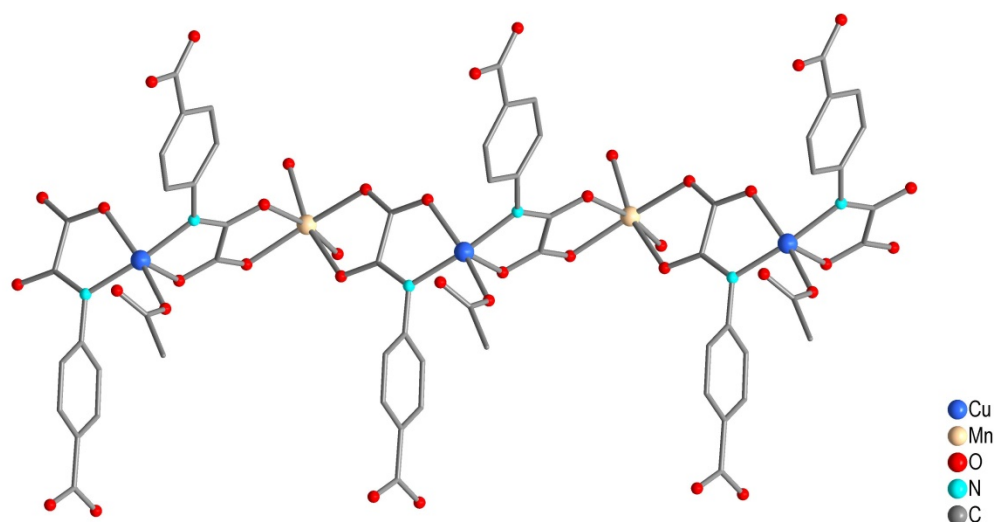


Figure 4.2 Perspective view of the oxamate-bridged {Cu-Mn} chain sub-unit and its pendant carboxylate groups.

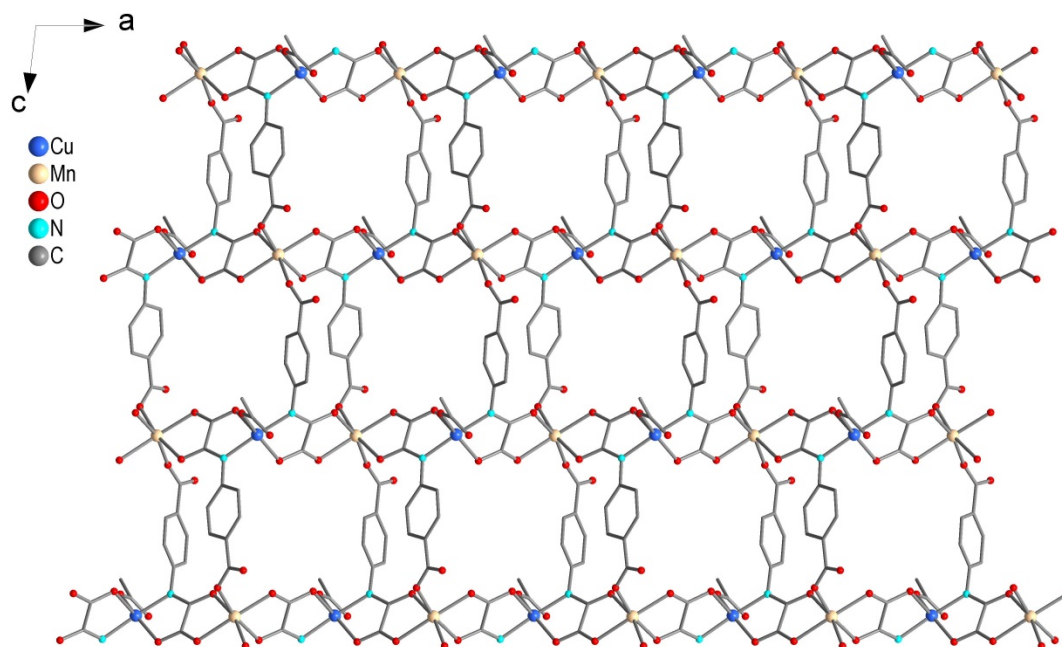


Figure 4.3 Perspective view along *b* of the 2D layer in 4.1, hydrogen atoms, water molecules and TMA⁺ counterions have been omitted for clarity.

In comparison to the previously reported 2D brick-wall structures with oxamate ligands, **4.1** shows one striking difference with its metalloligand building unit^{1,2}. Where tetrakis-bidendate {Cu₂L₂} metalloligands obtained from bis-oxamic ligand are traditionally used, here the monometallic [Cu(paba)₂]⁺ complex is –thanks to the additional coordinating groups– able to generate the same connectivity. As a consequence, the “rungs” and cavities of the brick-wall structure differs. Previously, the bimetallic metalloligand acted as the rung, and decametallenic cavities were observed

(Figure 4.4). In **4.1**, two half-metalloligands act as links between the 1D sub-units and smaller tetrametallic cavities are obtained. The alternating pendant carboxylato groups, instead of the alternating metalloligands, actually give rise to a higher cross-linking of the chains.

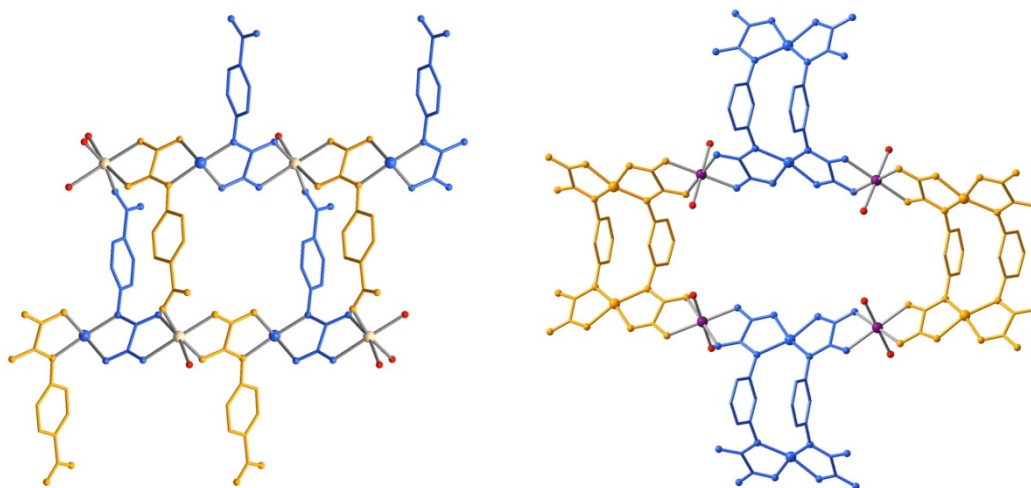


Figure 4.4 Comparison of the brick-wall arrangement in **4.1** (left) and in $[\text{Cu} [\text{Co}_2\text{Cu}_2(\text{mpba})_2(\text{H}_2\text{O})_6]$ (right).¹

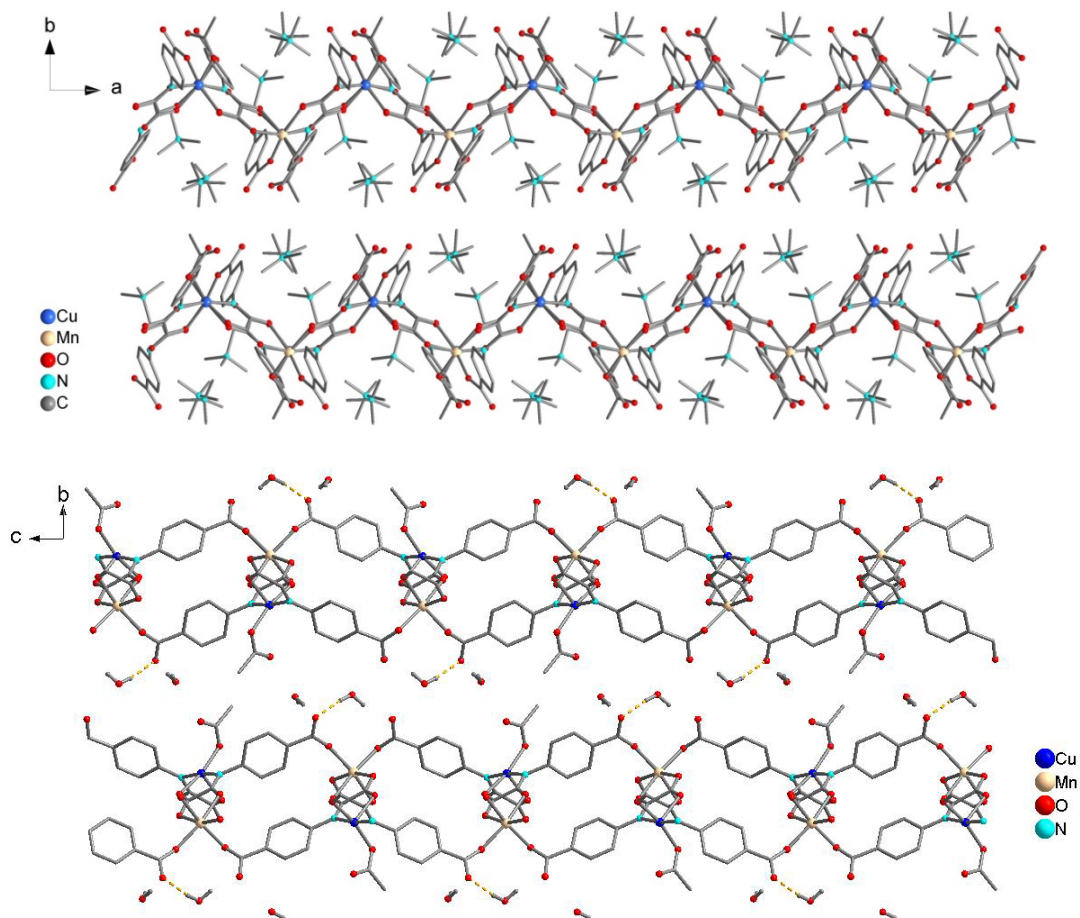


Figure 4.5 Top: View of the layers along *c* and representation of the TMA^+ cations. Bottom: View of layers along *a* and representation of the hydrogen bonds (yellow dotted lines) between water molecule and paba ligands.

4.1.2 Thermal studies of $(\text{TMA})_3[\text{CuMn}(\text{paba})_2(\text{OAc})]\cdot 7\text{H}_2\text{O}$

In order to analyze the thermal stability of compound **4.1**, thermogravimetric analysis (TGA) and thermodiffraction measurements have been performed.

From figure 4.6, TGA shows a two steps weight loss of 14% between room temperature and 90 °C that corresponds to the water solvent molecules (ca. 13.4 %), and then a plateau up to 200-210 °C before a sharp 70 % weight loss under air that should correspond to the organic content (ca. 74%). Indeed, TGA of the ligand shows decomposition between 200 and 250 °C. At 800 °C under air, the final weight percentage of 17 % supports the formula when assuming the formation of stoichiometric amounts of CuO and Mn_2O_3 (16.8 %).

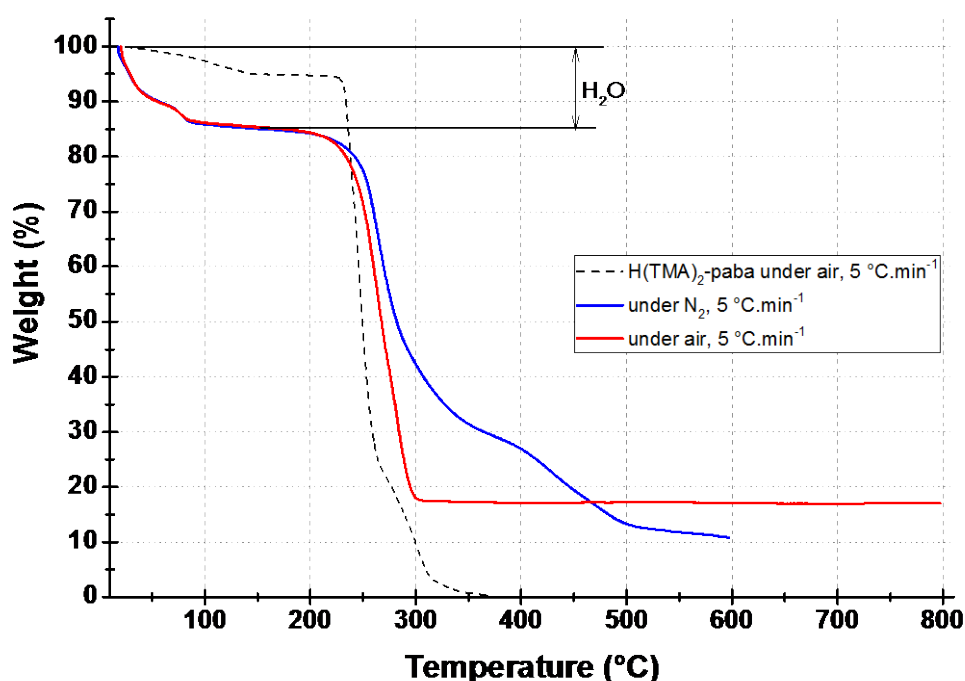


Figure 4.6 Thermogravimetric analysis of $(\text{TMA})_3[\text{CuMn}(\text{paba})_2(\text{OAc})]\cdot 7\text{H}_2\text{O}$

Temperature-dependent powder X-Ray diffraction measurements have been performed on **4.1**, under nitrogen and between room temperature and 600 °C (Figure 4.7). This investigation shows that the structure of the compound remains stable up to 90 °C. At this temperature, both peak shifts and peak appearances/disappearances indicate a phase transition. The formed phase is then stable up to 200 °C before intensities drop and the structure collapses. At higher temperature (> 240°C) the formation of oxides starts and is observed with the appearance of the corresponding diffraction peaks

(CuO and CuMn₂O).

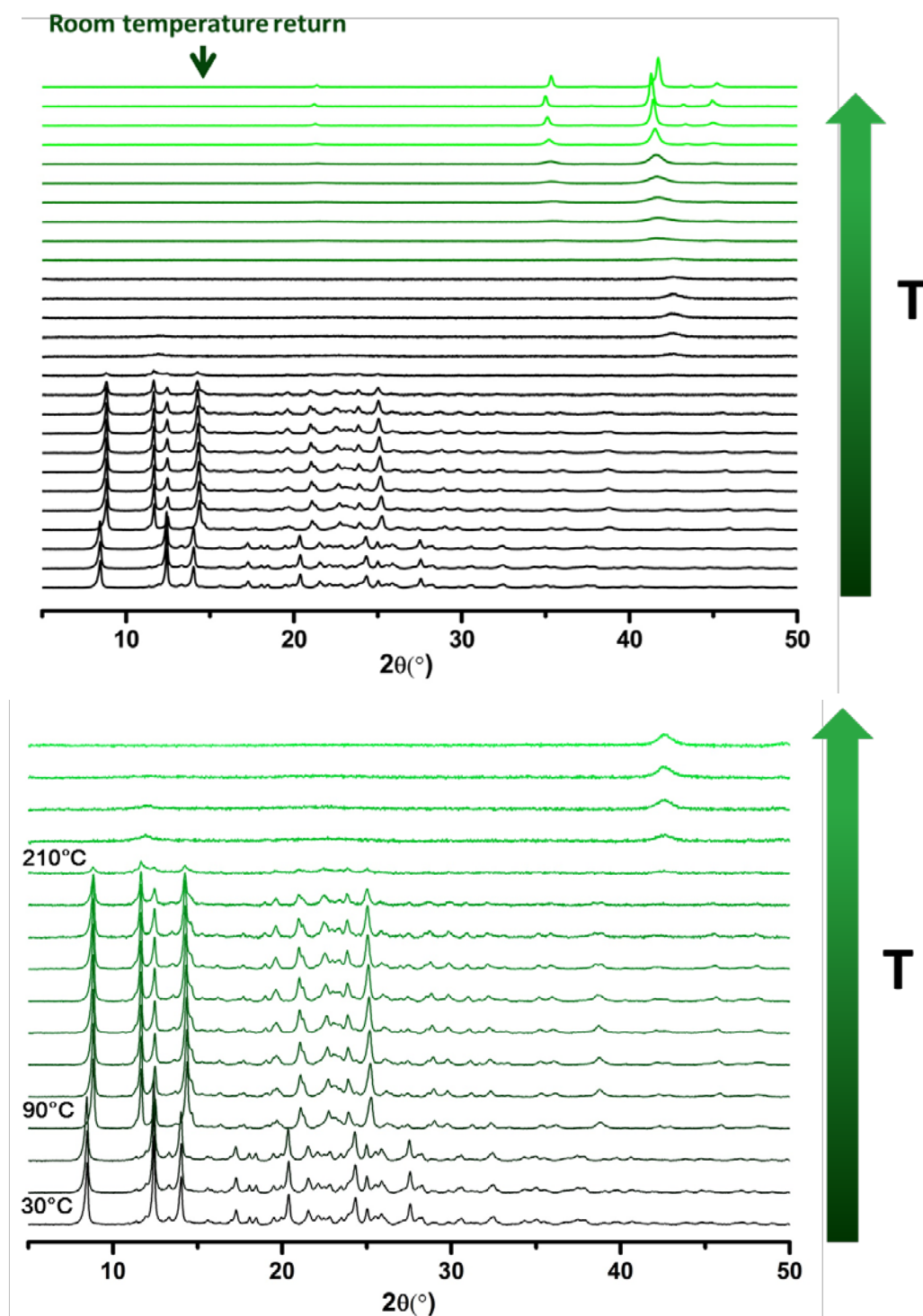


Figure 4.7 Thermodiffractograms of compound 4.1: from 30 °C to 600 °C and room temperature return (top); zoom in the 30-250 °C region (bottom).

4.1.3 Structural characterization of (TMA)₃[CuMn(paba)₂(OAc)]

To investigate the phase transition observed in the thermodiffraction measurement, we have

collected the single crystal X-ray diffraction data on a sample that was heated at 5 °C/min to 92 °C under the nitrogen stream of the diffractometer. It has revealed that the obtained phase, which belongs to the same space group, is the dehydrated form of the 2D network, (TMA)₃[CuMn(paba)₂(OAc)] (**4.2**). The water removal leads to a moderate unit cell shrinkage, the initial volume of 4096 Å³ decreases to 3772 Å³. Within the 2D layers the corrugated shape is accentuated, with a Mn-Cu-Mn angle decreased by 7°. In the lattice, shorter metal-metal interlayer distances are observed and the packing of the layers is closer to an eclipsed arrangement (Figure 4.8). The structure of **4.2** also presents several conformational differences with **4.1**. The dihedral angles between the phenyl and the oxamate planes in the ligands decrease in **4.2**, going from 88° and 30° to 60° and 16° (Figure 4.9). There is also a decrease of the dihedral angle between the phenyl rings (63 and 58° for **4.1** and **4.2** respectively). There are no significant differences in bonds lengths or angles in the coordination spheres of the metal ions between **4.1** and **4.2**. Cu-O/N_{eq} distances vary from 1.96(2) to 2.06(2) Å, with an apical Cu-O distance of 2.18(1) Å; Mn-O distances average at 2.19 Å. Besides, the unfortunately low resolution of the X-Ray data for **4.2** (1.19 Å) limits any further comparison.

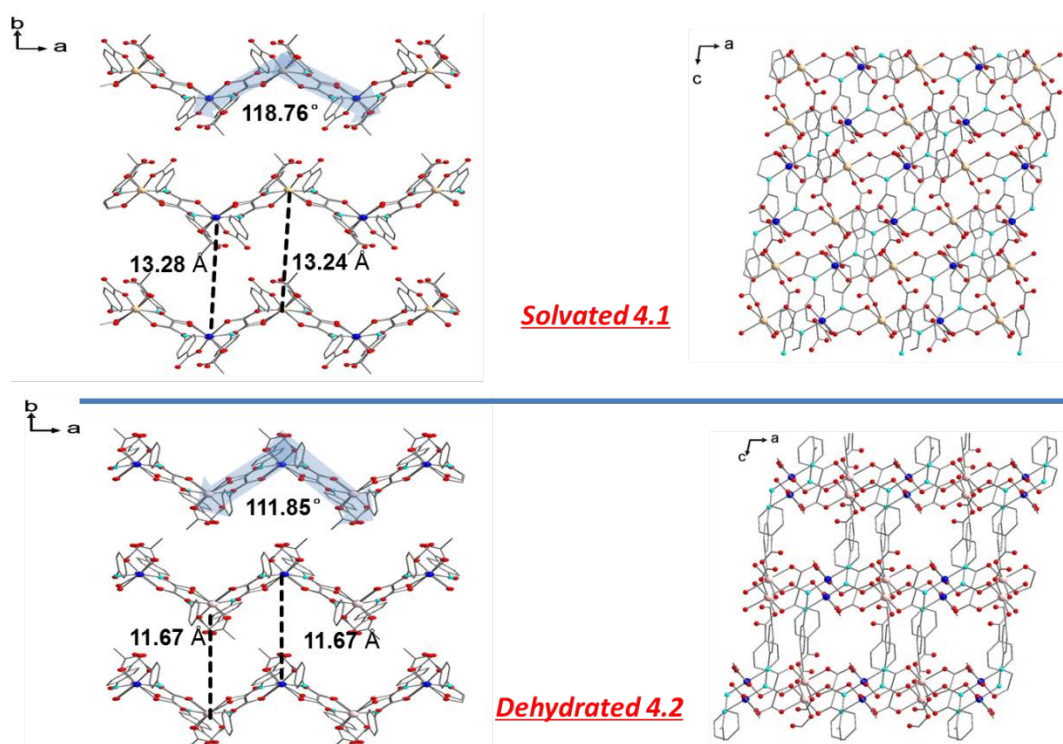


Figure 4.8 Crystal packing of the corrugated 2D layers of the solvated compound **4.1** and the dehydrated compound **4.2** in the (*ac*) and (*bc*) planes ; Mn-Cu-Mn angles and interlayer distances.

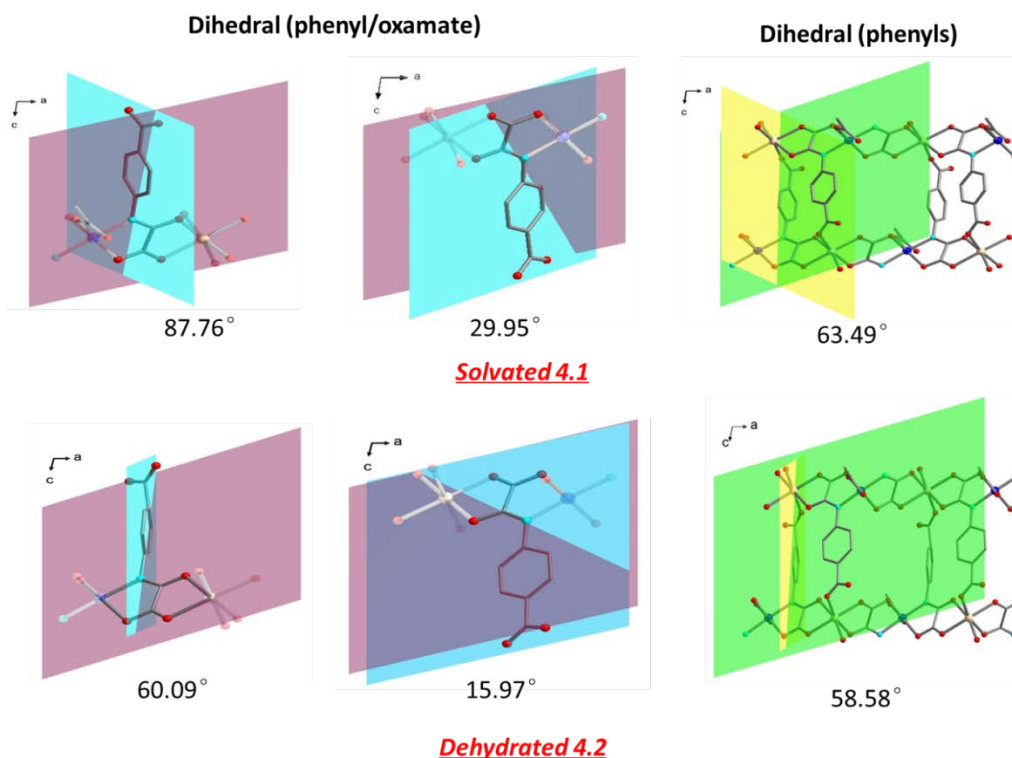


Figure 4.9 Schematic view of the dihedral angles between oxamate groups and phenyl rings and between phenyl rings for the paba ligands.

4.1.4 Magnetic Property

4.1.4.1 DC magnetic property

The DC magnetic properties of compounds **4.1** and **4.2** under an applied field of 2500 Oe in the form of $\chi_M T$ versus T plots are shown in Figure 4.10. The value of $\chi_M T$ for **4.1** and **4.2** at room temperature are equal to 4.8 and 4.6 cm³ K mol⁻¹ respectively. These values are consistent with the expected value for non-interacting Cu^{II} and Mn^{II} ions (4.78 cm³ K mol⁻¹). Upon cooling, both $\chi_M T$ products decrease slowly down to 65 and 58 K and reach minima of 4.1 cm³ K mol⁻¹ and 3.8 cm³ K mol⁻¹, for **4.1** and **4.2** respectively. Upon further cooling, the $\chi_M T$ products increase, following an expected ferrimagnetic behavior. They reach maxima of 14.4 and 17.3 cm³ K mol⁻¹ at 4 and 4.5 K, for **4.1** and **4.2** respectively, before decreasing to 9.8 and 11.9 cm³ K mol⁻¹ at 2K. In the inset of Figure 4.10 an enlargement of the curves' minimum region is depicted. It clearly shows that there is an anomaly around 40 K. Under a lower field (100 Oe), this anomaly becomes more visible (Figure 4.11). The presence of a bump the intensity of which decreases when increasing the magnetic field is the signature of the presence of a saturated ferromagnetic impurity. The ordering temperature near 40

K indicates that it is an impurity of Mn_3O_4 , which displays magnetic ordering at 43 K³⁻⁶.

Under a field of 100 Oe, the $\chi_M T$ products abruptly increase between 8 and 2 K, reaching values of 49.4 cm³ K mol⁻¹ for the solvated phase **4.1**, and 99.4 cm³ K mol⁻¹ for **4.2** (see Figure 4.12). This sudden rise of $\chi_M T$ is a precursor sign of a magnetic ordering.

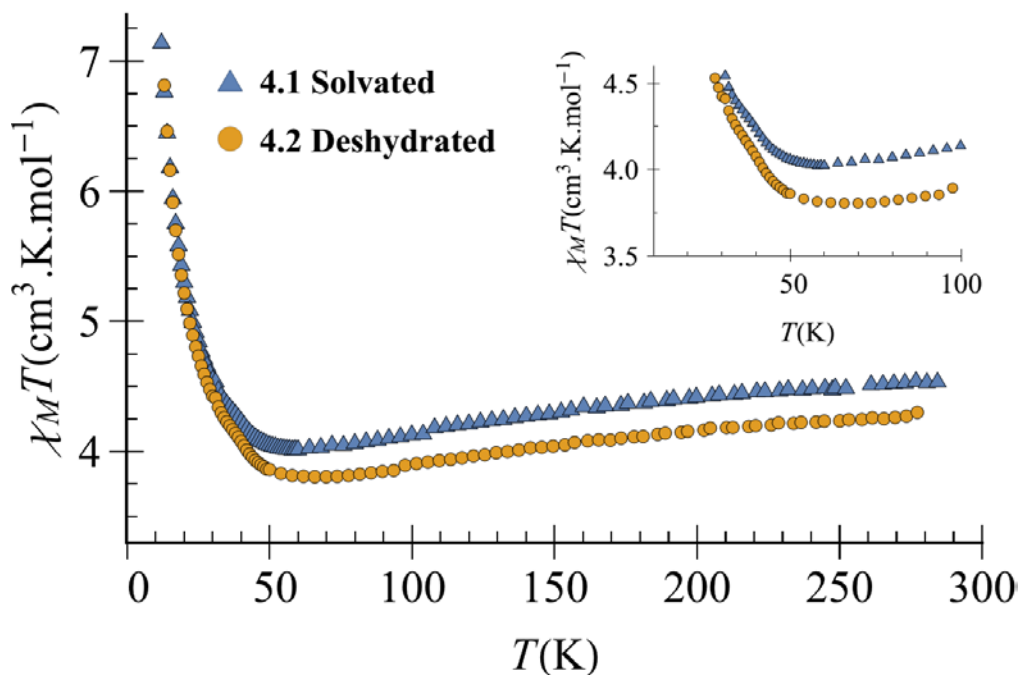


Figure 4.10 Temperature dependence of $\chi_M T$ for compounds 4.1 and 4.2. Inset: $\chi_M T$ plots between 25 and 100 K.

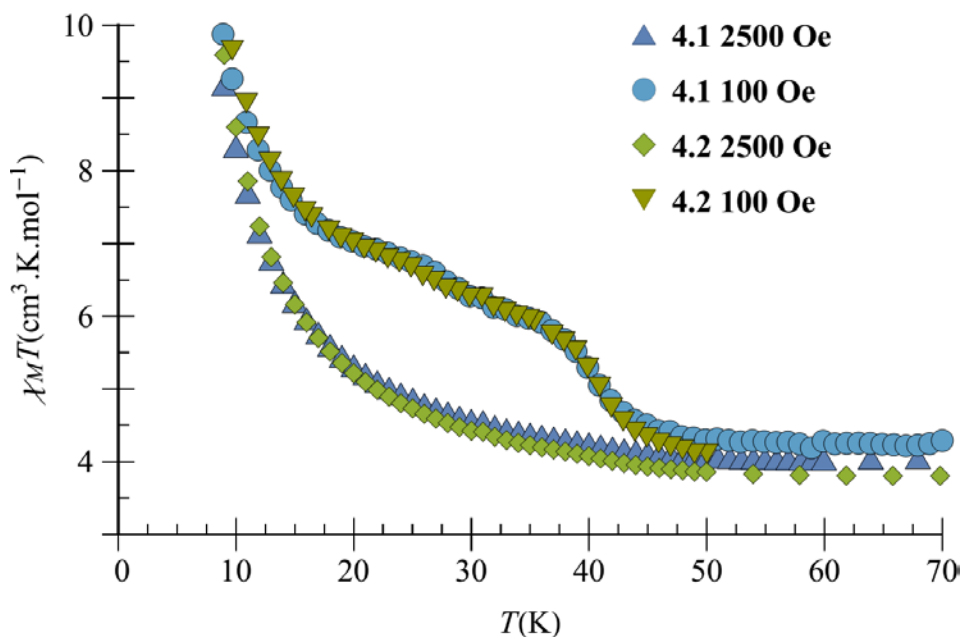


Figure 4.11 Temperature dependence of $\chi_M T$ for compounds 4.1 and 4.2 in the 70-10 K temperature range under a field of 100 Oe and 2500 Oe

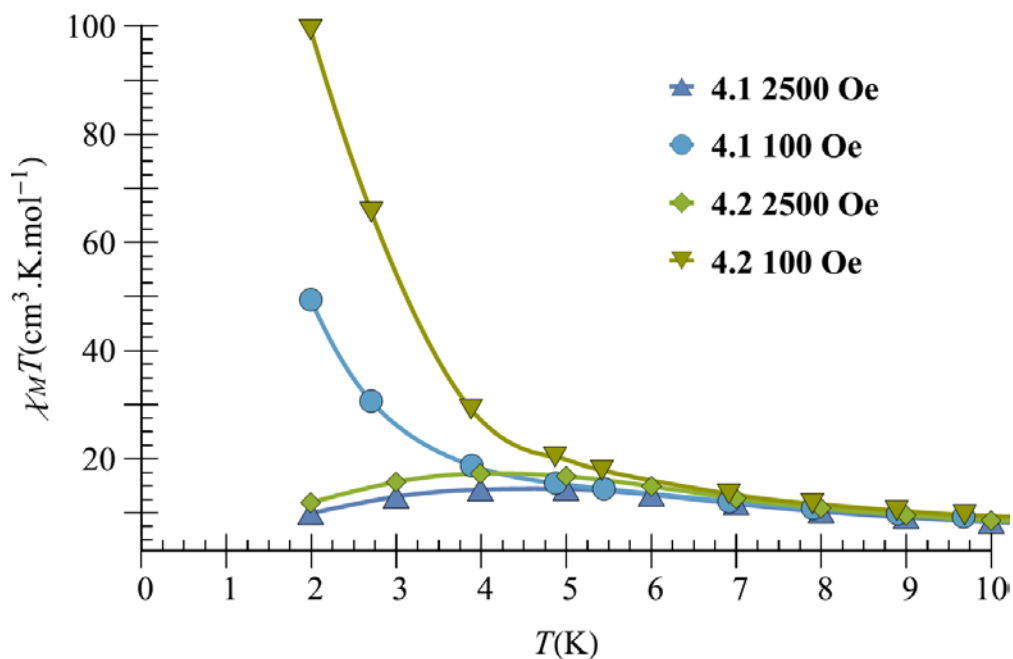


Figure 4.12 Temperature dependence of $\chi_M T$ for compounds 4.1 and 4.2 in the 10-2 K temperature range. The solid lines are guide for the eye.

The field-dependent behavior below 8 K can be attributed to non-linearity in the curve of magnetisation versus field.

The magnetic ordering is confirmed by the ZFC/FC curves for **4.1** depicted in Figure 4.13. The curves diverge at 2.8 K showing a magnetic ordering toward a ferrimagnetic phase at this temperature.

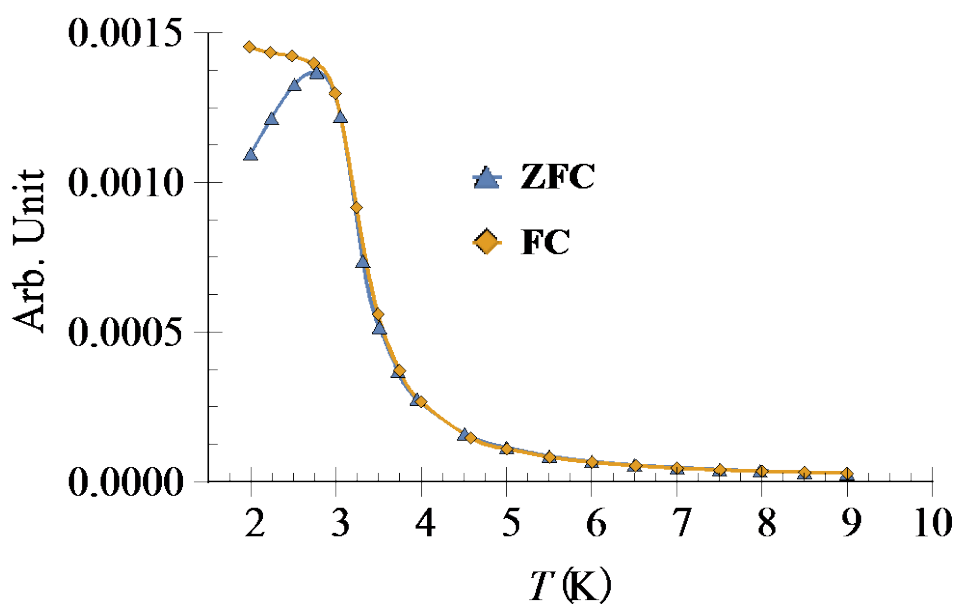


Figure 4.13 ZFC and FC curves for 4.1 under a magnetic field of 100 Oe

4.1.4.2 AC magnetic property

The AC magnetic measurement for **4.1** (Figure 4.14) shows a frequency-independent maximum of χ_M'' at 2.5 K, supporting the existence of the magnetic ordering observed in the ZFC/FC curves. The origin of the feature around 3.75 K is unclear and has no equivalent in the DC measurements.

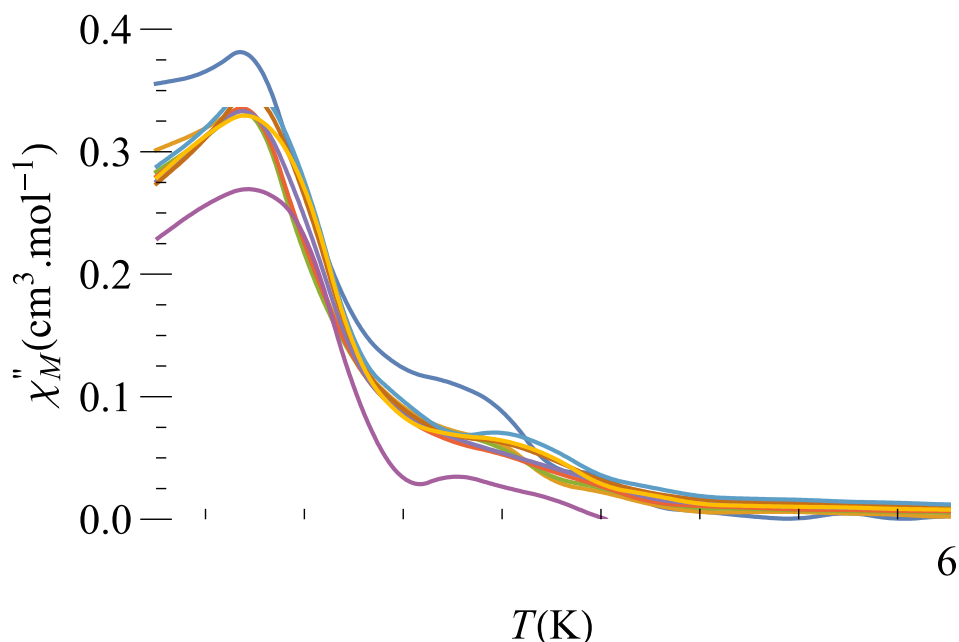


Figure 4.14 The χ_M'' versus T plot of compound 4.1 from 10 to 10000Hz, The solid lines are guide for the eye

4.1.4.3 Magnetization property

Field dependence of the magnetization was also investigated at 2 K for the two compounds (Figure 4.15 and 4.16). In the solvated compound, **4.1**, a butterfly-shaped loop⁷ is observed, the curves measured with increasing or decreasing field values do not superimpose. This behavior is considerably diminished in **4.2**, but still exist. For compound **4.1** the magnetization reaches 3.84 N β at 7 Tesla, close to the expected value for an antiferromagnetically coupled {CuMn} pair ($S = 2$). The origin of the butterfly-shaped loop is puzzling but it is probably an artifact due to the reorientation of the micro crystals in the sample under the effect of the magnetic field. The fact that the first magnetization curve is lower than the hysteresis curve supports this hypothesis. Compound **4.1** contains only Cu^{II} and Mn^{II} ions, which are not very anisotropic ions, and the measurements were done on a powder just blocked in a film, without ecosane or paratone. The butterfly shape of the hysteresis curve indicates that it is not enough to restrain the sample, and that the measurements must be repeated with the microcrystals more thoroughly blocked. For compound 4.2, the hysteresis curve

is also abnormal with a rising magnetic field curve above the decreasing field curve. These measurements must be repeated by blocking the sample with ecosan or paratone.

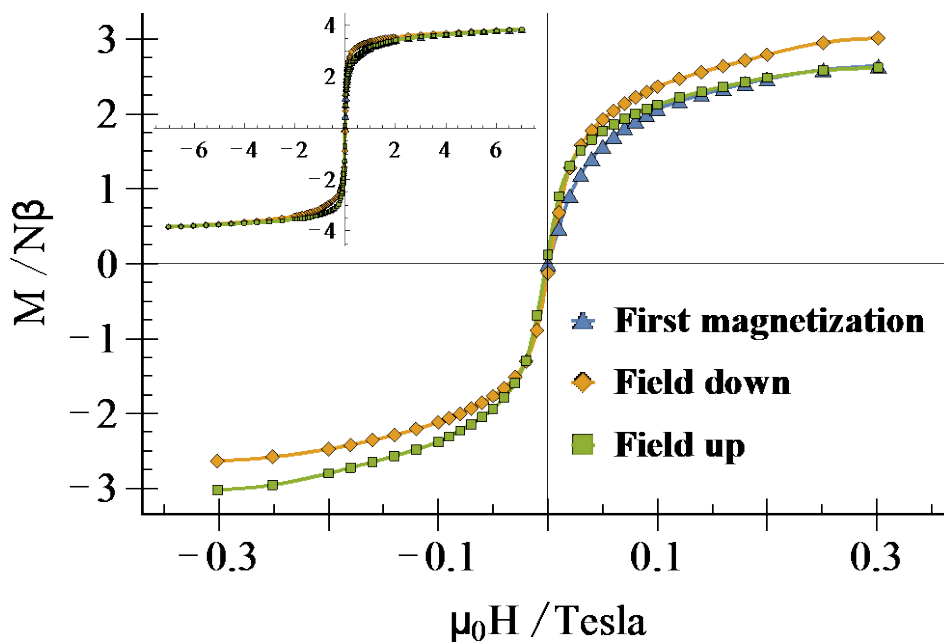


Figure 4.15 The hysteresis loop curve for compound 4.1 at 2 K, The solid lines are guide for the eye.

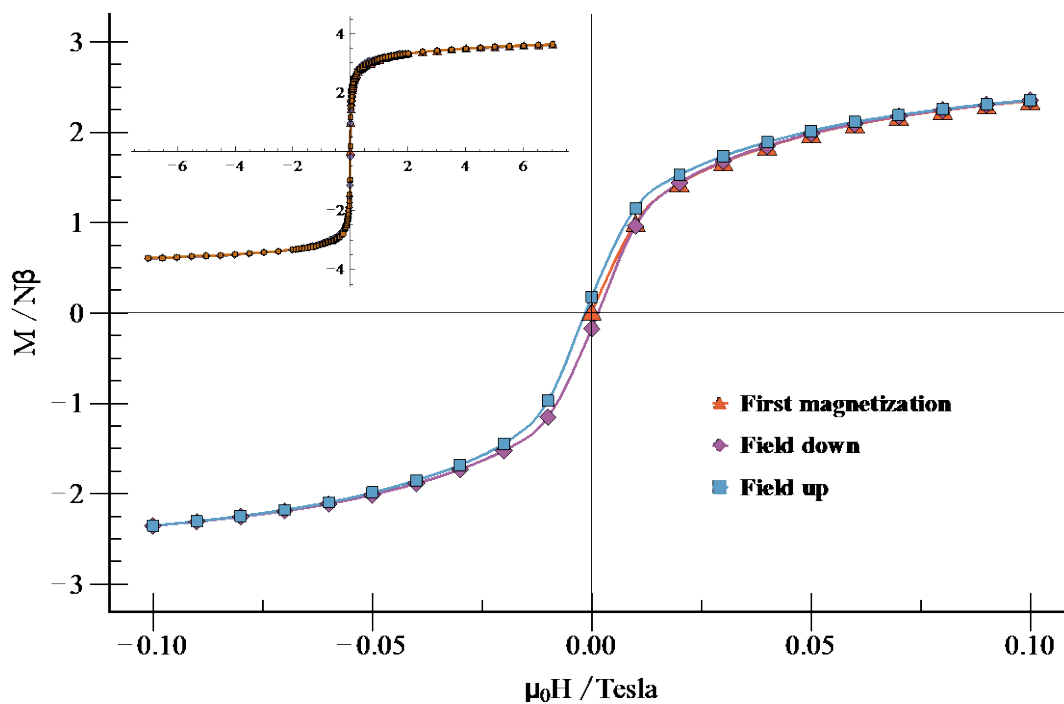


Figure 4.16 The hysteresis loop curve for compound 4.2 at 2 K, The solid lines are guide for the eye

4.1.4.4 Discussion

It is well established that the interaction between a Cu^{II} ion and a Mn^{II} ion through an oxamato bridge is antiferromagnetic^{8–10}. On the other hand, the interaction between the Cu^{II} and Mn^{II} ions through the phenylcarboxylato bridge is not known, and magnetic measurements show that it is also antiferromagnetic. If this were not the case, the fundamental state of the $\{\text{CuMn}\}$ planes would be non-magnetic, as shown in Figure 4.17. A ferromagnetic coupling between the Cu^{II} and Mn^{II} ions through the phenylcarboxylato bridge would lead to an effective antiferromagnetic coupling between the $\{\text{CuMn}\}$ chains. The magnetic moment of a chain being annihilated by its neighbor. Only an antiferromagnetic coupling between the divalent ions allows an effective ferromagnetic coupling between the chains that results in a ferromagnetic plane (left scheme).

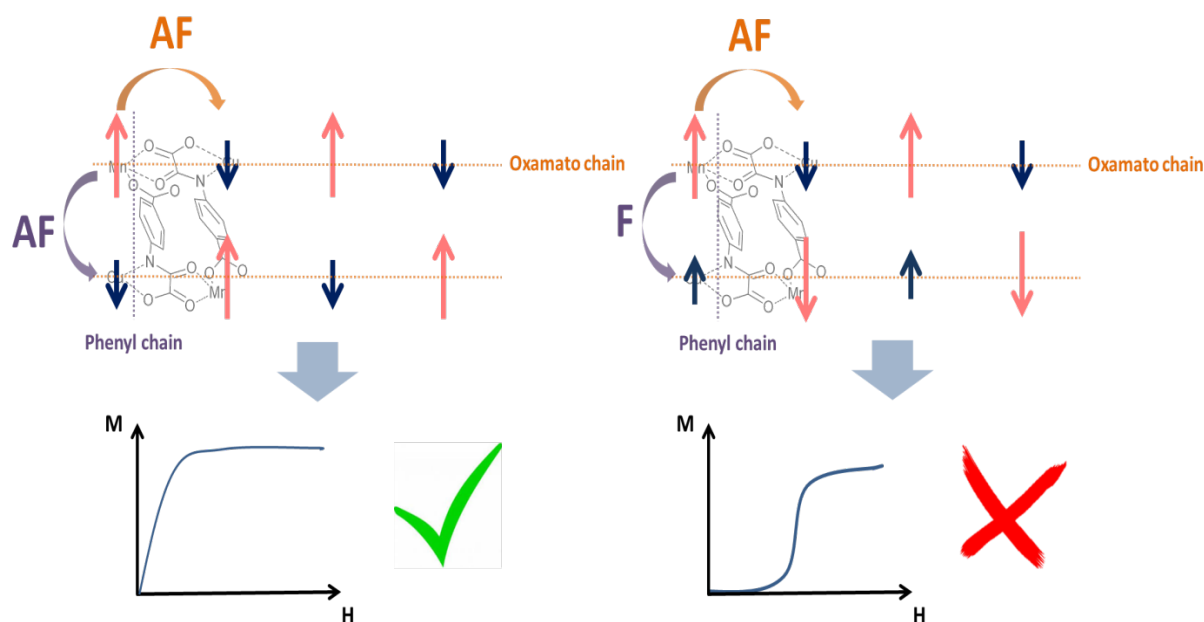


Figure 4.17 Possible coupling schemes in the 2D layer and hypothetical resulting magnetization curves.

As stated before the Cu^{II} and Mn^{II} ions are not anisotropic and the ferrimagnetic plane is of Heisenberg type. It cannot lead to a magnetic ordering in 2D. To obtain a magnetic order, ferromagnetic interplane interactions are compulsory. This interaction, probably dipolar in origin, is weak. This explains the very low critical temperature of 2.5 K measured for compound **4.1**. It is worthy of note that interplanar antiferromagnetic interactions would lead to a metamagnetic behavior that was not observed.

4.2 Conclusion

In this chapter, a novel 2D heterometallic compound $(\text{TMA})_3[\text{CuMn}(\text{paba})_2(\text{OAc})] \cdot 7\text{H}_2\text{O}$ was synthesized solvothermally. Its structure is that of a brick-wall arrangement, bearing similarities with previously reported corrugated oxamato-bridged 2D open-framework. Nevertheless, the use of an heterotopic ligand has also yielded important differences regarding the constitutive units. Mainly, the presence of the additional carboxylato coordinating groups allowed the construction of the 2D structure from monometallic bis-oxamato complexes, instead of the bimetallic tetra-oxamato metalloligands traditionally used.

Temperature dependent X-ray diffraction revealed that the compound can withstand desolvation, retain its crystallinity and remain stable up to 200 °C.

Finally, magnetic measurements indicated the obtainment of a ferrimagnetic compound showing a critical temperature of 2.8 K resulting from both intra-layer antiferromagnetic interactions via both the oxamato and the phenylcarboxylato bridges and inter-layer ferromagnetic interaction. Unfortunately, low field measurements also revealed the existence of a manganese oxide impurity, despite our best efforts at purification.

References

- 1 C. L. M. Pereira, E. F. Pedroso, H. O. Stumpf, M. A. Novak, L. Ricard, R. Ruiz-García, E. Rivière and Y. Journaux, *Angew. Chem. Int. Ed.*, 2004, **43**, 956–958.
- 2 J. Ferrando-Soria, J. Pasán, C. Ruiz-Pérez, Y. Journaux, M. Julve, F. Lloret, J. Cano and E. Pardo, *Inorg. Chem.*, 2011, **50**, 8694–8696.
- 3 B. Boucher, R. Buhl and M. Perrin, *Journal of Physics and Chemistry of Solids*, 1971, **32**, 2429–2437.
- 4 B. Boucher, R. Buhl and M. Perrin, *Journal of Applied Physics*, 1971, **42**, 1615–1617.
- 5 M. Nogues and P. Poix, *Solid State Communications*, 1974, **15**, 463–470.
- 6 G. B. Jensen and O. V. Nielsen, *J. Phys. C: Solid State Phys.*, 1974, **7**, 409–424.
- 7 W. Gao, F. Liu, X.-M. Zhang, J.-P. Liu and Q.-Y. Gao, *Journal of Solid State Chemistry*, 2018, **268**, 108–114.
- 8 Y. Pei, Y. Journaux, O. Kahn, A. Dei and D. Gatteschi, *J. Chem. Soc., Chem. Commun.*, 1986, 1300–1301.
- 9 V. Baron, B. Gillon, J. Sletten, C. Mathoniere, E. Codjovi and O. Kahn, *Inorganica chimica acta*, 1995, **235**, 69–76.
- 10 E. Pardo, R. Ruiz-García, F. Lloret, J. Faus, M. Julve, Y. Journaux, M. A. Novak, F. S. Delgado and C. Ruiz-Pérez, *Chem. - Eur. J.*, 2007, **13**, 2054–2066.

Chapter 5:

*Synthesis, characterization and magnetic properties
of oxamato bridged homo- and hetero-metallic 3D
compounds.*

Chapter 5. Synthesis, characterization and magnetic properties of oxamate bridged homo- and hetero-metallic 3D compounds.

In this chapter, two 3D homometallic networks $[\text{Mn}(\text{H}_2\text{O})(\text{Hpaba})]$ (compound **5.1**), $(\text{TMA})[\text{Cu}(\text{paba})]\cdot 1.5\text{H}_2\text{O}$ (compound **5.2**) and one heterometallic compound $(\text{TMA})_2[\text{CuMn}_2(\text{ox})(\text{paba})_2]\cdot (\text{DMF})\cdot 3\text{H}_2\text{O}$ (compound **5.3**) will be presented. They were all obtained from para substituted phenyloxamate ligand with carboxylic acid. All the compounds were synthesized solvothermally.

5.1 Homometallic 3D compound, $[\text{Mn}(\text{H}_2\text{O})(\text{Hpaba})]$

5.1.1 Synthesis and structural characterization of $[\text{Mn}(\text{H}_2\text{O})(\text{Hpaba})]$

Compound **5.1** was firstly synthesized in the presence of both CuCl_2 and MnCl_2 at $150\text{ }^\circ\text{C}$ in DMF and water mixture solution. Since the isolated solid was pale yellow and indicated the absence of Cu^{II} , the synthesis was reproduced with MnCl_2 only, and it succeeded. Here solvothermal conditions are not sufficient to deprotonate the amide. Prior to X-ray diffraction analysis, it has been identified with FT-IR spectroscopy, and the presence of N-H vibration bands^{1,2} above 3200 cm^{-1} .

Compound **5.1** crystallizes in the $P2_1/c$ space group. The asymmetric unit consists of one partially deprotonated $(\text{Hpaba})^-$ ligand, one Mn^{II} ion and a molecule of water. Each ligand binds four Mn^{II} ions: one via the chelating carbonyl groups of the oxamate function (O2, O3), one via the remaining oxygen atom of the oxamate group (O1), and one ion through each oxygen atom of the carboxylate group (O4, O5, Figure 5.2). The ligand is fairly planar with a dihedral angle between the oxamate group and the phenyl ring of 18° (Figure 5.2) Its coordination mode (Figure 5.1a and 5.2) resembles that of partially deprotonated oxamate ligands found in the literature¹⁻⁴.

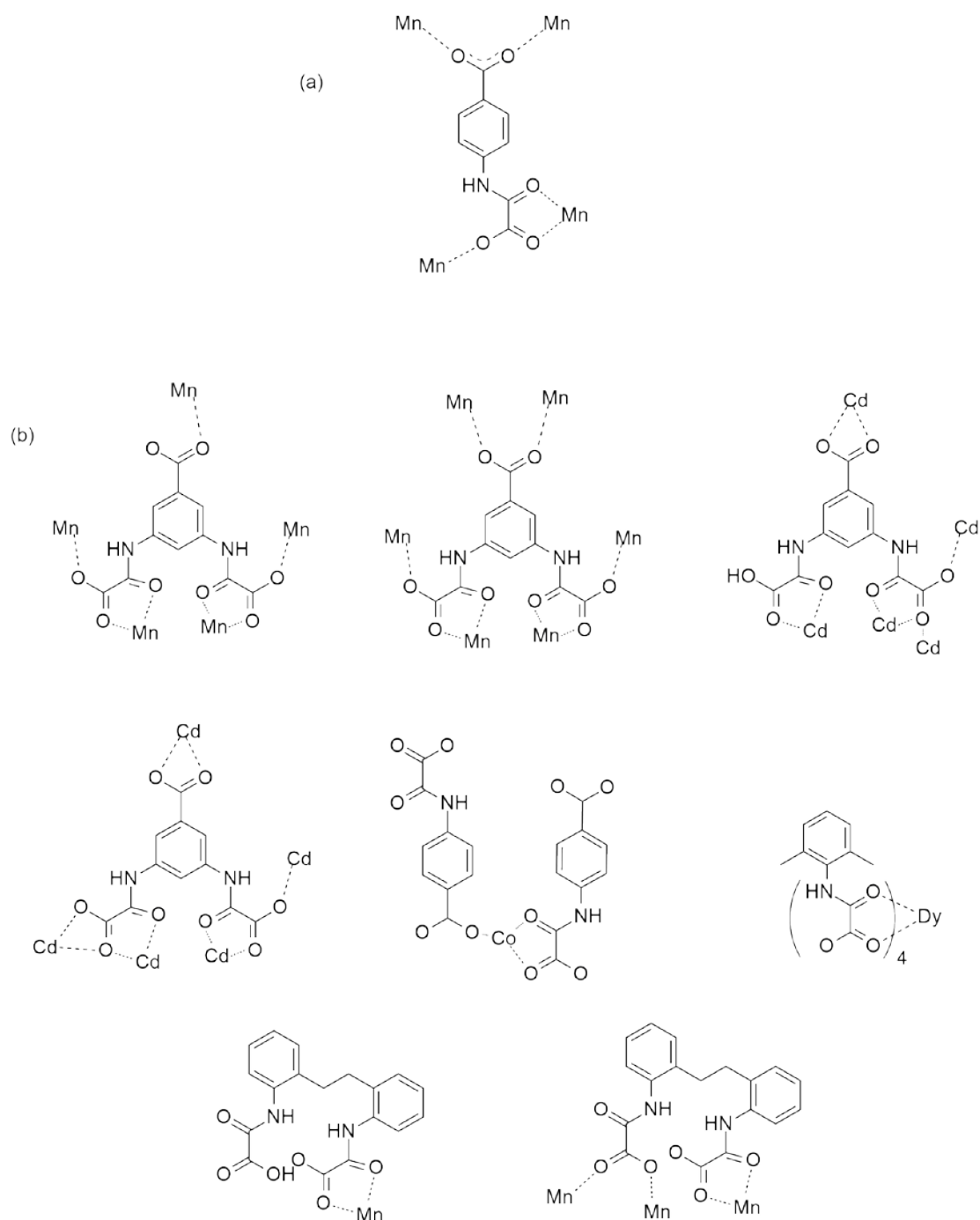


Figure 5.1 (a) Coordination mode of Hpaba^- ligand in compound **5.1** and (b) Coordination modes of non-deprotonated amide oxamato ligand in previous literatures¹⁻⁴.

The Mn^{II} ions in compound **5.1** are six-coordinate with distorted octahedral surrounding. Each metal ion is bound to four $(\text{Hpaba})^-$ ligands and one molecule of water (Figure 5.2). Three of these $(\text{Hpaba})^-$ ligands are mono-coordinated to the metal ion (O1, O4, O5), one is chelated (O2, O3). The Mn-O distances are quite homogenous (2.182 Å [2.111(1) - 2.266 (1)]) and consistent with previously reported oxamato-based manganese(II) compounds⁵⁻⁷. The O-Mn-O angles vary from 74

to 103° , and deviate on average by 5° from orthogonality.

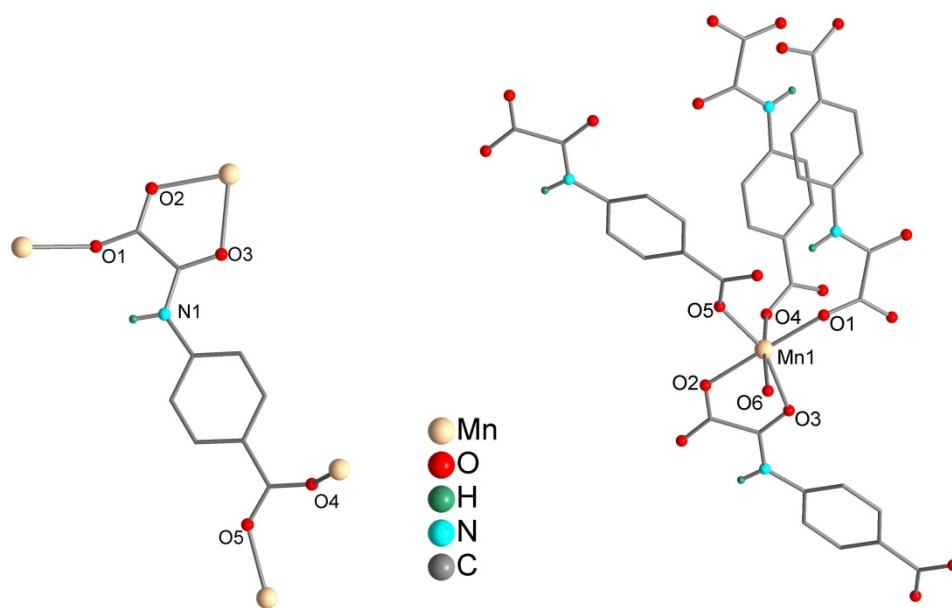


Figure 5.2 Perspective view of the coordination mode of the ligand and of the Mn^{II} ion in 5.1. Amide hydrogen atom is shown in green.

Overall, the $(\text{Hpaba})^-$ ligands bridge the manganese ions into two sub-sets of perpendicular chains that are linked by the phenyl groups spacers into a 3D network. The μ -carboxylato groups create Mn^{II} chains that run along the crystallographic c axis, while the μ -oxamato groups generate chains along b . The crossing of the chains at the Mn^{II} centres generates 2D plans parallel to (bc) and they are linked into a 3D networks by the phenyl spacers that alternate along the oxamato-bridged chain (Figure 5.3 and 5.4). In the solid, H-bonds are found between the coordinated water molecule and oxygen atoms from two neighbouring oxamate groups at 2.04 \AA ($\text{H}\cdots\text{O}$), as well as between the protonated amide and an adjacent oxygen atom from a carboxylate group at 2.21 \AA (Figure 5.5).

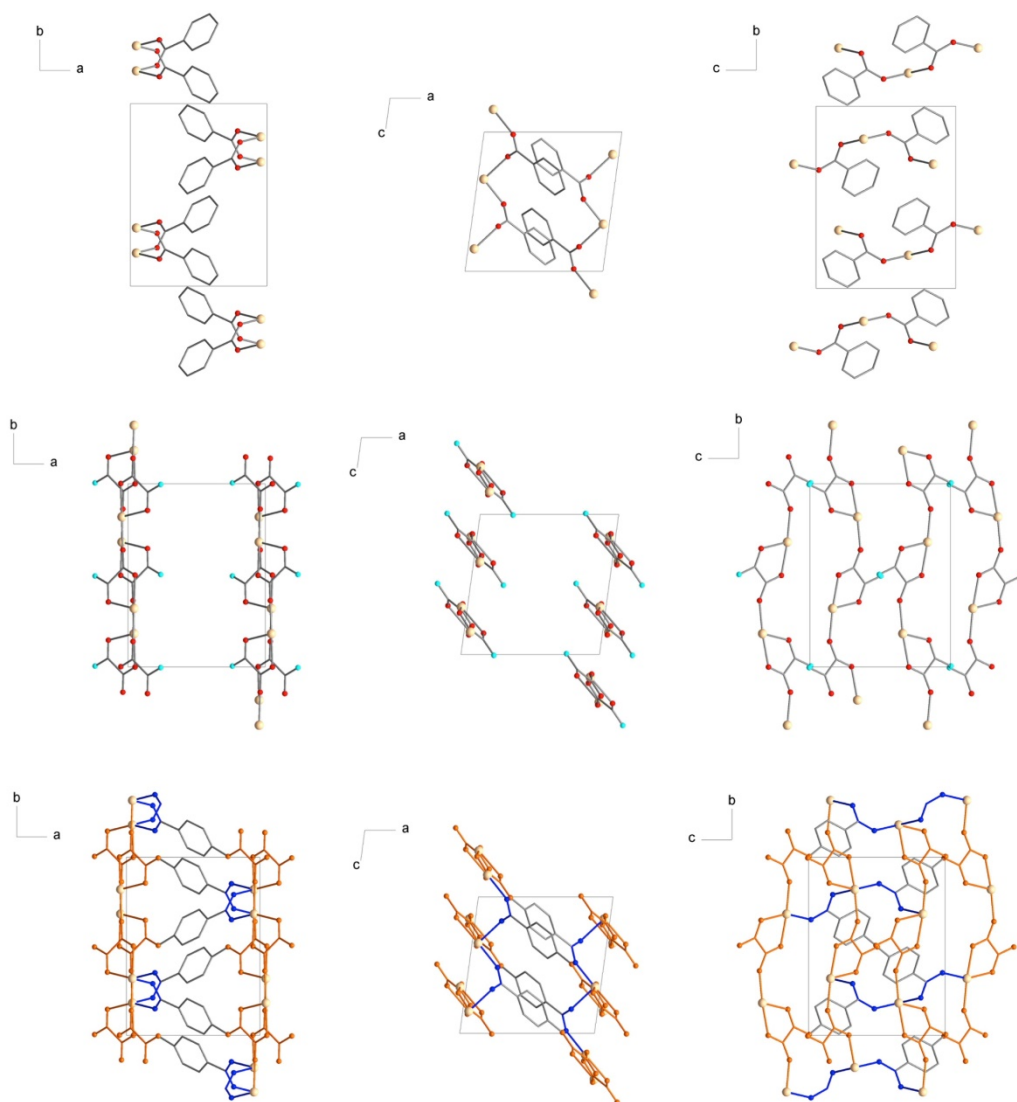


Figure 5.3 View of the carboxylato- and oxamato-bridged chains along each crystallographic axis, and their connection via the phenyl spacers.

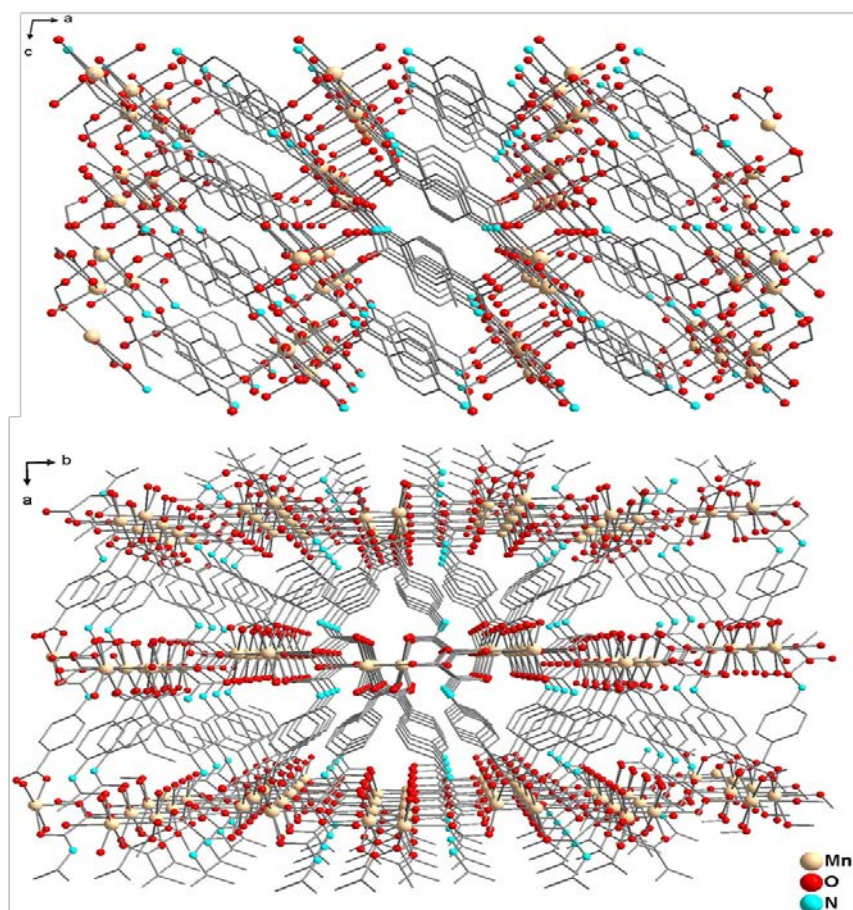


Figure 5.4 (a) Perspective view of the 3D structure of 5.1 along the crystallographic *b* and *c* axis.

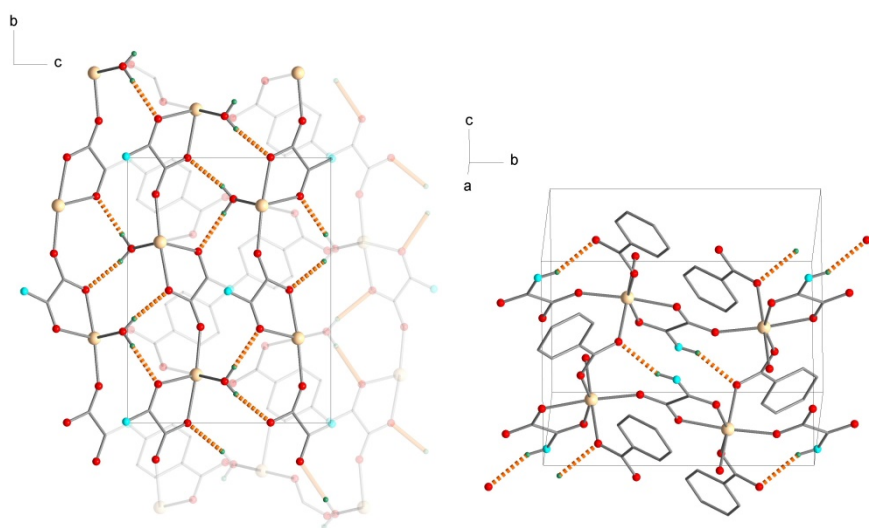


Figure 5.5 View of the H-bonds in the structure, (left) between the water molecule and the oxamate groups; (right) between the amide proton and the carboxylate bridges.

5.1.2 Magnetic Property of [Mn(H₂O)(Hpaba)]

The magnetic properties of compound **5.1** were investigated in the 2.0-300 K temperature range at 250 Oe (2-180 K) and 2500 Oe (180-300 K) (Figure 5.6). At room temperature, $\chi_M T$ was equal to 4.35 cm³ mol⁻¹ K, in accordance to the expected value for one Mn^{II} with no interactions ($\chi_M T = 4.375$ cm³ mol⁻¹ K with $g_{Mn} = 2$)

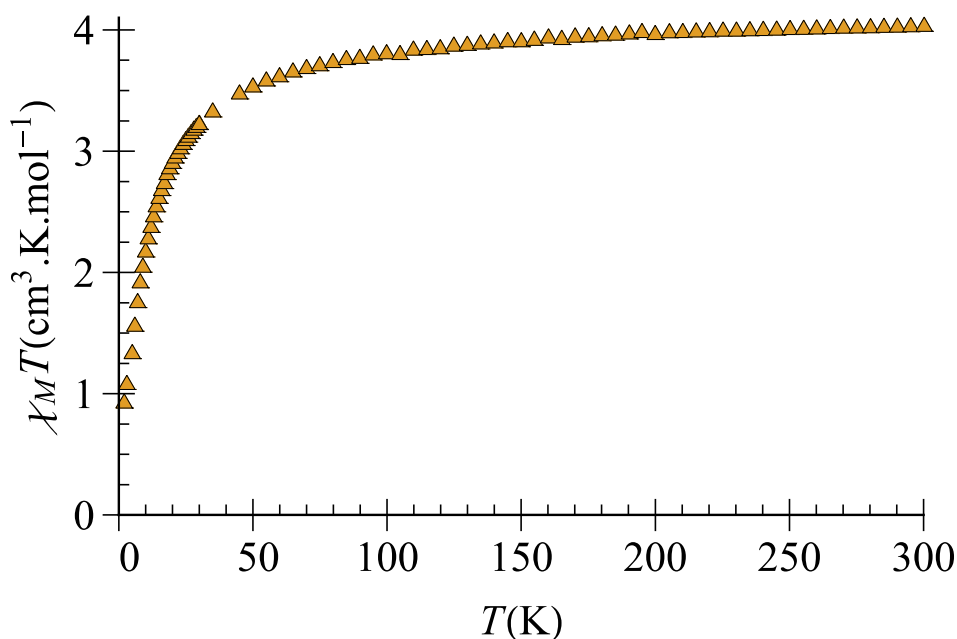


Figure 5.6 Temperature dependence of the $\chi_M T$ product for compound **5.1** under an applied field of 2500 Oe (180–300K) and 250 Oe ($T \leq 180$ K).

Upon cooling, $\chi_M T$ decreases continuously between 300 K and 50 K, and then decreases sharply to $\chi_M T = 1$ cm³ mol⁻¹ K at 2 K. A local quasi maximum of χ_M was observed near 5 K in the χ_M vs. T curve (Figure 5.7). These features show that the magnetic properties of **5.1** are dominated by antiferromagnetic interactions. However, the smooth shape of the curve near 5 K almost excludes the existence of an antiferromagnetic ordering at this temperature. At lower temperature the increase of χ_M probably comes from a small amount of paramagnetic impurity. In contrast to compound **4.1** and **4.2**, no field dependent feature due to Mn₃O₄ is observed around 40 K.

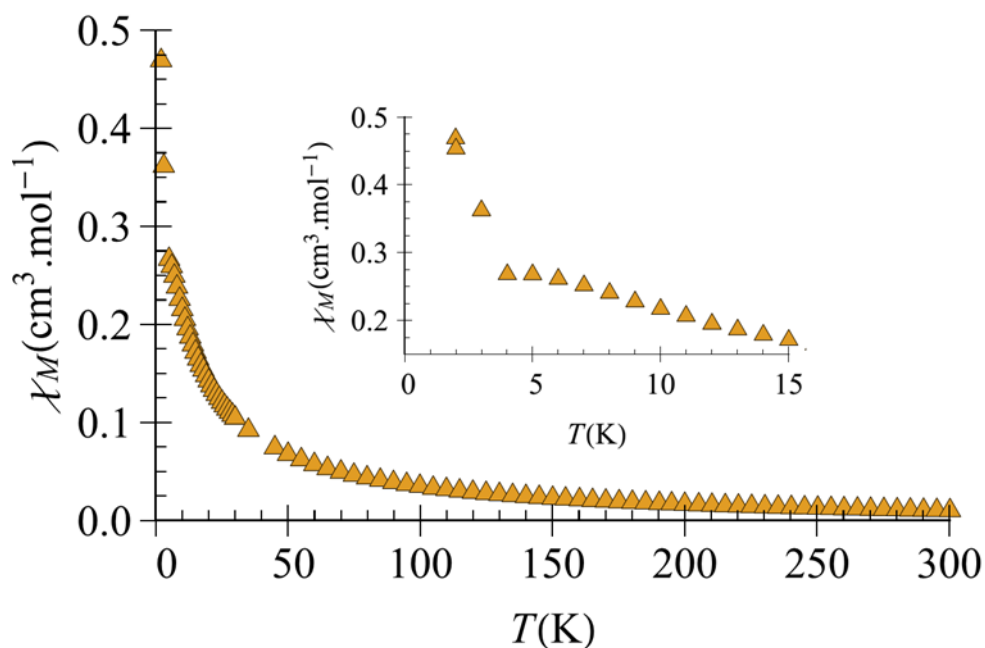


Figure 5.7 Temperature dependence of χ_M for compound 5.1 under an applied field of 250 Oe between 10 and 2 K. Inset : magnification of the 2K-15K temperature range .

Any quantitative interpretation of the magnetic data is impossible with three different types of Mn-Mn interactions. Actually, even with only one kind of interaction the Heisenberg model cannot be solved in 3D, only the Ising model has been solved in 2D⁸ and it is computationally intractable in 3D⁹. Nevertheless, experimental results show that antiferromagnetic interactions are dominant. Even if it is not the shortest Mn-Mn distance, the strongest interaction should be along the chain parallel to the *b* axis, through the oxamate bridges, since the $d_{x^2-y^2}$ orbitals of the Mn(II) ions almost share the same plane with the oxamate bridge. A modeling using Fisher's law for a classical spin chain was attempted but unsuccessful¹⁰. No acceptable fit was obtained. The magnetic properties are rather that of a 2D plane involving also the interactions via the carboxylato bridges, which correspond to the shortest Mn-Mn distance. Finally, the weakest interaction is likely the one through the phenyl ring, but this interaction is not large enough to induce a visible antiferromagnetic ordering in the studied temperature range.

5.2 Homometallic 3D compound, (TMA)[Cu(paba)]·1.5H₂O

5.2.1 Synthesis and structural characterization of (TMA)[Cu(paba)]·1.5H₂O

The homometallic (TMA)[Cu(paba)]·1.5H₂O network (compound **5.2**) was originally obtained in the presence of both Cu(OAc)₂ and Mn(OAc)₂ and using H₂Li-paba·H₂O as the ligand source. In order to obtain a more satisfactory synthesis procedure, Mn(OAc)₂ was abandoned and H(TMA)₂-paba·1.5H₂O was also screened, since TMA⁺ was found in the structure and it allowed us to probe the need for TMAOH. This has resulted in a successful synthesis with an excellent yield (85 %) and little to no side-products.

Compound **5.2** crystallizes in the monoclinic *Cc* space group. Its structure consists of anionic paba-based Cu^{II} 3D network with tetramethylammonium counter-ions. The amount of co-crystallized water molecules was determined by elemental analysis and TGA measurements. The coordination mode of the (paba)³⁻ ligand in **5.2** is shown in Figure 5.8.

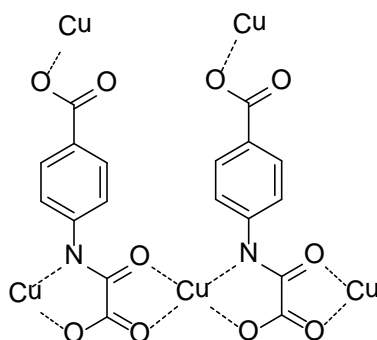


Figure 5.8 Coordination modes of (paba)³⁻ ligand in compound **5.2**

The asymmetric unit of **5.2** consists of two crystallographically non-equivalent (paba)³⁻ ligands and two non-equivalent Cu^{II} atoms (Figure 5.9), although both metal ions have similar coordination spheres. Each Cu^{II} atom is five-coordinate and adopts a distorted square pyramidal coordination geometry. Each Cu^{II} ions is coordinated to three paba ligands. One ligand binds via its nitrogen and oxygen atoms of the oxamate group (N1,O1 for Cu1; N2,O6 for Cu2), a second via two oxamate oxygen atoms (O7,O8 for Cu1; O2,O3 for Cu2), and the third via a monocoordinated carboxylate oxygen atom (O4 for Cu1 and O9 for Cu2). The two ligands binding via their oxamate groups are cis-coordinated to the metallic center. As a result, the base of the Cu^{II} square pyramidal geometry is

defined by one nitrogen atom and three oxygen atoms coming from three distinct ligands, the apical position being occupied by one oxygen atom coming from one oxamate group. However, Cu1 and Cu2 differ in their configurations (Figure 5.9). Cu-N/O_{eq} bond lengths average to 1.977 Å ([1.944(11)-2.005(12)]), with Cu-O apical distances of 2.244(10) and 2.296(12) Å. O/N-Cu-O/N angles vary from 78 to 99° for an averaged deviation to orthogonality of 6°. These distances and angles are quite comparable with the ones found in compound **4.1**. The dihedral angles between the phenyl rings and the oxamate groups in each ligand are 87° (Cu1) and 59° (Cu2), and more importantly, the angle between the pendant phenylcarboxylato groups around the oxamate-bridged copper pairs is of 59° (Figure 5.10).

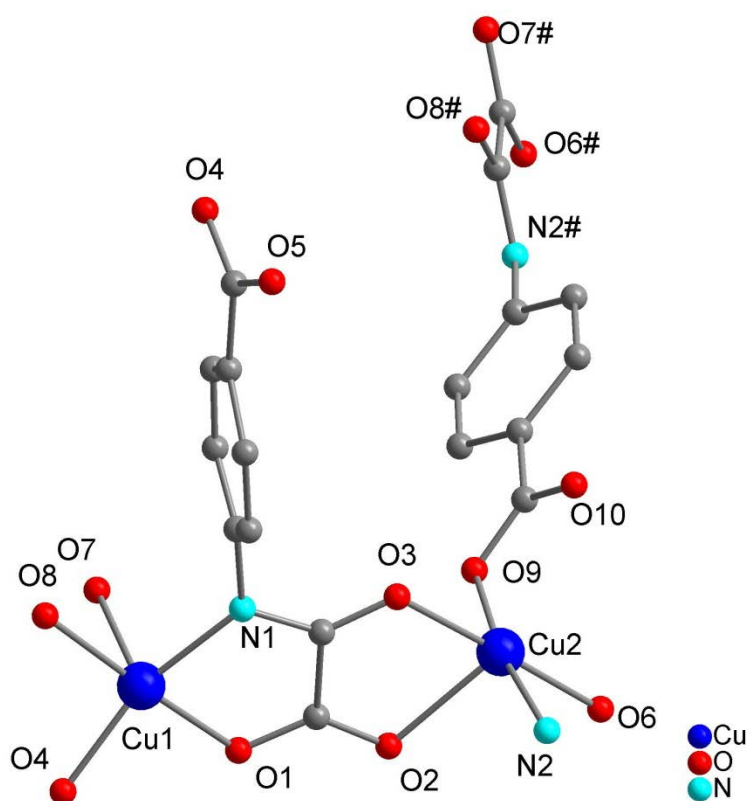


Figure 5.9 Perspective view of the asymmetric unit of compound 5.2 showing the coordination environment of two Cu^{II} ions together with atom labels.

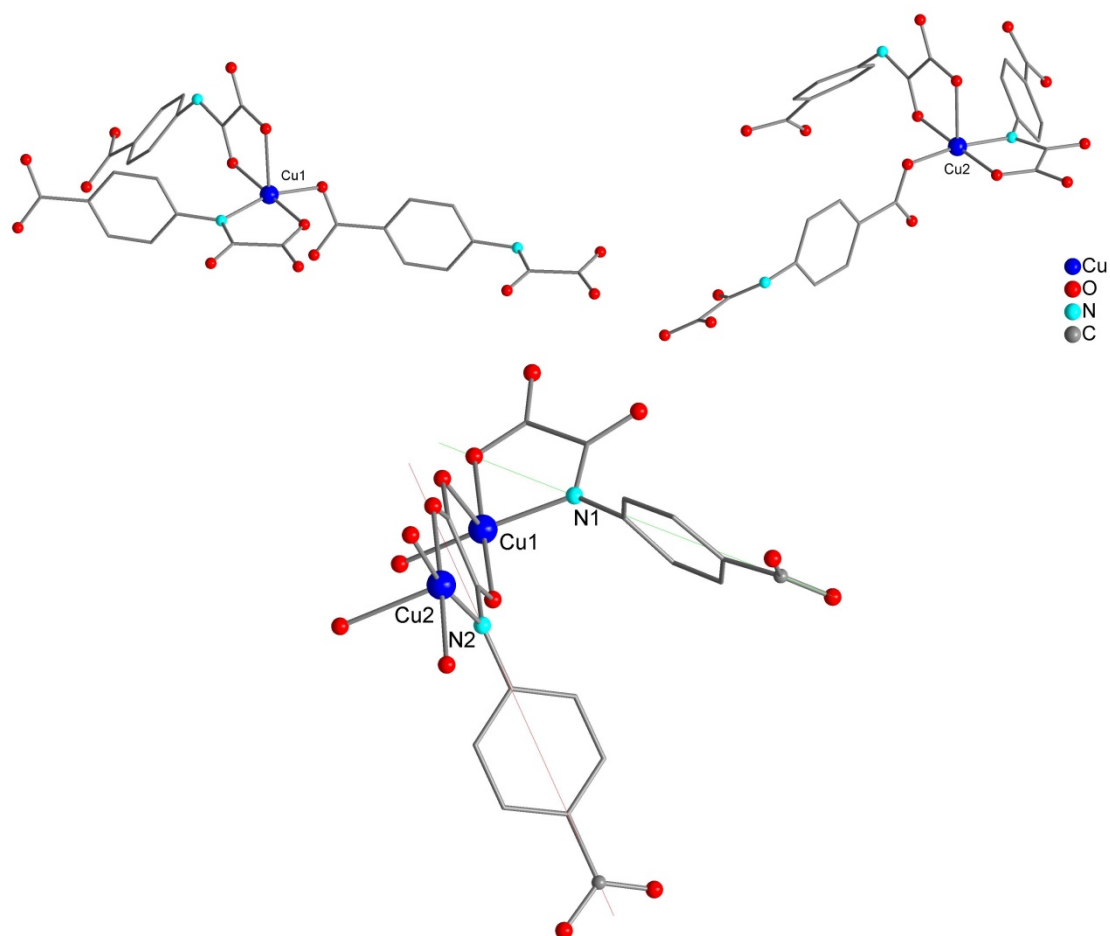


Figure 5.10 View of the configurations of the two Cu^{II} ions, and directionality of the carboxylate groups.

The 3D network of compound **5.2** can be described as stacked planes of 1D Cu-oxamate chains. The connection of the chains occurs within a plane or between the planes via the phenylcarboxylato groups. The $[\text{Cu}(\text{paba})]^-$ metalloligand generates oxamato-bridged zig-zag chains that are linked alternatively via the phenylcarboxylato groups (i) to an adjacent and parallel chain to form a plane and (ii) to an adjacent and almost perpendicular chain above the 2D plane to form the 3D network. The planes are parallel to the (ab) crystallographic plane, and are thus stacked along the c axis. The 3D networks corresponds to an ABA type of planes arrangement with two distinct directions adopted by the chains, $[1,-1,0]$ and $[1,1,0]$. This results in an 83° angle between the chains from two adjacent plane (Figure 5.11). The TMA^+ fill the channels of the network, leaving no accessible void, even for small molecules such as N_2 .

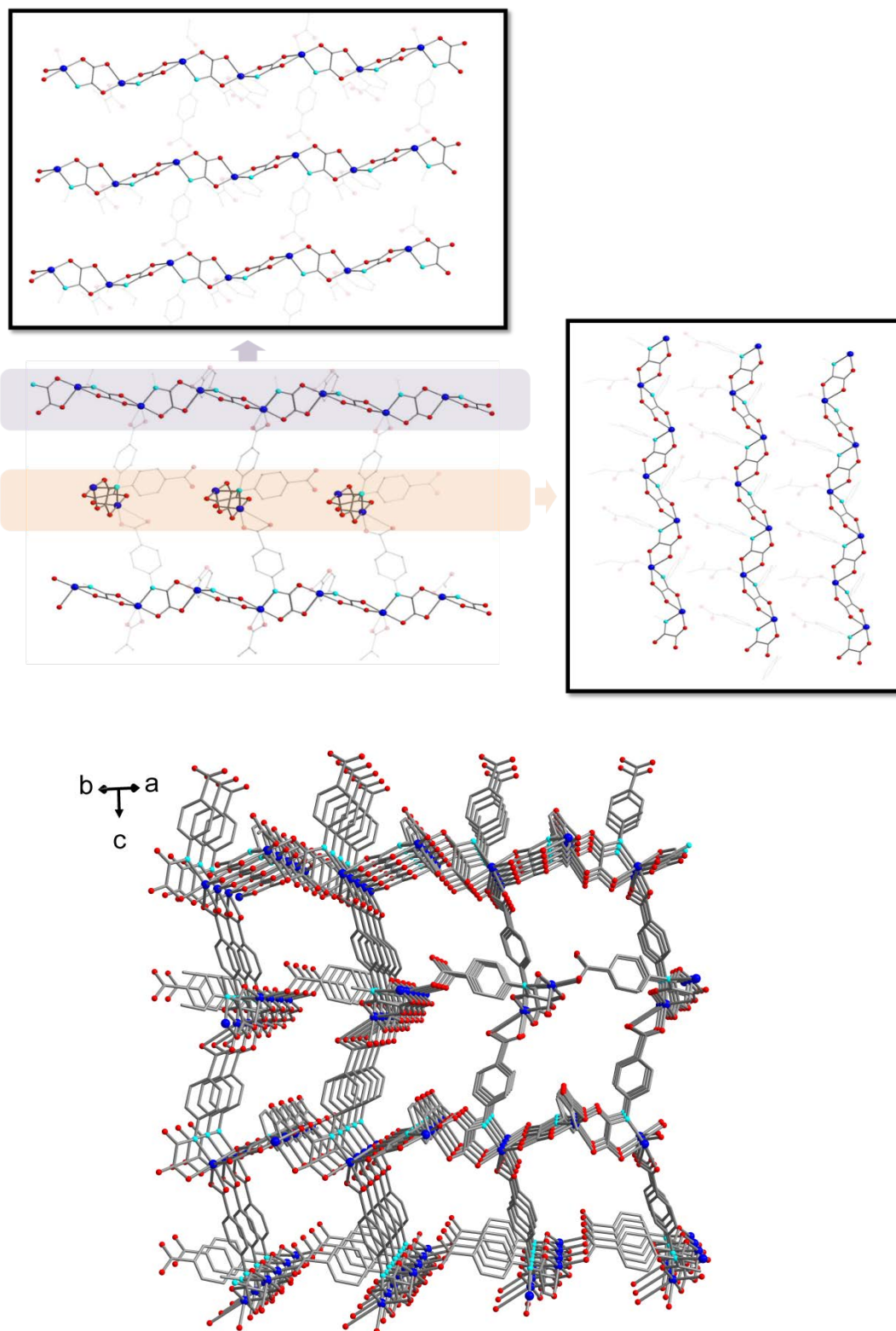


Figure 5.11 Top: Scheme of the 3D arrangement in compound 5.2.
Bottom: Perspective view of compound 5.2.

5.2.2 Thermal Property of (TMA)[Cu(paba)]·1.5H₂O

TGA shows a first weight loss of 7 % (in air) that matches well the water content in **5.2** (ca. 7.3 %). It is followed by a plateau up to 250-270 °C and abrupt drops that represent however less than the expected loss for all the organic content (ca. 55 % for the ligand and 20 % for the TMA⁺). Under air, the decomposition is accompanied by a combustion phenomenon, the measured temperature exceeds the settings and a sharp intense peak in the heat flow is observed (Figure 5.12). At 800 °C under air, the final weight (21 %) corresponds to the formation of CuO (ca. 21.5 %).

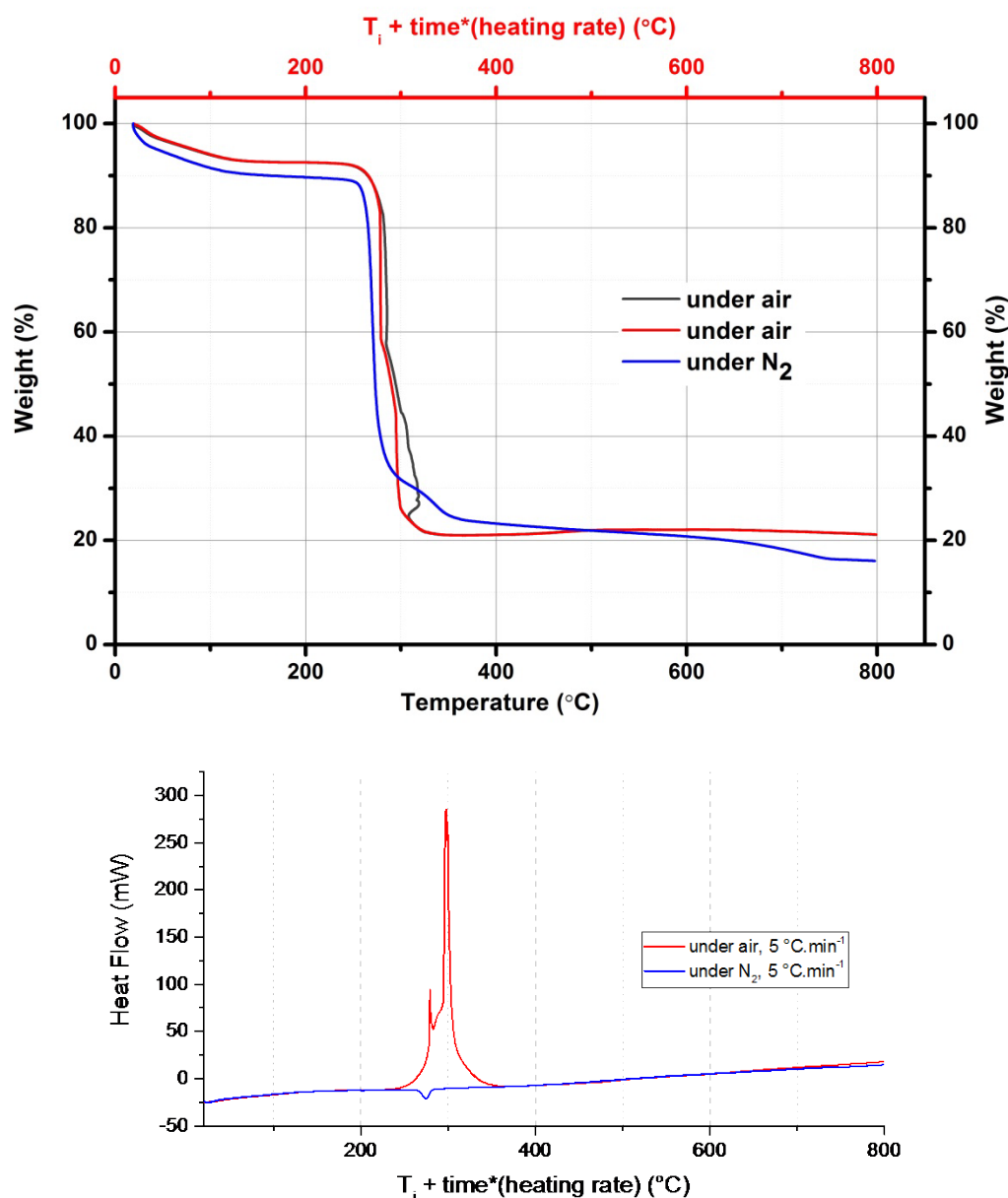


Figure 5.12 Thermogravimetric analysis of (TMA)[Cu(paba)]·1.5H₂O at 5 °C per min

Temperature-dependent powder X-Ray diffraction measurements have been performed on **5.2**,

under nitrogen and between room temperature and 800 °C (Figure 5.13). The diagrams reveal that the structure is stable up to 240 °C when some broad peaks associated to CuO start appearing at 41 and 45 ° and before it collapses entirely at 270 °C.

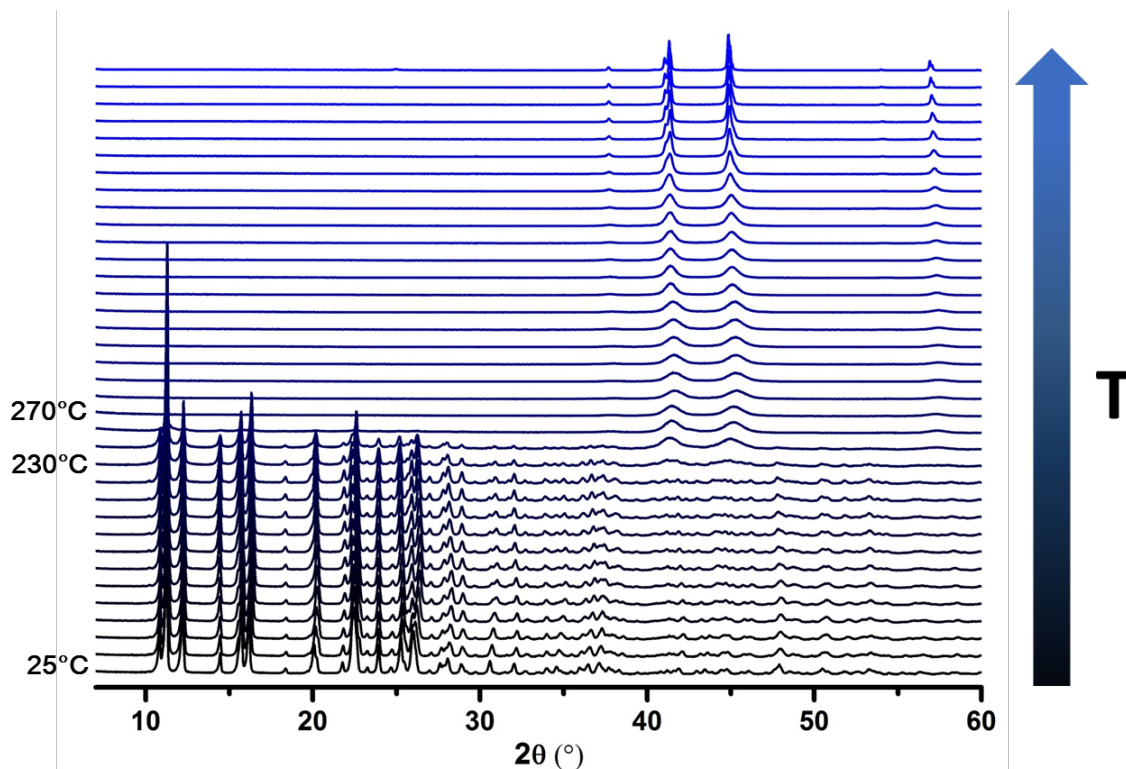


Figure 5.13 Thermodiffractograms of compound 5.2 from 25 to 800 °C.

5.2.3 Magnetic Property of (TMA)[Cu(paba)]·1.5H₂O

The magnetic property of compound **5.2** was studied in the 2-300 K temperature range with applied fields of 2000 Oe ($T < 100$ K) and 1 T ($T > 100$ K). At room temperature, $\chi_M T$ is equal to $0.258 \text{ cm}^3 \text{ mol}^{-1} \text{ K}$. This value is much smaller than the expected one for an isolated Cu^{II} ion ($\chi_M T = 0.413 \text{ cm}^3 \text{ mol}^{-1} \text{ K}$ with $g_{\text{Cu}} = 2.1$). This large difference reveals the existence of strong antiferromagnetic interaction between the oxamato-bridged Cu^{II} ions (Figure 5.14).

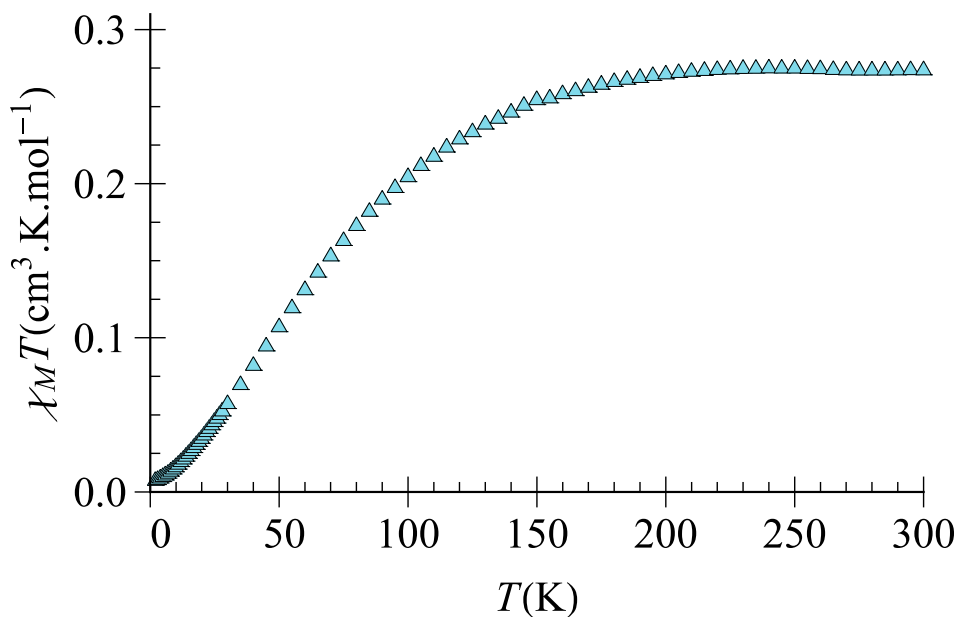


Figure 5.14 Temperature dependence of $\chi_M T$ plot of compound 5.2 under an applied field of 2000 Oe ($T \leq 100$ K) and 1 T (100–300 K).

Upon cooling, the $\chi_M T$ product decreases slowly between 300 K and 100 K, and then more rapidly to reach almost 0 at 2 K. This also confirms the existence of predominant antiferromagnetic interactions. From the χ_M versus T curve, a round maximum is observed at 65 K (Figure 5.15).

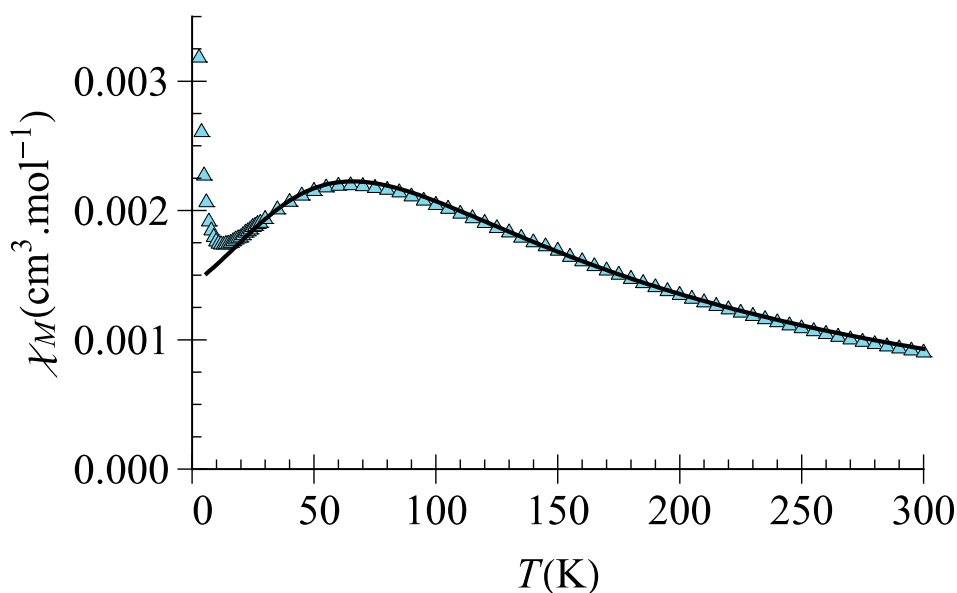


Figure 5.15 Temperature dependence of χ_M for compound 5.2 under an applied field of 2000 Oe ($T \leq 100$ K) and 1 T (100–300 K). The solid black line is the best fit curve using the Bonner Fisher's law for 1D $S=1/2$ chain¹¹.

As for compound **5.1**, any quantitative modelization of the magnetic properties of **5.2** seems difficult due to the 3D nature of the network. Nevertheless, the observed broad maximum at a relatively high temperature of 65 K, which is associated with the presence in the structure of 1D Cu-oxamate chains, suggests that the magnetic behavior could be close to that of a Cu^{II} ion chain. Indeed, a good fit in the 26 -300 K temperature range is obtained using Bonner Fisher's empirical law¹¹ as shown in Figure 5.15. The best fit parameters are equal to $J = -70.8 \text{ cm}^{-1}$, $g_{Cu} = 2.14$, with an agreement factor $F = 5.4 \cdot 10^{-5}$. The J value is in the expected range for an oxamato-bridged copper chain with an orbital reversal configuration^{12,13}. The increase of χ_M below 10K is due to a small amount of paramagnetic impurity.

Despite its three-dimensional structure, the magnetic behavior is that of a copper chain. The Cu-Cu interaction across the oxamate bridge is much greater than that of the coupling across the phenylcarboxylato groups and determines the magnetic behavior of **5.2**. The interaction through the phenylcarboxylato groups is too weak to be visible and its effect is masked by the presence of the small amount of paramagnetic impurity.

5.3 Heterometallic 3D compound, $(\text{TMA})_2[\text{CuMn}_2(\text{ox})(\text{paba})_2] \cdot (\text{DMF}) \cdot 3\text{H}_2\text{O}$

5.3.1 Synthesis and structural characterization of $(\text{TMA})_2[\text{CuMn}_2(\text{ox})(\text{paba})_2] \cdot (\text{DMF}) \cdot 3\text{H}_2\text{O}$

Like the previous compounds, the heterometallic 3D network $(\text{TMA})_2[\text{CuMn}_2(\text{ox})(\text{paba})_2] \cdot (\text{DMF}) \cdot 3\text{H}_2\text{O}$ (compound **5.2**) was obtained through our solvothermal reactivity screening. This initial synthesis gave single-crystals in a low yield, as well as many inhomogeneous side-products and thorough washings in ethanol were necessary. Despite our best efforts at altering the synthetic conditions, unwanted side-products were systematically formed. We have however managed to improve the yield, moderately. The single-crystal X-ray diffraction measurement has revealed the presence of oxalate ligands (ox) that must come from the hydrolysis of the oxamate ligand. This side reaction has already been observed in oxamate chemistry¹⁴.

Compound **5.3** crystallizes in the triclinic $P-1$ space group, and consists of an anionic 3D network with TMA^+ counter-cation. The 3D network is made of μ_4 -paba and μ -oxalate bridging ligands. The coordination modes of the ligands are shown in Figure 5.16.

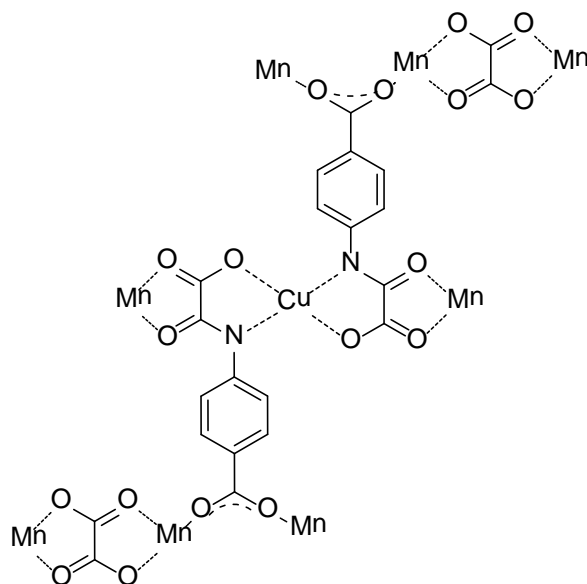


Figure 5.16 Coordination modes of the (paba)³⁻ and (ox)²⁻ ligands in compound 5.3

The Cu^{II} ions are four-coordinate and adopt a square-planar geometry. They are coordinated by two (paba)³⁻ ligands via the nitrogen and oxygen atoms of the oxamato groups (N1, O1). The carboxylato groups of these two (paba)³⁻ ligands point in opposite directions. The Cu-N (1.947(2) Å) and Cu-O (2.002(2) Å) distances resemble that of compounds **4.1** and **5.2**, and are slightly longer than in other {CuMn} 3D networks built on mono-oxamate ligands^{5,15}. Two DMF molecules can also be found at elongated apical positions, with a Cu...O distance of 2.849(2) Å.

The Mn^{II} ion is six-coordinate with a distorted octahedral geometry. Its coordination sphere consists of six oxygen atoms coming from the oxamato group of the paba ligand (O2, O3), two carboxylato groups from two paba ligands (O4, O5) and the oxalate ligand (O6, O7). Mn-O distances are homogeneous and range from 2.100(1) to 2.282(1) Å (av. 2.194 Å). The O-Mn-O angles vary from 74 to 105°, and deviate on average by 7° from orthogonality (Figure 5.17).

The 3D structure of compound **5.3** can be interpreted as follows: the [Cu(paba)₂]⁻ metalloligand binds two Mn^{II} centers via the oxamate bridges to form trimetallic subunits. These subunits are then linked into chains via the oxalate bridging the peripheral Mn^{II} ions, and these chains are connected into the plane and between the planes via bis(μ-carboxylato) bridges that come from metalloligands situated above and below the plane (Figure 5.18). TMA⁺ cations and DMF solvent molecules fill the channels, leaving no accessible void.

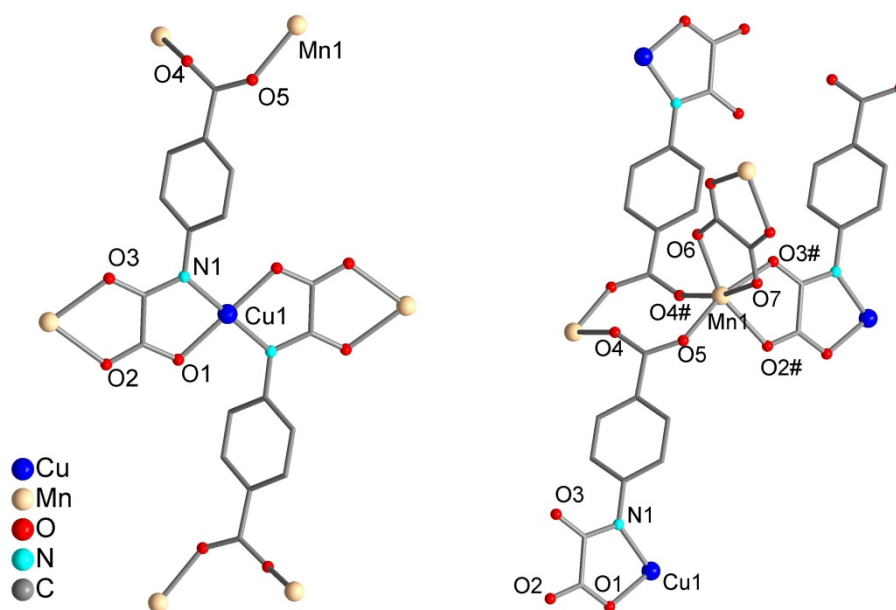


Figure 5.17 View of the Cu^{II} and Mn^{II} environments, with atom labels.

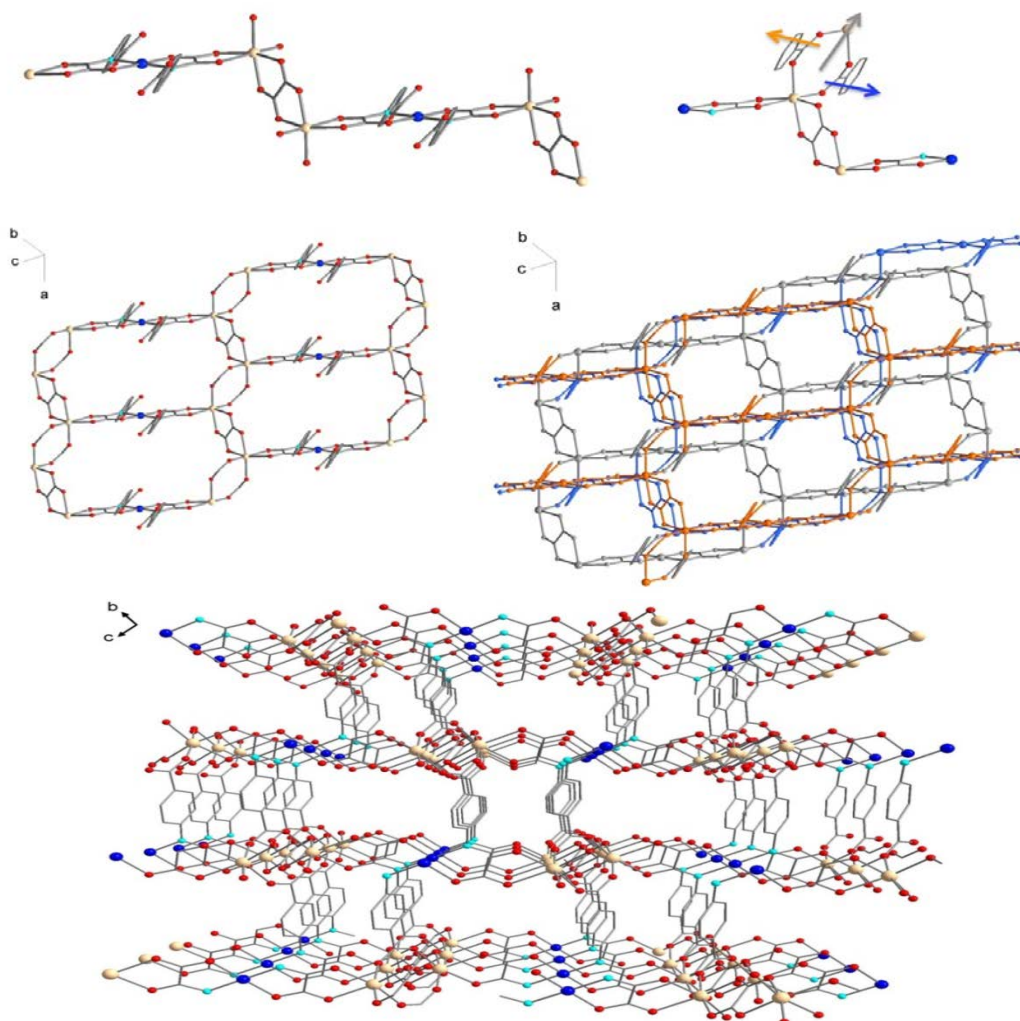


Figure 5.18 Upper: Schematic view of the structuring in the network.

Down: perspective view of compound 5.3 along *a*.

5.3.2 Thermal property of $(\text{TMA})_2[\text{CuMn}_2(\text{ox})(\text{paba})_2]\cdot(\text{DMF})\cdot 3\text{H}_2\text{O}$

TGA shows a first 5.1 % weight loss before 100 °C, that would corresponds to the water removal (*ca.* 5.6 %). It is followed under air by an abrupt loss of more than 50 % after 200 °C, accompanied by a combustion phenomenon. At 800 °C, the final weight (30 %) corresponds to the stoichiometric formation of CuO and Mn₂O₃ (8.4 and 16.6 %). After 150 °C under N₂, the loss occurs in several steps and span over more than 300 °C (Figure 5.19).

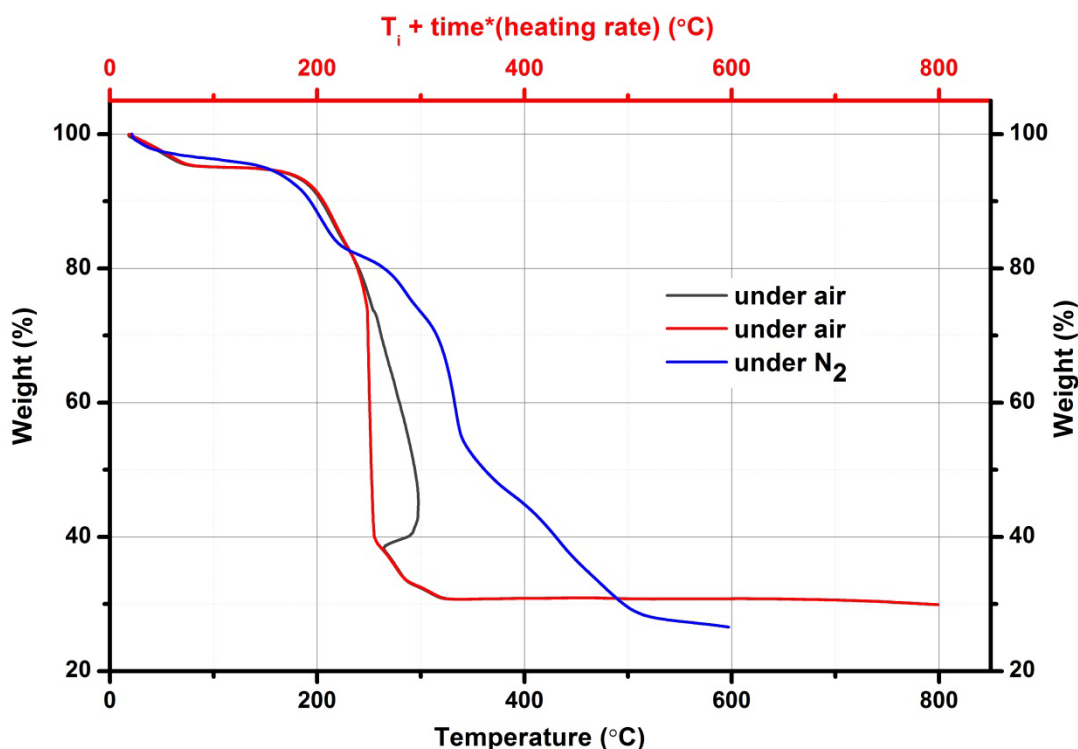


Figure 5.19 Thermogravimetric analysis of $(\text{TMA})_2[\text{CuMn}_2(\text{ox})(\text{paba})_2]\cdot(\text{DMF})\cdot 3\text{H}_2\text{O}$

The thermal stability of the structure of **5.3** was investigated by X-ray powder diffraction between 30 and 600 °C under N₂ (Figure 5.20). There is a clearly visible change in the pattern at 150 °C, yet it probably starts at 130 °C. The main features include the disappearance of the peaks at 9.4, 10.3 and 11.7°, the appearance of a peak 10.9°, and the appearance or separation of a peak at 13.15°. The structural changes seem to be completed at 170°C and yield a structure that remains stable up to 220 °C with no intensity modifications, before a final collapse at 250 °C. Unfortunately, our attempts at refining the high temperature powder pattern or at collecting single-crystal data at 180°C have failed so far.

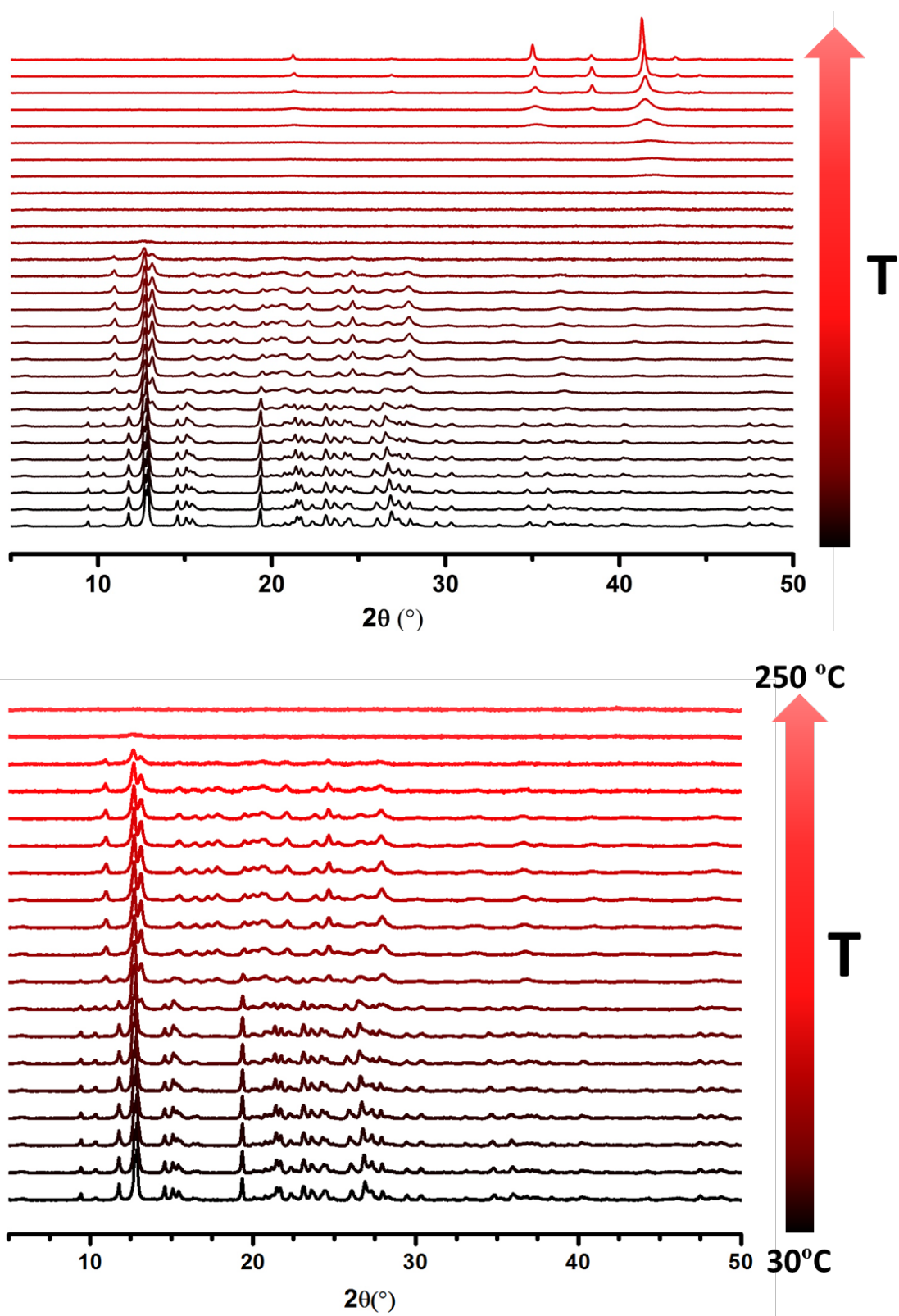


Figure 5.20 PXRD patterns of compound 5.3 between 30 and 600 °C (top) and zoom in the 30-250 °C region (bottom).

5.3.3 Magnetic Property of $(\text{TMA})_2[\text{CuMn}_2(\text{ox})(\text{paba})_2]\cdot(\text{DMF})\cdot 3\text{H}_2\text{O}$

The DC magnetic property of compound **5.3** in the form of $\chi_M T$ versus T plot is shown in Figure 5.21 (χ_M is the magnetic susceptibility per $\text{Cu}^{\text{II}}\text{Mn}^{\text{II}}_2$ unit), the value of $\chi_M T$ at room temperature is $10.49 \text{ cm}^3 \text{ mol}^{-1} \text{ K}$, which is higher than expected for one Cu^{II} and two Mn^{II} non interacting ions ($9.15 \text{ cm}^3 \text{ mol}^{-1} \text{ K}$). Upon cooling, the $\chi_M T$ value decreases continuously from 300 to 53 K. Afterwards, a field dependence of the $\chi_M T$ product is observed. At high field (2500G), the $\chi_M T$ product attains a plateau of $7.7 \text{ cm}^3 \text{ mol}^{-1} \text{ K}$ between 40 and 53 K, and then abruptly decreases to 0 at 2K. At low field (100G), the $\chi_M T$ value rises rapidly to sharp maxima at 35 and 12 K ($\chi_M T$: $12.43 \text{ cm}^3 \text{ K mol}^{-1}$ and $10 \text{ cm}^3 \text{ K mol}^{-1}$), before dropping to $1.7 \text{ cm}^3 \text{ K mol}^{-1}$ at 2 K.

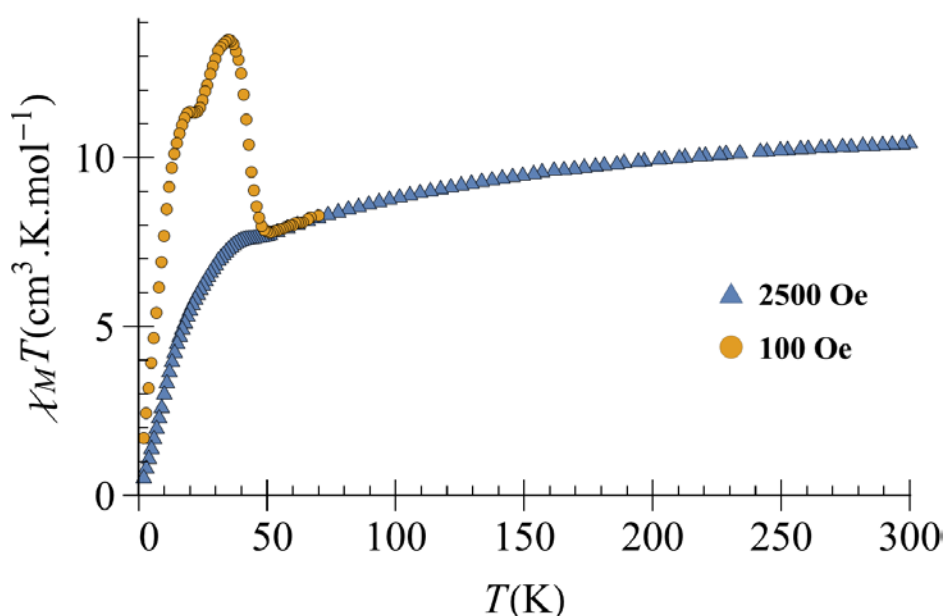


Figure 5.21 Temperature dependence of $\chi_M T$ of compound **5.3** under an applied field of 2500 Oe (2–300K) and 100 Oe ($T < 70 \text{ K}$).

The presence, under a low applied magnetic field (100 Oe), of a peak that turns into a plateau for a higher applied magnetic field (2500 Oe) is the signature of the presence of a saturated ferromagnetic impurity. The ordering temperature around 40 K indicates that, as for compound **4.1**, the synthetic conditions produce a small amount of Mn_3O_4 impurity that displays magnetic ordering at 42 K^{16-18} . For compound **5.3**, the presence of this impurity is highly visible because in this compound antiferromagnetic interactions predominate and lead to a non-magnetic state at low temperature, as shown by the evolution of the $\chi_M T$ product under 2500 Oe, which tends towards zero at 2 K.

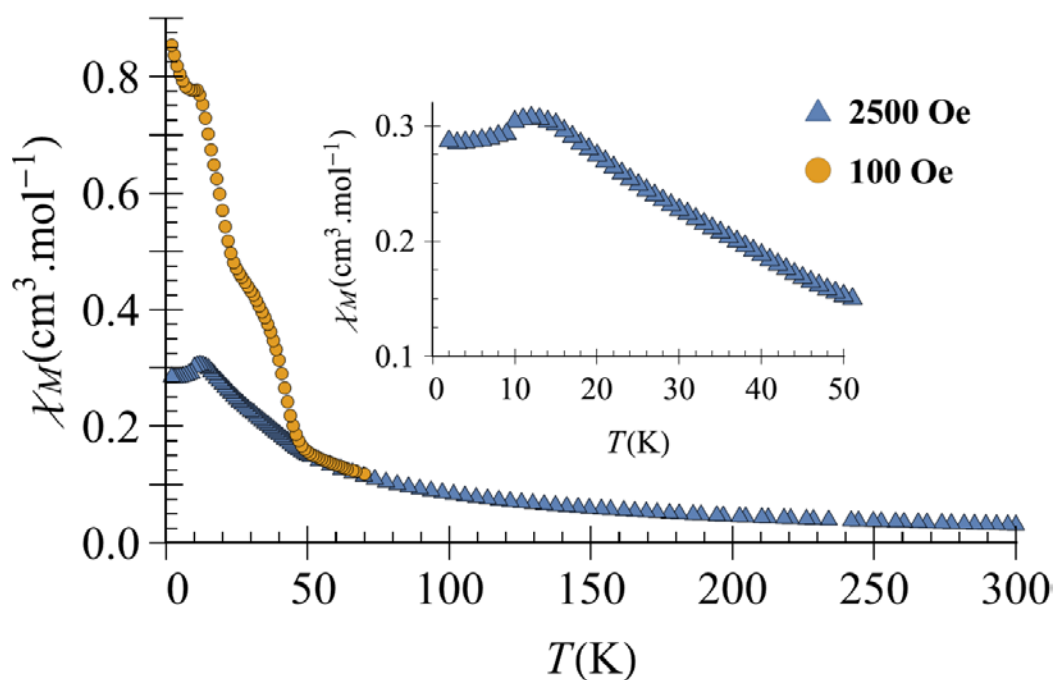


Figure 5.22 Temperature dependence of χ_M plot of compound 5.3 under an applied field of 100 Oe ($T \leq 70$ K) and 2500 Oe (2–300 K). Inset : magnification of the 2K-50K temperature range

The presence of Mn_3O_4 impurity is confirmed by the χ_M versus temperature plot with a field dependent signal below 50 K. It should nevertheless be noted that the high field curve has a maximum at 12 K associated to a plateau at the same temperature in the low field curve. It is tempting to attribute this maximum to the establishment of an antiferromagnetic order but this transition needs to be confirmed. The magnetic properties of compound **5.3** are probably dominated by the interaction between the Mn^{II} ions within the chain formed by the oxalato and carboxylato groups. The interaction between two Mn^{II} ions through an oxalate bridge is antiferromagnetic¹⁹. Whatever the sign of the interaction between the Mn^{II} ions bridged by the bis μ syn-syn carboxylato, the ground state of the Mn chain is non-magnetic. The relatively large antiferromagnetic interaction between the Cu^{II} and Mn^{II} ions through the oxamato bridge²⁰ leads to an effective ferromagnetic coupling between the Mn ions of adjacent chains through the trimetallic subunit. However, this cannot lead to a transition toward a ferrimagnetic compound because the Mn^{II} ion chains have a non-magnetic ground state (Figure 5.22).

5.4 Conclusion

Three 3D networks have been obtained solvothermally using the paba ligand. Compound **5.1** indicates that solvothermal conditions are probably not sufficient to promote the full deprotonation of the oxamate function. The use of base seems necessary, yet the results on compound **5.3** – assuming it is not specifically related to Mn^{II} ions– show that it is accompanied with impurity issues. In comparison, starting with $(\text{TMA})_2\text{H-paba}$ seems more promising, although the use of copper acetate in the case of **5.2** must also play a role and the extension to other metal acetate salts in the absence of Cu^{II} remains to be investigated.

Nevertheless, **5.2** and **5.3** represent the first two examples of 3D networks obtained solvothermally and featuring fully deprotonated oxamate ligands. Besides, their structure stability, while being moderate, remains considerably higher than that of reported 3D oxamate-networks prepared on the bench.

References

- 1 T. L. Oliveira, L. H. G. Kalinke, E. J. Mascarenhas, R. Castro, F. T. Martins, J. R. Sabino, H. O. Stumpf, J. Ferrando, M. Julve, F. Lloret and D. Cangussu, *Polyhedron*, 2014, **81**, 105–114.
- 2 J. Parreiras, E. N. Faria, W. X. C. Oliveira, W. D. D. Pim, R. V. Mambrini, E. F. Pedroso, M. Julve, C. L. M. Pereira and H. O. Stumpf, *J. Coord. Chem.*, 2018, **71**, 797–812.
- 3 L. Hou, L.-N. Ma, X.-Y. Li, Y.-Z. Li, W.-J. Shi, G. Liu and Y.-Y. Wang, *ChemPlusChem*, 2019, **84**, 62–68.
- 4 F. R. Fortea-Pérez, J. Vallejo, M. Julve, F. Lloret, G. De Munno, D. Armentano and E. Pardo, *Inorg. Chem.*, 2013, **52**, 4777–4779.
- 5 J. Ferrando-Soria, T. Grancha, M. Julve, J. Cano, F. Lloret, Y. Journaux, J. Pasán, C. Ruiz-Pérez and E. Pardo, *Chem. Commun.*, 2012, **48**, 3539–3541.
- 6 J. Ferrando-Soria, J. Pasán, C. Ruiz-Pérez, Y. Journaux, M. Julve, F. Lloret, J. Cano and E. Pardo, *Inorg. Chem.*, 2011, **50**, 8694–8696.
- 7 H. O. Stumpf, Y. Pei, O. Kahn, J. Sletten and J. P. Renard, *J. Am. Chem. Soc.*, 1993, **115**, 6738–6745.
- 8 L. Onsager, *Physical Review*, 1944, **65**, 117.
- 9 S. Istrail, in *32nd ACM Symposium on the Theory of Computing*, ACM Press, 2000, pp. 87–96.
- 10 M. E. Fisher, *Am. J. Physics*, 1964, **32**, 343–346.
- 11 J. C. Bonner and M. E. Fisher, *Phys. Rev.*, 1964, **135**, A640–A658.
- 12 M. Julve, M. Verdaguer, A. Gleizes, M. Philoche-Levisalles and O. Kahn, *Inorg. Chem.*, 1984, **23**, 3808–3818.
- 13 Y. Journaux, J. Sletten and O. Kahn, *Inorg. Chem.*, 1985, **24**, 4063–4069.
- 14 T. S. Fernandes, W. D. C. Melo, L. H. G. Kalinke, R. Rabelo, A. K. Valdo, C. C. da Silva, F. T. Martins, P. Amorós, F. Lloret, M. Julve and D. Cangussu, *Dalton Trans.*, 2018, **47**, 11539–11553.
- 15 T. Grancha, M. Mon, F. Lloret, J. Ferrando-Soria, Y. Journaux, J. Pasán and E. Pardo, *Inorg. Chem.*, 2015, **54**, 8890–8892.
- 16 B. Boucher, R. Buhl and M. Perrin, *Journal of Physics and Chemistry of Solids*, 1971, **32**, 2429–2437.

- 17 M. Nogués and P. Poix, *Solid State Communications*, 1974, **15**, 463–470.
- 18 G. B. Jensen and O. V. Nielsen, *J. Phys. C: Solid State Phys.*, 1974, **7**, 409–424.
- 19 J. Glerup, P. A. Goodson, D. J. Hodgson and K. Michelsen, *Inorg. Chem.*, 1995, **34**, 6255–6264.
- 20 Y. Pei, Y. Journaux and O. Kahn, *Inorg. Chem.*, 1988, **27**, 399–404.

Conclusions and Perspectives

Conclusions and Perspectives

Oxamate ligands are largely used in coordination chemistry for the preparation of multi-dimensional magnetic coordination polymers. Substituents variation on the nitrogen atom of the oxamate function allows many types of mono-oxamate, poly-oxamate or amino-acid-based oxamate precursors to be used to design metalloligands. These metalloligands then display numerous topologies that efficiently lead to magnetic coordination polymers.

In this manuscript, we have focused on heterotopic oxamate ligands, based on the assumption that the introduction of additional coordination groups would provide original architectures, and ultimately lead to the preparation of porous magnets. Hydroxy and carboxylic groups were introduced on the *ortho* and *para* positions of the phenyloxamate ligand.

The reactivity of these heterotopic oxamate ligands was investigated under both bench and solvothermal conditions. Results have been obtained for both carboxylato substituted phenyloxamate ligands (oaba, paba), and for one hydroxyl substituted phenyloxamate ligands (ohpma). They show that *o*-substituted ligands lead to 1D compounds while the *p*-substituted ligand (paba) has led to 2D and 3D compounds.

On bench conditions, we have synthesized a homometallic Cu^{II} chain with a rare helicoidal configuration. We have also synthesized a mixed-valent hexametalllic Co^{II/III} coordination ring. It displays field-induced SMM behavior, as revealed by the AC magnetic measurements.

Solvothermally, a series of isostructural heterobi- and heterotri-metallic chain compounds based on the ohpma ligands have been synthesized. The oaba ligand has also afforded one heterobimetallic chain solvothermally. Unfortunately, none of the cobalt(II)-based chains displayed SCM properties, and as illustrated by the [Cu₄Co₃(oaba)₄(OH)₂(DMF)₄] chain, the gain in novelty for the coordination mode of the ligand comes with a lack of design regarding the possible magnetic exchange pathways.

Using the *para*-substituted paba ligand, solvothermal reactions have successfully led to one 2D and three 3D coordination networks. The 2D heterobimetallic compound (TMA)₃[CuMn(paba)₂(OAc)]·7H₂O presents an alternative brick-wall structure that is robust enough to undergo complete desolvation and maintain crystallinity. The 2D network shows typical ferrimagnetic behavior and magnetic ordering at low temperature through the 2D planes. The 3D

networks obtained during this work include two homometallic compounds and one heterometallic polymer. The $[\text{Mn}(\text{H}_2\text{O})(\text{Hpaba})]$ and $(\text{TMA})_2[\text{CuMn}_2(\text{ox})(\text{paba})_2]$ compounds illustrate well the difficulty of reacting oxamate ligands solvothermally. The lack of base is problematic for the deprotonation of the ligand, which prevent the oxamate group to act as the excellent magnetic coupler it should be. On the other hand, basic media are probably the cause of the oxide impurities and of the ligand decomposition observed for our heterobimetallic 3D compound. This makes the $(\text{TMA})[\text{Cu}(\text{paba})]\cdot 1.5\text{H}_2\text{O}$ network all the more interesting, chemically speaking. If it does lack relevance for its magnetic properties, it nevertheless shows that solvothermal synthesis can afford robust oxamate-based 3D networks in excellent yields.

Overall, we find that heterotopic oxamate ligands are promising and that solvothermal reactions merit further investigations. Looking at the 3D structures, the paba ligand appears as an excellent candidate. It is unfortunate that the phpma ligand failed, yet other para-substitued ligands, such as the 4-oxamatopyridine may prove relevant, so would the 3,5-dicarboxylatophenyloxamate ligand. Actually, these ligands would potentially change the charge of the network and help address another drawback so far, the lack of porosity due to the presence of counter-ions in the channels. This issue could also be investigated via the use of tri-valent metal ions, such as Fe^{III} . Concerning the stability of the ligand and/or the formation of undesired oxides in solvothermal conditions, some prospects can be drawn from the successful use of the TMA^+ salt of the paba ligand. Preforming the metalloligands would help limit the use of base and give some choice over the cations nature. One could also imagine that the optimization of the solvothermal conditions on our metalloligands would allow an extension to the classical ones, and a revisiting into more robust structures of the known oxamate-based MCPs.

Appendix

Appendix

Content

1. Ligand synthesis and characterization.....	
2. Chapter 2.....	
3. Chapter 3.....	
4. Chapter 4.....	
5. Chapter 5.....	
6. Instruments.....	
7. BVS calculations.....	
8. Crystallographic tables.....	

References

1. Ligands synthesis and characterisation

1.1. H₂Et-ohpma — Ethyl N-(2-hydroxyphenyl)oxamate

To 5.0 g of 2-aminophenol ($M=109.13 \text{ gmol}^{-1}$, 45.8 mmol) in 150 mL of THF were added dropwise 5.2 mL of ethyloxalyl chloride (98%; 1eq.) under strong stirring. The mixture was refluxed for 90 min. The resulting dark red solution was left to cool down and filtered on paper. Removal of the solvent under reduced pressure yielded a grey powder. The powder was washed with 400 mL of H₂O under stirring for 30 min and then collected on a sintered glass filter. Further washing was performed with cold 96% ethanol and the solid was dried with ether and then in air. The final product was collected as a white powder (6.36 g, Yield: 66.39 %, $M=209.2 \text{ gmol}^{-1}$).

¹H-NMR (300 MHz, DMSO) δ (ppm): 10.19 (s, 1H), 9.60 (s, 1H), 7.94 (dd, $J = 8.0, 1.4 \text{ Hz}$, 1H), 6.93 (m, 3H), 4.29 (q, $J = 7.1 \text{ Hz}$, 2H), 1.30 (t, $J = 7.1 \text{ Hz}$, 3H).

¹³C-NMR (75 MHz, DMSO) δ (ppm): 160.97 (s, -COO-), 154.85 (s, -CONH-), 148.02 (s, Ph), 126.08 (s, Ph), 125.17 (s, Ph), 121.35 (s, Ph), 119.65 (s, Ph), 115.29 (s, Ph), 63.09 (s, -CH₂-), 14.29 (s, -CH₃).

FTIR (cm⁻¹): 3361 (m), 3241 (m), 1723 (m), 1682 (s), 1595 (s), 1540 (s), 1507 (m), 1462 (s), 1397 (s), 1369 (m), 1347 (m), 1326 (m), 1266 (s), 1227 (m), 1188 (m), 1103 (m), 1022 (m), 947 (m), 877 (s), 834 (s), 743 (m), 703 (m), 652 (m), 571 (m), 453 (m), 350 (s).

Elemental analysis (%): calc. for C₁₀H₁₁NO₄. C, 57.41; H, 5.30; N, 6.70. Found: C, 57.12; H, 5.26; N, 6.71.

1.2. H_{2.5}Na_{0.5}-ohpma·0.5(H₂O) — N-(2-hydroxyphenyl)oxamic acid hydrate, mixed sodium salt

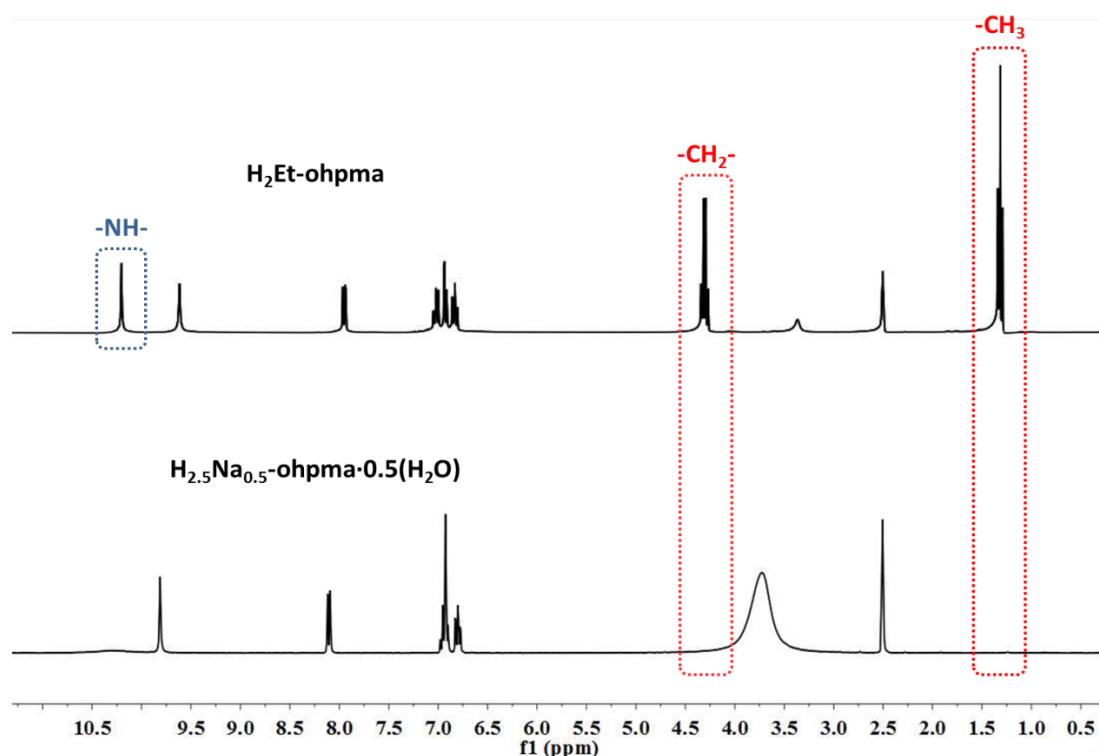
To 6.25 g of H₂Et-ohpma ($M = 209.2 \text{ gmol}^{-1}$; 29.88 mmol) suspended in 400 mL of water were slowly added 45.1 mL of 2M NaOH (3eq.). The solution was stirred for 30 min and filtered on paper. Under stirring, 22.5 mL of 4M HCl (3eq.) were added dropwise to the filtrate and stirring was maintained for 1 hr in an ice bath. The precipitate that formed was collected on a sintered glass filter. Further washing was done with cold 96% ethanol and the resulting white solid was dried with ether and then in air. (5.66 g, Yield: 94.17%, $M=201.14 \text{ gmol}^{-1}$).

$^1\text{H-NMR}$ (400 MHz, DMSO) δ (ppm): 10.36 (s, 1H), 9.81 (s, 1H), 8.11 (m, 1H), 6.87 (m, 3H).

$^{13}\text{C-NMR}$ (101 MHz, DMSO) δ (ppm): 162.18 (s, -COO-), 158.86 (s, -CONH-), 146.72 (s, Ph), 125.61 (s, Ph), 124.48 (s, Ph), 119.32 (s, Ph), 119.04 (s, Ph), 114.88 (s, Ph).

FTIR (cm^{-1}): 3488 (w), 3381 (w), 3076 (s), 1771 (m), 1676 (s), 1612 (m), 1594 (w), 1540 (s), 1469 (s), 1357 (m), 1278 (m), 1192 (w), 1103 (w), 930 (w), 805 (m), 749 (s), 692 (m), 599 (m), 504 (s), 452 (m), 317 (m).

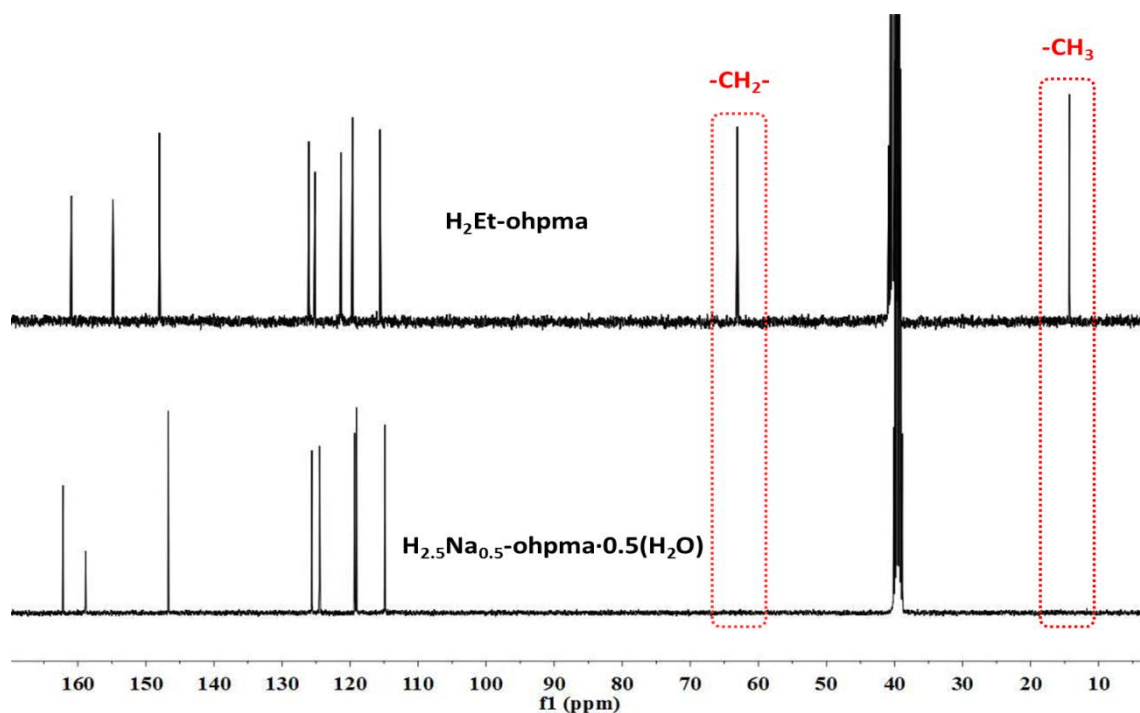
Elemental analysis (%): calc. for $\text{C}_8\text{H}_{7.5}\text{NNa}_{0.5}\text{O}_{4.5}$. C, 47.77; H, 3.76; N, 6.96. Found: C, 47.94; H, 3.68; N, 6.95.



$^1\text{H-NMR}$ spectrum in DMSO- d_6 for $\text{H}_2\text{Et-ohpma}$ and $\text{H}_{2.5}\text{Na}_{0.5}\text{-ohpma}\cdot 0.5(\text{H}_2\text{O})$

$\text{H}_2\text{Et-ohpma}$ experimental $^1\text{H-NMR}$ (300 MHz, DMSO) δ (ppm): 10.19 (s, 1.00H), 9.60 (s, 1.07H), 7.94 (dd, $J = 8.0$ Hz, 1.00H), 6.93 (m, 3.47H), 4.29 (q, $J = 7.1$ Hz, 2.24H), 1.30 (t, $J = 7.1$ Hz, 3.36H).

$\text{H}_{2.5}\text{Na}_{0.5}\text{-ohpma}\cdot 0.5(\text{H}_2\text{O})$ experimental $^1\text{H-NMR}$ (400 MHz, DMSO) δ (ppm): 10.36 (s, 0.67H), 9.81 (s, 1.07H), 8.11 (m, 1.00H), 6.87 (m, 3.06H).



^{13}C -NMR spectrum in DMSO- d_6 for $\text{H}_2\text{Et-ohpma}$ and $\text{H}_{2.5}\text{Na}_{0.5}\text{-ohpma}\cdot 0.5(\text{H}_2\text{O})$

1.3. $\text{H}_2\text{Et-ohpma}$ — Ethyl N-(4-hydroxyphenyl)oxamate

To 5.0 g of 4-aminophenol ($M=109.13 \text{ gmol}^{-1}$, 45.8 mmol) in 200 mL of THF were added dropwise 5.2 mL of ethyloxalyl chloride (98%; 1eq.) under strong stirring. The mixture was refluxed for 90 min. The resulting dark yellow solution was left to cool down and filtered on paper. Removal of the solvent under reduced pressure yielded a white powder. The powder was washed with copious amount of water under stirring for 30 min and then collected on a sintered glass filter. Further washing was done with cold 96% ethanol and the solid was dried with ether and then in air. The final product was collected as a white powder (8.69 g, Yield: 90.72 %, $M=209.2 \text{ gmol}^{-1}$).

^1H -NMR (300 MHz, DMSO) δ (ppm): 10.54 (s, 1H), 9.37 (s, 1H), 7.52 (d, $J = 8.0 \text{ Hz}$, 2H), 6.74 (d, $J = 8.0 \text{ Hz}$, 2H), 4.29 (q, $J = 7.1 \text{ Hz}$, 2H), 1.31 (t, $J = 7.1 \text{ Hz}$, 3H).

^{13}C -NMR (75 MHz, DMSO) δ (ppm): 161.43 (s, -COO-), 155.45 (s, -CONH-), 154.92 (s, Ph), 129.48 (s, Ph), 122.61 (s, Ph), 115.58 (s, Ph), 62.67 (s, -CH₂-), 14.33 (s, -CH₃).

FTIR (cm^{-1}): 3361 (m), 3241 (m), 1723 (m), 1682 (s), 1595 (s), 1540 (s), 1507 (m), 1462 (s), 1397 (s), 1369 (m), 1347 (m), 1326 (m), 1266 (s), 1227 (m), 1188 (m), 1103 (m), 1022 (m), 947 (m), 877 (s), 834 (s), 743 (m), 703 (m), 652 (m), 571 (m), 453 (m), 350 (s).

Elemental analysis (%): calc. for $C_{10}H_{11}NO_4$. C, 57.41; H, 5.30; N, 6.70. Found: C, 57.54; H, 5.26; N, 6.63.

1.4. H_2Na -phpma $\cdot 0.5(H_2O)$ — N-(4-hydroxyphenyl)oxamic acid hydrate, mixed sodium salt

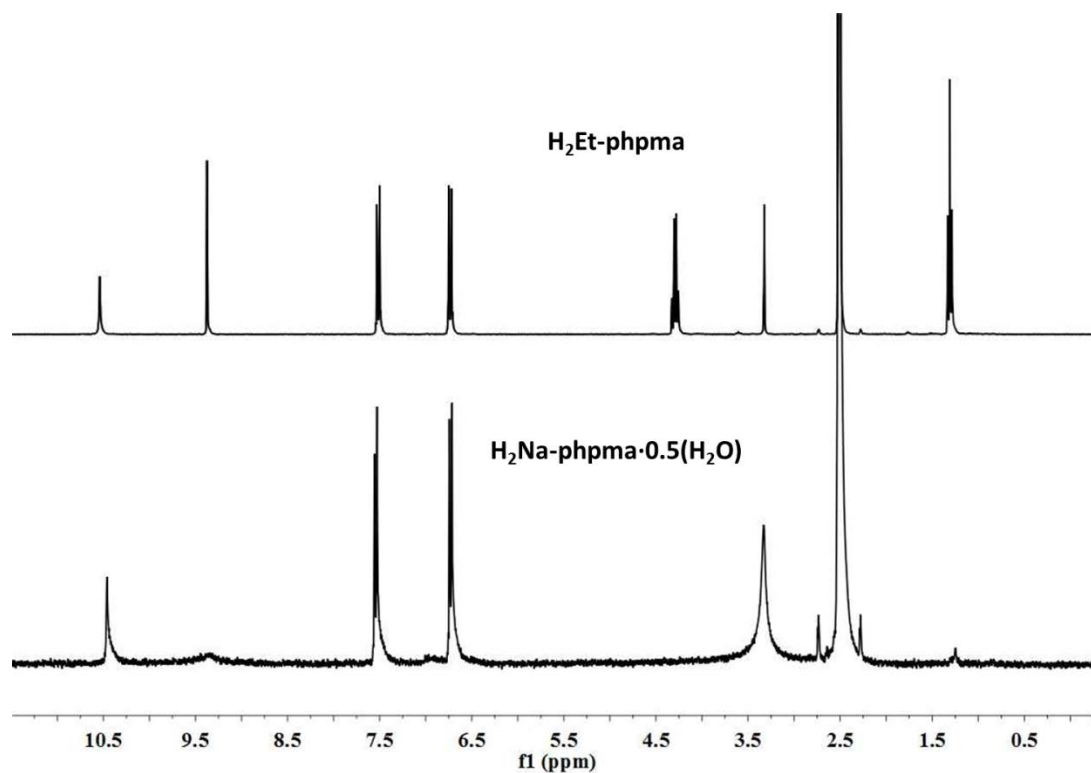
To 6.5 g of H_2Et -phpma ($M = 209.2 \text{ gmol}^{-1}$; 31.07 mmol) suspended in 400 mL of water were slowly added 46.9 mL of 2M NaOH (3eq.). The solution was stirred for 30 min and filtered on paper. Under stirring, 24.4 mL of 4M HCl (3eq.) were added dropwise to the filtrate and the stirring was maintained for 1 hr in an ice bath. The precipitate that formed was collected on a sintered glass filter. Further washing was done with cold 96% ethanol and the white solid was dried with ether and then dried at 70 °C in an oven overnight (6.01 g, Yield: 91.2 %, $M=212.13 \text{ gmol}^{-1}$).

1H -NMR (300 MHz, DMSO) δ (ppm): 10.47 (s, 1H), 9.37 (s, 1H), 7.54 (d, $J = 8.0 \text{ Hz}$, 2H), 6.73 (d, $J = 8.0 \text{ Hz}$, 2H).

^{13}C -NMR (75 MHz, DMSO) δ (ppm): 162.84 (s, -COO-), 156.92 (s, -CONH-), 154.86 (s, Ph), 129.66 (s, Ph), 122.37 (s, Ph), 115.57 (s, Ph).

FTIR (cm^{-1}): 3301 (s), 1760 (s), 1676 (s), 1554 (m), 1515 (m), 1458 (w), 1388 (s), 1307 (s), 1238 (m), 1174 (m), 1111 (w), 931 (m), 836 (s), 792 (w), 746 (m), 713 (w), 684 (m), 619 (w), 559 (w), 493 (s).

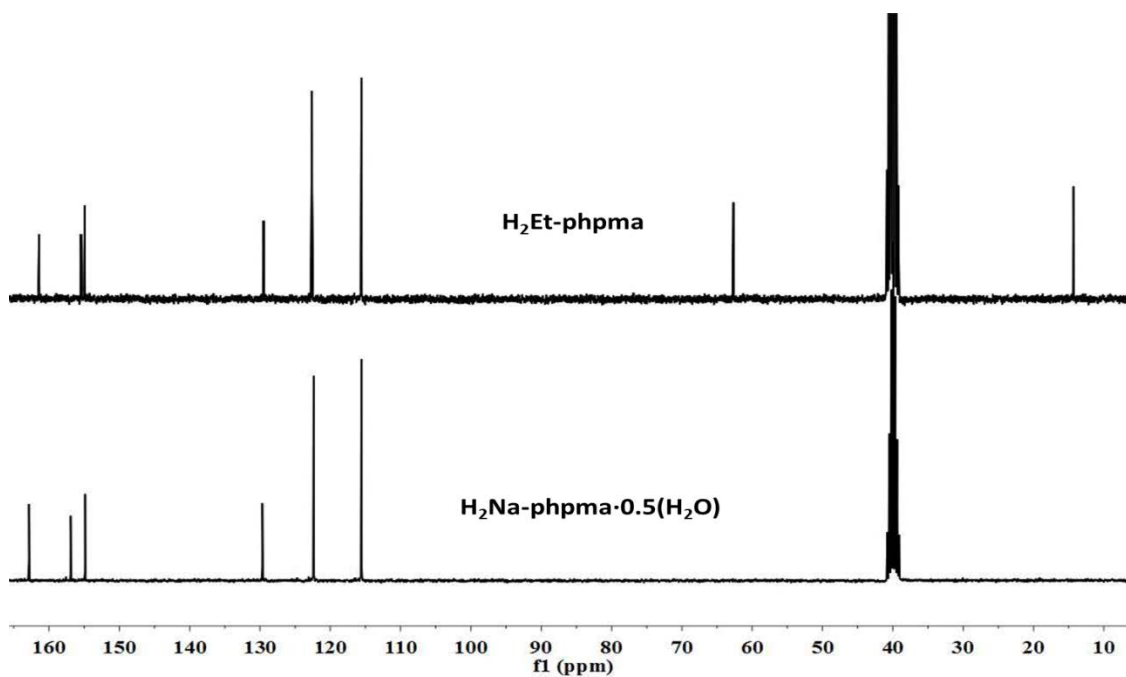
Elemental analysis (%): calc. for $C_8H_7NNaO_{4.5}$. C, 45.29; H, 3.32; N, 6.60. Found: C, 44.48; H, 3.27; N, 6.45.



$^1\text{H-NMR}$ spectrum in DMSO- d_6 for $\text{H}_2\text{Et-phpma}$ and $\text{H}_2\text{Na-phpma}\cdot 0.5(\text{H}_2\text{O})$

$\text{H}_2\text{Et-phpma}$ experimental $^1\text{H-NMR}$ (300 MHz, DMSO) δ (ppm): 10.54 (s, 0.98H), 9.37 (s, 1.00H), 7.52 (d, $J = 8.0$ Hz, 1.99H), 6.74 (d, $J = 8.0$ Hz, 2.04H), 4.29 (q, $J = 7.1$ Hz, 2.00H), 1.31 (t, $J = 7.1$ Hz, 3.03H).

$\text{H}_2\text{Na-phpma}\cdot 0.5(\text{H}_2\text{O})$ experimental $^1\text{H-NMR}$ (300 MHz, DMSO) δ (ppm): 10.47 (s, 1.00H), 9.37 (s, 0.67H), 7.54 (d, $J = 9.0$ Hz, 1.98H), 6.73 (d, $J = 9.0$ Hz, 2.39H).



$^{13}\text{C-NMR}$ spectrum in DMSO- d_6 for $\text{H}_2\text{Et-phpma}$ and $\text{H}_2\text{Na-phpma}\cdot 0.5(\text{H}_2\text{O})$

1.5. H₂Et-paba — 4-(ethyloxamate)benzoic acid

To 6.0 g of 4-aminobenzoic acid ($M=137.14 \text{ gmol}^{-1}$, 43.75 mmol) in 250 mL of THF were added dropwise 5.5 mL of ethyloxalyl chloride (98%; 1.1eq.) under strong stirring. The mixture was refluxed for 90 min and filtered on paper while hot. The removal of the solvent under reduced pressure yielded a white powder. The powder was washed with 200 mL of H₂O under stirring for 60 min and then collected on a sintered glass filter. Further washing was done with cold 96% ethanol and the solid was dried with ether and then in air. The final product was collected as a white powder (9.41 g, Yield: 90.7%, $M=237.2 \text{ gmol}^{-1}$).

¹H-NMR (400 MHz, DMSO) δ (ppm): 12.82 (s, 1H), 11.02 (s, 1H), 7.95 (d, 8.0 Hz, 2H), 7.88 (d, 8.0 Hz, 2H), 4.31 (q, $J = 6.9 \text{ Hz}$, 2H), 1.31 (t, $J = 7.0 \text{ Hz}$, 3H).

¹³C-NMR (101 MHz, DMSO) δ (ppm): 166.39 (s, -COOH), 159.95 (s, -CO-), 155.44 (s, -CONH-), 141.08 (s, Ph), 129.84 (s, Ph), 126.24 (s, Ph), 119.46 (s, Ph), 62.13 (s, -CH₂-), 13.41 (s, -CH₃).

FTIR (cm⁻¹): 3332 (m), 2536 (w), 1706 (s), 1676 (s), 1593 (m), 1539 (m), 1419 (m), 1371 (m), 1286 (s), 1169 (s), 1112 (m), 1012 (m), 938 (m), 874 (m), 847 (m), 811 (w), 775 (m), 764 (m), 710 (s), 640 (w), 546 (m), 490 (s), 325 (m).

Elemental analysis (%): calc. for C₁₁H₁₁NO₅. C, 55.69; H, 4.67; N, 5.90. Found: C, 55.74; H, 4.71; N, 5.95.

1.6. H₂Li-paba·H₂O — 4-(oxamate)benzoic acid monohydrate, mixed lithium salt

To 1.0 g of H₂Et-paba ($M = 237.2 \text{ gmol}^{-1}$; 4.2 mmol) suspended in 150 mL of water were slowly added 4.2 mL of 2M LiOH (2eq.). The solution was stirred for 30 min and filtered on paper. Under stirring, a further 60 mL of water were added, followed by the slow addition of 3.16 mL of 4M HCl (3eq.). A white precipitates formed rapidly. The stirring was maintained for 30 min and the solid was collected on a sintered glass filter, dried in air for several hours and in an oven at 80 °C overnight. (0.87 g, Yield: 88.7%, $M=233.1 \text{ gmol}^{-1}$).

¹H-NMR (300 MHz, DMSO) δ (ppm): 10.92 (s, 1H), 7.91 (m, , 4H).

¹³C-NMR (101 MHz, DMSO) δ (ppm): 167.28 (s, -COO-), 162.33 (s, oxamatic -COO-), 157.90 (s, -CONH-), 142.17 (s, Ph), 130.68 (s, Ph), 126.88 (s, Ph), 120.15 (s, Ph).

FTIR (cm⁻¹): 3454 (m), 3312 (s), 2610 (s), 1723 (w), 1670 (s), 1584 (m), 1545 (m), 1430 (m), 1311

(w), 1235 (s), 1183 (s), 1117 (m), 938 (m), 851 (m), 768 (s), 725 (s), 651 (w), 531 (m), 476 (m), 391 (m), 352 (m), 263 (m).

Elemental analysis (%): calc. for $C_9H_8LiNO_6$. C, 46.37; H, 3.46; N, 6.01. Found: C, 46.94; H, 3.94; N, 6.12.

1.7. H(TMA)₂-paba·1.5H₂O — 4-(oxamate)benzoic acid hydrate, mixed tetramethylammonium salt

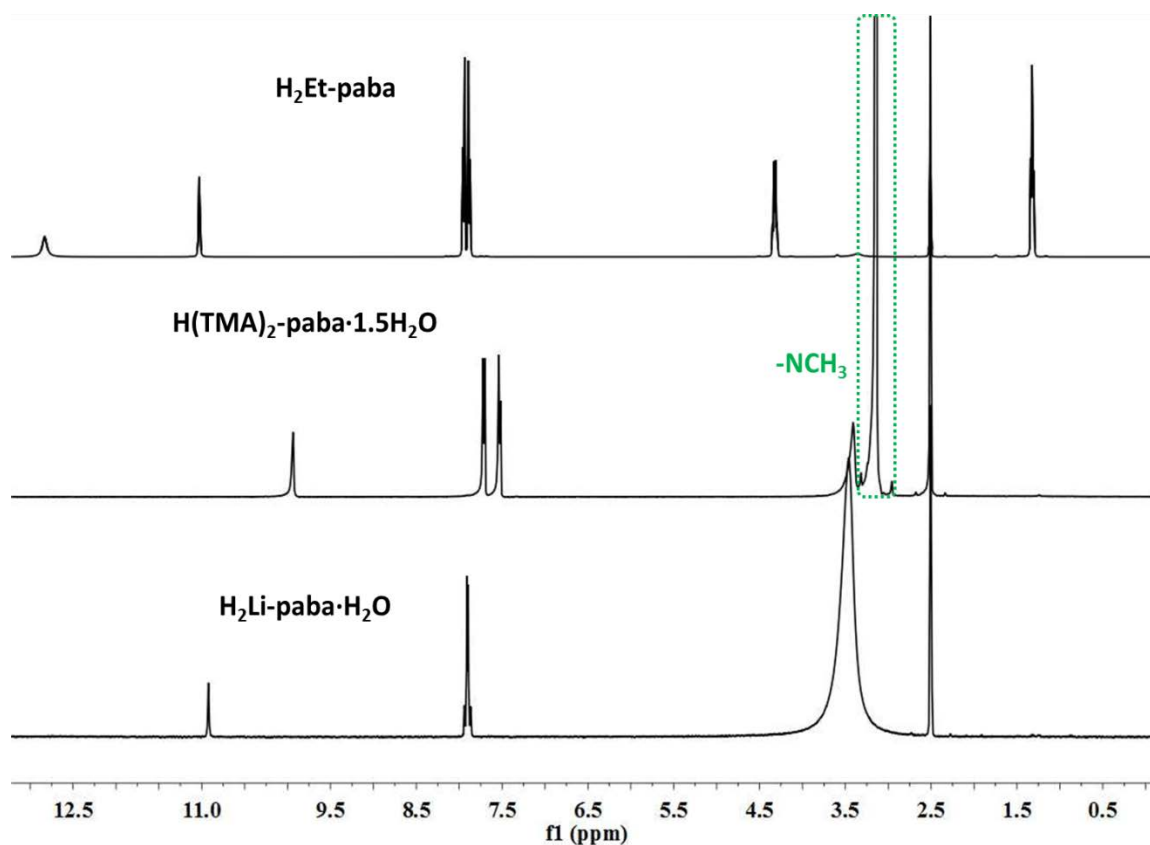
To 3.0 g of H₂Et-paba ($M=237.2 \text{ gmol}^{-1}$; 12.6 mmol) suspended in 300 mL of MeOH were added slowly 10.5 mL of TMAOH (2eq., 25% w/w in MeOH). The solution was stirred for 30 min and filtered on paper. Removal of the solvent under reduced pressure yielded the final product as a white solid, dried and kept in a desiccator. (3.14 g, Yield: 62.4%, $M=382.45 \text{ gmol}^{-1}$).

¹H-NMR (400 MHz, DMSO) δ (ppm): 9.92 (s, 1H), 7.70 (d, $J = 8.3 \text{ Hz}$, 2H), 7.52 (d, $J = 8.3 \text{ Hz}$, 2H), 3.13 (s, 24H).

¹³C-NMR (75 MHz, DMSO) δ (ppm): 168.60(s, -COO-), 165.00 (s, oxamatic -COO-), 163.06 (s, -CONH-), 139.37 (s, Ph), 137.18 (s, Ph), 129.81 (s, Ph), 117.56 (s, Ph), 54.79 – 54.69 (t, -NCH₃).

FTIR (cm^{-1}): 3301 (w), 3027(m), 1699 (w), 1653(w), 1598(s), 1513(m), 1485 (s), 1402 (w), 1355 (s), 1302 (s), 1244 (m), 1174 (w), 1151 (w), 1104 (w), 1018 (w), 951 (m), 877 (m), 789 (m), 758 (sd), 702 (w), 480 (m), 458 (m), 428 (m), 364 (s), 309 (m), 229 (w).

Elemental analysis (%): calc. for $C_{17}H_{32}N_3O_{6.5}$. C, 53.38; H, 8.43; N, 10.98. Found: C, 52.98; H, 8.92; N, 11.49.

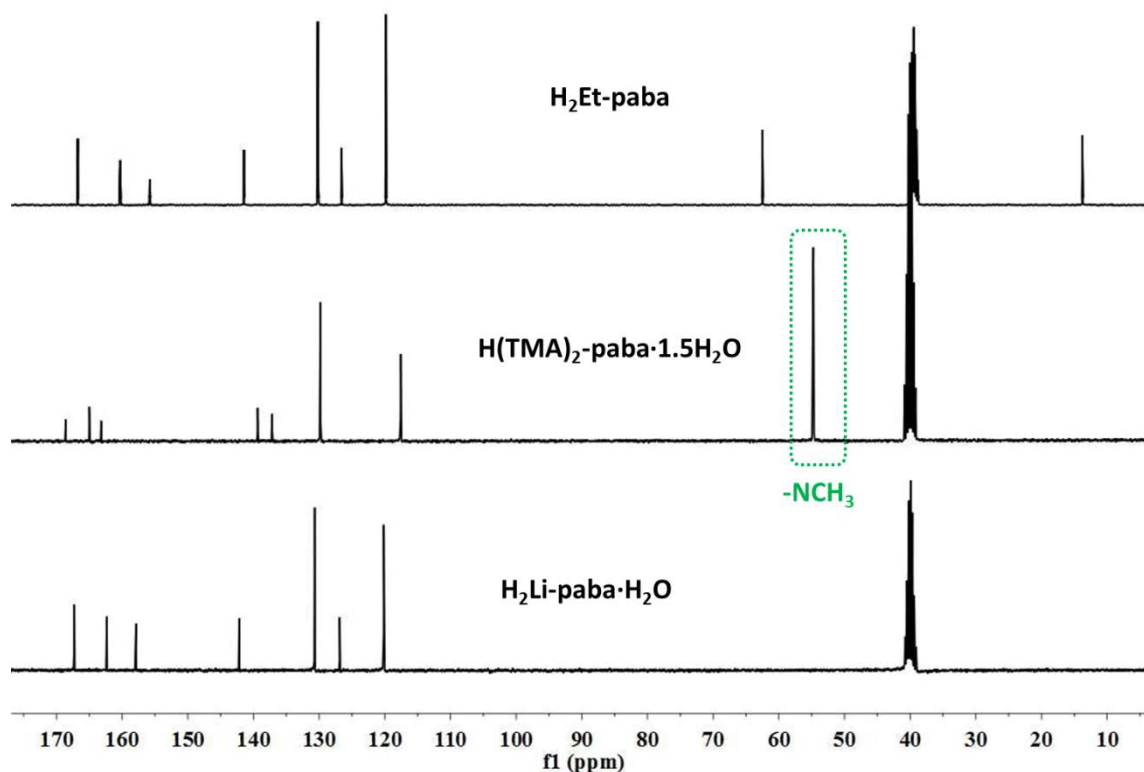


$^1\text{H-NMR}$ spectrum in DMSO- d_6 for $\text{H}_2\text{Et-paba}$, $\text{H}_2\text{Li-paba}\cdot \text{H}_2\text{O}$ and $\text{H(TMA)}_2\text{-paba}\cdot 1.5\text{H}_2\text{O}$

$\text{H}_2\text{Et-paba}$ experimental $^1\text{H-NMR}$ (400 MHz, DMSO) δ (ppm): 12.82 (s, 0.91H), 11.02 (s, 1H), 7.95 (d, 8.0 Hz, 2H), 7.88 (d, 8.0 Hz, 2H), 4.31 (q, $J = 6.9$ Hz, 2.02H), 1.31 (t, $J = 7.0$ Hz, 2.99H).

$\text{H}_2\text{Li-paba}\cdot \text{H}_2\text{O}$ experimental $^1\text{H-NMR}$ (300 MHz, DMSO) δ (ppm): 10.92 (s, 1.00H), 7.91 (m, , 4.17H)

$\text{H(TMA)}_2\text{-paba}\cdot 1.5\text{H}_2\text{O}$ experimental $^1\text{H-NMR}$ (400 MHz, DMSO) δ (ppm): 9.92 (s, 1H), 7.70 (d, $J = 8.3$ Hz, 2.09H), 7.52 (d, $J = 8.3$ Hz, 2H), 3.13 (s, 24H).



^{13}C -NMR spectrum in DMSO- d_6 for $\text{H}_2\text{Et-paba}$, $\text{H}_2\text{Li-paba}\cdot \text{H}_2\text{O}$ and $\text{H(TMA)}_2\text{-paba}\cdot 1.5\text{H}_2\text{O}$

1.8. $\text{H}_2\text{Et-oaba}$ — 2-(ethyloxamate)benzoic acid

To 6.0 g of anthranilic acid ($M=137.14 \text{ gmol}^{-1}$, 43.75 mmol) in 250 mL of THF were added dropwise 5.5 mL of ethyloxalyl chloride (98%; 1eq.) under strong stirring. The mixture was refluxed for 120 min and filtered on paper while hot (some white residue is filtered off). Removal of the solvent under reduced pressure yielded a white powder. The powder was washed with 700 mL of water under stirring for 30 min and then collected on a sintered glass filter. Further washing was done with cold 50 % ethanol and the solid was dried in air. The final product was collected as a white powder (9.15 g, Yield: 88.17 %, $M=237.2 \text{ gmol}^{-1}$).

^1H -NMR (400 MHz, DMSO) δ (ppm): 12.56 (s, 1H), 8.57 (dd, $J = 8.4, 0.8 \text{ Hz}$, 1H), 8.02 (dd, $J = 8.4, 0.8 \text{ Hz}$, 1H), 7.67 (td, $J = 8.6, 1.6 \text{ Hz}$, 1H), 7.26 (td, $J = 8.6, 1.6 \text{ Hz}$, 1H), 4.29 (q, $J = 7.1 \text{ Hz}$, 2H), 1.30 (t, $J = 7.1 \text{ Hz}$, 3H).

^{13}C -NMR (75 MHz, DMSO) δ (ppm): 169.20 (s, $-\text{COO}-$), 159.76 (s, $-\text{COO}-$), 154.32 (s, $-\text{CONH}-$), 139.27 (s, $-\text{PhNH}-$), 134.34 (s, Ph), 131.37 (s, Ph), 123.98 (s, Ph), 119.56 (s, Ph), 116.90 (s, PhCOOH), 62.82 (s, $-\text{CH}_2-$), 13.74 (s, $-\text{CH}_3$).

FTIR (cm⁻¹): 3501 (m), 3416 (m), 2982 (w), 2481 (w), 1755 (s), 1689 (s), 1663 (s), 1589 (m), 1519 (s), 1466 (m), 1452 (w), 1428 (w), 1297 (m), 1248 (s), 1188 (s), 1092 (w), 999 (m), 929 (w), 858 (m), 822 (w), 789 (s), 762 (s), 698 (m), 660 (m), 602 (m), 510 (m), 356 (m), 320 (m), 275 (m).

Elemental analysis (%): calc. for C₁₁H₁₁NO₅. C, 55.70; H, 4.67; N, 5.90 Found: C, 55.46; H, 4.59; N, 5.96.

1.9. H_{2.5}Na_{0.5}-oaba·0.5(H₂O) — 2-(oxamate)benzoic acid hydrate, mixed sodium salt

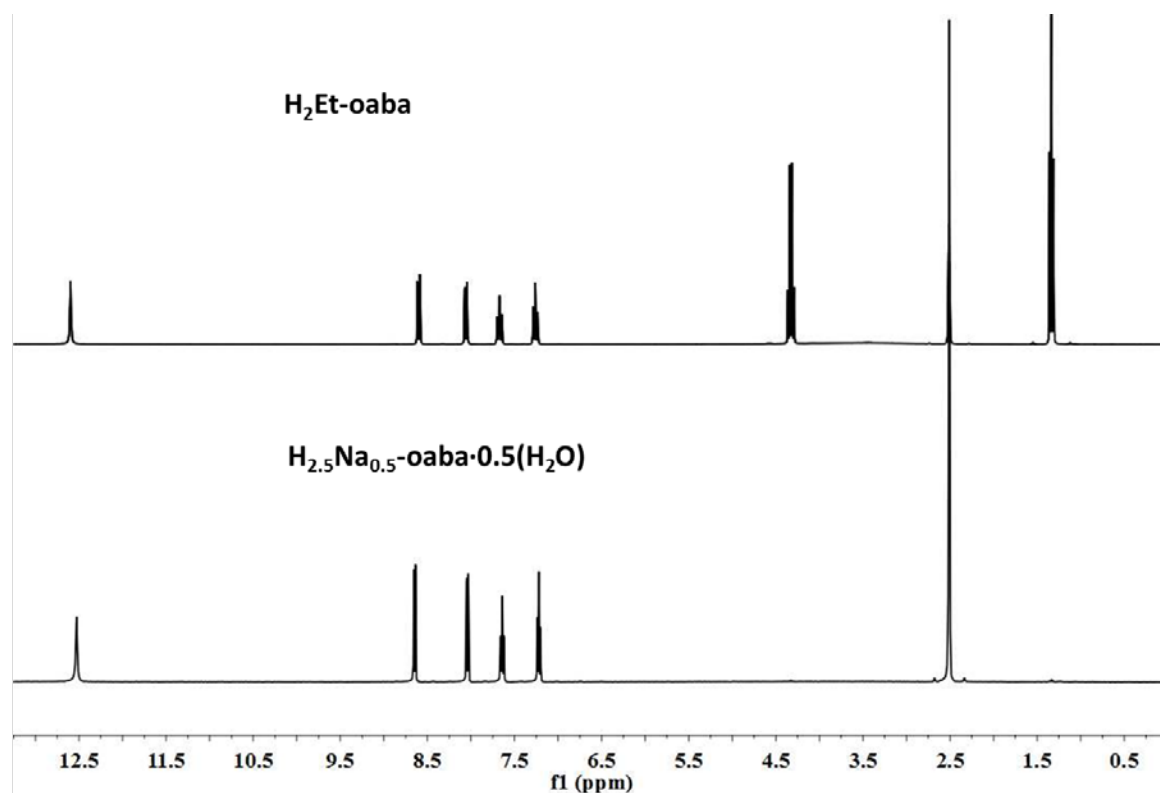
To 2.7 g of H₂Et-oaba (M = 237.2 gmol⁻¹; 11.38 mmol) suspended in 300 mL of water were slowly added 11.3 mL of 2M NaOH (2eq). The solution was stirred for 30 min and filtered on paper. Under stirring, 5.7 mL of 4M HCl (3eq.) were added dropwise and a precipitate formed gradually. The stirring was maintained for another 30 min and the solid was collected on a sintered glass filter, and dried in the oven at 70 °C overnight. (2.34 g, Yield: 89.75 %, M= 229.1 gmol⁻¹).

¹H-NMR (400 MHz, DMSO) δ (ppm): 12.53 (s, 1H), 8.65 (dd, *J* = 8.5, 0.9 Hz, 1H), 8.03 (d, *J* = 8.5, 0.9 Hz, 1H), 7.64 (t, *J* = 7.7 Hz, 1H), 7.22 (t, *J* = 7.7 Hz, 1H).

¹³C-NMR (101 MHz, DMSO) δ (ppm): 169.41 (s, -COOH), 161.96 (s, oxamaic -COOH), 157.41 (s, -CONH-), 139.96 (s, -PhNH-), 134.64 (s, Ph), 131.84 (s, Ph), 124.16 (s, Ph), 119.98 (s, Ph), 117.55 (s, -PhCOOH).

FTIR (cm⁻¹): 3213 (w), 1689 (s), 1601 (m), 1586 (m), 1531 (m), 1452 (w), 1375 (m), 1290 (m), 1213 (s), 1190 (s), 1140 (m), 1078 (w), 903 (w), 837 (w), 780 (s), 751 (s), 651 (m), 557 (m), 484 (m), 379 (s), 276 (m).

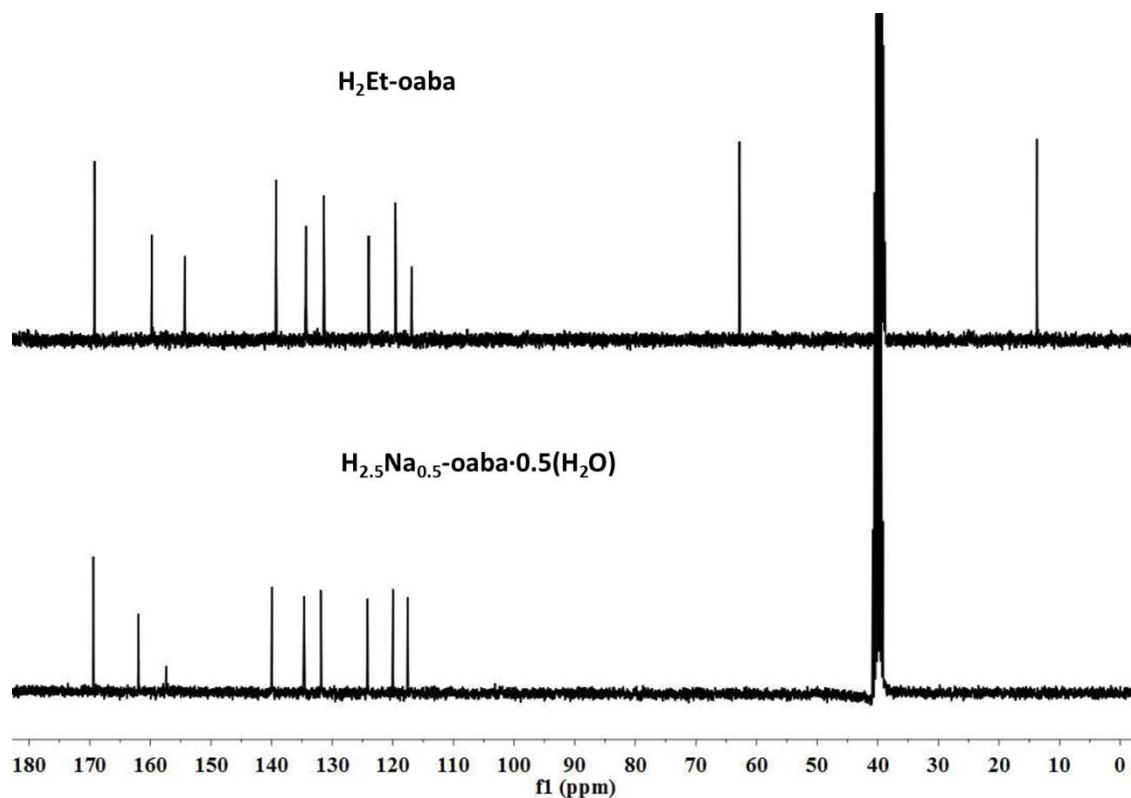
Elemental analysis (%): calc. for C₉H_{7.5}NO_{5.5}Na_{0.5}. C, 47.17; H, 3.30; N, 6.11 Found: C, 47.95; H, 3.29; N, 6.15.



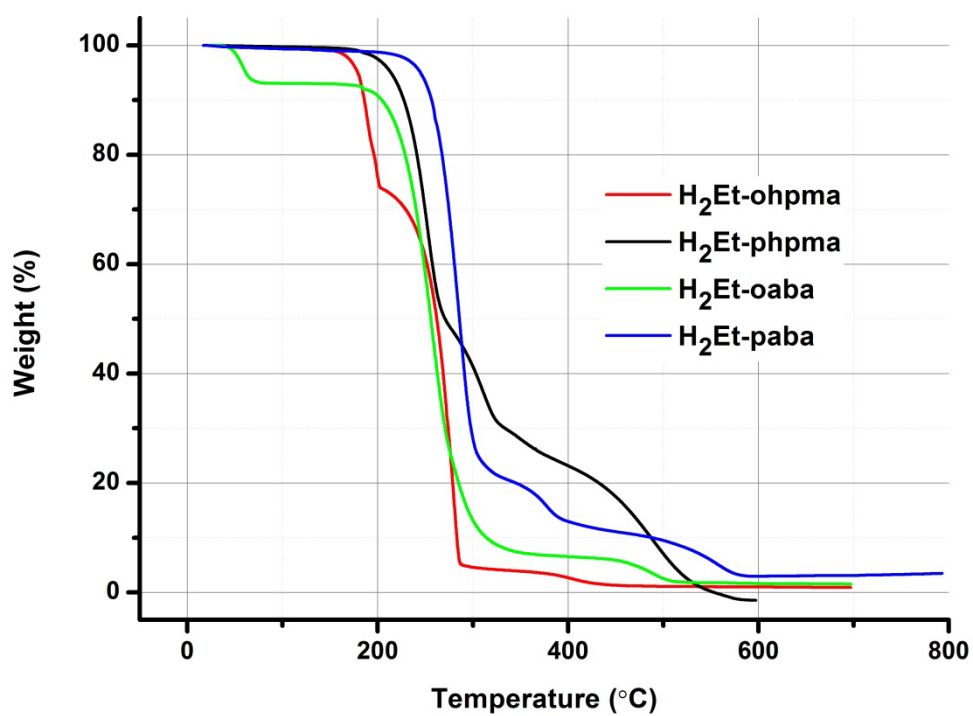
¹H-NMR spectrum in DMSO-d₆ for H₂Et-oaba and H_{2.5}Na_{0.5}-oaba·0.5(H₂O)

H₂Et-oaba experimental ¹H-NMR (300 MHz, DMSO) δ (ppm): 12.56 (s, 1.03H), 8.57 (dd, *J* = 8.4, 0.8 Hz, 1.00H), 8.02 (dd, *J* = 8.4, 0.8 Hz, 1.00H), 7.67 (td, *J* = 8.6, 1.6 Hz, 0.96H), 7.26 (td, *J* = 8.6, 1.6 Hz, 1.00H), 4.29 (q, *J* = 7.1 Hz, 2.15H), 1.30 (t, *J* = 7.1 Hz, 3.07H).

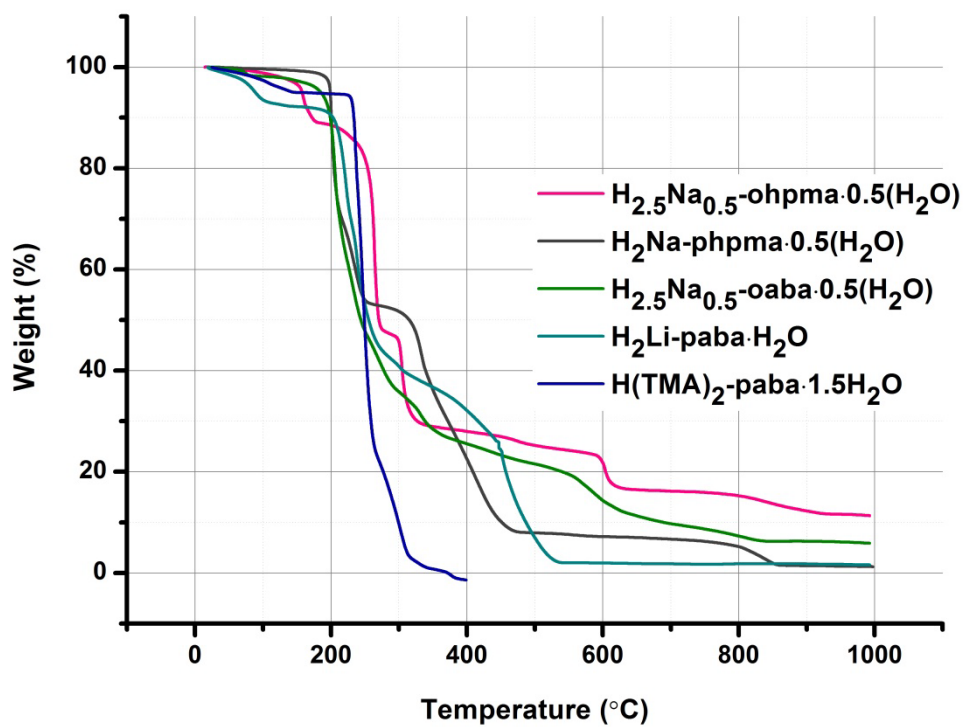
H_{2.5}Na_{0.5}-oaba·0.5(H₂O) experimental ¹H-NMR (300 MHz, DMSO) δ (ppm): 12.53 (s, 1.00H), 8.65 (dd, *J* = 8.5, 0.9 Hz, 0.97H), 8.03 (dd, *J* = 8.5, 0.9 Hz, 0.95H), 7.64 (t, *J* = 7.7 Hz, 1H), 7.22 (t, *J* = 7.7 Hz, 1H).



^{13}C -NMR spectrum in DMSO- d_6 for $\text{H}_2\text{Et-oaba}$ and $\text{H}_{2.5}\text{Na}_{0.5}\text{-oaba}\cdot 0.5(\text{H}_2\text{O})$



Thermogravimetric analysis (TGA) of ester proligands



Thermogravimetric analysis (TGA) of Li/Na/TMA salt of acidic ligand

2. Chapter 2 Bench reactivity screening, 0D complexes and 1D chain compound structural characterization and magnetic properties.

2.1 Synthesis of $\text{Li}_2[\text{Cu}(\text{ohpma})(\text{OH})]\cdot 5\text{H}_2\text{O}$

A suspension of $\text{H}_2\text{Et-ohpma}$ (200 mg, 0.95 mmol) in water (15 mL) was treated with 1.43 mL of 2 M LiOH (2.86 mmol), stirred at room temperature until complete dissolution of the ligand, and filtered. An aqueous solution of $\text{Cu}(\text{NO}_3)_2\cdot 3\text{H}_2\text{O}$ (115 mg, 0.47 mmol, 5 mL) was then added dropwise to the oxamate solution resulting in a deep green solution of the copper(II) complex that was stirred for 10 min at room temperature, and filtered. Green crystals of $\text{Li}_2[\text{Cu}(\text{ohpma})(\text{OH})]\cdot 5\text{H}_2\text{O}$ suitable for single crystal X-Ray diffraction were obtained after several days by slow diffusion of acetone.

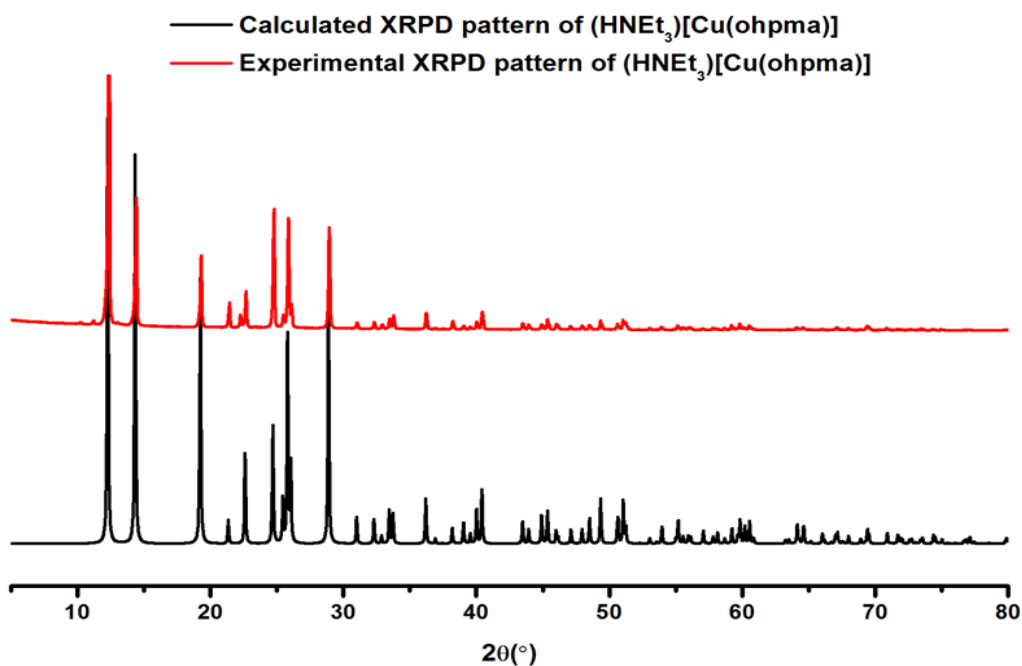
2.2 Synthesis of $\text{Li}_4[\text{Cu}(\text{paba})_2(\text{H}_2\text{O})]\cdot 9\text{H}_2\text{O}$

A suspension of $\text{H}_2\text{Et-paba}$ (200 mg, 0.84 mmol) in water (10 mL) was treated with 1.26 mL of 2 M LiOH (2.52 mmol), stirred at room temperature until complete dissolution of the ligand, and filtered. An aqueous solution of $\text{Cu}(\text{NO}_3)_2\cdot 3\text{H}_2\text{O}$ (102 mg, 0.42 mmol, 4 mL) was then added dropwise to the oxamate solution resulting in a deep green solution of the copper(II) complex that was stirred for 10 min at room temperature, and filtered. Green crystals of $\text{Li}_4[\text{Cu}(\text{paba})_2(\text{H}_2\text{O})]\cdot 9\text{H}_2\text{O}$ suitable for single crystal X-Ray diffraction were obtained after several days by slow diffusion of acetone.

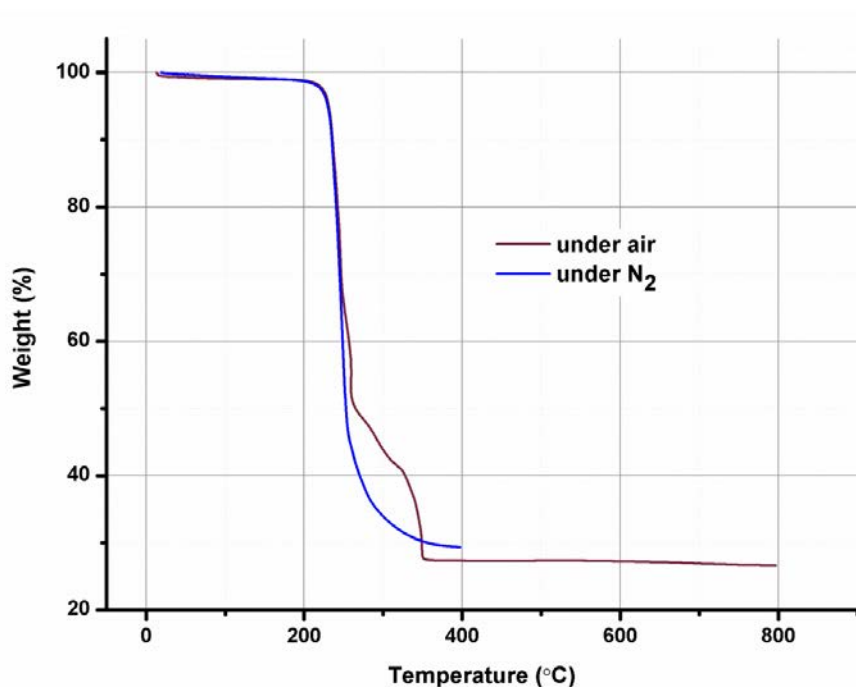
2.3 Synthesis of $(\text{HNEt}_3)[\text{Cu}(\text{ohpma})]$

To a 15 mL acetonitrile solution of $\text{H}_{2.5}\text{Na}_{0.5}\text{-ohpma}\cdot 0.5(\text{H}_2\text{O})$ (100 mg, 0.5 mmol) was added 0.24 mL of NEt_3 (85%, 1.5 mmol), and the solution was stirred for 15 min. An aqueous solution of $\text{CuCl}_2\cdot 2\text{H}_2\text{O}$ (84 mg, 0.5 mmol, 5 mL) was then added dropwise. The resulting green solution was kept under stirring for 2 h and then filtered. Green block crystals of $(\text{HNEt}_3)[\text{Cu}(\text{ohpma})]$ were obtained after several days by slow evaporation of the solution and washed with acetonitrile. Yield: 132 mg, 76.8% (based on copper, $M=343.8 \text{ g mol}^{-1}$). Elemental analysis (%): calc. for

$C_{14}H_{20}CuN_2O_4$: C, 48.90; H, 5.86; N, 8.15. Found: C, 48.37; H, 5.75; N, 7.90. Selected IR data (cm^{-1}): 2992(w), 1647(m), 1605(s), 1576(m), 1465(s), 1405(m), 1326(m), 1305(m), 1290(m), 1265(s), 1240(s), 1182(m), 1148(m), 1103(w), 1026(w), 878(s), 780(s), 594(m), 557(m), 493(w), 456(w), 336(m).



Experimental and calculated PXRD patterns for $\{(HNEt_3)[Cu(ohpma)]\}$



Thermogravimetric analysis (TGA) of $(HNEt_3)[Cu(ohpma)]$

TGA shows that before the decomposition of $(\text{HNEt}_3)[\text{Cu}(\text{C}_8\text{H}_4\text{NO}_4)]$ at $220\text{ }^\circ\text{C}$, there is no co-crystallization solvent loss, and weight percentage at $800\text{ }^\circ\text{C}$ is in accordance with the theoretical value (23%) assuming the formation of CuO .

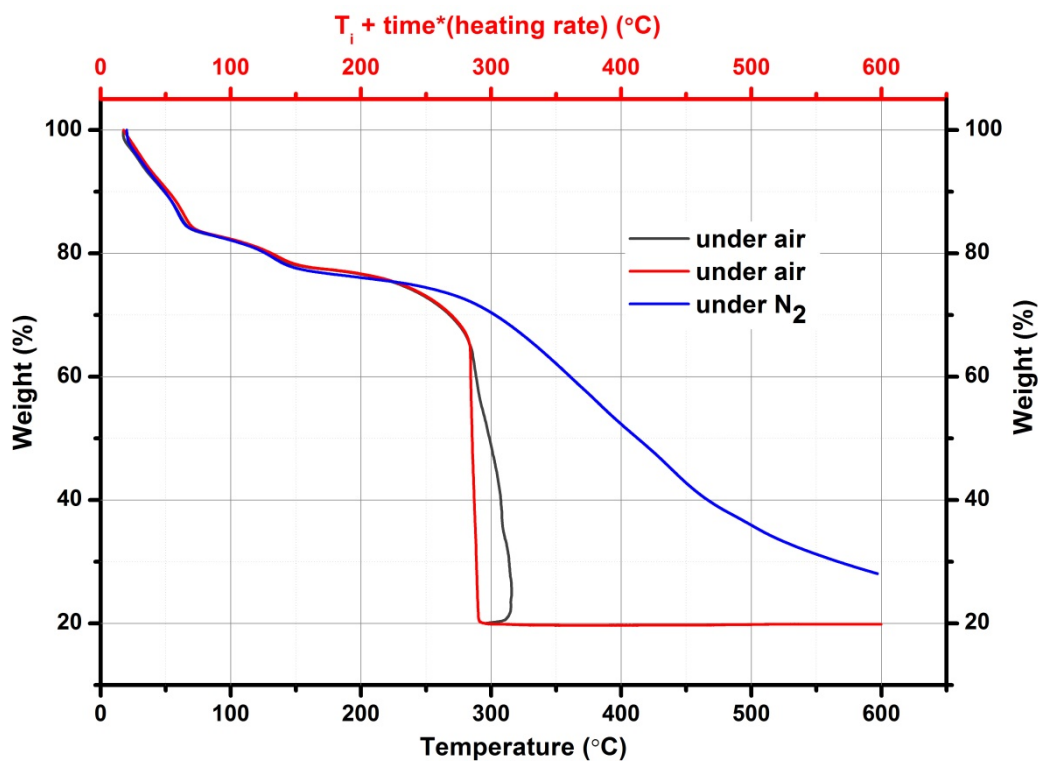
2.4 Synthesis of $[\text{Co}_2(\text{H}_2\text{O})(\text{O}_2\text{CCMe}_3)_4(\text{HO}_2\text{CCMe}_3)_4]$, $\{\text{Co}_2\text{Piv}\}$

$\{\text{Co}_2\text{Piv}\}$ was prepared according to the literature procedure¹.

Yield: 8.4 g, 52.64 % (based on cobalt ion; $M=948.9\text{ gmol}^{-1}$). Selected IR data (cm^{-1}): 2962(m), 1673(s), 1603(s), 1480(m), 1403(m), 1345(m), 1204(s), 872(s), 794(m), 597(m), 541(m), 418(m), 369(m), 317(w), 263(m).

2.5 Synthesis of $(\text{TMA})_3[\{\text{Co}^{\text{III}}(\text{ohpma})_2\text{Co}^{\text{II}}(\text{MeOH})_2\}_3]\cdot 10\text{H}_2\text{O}\cdot 5\text{MeOH}$

To a 15 mL MeOH solution of $\text{H}_{2.5}\text{Na}_{0.5}\text{-ohpma}\cdot 0.5(\text{H}_2\text{O})$ (100 mg, 0.5 mmol) was added 0.69 mL of TMAOH (25% w/w in MeOH, 1.5 mmol) and the resulting solution was stirred for 15 min. $\{\text{Co}_2\text{Piv}\}$ (474 mg, 0.5 mmol, $M=948.9\text{ gmol}^{-1}$, 1eq.) was then added directly into the solution. The solid $\{\text{Co}_2\text{Piv}\}$ dissolved immediately with the apparition of light precipitates that quickly disappeared; giving a red-brown solution. Stirring was maintained for 2 h and the solution was filtered and left to crystallize by slow evaporation at the room temperature. Dark brown block crystals of $(\text{TMA})_3[\{\text{Co}^{\text{III}}(\text{ohpma})_2\text{Co}^{\text{II}}(\text{MeOH})_2\}_3]\cdot 10\text{H}_2\text{O}\cdot 5\text{MeOH}$ were obtained overnight. Yield: 100 mg, 58% (based on ohpma; $M=2071.1\text{ gmol}^{-1}$). Elemental analysis (%): calc. for $\text{C}_{63}\text{H}_{100}\text{Co}_6\text{N}_{10}\text{O}_{45}$: C, 36.53; H, 4.87; N, 6.76. Found: C, 36.37; H, 4.81; N, 6.54. Selected IR data (cm^{-1}): 3185(sd), 2929(w), 1602(m), 1465(m), 1421 (w), 1338(m), 1301(w), 1273(s), 1241(m), 1151(w), 1105(w), 1025(w), 962(m), 950(w), 892(m), 844(s), 745(m), 645(w), 607(m), 451(w), 403(m), 329(m), 235(w).



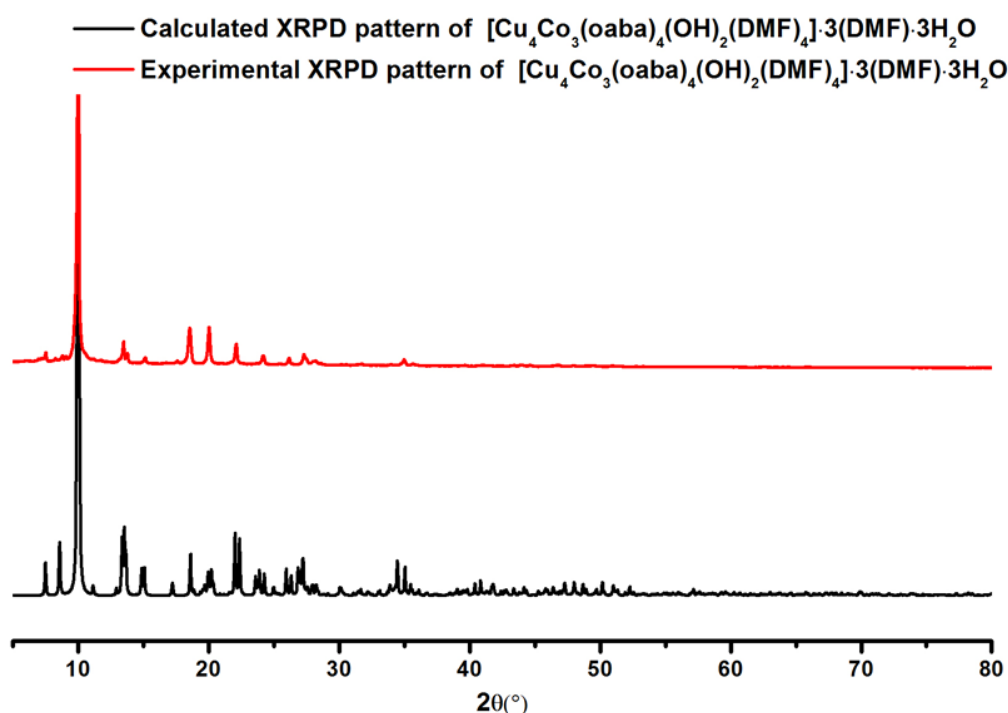
Thermogravimetric analysis of $(\text{TMA})_3[\{\text{Co}^{\text{III}}(\text{ohpma})_2\text{Co}^{\text{II}}(\text{MeOH})_2\}_3] \cdot 10\text{H}_2\text{O} \cdot 5\text{MeOH}$

TGA shows that before 60 °C, both MeOH (exp. 17% ca. 16%) and H₂O (exp. 7%, ca. 8.6%) are lost. Decomposition of $(\text{TMA})_3[\{\text{Co}^{\text{III}}(\text{ohpma})_2\text{Co}^{\text{II}}(\text{MeOH})_2\}_3] \cdot 10\text{H}_2\text{O} \cdot 5\text{MeOH}$ starts at 250 °C and the curve drops rapidly, weight percentage after 300 °C is stable around 20%, which is in accordance with formation of CoO or Co₂O₃ (cal 21% and 23%).

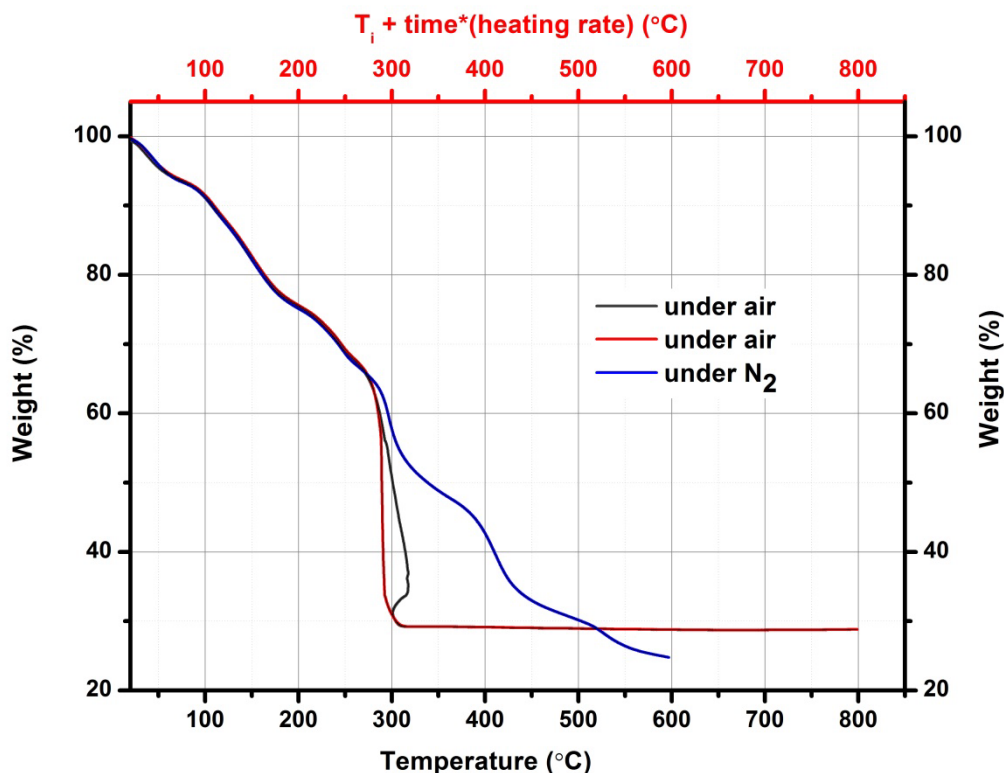
3. Chapter 3 Reactivity screening in solvothermal conditions and 1D chain compounds structural characterization and magnetic properties

3.1 Synthesis of $[\text{Cu}_4\text{Co}_3(\text{oaba})_4(\text{OH})_2(\text{DMF})_4]\cdot 3(\text{DMF})\cdot 3\text{H}_2\text{O}$

$\text{H}_{2.5}\text{Na}_{0.5}\text{-oaba}\cdot 0.5(\text{H}_2\text{O})$ (0.54 mmol, 124 mg) $\text{Cu}(\text{OAC})_2\cdot \text{H}_2\text{O}$ (0.5 mmol, 99 mg), and $\text{Co}(\text{OAC})_2\cdot 4\text{H}_2\text{O}$ (0.5 mmol, 124 mg) were placed in a 23 mL Teflon-lined autoclave reactor filled with DMF (4 mL). The reactor was heated to 80°C in 2 h, kept at this temperature for 72 h and then cooled down to room temperature in 24 h. Dark purple crystals of $[\text{Cu}_4\text{Co}_3(\text{oaba})_4(\text{OH})_2(\text{DMF})_4]\cdot 3(\text{DMF})\cdot 3\text{H}_2\text{O}$ were collected and washed by sonication in EtOH. Yield: 123 mg, 51% (based on copper; $M=1855.22\text{ gmol}^{-1}$). Elemental analysis (%): calc. for $\text{C}_{57}\text{H}_{71}\text{Co}_3\text{Cu}_4\text{N}_{11}\text{O}_{31}$: C, 37.26; H, 3.89; N, 8.38; Co, 9.62; Cu, 13.83 (wt/ Cu/Co=1,44). Found: C, 36.97; H, 3.97; N, 8.70; Co, 9,27; Cu, 12,79 (wt. Cu/Co=1.38). Selected IR data (cm^{-1}): 2934(w), 1635(s), 1571(s), 1433(w), 1383(w), 1347(m), 1251(w), 1184(m), 1095(m), 1051(m), 883(w), 852(w), 804(m), 767(m), 716(w), 678(m), 619(w), 580(w), 495(m), 374 (m), 323(m).



Experimental and calculated PXRD patterns for $[\text{Cu}_4\text{Co}_3(\text{oaba})_4(\text{OH})_2(\text{DMF})_4]\cdot 3(\text{DMF})\cdot 3\text{H}_2\text{O}$



Thermogravimetric analysis of $[\text{Cu}_4\text{Co}_3(\text{oaba})_4(\text{OH})_2(\text{DMF})_4] \cdot 3(\text{DMF}) \cdot 3\text{H}_2\text{O}$

TGA shows that before 250 °C, co-crystallized H_2O and DMF molecules are removed (exp. H_2O 5 %, DMF 30 %; ca. H_2O 3 %, DMF 27.85 %). Then the curve drops abruptly. Weight percentage after 300 °C is stable around 30% in air, which is in accordance with assumed formation of oxides (CuO 17% and Co_2O_3 , 13.5 %, or CoO , 12 %).

3.2 Synthesis of $[\text{Cu}(\text{ohpma})\text{Co}(\text{OAc})(\text{DMF})_2]$

$\text{H}_{2.5}\text{Na}_{0.5}\text{-ohpma} \cdot 0.5(\text{H}_2\text{O})$ (0.42 mmol, 86 mg), $\text{Cu}(\text{OAc})_2 \cdot \text{H}_2\text{O}$ (0.5 mmol, 99 mg) and $\text{Co}(\text{OAc})_2 \cdot 4\text{H}_2\text{O}$ (0.5 mmol, 124 mg) were placed in a 23 mL Teflon-lined autoclave reactor filled with DMF (3 mL) and H_2O (1mL). The reactor was heated to 80°C in 2 h, kept at this temperature for 72 h and then cooled down to room temperature in 24 h. Dark green block crystals of $[\text{Cu}(\text{ohpma})\text{Co}(\text{OAc})(\text{DMF})_2]$ were collected and washed with DMF. Yield: 190 mg, 89.6% (based on $\text{H}_{2.5}\text{Na}_{0.5}\text{-ohpma} \cdot 0.5(\text{H}_2\text{O})$; $M=505.8 \text{ gmol}^{-1}$). Elemental analysis (%): calc. for $\text{C}_{16}\text{H}_{21}\text{CuCoN}_3\text{O}_8$: C, 37.99; H, 4.18; N, 8.31; Co, 11.65; Cu, 12.56 (wt. Cu/Co: 1.08). Found: C, 37.83; H, 4.20; N, 8.16; Co, 10.09; Cu, 11.31 (wt. Cu/Co: 1.12). Selected IR data (cm^{-1}): 2932(m), 1627(s), 1566(s),

1473(s), 1370(m), 1344(s), 1297(m), 1274(s), 1242(s), 1110(m), 1027(m), 972(w), 932(w), 886(s), 786(w), 750(s), 675(s), 565(m), 534(m), 373 (m), 325(s).

3.3 Synthesis of [Cu(ohpma)Mn(OAc)(DMF)₂]

H_{2.5}Na_{0.5}-ohpma·0.5(H₂O) (0.42 mmol, 86 mg), Cu(OAc)₂·H₂O (0.5 mmol, 99 mg) and Mn(OAc)₂·4H₂O (0.5 mmol, 116 mg) were placed in a 23 mL Teflon-lined autoclave reactor filled with DMF (4 mL). The reactor was heated to 80°C in 2 h, kept at this temperature for 72 h and then cooled down to room temperature in 24 h. Dark green block crystals of [Cu(ohpma)Mn(OAc)(DMF)₂] were collected and washed with DMF. Yield: 131 mg, 62.4% (based on H_{2.5}Na_{0.5}-ohpma·0.5(H₂O), M=501.8 gmol⁻¹). Elemental analysis (%): calc. for C₁₆H₂₁CuMnN₃O₈: C, 38.29; H, 4.22; N, 8.37; Mn, 10.94; Cu, 12.66 (wt. Cu/Mn=1.16). Found: C, 38.11; H, 4.24; N, 8.19; Mn, 11.72; Cu, 13.53 (wt. Cu/Mn=1.15). Selected IR data (cm⁻¹): 2932(m), 1627(s), 1562(s), 1472(m), 1416(m), 1371(s), 1342(w), 1296(m), 1274(m), 1242(m), 1150(m), 1105(m), 1061(m), 1027(m), 931(w), 838(s), 784(m), 750(m), 670(m), 593 (m), 563(s), 533(m), 446(m), 362(m), 327(m), 285(m).

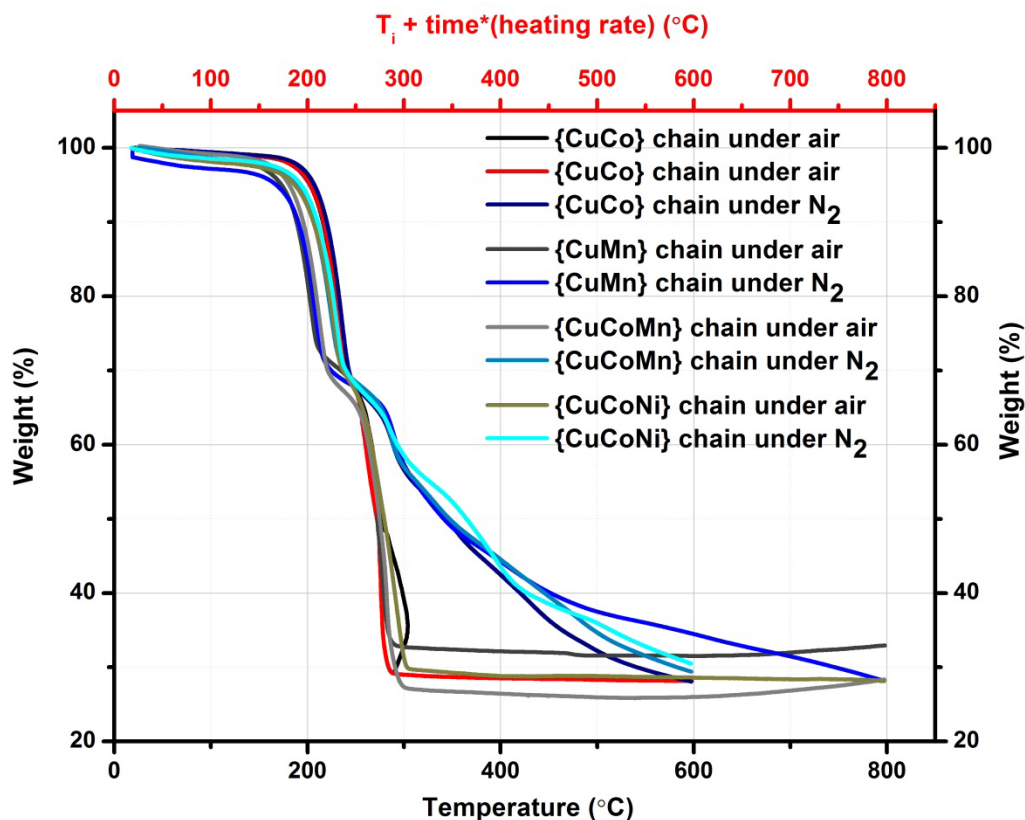
3.4 Synthesis of [Cu(ohpma)Co_{0.57}Mn_{0.43}(OAc)(DMF)₂]

H_{2.5}Na_{0.5}-ohpma·0.5(H₂O) (0.42 mmol, 86 mg), Cu(OAc)₂·H₂O (0.5 mmol, 99 mg), Co(OAc)₂·4H₂O (0.25 mmol, 62 mg) and Mn(OAc)₂·4H₂O (0.25 mmol, 58 mg) were placed in a 23 mL Teflon-lined autoclave reactor filled with DMF (3 mL) and H₂O (1mL). The reactor was heated to 80°C in 2 h, kept at this temperature for 72 h and then cooled down to room temperature in 24 h. The resulting green solution was then left to crystallise at room temperature in a sealed vial. After 1 day, dark crystals of [Cu(ohpma)Co_{0.57}Mn_{0.43}(OAc)(DMF)₂] were collected and washed with DMF. Yield: 179 mg, 85% (based on H_{2.5}Na_{0.5}-ohpma·0.5(H₂O), M=504.1 gmol⁻¹). Elemental analysis (%): calc. for C₁₆H₂₁CuCo_{0.57}Mn_{0.43}N₃O₈: C, 38.12; H, 4.19; N, 8.33; Co, 6.66; Cu, 12.60; Mn, 4.68 (wt. Cu/Co=1.89, Cu/Mn=2.69; Co/Mn=1.42). Found: C, 37.54; H, 4.01; N, 8.19; Mn, 4.19; Co, 5.99; Cu, 11.44 (wt. Cu/Co=1.91, Cu/Mn=2.73; Co/Mn=1.43). Selected IR data (cm⁻¹): 2930(w), 1628(s), 1565(s), 1472(m), 1371(m), 1343(s), 1296(m), 1274(s), 1242(s), 1109(m), 1027(m), 950(w), 885(s),

785(w), 750(s), 673(s), 564(m), 534(m), 457 (m).

3.5 Synthesis of [Cu(ohpma)Co_{0.6}Ni_{0.4}(OAc)(DMF)₂]

H_{2.5}Na_{0.5}-ohpma·0.5(H₂O) (0.42 mmol, 86 mg), Cu(OAc)₂·H₂O (0.5 mmol, 99 mg), Co(OAc)₂·4H₂O (0.25 mmol, 62 mg) and Ni(OAc)₂·4H₂O (0.25 mmol, 62 mg) were placed in a 23 mL Teflon-lined autoclave reactor filled with DMF (3 mL) and H₂O (1mL). The reactor was heated to 80°C in 2 h, kept at this temperature for 72 h and then cooled down to room temperature in 24 h. The resulting solution was then left to crystallise at room temperature in a sealed vial. After 1 day, dark crystals of [Cu(ohpma)Co_{0.6}Ni_{0.4}(OAc)(DMF)₂] were collected and washed with DMF. Yield: 109 mg, 51% (based on H_{2.5}Na_{0.5}-ohpma·0.5(H₂O); M=505.72 g mol⁻¹). Elemental analysis (%): calc. for C₁₆H₂₁Co_{0.6}CuNi_{0.4}N₃O₈: C, 37.99; H, 4.18; N, 8.31; Co, 6.99; Cu12.56; Ni, 4.64 (wt. Cu/Co=1.79; Cu/Ni=2.70; Co/Ni=1.51). Found: C, 37.83; H, 4.20; N, 8.16; Co, 6.40; Cu, 12.38; Ni, 4.29 (wt. Cu/Co=1.93; Cu/Ni=2.88; Co/Ni=1.49). Selected IR data (cm⁻¹): 2931(s), 1629(s), 1567(s), 1472(s), 1371(m), 1344(s), 1297(m), 1274(s), 1242(s), 1110(m), 1027(m), 972(w), 932(w), 885(s), 786(w), 750(s), 676(s), 565(m), 535(m), 458 (m).



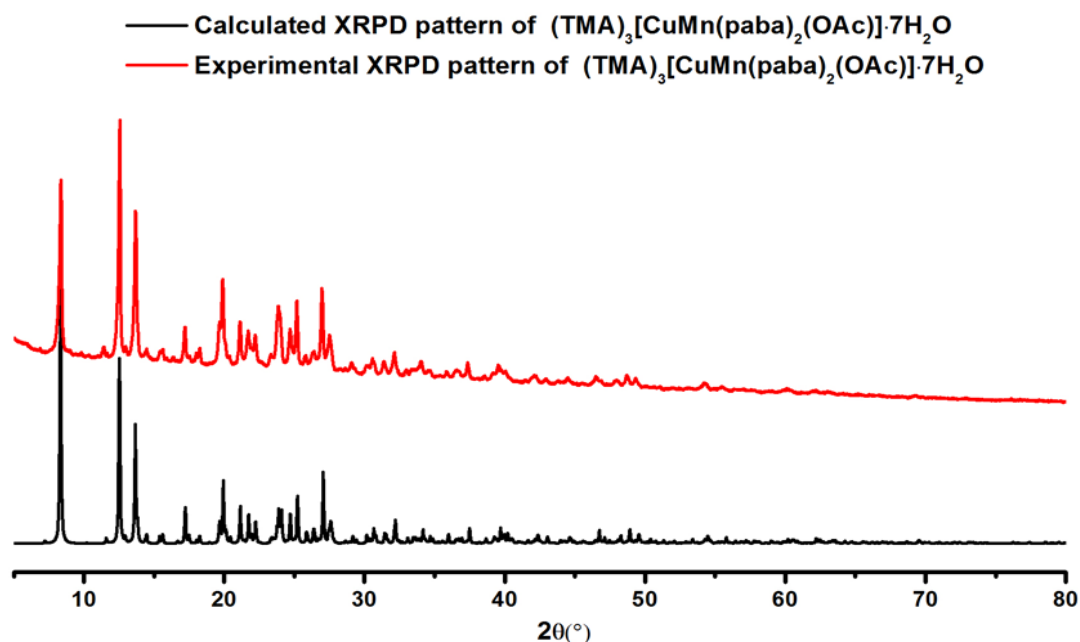
Thermogravimetric analysis of {CuCo}, {CuMn}, {CuCoMn} and {CuMnNi} chains based on ohpma ligand.

TGA curves of the four chains are similar, firstly coordinated DMF molecules are removed (28-29 %, ca. 28.9-29.1 %), and then a rapid loss of all the organic content is observed. At high temperature the final weight is consistent with the formation of the corresponding oxides (approx. 29-30 %).

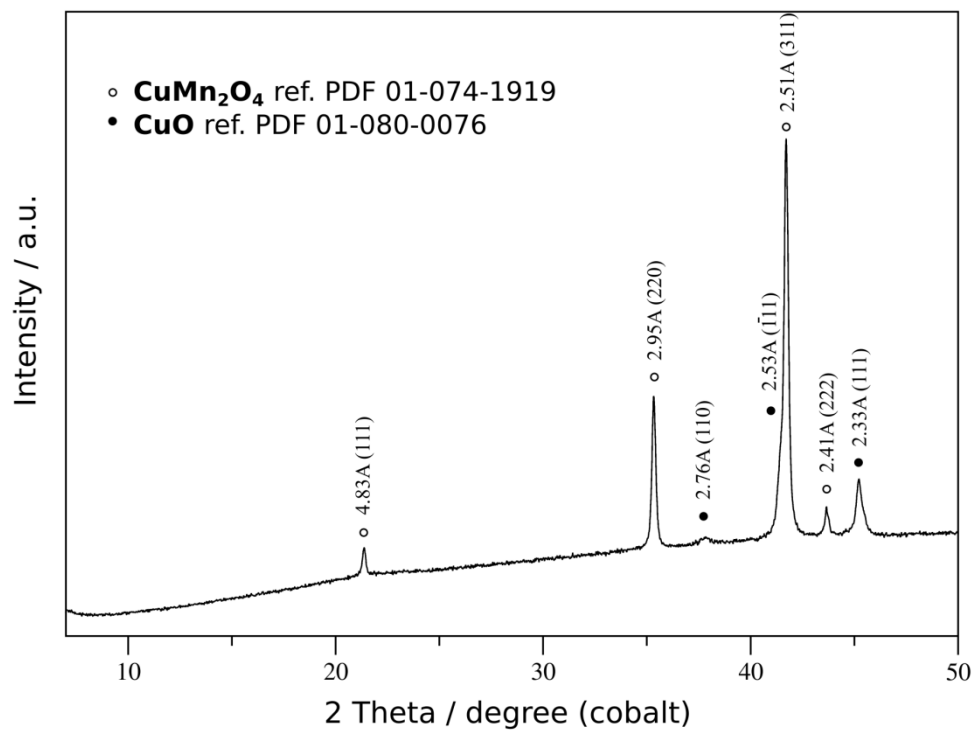
4. Chapter 4 Synthesis, characterization and magnetic properties of an oxamato bridged hetero-metallic 2D compound

4.1. Synthesis of $(\text{TMA})_3[\text{CuMn}(\text{paba})_2(\text{OAc})]\cdot 7\text{H}_2\text{O}$

$\text{H}(\text{TMA})_2\text{-paba}\cdot 1.5\text{H}_2\text{O}$ (0.95 mmol, 356 mg), $\text{Cu}(\text{OAc})_2\cdot \text{H}_2\text{O}$ (0.5 mmol, 99 mg), $\text{Mn}(\text{OAc})_2\cdot 4\text{H}_2\text{O}$ (0.5 mmol, 122 mg) and 0.36 mL of TMAOH (25% wt. in water, 1 eq.) were placed in a 23 mL Teflon-lined autoclave reactor filled with DMF (4 mL). The reactor was heated to 120 °C in 2 h, kept at this temperature for 12 h and then cooled down to room temperature in 10 h. Green crystals of $(\text{TMA})_3[\text{CuMn}(\text{paba})_2(\text{OAc})]\cdot 7\text{H}_2\text{O}$ were collected and washed with EtOH for single-crystal X-ray diffraction studies. Further washing was done by sonication in EtOH prior to all other characterizations. Yield: 135 mg, 31% (based on $\text{H}(\text{TMA})_2\text{-paba}\cdot 1.5\text{H}_2\text{O}$, $M=938,3 \text{ gmol}^{-1}$). Elemental analysis (%): calc. for $\text{C}_{32}\text{H}_{61}\text{CuMnN}_5\text{O}_{19}$: C, 40.96; H, 6.55; N, 7.46; Mn, 5.85; Cu, 6.77 (wt. Cu/Mn=1.16). Found: C, 40.44; H, 5.85; N, 7.31; Mn, 5.73; Cu, 6.61 (wt. Cu/Co=1.15). Selected IR data (cm^{-1}): 3372(sd), 1627(s), 1583(s), 1559(s), 1486(m), 1373(s), 1334(s), 1168(s), 1099(w), 1016(w), 949(s), 880(w), 841(w), 797(m), 778(s), 707(w), 663(s), 526(w), 496(w), 437 (w).



Experimental and calculated PXRD patterns for $(\text{TMA})_3[\text{CuMn}(\text{ohpma})_2(\text{OAc})]\cdot 7\text{H}_2\text{O}$



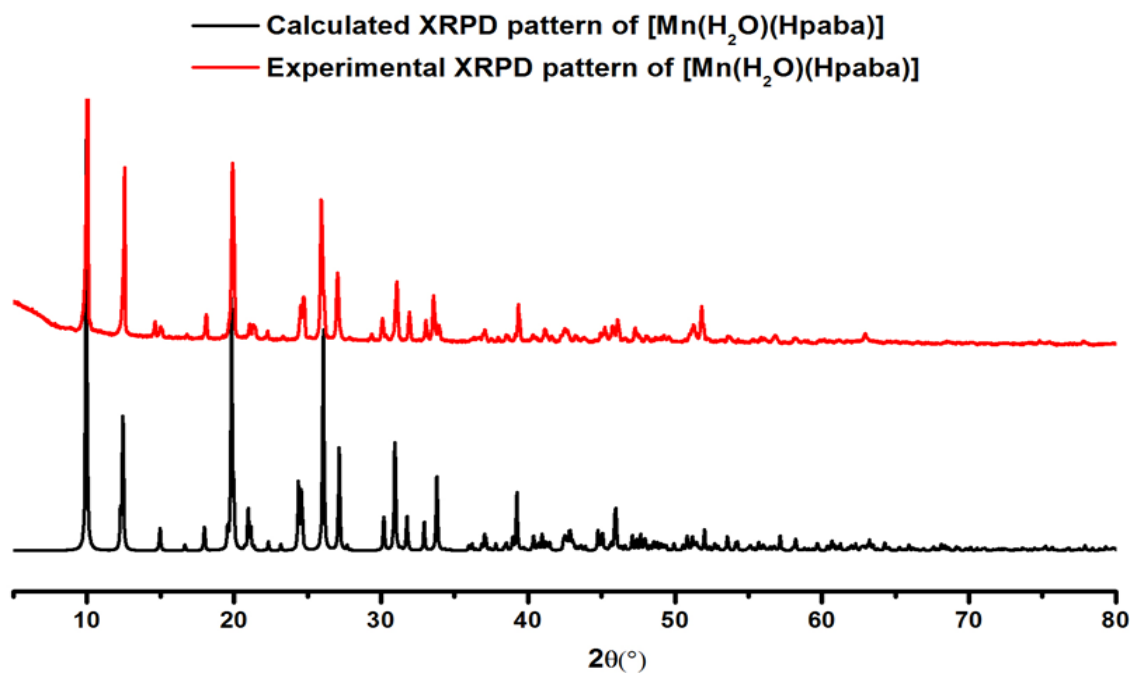
Experimental PXRD patterns for $(\text{TMA})_3[\text{CuMn}(\text{ohpma})_2(\text{OAc})] \cdot 7\text{H}_2\text{O}$ at high temperature

From the PXRD pattern of heated compound **4.1** (600°C), the observed diffraction peaks can be attributed to the formation of Cu and Mn oxide (CuO and CuMn_2O_4).

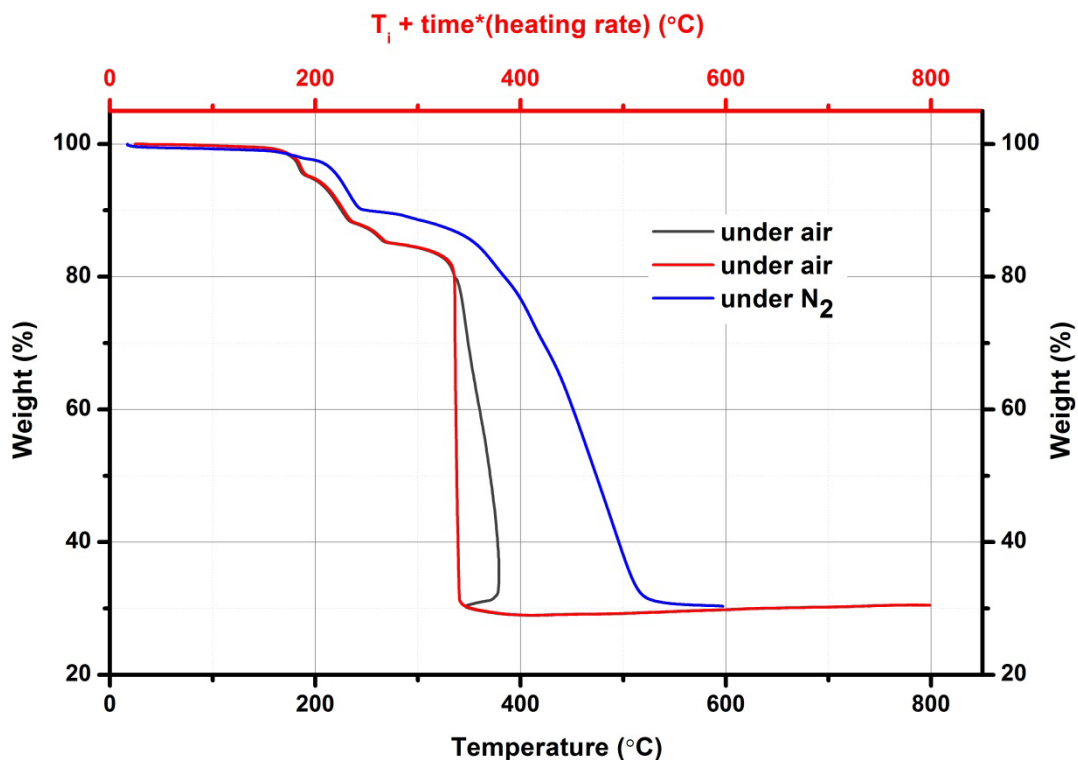
5. Chapter 5 Synthesis, characterization and magnetic properties of oxamato bridged homo- and hetero-metallic 3D compounds

5.1 Synthesis of $[\text{Mn}(\text{H}_2\text{O})(\text{Hpaba})]$

$\text{H}_2\text{Li-paba}\cdot\text{H}_2\text{O}$ (0.44 mmol, 104.5 mg) and $\text{MnCl}_2\cdot 4\text{H}_2\text{O}$ (0.5 mmol, 99 mg) were placed in a 23 mL Teflon-lined autoclave reactor filled with DMF (3.5 mL) and water (0.5 mL). The reactor was heated up to 150 °C in 2 h, kept at this temperature for 12 h and then cooled down to room temperature in 10 h. Pale yellow crystals of $[\text{Mn}(\text{H}_2\text{O})(\text{Hpaba})]$ were collected and washed with DMF. Yield: 114 mg, 92.53% (based on $\text{H}_2\text{Li-paba}\cdot\text{H}_2\text{O}$; $M=280.1 \text{ g mol}^{-1}$). Elemental analysis (%): calc. for $\text{C}_9\text{H}_7\text{MnNO}_6$: C, 38.59; H, 2.52; N, 5.00. Found: C, 37.54; H, 2.77; N, 4.98. Considering a partially hydrated solid gives a better match with the found EA percentages ($[\text{Mn}(\text{H}_2\text{O})(\text{Hpaba})]\cdot 0.4(\text{H}_2\text{O})$: C, 37.62; H, 2.73; N, 4.87; $M=287.3 \text{ g mol}^{-1}$), yet TGA supports the absence of solvents (see below), which would indicate a slight water adsorption in air. Selected IR data (cm^{-1}): 3459(w), 3331(w), 3214(w), 1682(w), 1649(m), 1603(m), 1529(m), 1378(s), 1314(w), 1242(w), 1209(w), 1016(w), 941(w), 842(w), 789(s), 697(w), 637(w), 560(w), 487(m), 430(w), 347(w).



Experimental and calculated PXRD patterns for $[\text{Mn}(\text{H}_2\text{O})(\text{Hpaba})]$



Thermogravimetric analysis of $[\text{Mn}(\text{H}_2\text{O})(\text{Hpaba})]$

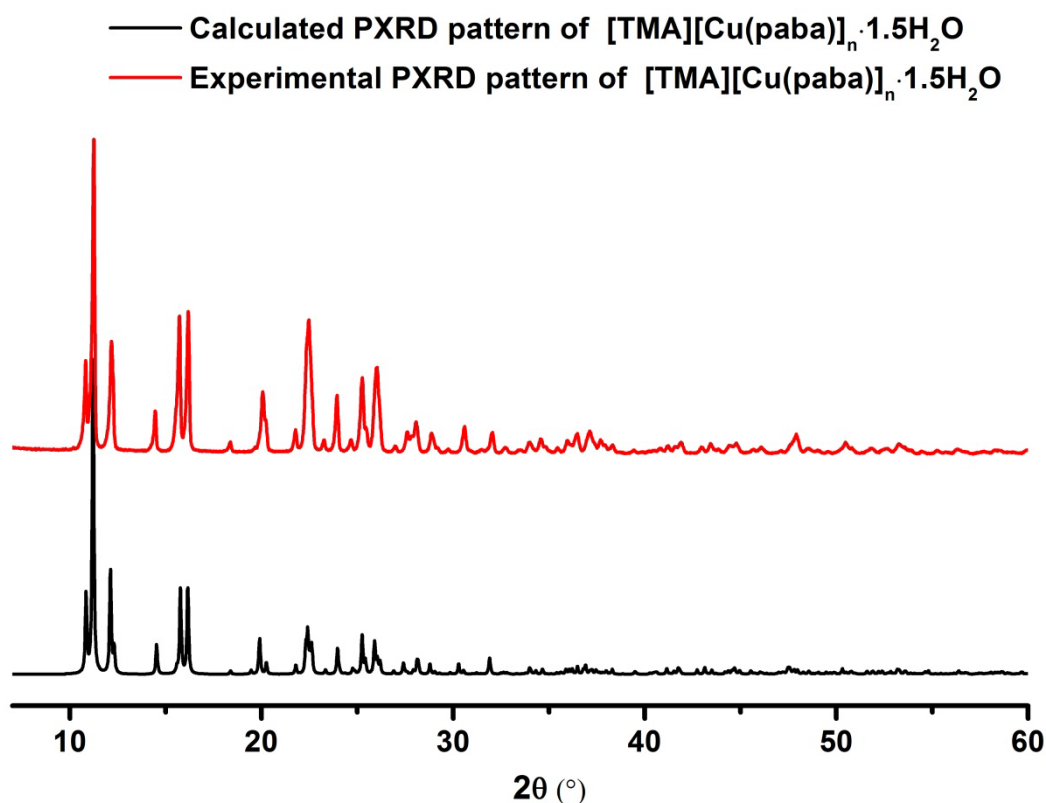
Under air, TGA shows the loss of the coordinated water molecule after 150 °C (ca. 6.4%, exp. 5.4%), followed by a multi-step the decomposition of the compound ending in a massive loss at 330 °C. The latter is actually accompanied by a combustion phenomenon, the measured temperature exceeds the settings. Weight percentage at 800 °C reaches 30%, close to the expected value for the formation of Mn_2O_3 (28.2 %).

5.2 Synthesis of $(\text{TMA})[\text{Cu}(\text{paba})]\cdot 1.5\text{H}_2\text{O}$ (1)

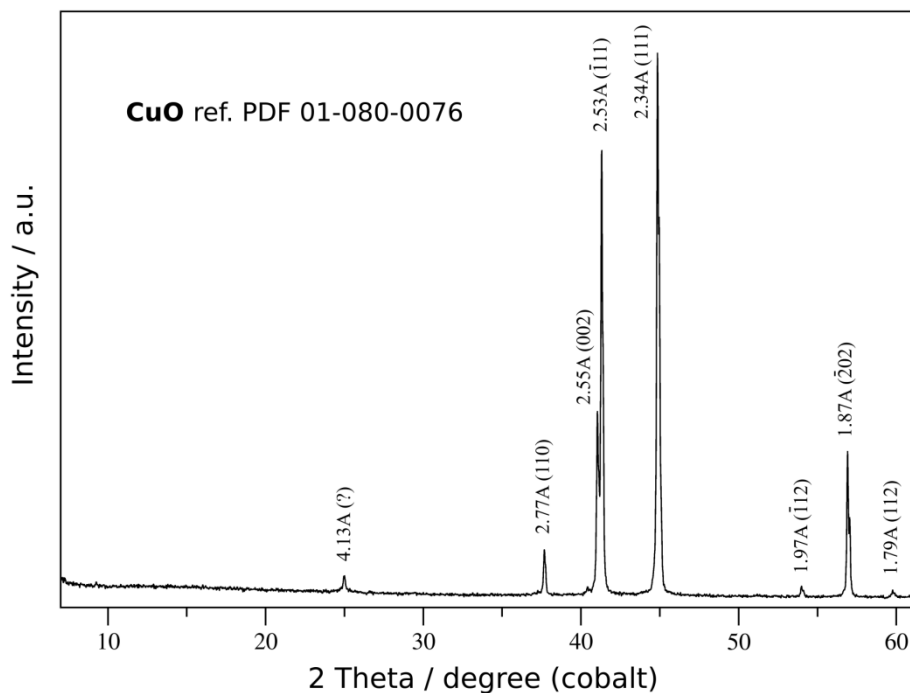
$\text{H}_2\text{Li-paba}\cdot\text{H}_2\text{O}$ (0.49 mmol, 116 mg), $\text{Cu}(\text{OAc})_2\cdot 4\text{H}_2\text{O}$ (0.5 mmol, 99 mg), $\text{Mn}(\text{OAc})_2\cdot 4\text{H}_2\text{O}$ (0.5 mmol, 122 mg) and 0.54 mL of TMAOH (25% wt. in water, 3 eq.) were placed in a 23 mL Teflon-lined autoclave reactor filled with DMF (3.5 mL) and water (0.5 mL). The reactor was heated up to 80 °C in 2 h, kept at this temperature for 72 h and then cooled down to room temperature in 24 h. The resulting mixture was collected, and EtOH was used to isolate crystals of $(\text{TMA})[\text{Cu}(\text{paba})]\cdot 1.5\text{H}_2\text{O}$ suitable for single-crystal X-ray diffraction from a greenish powder.

5.3 Synthesis of (TMA)[Cu(paba)]·1.5H₂O (2)

H(TMA)₂-paba·1.5H₂O (0.93 mmol, 356 mg) and Cu(OAc)₂·4H₂O (0.5 mmol, 99 mg) were placed in a 23 mL Teflon-lined autoclave reactor filled with DMF (3.5 mL) and water (0.5 mL). The reactor was heated up to 80 °C in 2 h, kept at this temperature for 12 h and then cooled down to room temperature in 10 h. The polycrystalline blue powder of (TMA)[Cu(paba)]·1.5H₂O was collected by centrifugation, and washed by sonication in EtOH.. Yield: 158 mg, 85% (based on copper; M=370.8 gmol⁻¹). Elemental analysis (%):calc. for C₁₃H₁₉CuN₂O_{6.5}: C, 42.10; H, 5.16; N, 7.55; Cu, 17.13. Found: C, 41.47; H, 4.73; N, 7.40; Cu, 16.48. Selected IR data (cm⁻¹): 3471(sd), 2931(w), 1662(s), 1579(s), 1501(w), 1437(w), 1385(m), 1351(m), 1254(m), 1180(w), 1093(s), 1062(w), 1020(s), 888(w), 862(w), 802(m), 781(m), 659(m), 481(m), 352 (m), 318(s).



Experimental and calculated PXRD patterns for (TMA)[Cu(paba)]·1.5H₂O



Experimental PXRD patterns for (TMA)[Cu(paba)]·1.5H₂O at high temperature

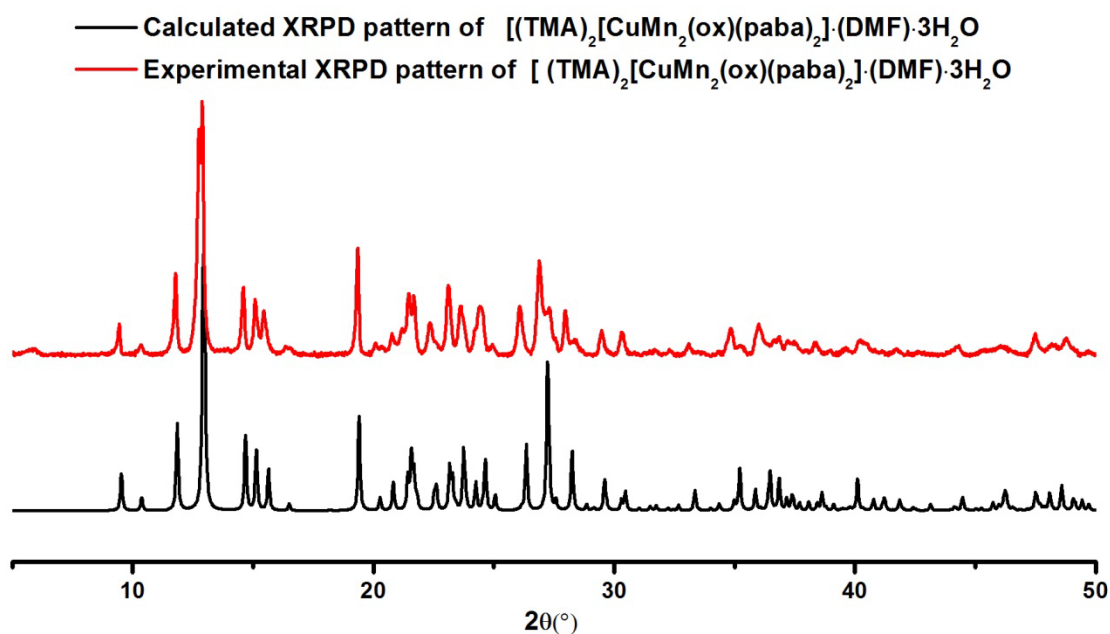
From the PXRD pattern of heated compound **5.2**(600°C), the observed diffraction peaks can be attributed to the formation of Cu oxide (CuO).

5.4 Synthesis of (TMA)₂[CuMn₂(ox)(paba)₂](DMF)·3H₂O (**1**)

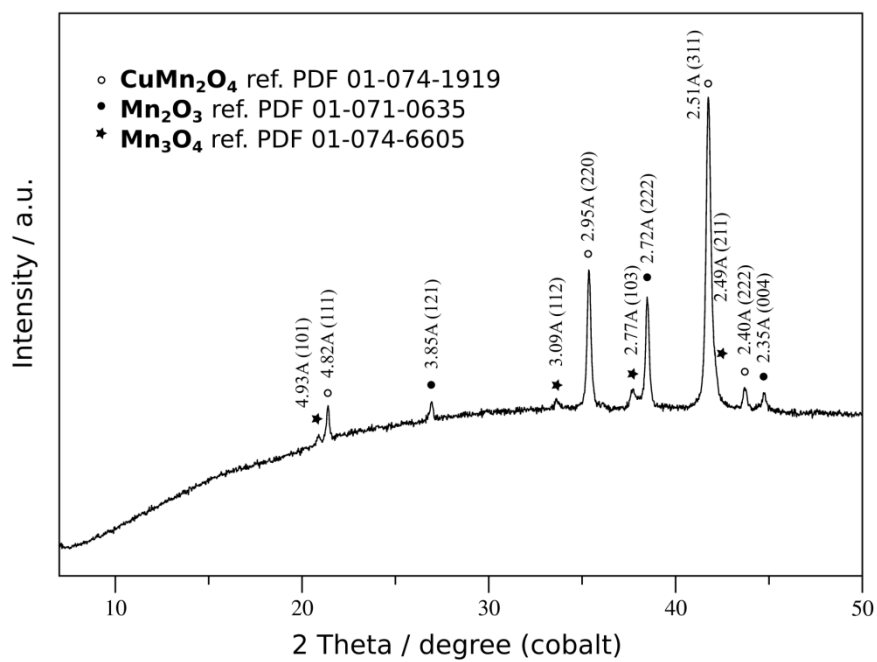
H₂Li-paba·H₂O (0.49 mmol, 116 mg), Cu(OAc)₂·H₂O (0.5 mmol, 99 mg) and Mn(OAc)₂·4H₂O (0.5 mmol, 122 mg) and 0.36 mL of TMAOH (25% wt. in water, 2 eq.) were placed in a 23 mL Teflon-lined autoclave reactor filled with DMF (3.5 mL) and water (0.5 mL). The reactor was heated up to 120 °C in 2 h, kept at this temperature for 72 h and then cooled down to room temperature in 24 h. The resulting mixture was collected, and EtOH was used to separate the green crystals of (TMA)₂[CuMn₂(ox)(paba)₂](DMF)·3H₂O suitable for single-crystal X-ray diffraction from a brownish powder. Further purification was done by sonication in EtOH. Yield: 38 mg, 16% (based on H₂Li-paba·H₂O; M=949.1 gmol⁻¹). Elemental analysis (%): calc. for C₃₁H₄₅CuMn₂N₅O₁₈: C, 39.23; H, 4.79; N, 7.34. Found: C, 38.90; H, 4.43; N, 7.74. Selected IR data (cm⁻¹): 1652(m), 1587(s), 1554(s), 1385(m), 1335(m), 1314(m), 1176(w), 1099(s), 953(m), 887(w), 780(m), 706(m), 657(w), 550(w), 437(w), 369(w).

5.5 Synthesis of $(\text{TMA})_2[\text{CuMn}_2(\text{ox})(\text{paba})_2] \cdot (\text{DMF}) \cdot 3\text{H}_2\text{O}$ (2)

$\text{H}_2\text{Li-paba} \cdot \text{H}_2\text{O}$ (0.49 mmol, 116 mg), $\text{Cu}(\text{OAc})_2 \cdot \text{H}_2\text{O}$ (0.5 mmol, 99 mg) and $\text{Mn}(\text{OAc})_2 \cdot 4\text{H}_2\text{O}$ (0.5 mmol, 122 mg) and 0.54 mL of TMAOH (25% wt. in water, 3 eq.) were placed in a 23 mL Teflon-lined autoclave reactor filled with DMF (3.5 mL) and water (0.5 mL). The reactor was heated up to 120 °C in 2 h, kept at this temperature for 12 h and then cooled down to room temperature in 10 h. The polycrystalline green powder of $(\text{TMA})_2[\text{CuMn}_2(\text{ox})(\text{paba})_2] \cdot (\text{DMF}) \cdot 3\text{H}_2\text{O}$ was collected and washed by sonication in EtOH. Yield: 124 mg, 58% (based on $\text{H}_2\text{Li-paba} \cdot \text{H}_2\text{O}$, $M=858$). Elemental analysis (%): calc. for $\text{C}_{31}\text{H}_{45}\text{CuMn}_2\text{N}_5\text{O}_{18}$: C, 39.23; H, 4.79; N, 7.34. Found: C, 37.18; H, 4.18; N, 7.07.



Experimental and calculated XRPD patterns for $(\text{TMA})_2[\text{CuMn}_2(\text{ox})(\text{paba})_2] \cdot (\text{DMF}) \cdot 3\text{H}_2\text{O}$



Experimental PXRD patterns for $(\text{TMA})_2[\text{CuMn}_2(\text{ox})(\text{paba})_2] \cdot (\text{DMF}) \cdot 3\text{H}_2\text{O}$ at high temperature

From the PXRD pattern of heated compound **5.3** (600°C), the observed diffraction peaks can be attributed to the formation of Cu and Mn oxide (CuMn_2O_4 , Mn_2O_3 , Mn_3O_4).

6. Instruments

NMR

The ligands are dissolved in DMSO-d₆ solution in a standard 5 mm NMR tube. The ¹H and ¹³C NMR spectra were collected at 298 K in Bruker AVANCE spectrometers (400MHz or 300MHz). The resulting NMR spectra were treated and evaluated with TOPSPIN 2.1 or with MestreNova^{2,3}. The chemical shifts, δ , are expressed in parts per millions (ppm) and are referenced using IUPAC recommendations⁴.

ATR/FT-IR

The ATR/FT-IR were measured between 4000 cm⁻¹ and 400 cm⁻¹ using a Bruker TENSOR 27 equipped with a simple reflection ATR diamond plate of the Harrick MPV2 series, the spectrums were treated with the accompanying software OPUS 5.5.

Elemental analysis

The elemental analysis were done in service de microanalyse de l'ICSN (CNRS, Gif/Yvette). (C, H, N) were carried out by combustion analysis using a vario MICRO cube apparatus from Elementar.

ICP

The metal contents of metallic compound samples for Mn, Cu, Co, Ni elements were characterized by an Inductively Coupled Plasma-Optical Emission Spectrometry (ICP-OES, ICP-OES iCAP6200 ThermoScientific).

X-ray diffraction

The data were collected on a Bruker Kappa-APEX-2 diffractometer with a bidimensional detector (Camera CCD- Charged Coupled Device), using a Mo-K α source and equipped with a low temperature system (cryosystems). During the measurement, the dual-space is scanned by ω and φ rotation of the crystal. The exposition time by plan is chosen depending on the size of crystal and its

ability to scatter: from 5 to 240 s. The measurements were performed using a distance of 4 cm between the camera and crystal. The data treatment was done using APEX2 software⁵.

Data treatment : a first set of diffraction spots allows to extract a lattice and a matrix of orientation that are continuously refined during data collection. The intensity of the diffraction spots collected were extracted using SAINT program (version 7.34A)⁵ and corrected (from absorption effects) using SADABS program (version 2007/4)⁶ based on Blessing empiric method⁷.

Resolution and structure refinement: SHELXTL⁸ programs:

From the corrected data, XPREP was enabled to determine the space group. It produces command files required for XS and XL implementation.

XS suggests a solution of structure based on the automatic interpretation of Patterson card or on a direct method. It allows the obtention of the heaviest atoms position.

Then, the previous structure was refined using XL by the least square method. Refinement of alternation cycle and DFT calculation allows to localize the structure atoms progressively.

H atoms were refined applying geometric constraint to maintain sp^2 and sp^3 geometry of C and N atoms.

Powder X-ray diffraction

Powder diffraction was performed using a PANALYTICAL X'Pert Pro MPD diffractometer with Cu ($\lambda(K\alpha_1) = 1.5406 \text{ \AA}$) or Co ($\lambda(K\alpha_1) = 1.7890 \text{ \AA}$) radiations and a X'Celerator detector. Prior to measurement, samples are grinded and flatten on silicon wafers. Backgrounds were treated automatically using the HighScore software. Le Bail refinements were performed using the FullProf suite of programs.

Synchrotron

The X-ray diffraction (XRD) measurement was performed on a selected single crystal at 100K (18,457keV / $\lambda = 0.67173 \text{ \AA}$) on the 4-circle diffractometer of the CRISTAL beamline (Synchrotron SOLEIL) equipped with a MAR165CCD detector. Data reduction, cell refinement, space group determination, scaling and empirical absorption correction were performed using *CrysAlisPro*

software⁹.

The structure was solved using *SHELXT*¹⁰ implemented in Olex2 program¹¹. The refinement was then carried out with *SHELXL*, by full-matrix least squares minimization and difference Fourier methods. For compound **4.1** all non H atoms were refined with anisotropic displacement parameters, excepted one tetramethylammonium molecule, due to a low data/parameter ratio and the limited resolution accessible from this tiny single crystal.

DC and AC Magnetic susceptibility measurements

The temperature and field dependent DC (Direct Current) magnetizations were measured on a Quantum Design MPMS-XL7 magnetometer. The polycrystalline sample was restrained in medical capsule or PVC film, according to the sample amount and to the measuring conditions (temperature and field). The sample with anisotropic metal center like $\text{Co}^{\text{II}}_{\text{HS}}$ was mixed with Paratone oil to prevent the re-orientation under high field and at low temperature. All samples with crystallized solvent molecules were introduced into the magnetometer under helium flow and frozen before purging under vacuum.

The AC (Alternative Current) magnetizations were measured on a Quantum Design PPMS-9T magnetometer. For the complex **2.5** which is a field – induced SMM (Single Molecular Magnet), the AC measurements were performed under a dc field of 1800 Oe with 30 frequencies varying logarithmically from 10 Hz to 10000 Hz. For a better stabilization of low temperature, an AC amplitude of 10 Oe was used in the low frequency range (10-279 Hz) and a smaller AC amplitude of 3 Oe, in the high frequency range (354-10000 Oe). For the compound **4.1** and **5.3** which show one or more magnetic orderings at low temperature, the AC measurements were carried out in the temperature range of 2-10 K for the former and of 2-50 K for the later. An unique AC amplitude of 3 Oe was applied with 25 frequencies ranging from 60 Hz to 10000 Hz.

Both DC and AC data were corrected for the diamagnetic contributions from the sample holder, the Paratone oil and from the sample molecules.

7. BVS calculations

2.5 (TMA)₃[[Co^{III}(ohpma)₂Co^{II}(MeOH)₂]₃]·10H₂O·5MeOH

Atoms	dist.	Co(II)	Co(III)	Atoms	dist.	Co(II)	Co(III)
Co1 N1	1.8764	0.542	0.711	Co2 O9	2.031	0.4	0.409
N2	1.8794	0.534	0.705	O3	2.0682	0.362	0.37
O4	1.8848	0.594	0.607	O13	2.0802	0.35	0.358
O8	1.8924	0.582	0.595	O12	2.1067	0.326	0.333
O5	1.9556	0.49	0.501	O10	2.111	0.322	0.329
O1	1.9685	0.474	0.484	O2	2.1676	0.277	0.283
		<u>3.22</u>	<u>3.602</u>			<u>2.037</u>	<u>2.081</u>
Co3 N3	1.8711	0.55	0.721	Co4 O20	2.0591	0.371	0.379
N4	1.8766	0.542	0.71	O19	2.0677	0.362	0.37
O14	1.8954	0.577	0.59	O17	2.0756	0.355	0.362
O18	1.8999	0.57	0.583	O23	2.0917	0.34	0.347
O15	1.949	0.499	0.51	O22	2.1132	0.32	0.327
O11	1.9491	0.499	0.51	O16	2.1469	0.292	0.299
		<u>3.238</u>	<u>3.624</u>			<u>2.04</u>	<u>2.085</u>
Co5 N6	1.8752	0.544	0.713	Co6 O27	2.0438	0.386	0.395
N5	1.8852	0.53	0.694	O30	2.0439	0.386	0.395
O28	1.8957	0.576	0.589	O7	2.0588	0.371	0.379
O24	1.9016	0.567	0.58	O29	2.124	0.311	0.318
O21	1.9253	0.532	0.544	O6	2.1475	0.292	0.298
O25	1.943	0.507	0.519	O26	2.1684	0.276	0.282
		<u>3.257</u>	<u>3.638</u>			<u>2.023</u>	<u>2.067</u>

3.1 [Cu₄Co₃(oaba)₄(OH)₂(DMF)₄]·3(DMF)·3H₂O

Atoms	dist.	Co(II)	Co(III)	Atoms	dist.	Co(II)	Co(III)
Co1 O4	2.0893	0.342	0.349	Co2 O13	2.081	0.349	0.357
O4	2.0896	0.341	0.349	O9	2.0815	0.349	0.357
O1	2.0929	0.338	0.346	O6	2.0875	0.343	0.351
O1	2.0936	0.338	0.345	O12	2.0875	0.343	0.351
O2	2.1038	0.328	0.336	O11	2.1136	0.32	0.327
O2	2.1049	0.328	0.335	O7	2.1347	0.302	0.309
		<u>2.016</u>	<u>2.056</u>			<u>2.007</u>	<u>2.051</u>

3.2 [Cu(ohpma)Co(OAc)(DMF)₂]

Atoms	dist.	Co(II)	Co(III)
Co1 O4	2.0605	0.369	0.377
O6	2.0735	0.357	0.364
O8	2.0929	0.338	0.345
O3	2.1093	0.324	0.331
O2	2.1135	0.320	0.327
O7	2.1335	0.303	0.309
		<u>2.011</u>	<u>2.055</u>

3.3 [Cu(ohpma)Mn(OAc)(DMF)₂]

Atoms	dist.	Mn(II)	Mn(III)
Mn1 O6	2.131	0.398	0.367
O4	2.1323	0.396	0.365
O8	2.1742	0.354	0.326
O3	2.1932	0.336	0.31
O2	2.2005	0.33	0.304
O7	2.2058	0.325	0.3
		<u>2.139</u>	<u>1.973</u>

4.1 (TMA)₃[CuMn(paba)₂(OAc)]·2H₂O

Atoms	dist.	Mn(II)	Mn(III)	Atoms	dist.	Mn(II)	Mn(III)
Mn1 O6	2.1179	0.412	0.38	Mn2O007	2.0671	0.473	0.436
O4	2.1181	0.412	0.38	O004	2.1477	0.38	0.351
O8	2.1394	0.389	0.358	O00A	2.1496	0.378	0.349
O3	2.1982	0.332	0.306	O003	2.2205	0.312	0.288
O2	2.2031	0.327	0.302	O008	2.2819	0.264	0.244
O7	2.2238	0.31	0.285	O00C	2.3036	0.249	0.23
		<u>2.182</u>	<u>2.012</u>			<u>2.058</u>	<u>1.898</u>

5.1 [Mn(H₂O)(Hpaba)]

Atoms	dist.	Mn(II)	Mn(III)
Mn1 O6	2.1115	0.419	0.387
O4	2.149	0.379	0.349
O8	2.1754	0.353	0.325
O3	2.1932	0.336	0.31
O2	2.1964	0.333	0.307
O7	2.2659	0.276	0.254
		<u>2.097</u>	<u>1.934</u>

5.3 (TMA)₂[CuMn₂(ox)(paba)₂]·(DMF)·3H₂O

Atoms	dist.	Mn(II)	Mn(III)
Mn1 O6	2.0998	0.433	0.399
O4	2.1493	0.378	0.349
O8	2.1902	0.339	0.312
O3	2.2166	0.316	0.291
O2	2.2255	0.308	0.284
O7	2.282	0.264	0.244
		<u>2.039</u>	<u>1.88</u>

8. Crystallographic tables

Please check the link:

<https://mycore.core-cloud.net/index.php/s/b4gLdw8QRGZEuH3?path=%2FCif%20files>

for all cif files and full crystallographic tables

(Document origin: *publCIF*)¹²

<u>2.1</u> Li₂[Cu(ohpma)(OH)]·5H₂O	
Chemical formula	C ₈ H ₅ CuLi ₂ NO ₅ ·5(H ₂ O)
<i>M_r</i>	362.6
Crystal shape	Needle
Crystal colour	Bluish green
Crystal system, space group	Orthorhombic, <i>P2₁2₁2₁</i>
Temperature [K]	200
<i>a</i> , <i>b</i> , <i>c</i> [Å]	4.9205 (2), 14.8300 (5), 18.4622 (6)
α[°], β[°], γ[°]	90, 90, 90.
<i>V</i> [Å ³]	1347.21 (8)
<i>Z</i>	4
ρ _{calc} [g cm ⁻³]	1.788
λ [Å]	0.71073
μ (MoKα)(mm ⁻¹)	1.67
Measured reflections	15902
Unique reflections	4709
Reflections <i>I</i> > 2σ(<i>I</i>)	4561
<i>R</i> _{int}	0.020
<i>R</i> ₁ , <i>wR</i> ₂ , <i>GOF</i>	0.031, 0.081, 1.12
No. of parameters	201
No. of restraints	3
Largest and smallest residuals [e Å ⁻³]	1.42, -0.40

2.2 $\text{Li}_4[\text{Cu}(\text{paba})_2(\text{H}_2\text{O})] \cdot 9\text{H}_2\text{O}$	
Chemical formula	$\text{C}_{18}\text{H}_{12}\text{CuLiN}_2\text{O}_{12} \cdot 2(\text{H}_2\text{O}) \cdot 6(\text{O})$
M_r	662.9
Crystal shape	Block
Crystal colour	Green
Crystal system, space group	Monoclinic, $P2_1/c$
Temperature [K]	200
a, b, c [Å]	14.703 (4), 10.415 (2), 17.839 (4)
α [°], β [°], γ [°]	90, 96.350 (9), 90.
V [Å ³]	2715.0 (11)
Z	4
ρ_{calc} [g cm ⁻³]	1.622
λ [Å]	0.71073
μ (MoK α) (mm ⁻¹)	0.90
Measured reflections	25105
Unique reflections	8010
Reflections $I > 2\sigma(I)$	5721
R_{int}	0.062
R_1, wR_2, GOF	0.159, 0.453, 1.95
No. of parameters	383
No. of restraints	0
Largest and smallest residuals [e Å ⁻³]	6.58, -1.43

The refinement of this crystal structure is still incomplete. The R factors remain high probably due to twinned data that we were not able to handle at the moment. Further investigation or a new data collection should be carried out

<u>2.3</u> {(HNEt ₃)[Cu(ohpma)]}	
Chemical formula	C ₈ H ₄ CuNO ₄ ·C ₆ H ₁₆ N
<i>M_r</i>	343.86
Crystal shape	Plate
Crystal colour	Green
Crystal system, space group	Trigonal, <i>P</i> 3 ₂
Temperature [K]	200
<i>a</i> , <i>b</i> , <i>c</i> [Å]	9.6625 (2), 9.6625 (2) 13.9393 (4)
α[°], β[°], γ[°]	90, 90, 120.
<i>V</i> [Å ³]	1127.07 (6)
<i>Z</i>	3
ρ _{calc} [g cm ⁻³]	1.520
λ [Å]	0.71073
μ (MoK _α)(mm ⁻¹)	1.47
Measured reflections	11904
Unique reflections	4907
Reflections <i>I</i> > 2σ(<i>I</i>)	4749
No. of parameters	194
No. of restraints	1
<i>R</i> _{int}	0.013
<i>R</i> ₁ , <i>wR</i> ₂ , <i>GOF</i>	0.020, 0.052, 1.06
Largest and smallest residuals [e Å ⁻³]	0.41, -0.16

2.4 $[\text{N}(\text{CH}_3)_4]_3[\{\text{Co}^{\text{III}}(\text{ohpma})_2\text{Co}^{\text{II}}(\text{ohpma})_2\}_3] \cdot 10\text{H}_2\text{O} \cdot 5\text{MeOH}$	
Chemical formula	$\text{C}_{74}\text{H}_{72.50}\text{Co}_6\text{N}_9\text{O}_{39}$
M_r	2065.49
Crystal shape	Block
Crystal colour	Purple
Crystal system, space group	Monoclinic, $P2_1/c$
Temperature [K]	200
a, b, c [Å]	9.9479 (3), 28.8849 (10), 32.8203 (10)
α [°], β [°], γ [°]	90, 97.123 (2), 90.
V [Å ³]	9357.9 (5)
Z	4
ρ_{calc} [g cm ⁻³]	1.466
λ [Å]	0.71073
μ (MoK α)(mm ⁻¹)	1.13
Measured reflections	77543
Unique reflections	21180
Reflections $I > 2\sigma(I)$	15639
R_{int}	0.051
R_1, wR_2, GOF	0.102, 0.233, 1.14
No. of parameters	1181
No. of restraints	0
Largest and smallest residuals [e Å ⁻³]	2.13, -1.60

3.1 [Cu ₄ Co ₃ (ohpma) ₄ (OH) ₂ (DMF) ₄]·3(DMF)·3H ₂ O	
Chemical formula	C ₄₈ H ₄₆ Co ₃ Cu ₄ N ₈ O ₂₆ ·5(C ₃ H ₇ NO)·0.3(H ₂ O)
<i>M_r</i>	1952.76
Crystal shape	Block
Crystal colour	Purple
Crystal system, space group	Triclinic, <i>P</i> ⁻ 1
Temperature [K]	200
<i>a</i> , <i>b</i> , <i>c</i> [Å]	11.192 (4), 13.437 (5), 15.800 (6)
α[°], β[°], γ[°]	111.817 (6), 105.923 (7), 98.564 (7)
<i>V</i> [Å ³]	2035.9 (13)
<i>Z</i>	1
ρ _{calc} [g cm ⁻³]	1.593
λ [Å]	0.71073
μ (MoKα)(mm ⁻¹)	1.71
Measured reflections	26439
Unique reflections	8461
Reflections <i>I</i> > 2σ(<i>I</i>)	5710
<i>R</i> _{int}	0.067
<i>R</i> ₁ , <i>wR</i> ₂ , <i>GOF</i>	0.115, 0.259, 1.09
No. of parameters	679
No. of restraints	373
Largest and smallest residuals [e Å ⁻³]	2.39, -1.38

3.2 [Cu(ohpma)Co(OAc)(DMF)₂]	
Chemical formula	C ₁₆ H ₂₁ CuCoN ₃ O ₈
M_r	505.83
Crystal shape	Prism
Crystal colour	Green
Crystal system, space group	Monoclinic, $P2_1/c$
Temperature [K]	200
a, b, c [Å]	15.3056 (4), 8.3802 (2), 15.8983 (4)
α [°], β [°], γ [°]	90, 98.204 (1), 90.
V [Å ³]	2018.31 (9)
Z	4
ρ_{calc} [g cm ⁻³]	1.665
λ [Å]	1.54178□
μ (Cu _{Kα})(mm ⁻¹)	8.18
Measured reflections	27128
Unique reflections	3637
Reflections $I > 2\sigma(I)$	3541
R_{int}	0.034
R_1, wR_2, GOF	0.027, 0.071, 1.02
No. of parameters	267
No. of restraints	0
Largest and smallest residuals [e Å ⁻³]	0.34, -0.55

3.3 [Cu(ohpma)Mn(OAc)(DMF)₂]	
Chemical formula	C ₁₆ H ₂₁ CuMnN ₃ O ₈
M_r	501.8
Crystal shape	Block
Crystal colour	Green
Crystal system, space group	Monoclinic, $P2_1/c$
Temperature [K]	200
a, b, c [Å]	15.1715 (7), 8.4796 (4), 16.1749 (7)
α [°], β [°], γ [°]	90, 98.443 (3), 90.
V [Å ³]	2058.32 (16)
Z	4
ρ_{calc} [g cm ⁻³]	1.619
λ [Å]	0.71073
μ (MoK α)(mm ⁻¹)	1.69
Measured reflections	17547
Unique reflections	6040
Reflections $I > 2\sigma(I)$	3797
R_{int}	0.053
R_1, wR_2, GOF	0.041, 0.083, 0.97
No. of parameters	267
No. of restraints	0
Largest and smallest residuals [e Å ⁻³]	0.42, -0.36

3.4 [Cu(ohpma)Co _{0.57} Mn _{0.43} (OAc)(DMF) ₂]	
Chemical formula	C ₁₆ H ₂₁ Co _{0.78} CuMn _{0.22} N ₃ O ₈
M_r	504.94
Crystal shape	Plate
Crystal colour	Green
Crystal system, space group	Monoclinic, $P2_1/c$
Temperature [K]	200
a, b, c [Å]	15.2626 (4), 8.4325 (2), 16.0027 (4)
α [°], β [°], γ [°]	90, 98.269 (1), 90
V [Å ³]	2038.17 (9)
Z	4
ρ_{calc} [g cm ⁻³]	1.646
λ [Å]	1.54178
μ (Cu _{Kα})(mm ⁻¹)	7.80
Measured reflections	17152
Unique reflections	3725
Reflections $I > 2\sigma(I)$	3437
R_{int}	0.031
R_1, wR_2, GOF	0.028, 0.070, 1.05
No. of parameters	268
No. of restraints	0
Largest and smallest residuals [e Å ⁻³]	0.26, -0.36

3.5 [Cu(ohpma)Co_{0.6}Ni_{0.4}(OAc)(DMF)₂]	
Chemical formula	C ₁₆ H ₂₁ Co _{0.28} CuN ₃ Ni _{0.72} O ₈
M_r	505.67
Crystal shape	Plate
Crystal colour	Pale green
Crystal system, space group	Monoclinic, $P2_1/c$
Temperature [K]	200
a, b, c [Å]	15.375 (4), 8.372 (2), 15.838 (4)
α [°], β [°], γ [°]	90, 98.090 (5), 90.
V [Å ³]	2018.3 (9)
Z	4
ρ_{calc} [g cm ⁻³]	1.664
λ [Å]	0.71073
μ (MoK α)(mm ⁻¹)	2.01
Measured reflections	60947
Unique reflections	6184
Reflections $I > 2\sigma(I)$	5155
R_{int}	0.032
R_1, wR_2, GOF	0.024, 0.060, 1.01
No. of parameters	268
No. of restraints	0
Largest and smallest residuals [e Å ⁻³]	0.56, -0.30

<u>4.1</u> $[\text{N}(\text{CH}_3)_4]_3[\text{CuMn}(\text{oaba})_2(\text{OAc})] \cdot 7\text{H}_2\text{O}$	
Chemical formula	$\text{C}_{20}\text{H}_{11}\text{CuMnN}_2\text{O}_{12} \cdot 2(\text{H}_2\text{O}) \cdot 2(\text{C}_4\text{H}_{12}\text{N}) \cdot 3(\text{O}) \cdot \text{C}_3\text{H}_6\text{NO}$
M_r	860.12
Crystal shape	Block
Crystal colour	Green
Crystal system, space group	Monoclinic, $P2_1/n$
Temperature [K]	293
a, b, c [Å]	9.5588 (4), 24.6546 (12), 17.5097 (5)
α [°], β [°], γ [°]	90, 96.887 (4), 90.
V [Å ³]	4096.7 (3)
Z	4
ρ_{calc} [g cm ⁻³]	1.395
λ [Å]	0.67173
μ ($\text{MoK}\alpha$) (mm ⁻¹)	0.90
Measured reflections	17780
Unique reflections	4283
Reflections $I > 2\sigma(I)$	2815
R_{int}	0.109
R_1, wR_2, GOF	0.065, 0.156, 1.05
No. of parameters	541
No. of restraints	0
Largest and smallest residuals [e Å ⁻³]	0.45, -0.46

4.2 [N(CH ₃) ₄] ₃ [CuMn(oaba) ₂ (OAc)]	
Chemical formula	C _{19.5} CuMnN ₂ O ₁₂ ·3(C ₄ N)
M_r	794.12
Crystal shape	Block
Crystal colour	Green
Crystal system, space group	Monoclinic, $P2_1/n$
Temperature [K]	363
a, b, c [Å]	9.2684 (16), 23.132 (4), 17.948 (3)
α [°], β [°], γ [°]	90, 101.351 (8), 90.
V [Å ³]	3772.7 (11)
Z	4
ρ_{calc} [g cm ⁻³]	1.398
λ [Å]	1.54178
$\mu(\text{Cu}_{\text{Ka}})$ (mm ⁻¹)	3.97
Measured reflections	15743
Unique reflections	2311
Reflections $I > 2\sigma(I)$	1112
R_{int}	0.177
R_I, wR_2, GOF	0.110, 0.288, 1.05
No. of parameters	195
No. of restraints	0
Largest and smallest residuals [e Å ⁻³]	0.54, -0.42

<u>5.1</u> [Mn(H₂O)(Hpaba)]	
Chemical formula	C ₉ H ₇ MnNO ₆
M_r	280.10
Crystal shape	Needle
Crystal colour	Light yellow
Crystal system, space group	Monoclinic, $P2_1/c$
Temperature [K]	200
a, b, c [Å]	8.9670 (3), 11.8499 (3), 9.1565 (3)
α [°], β [°], γ [°]	90, 97.806 (2), 90.
V [Å ³]	963.94 (5)
Z	4
ρ_{calc} [g cm ⁻³]	1.930
λ [Å]	0.71073
μ (MoK α)(mm ⁻¹)	1.39
Measured reflections	12195
Unique reflections	2834
Reflections $I > 2\sigma(I)$	2603
R_{int}	0.015
R_1, wR_2, GOF	0.027, 0.068, 1.07
No. of parameters	157
No. of restraints	0
Largest and smallest residuals [e Å ⁻³]	0.83, -0.32

5.2 [N(CH ₃) ₄][Cu(ohpma)]·1.5H ₂ O	
Chemical formula	C ₁₈ H ₈ Cu ₂ N ₂ O ₁₀ ·2(C ₄ H ₁₂ N)
M_r	687.63
Crystal shape	Block
Crystal colour	Blue
Crystal system, space group	Monoclinic, <i>Cc</i>
Temperature [K]	100
a, b, c [Å]	12.6677 (7), 14.1798 (6), 18.2869 (10)
α [°], β [°], γ [°]	90, 91.289 (5), 90.
V [Å ³]	3284.0 (3)
Z	4
ρ_{calc} [g cm ⁻³]	1.391
λ [Å]	0.6727
μ (mm ⁻¹)	1.16
Measured reflections	9142
Unique reflections	4485
Reflections $I > 2\sigma(I)$	3832
R_{int}	0.070
R_1, wR_2, GOF	0.079, 0.190, 1.1
No. of parameters	385
No. of restraints	2
Largest and smallest residuals [e Å ⁻³]	0.52, -0.62

5.3 $[\text{N}(\text{CH}_3)_4]_2[\text{CuMn}_2(\text{C}_2\text{O}_4)(\text{ohpma})_2](\text{DMF}) \cdot 3\text{H}_2\text{O}$	
Chemical formula	$\text{C}_{20}\text{H}_8\text{CuMn}_2\text{N}_2\text{O}_{14} \cdot 2(\text{C}_4\text{H}_{12}\text{N}) \cdot 2(\text{C}_3\text{H}_7\text{NO})$
M_r	968.19
Crystal shape	Prism
Crystal colour	Blue
Crystal system, space group	Triclinic, $P^- 1$
Temperature [K]	200
a, b, c [Å]	9.1876 (6), 10.5869 (7), 10.9009 (7)
α [°], β [°], γ [°]	97.788 (2), 91.326 (2), 108.941 (2)
V [Å ³]	991.10 (11)
Z	1
ρ_{calc} [g cm ⁻³]	1.622
λ [Å]	0.71073
μ ($\text{MoK}\alpha$) (mm ⁻¹)	1.24
Measured reflections	23082
Unique reflections	5800
Reflections $I > 2\sigma(I)$	4536
R_{int}	0.024
R_1, wR_2, GOF	0.039, 0.099, 1.02
No. of parameters	293
No. of restraints	5
Largest and smallest residuals [e Å ⁻³]	0.65, -0.42

References

- 1 G. Aromí, A. S. Batsanov, P. Christian, M. Helliwell, A. Parkin, S. Parsons, A. A. Smith, G. A. Timco and R. E. P. Winpenny, *Chem. – Eur. J.*, 2003, **9**, 5142–5161.
- 2 M. R. Willcott, *J. Am. Chem. Soc.*, 2009, **131**, 13180–13180.
- 3 T. Claridge, *J. Chem. Inf. Model.*, 2009, **49**, 1136–1137.
- 4 K. Harris, E. D. Becker, de M. S. M. Cabral, R. Goodfellow and P. Granger, *Pure Appl. Chem.*, 2009, **73**, 1795–1818.
- 5 BrukerAXS Inc, Madison, Wisconsin, USA., .
- 6 G. M. Sheldrick, *Acta Crystallogr. A*, 2008, **64**, 112–122.
- 7 R. H. Blessing, *Acta Crystallogr. A*, 1995, **51**, 33–38.
- 8 L. Palatinus and G. Chapuis, *J. Appl. Crystallogr.*, 2007, **40**, 786–790.
- 9 Rigaku Oxford Diffraction (2015). *CrysAlis PRO*. Rigaku Oxford Diffraction, Yarnton, England., .
- 10 G. M. Sheldrick, *Acta Crystallogr. Sect. Found. Adv.*, 2015, **71**, 3–8.
- 11 O. V. Dolomanov, L. J. Bourhis, R. J. Gildea, J. a. K. Howard and H. Puschmann, *J. Appl. Crystallogr.*, 2009, **42**, 339–341.
- 12 S. P. Westrip, *J. Appl. Crystallogr.*, 2010, **43**, 920–925.

New oxamate-based architectures and their properties

Abstract

The family of N-substituted aromatic oxamate ligands is considered as ideal for obtaining structures of predictable dimensionality and magnetic properties. During this PhD, we have introduced additional coordinating groups (hydroxyl and carboxylic acid) on the phenyloxamate ligand, in order to obtain novel magnetic coordination polymers with original architectures. Reactivity studies for these heterotopic ligands have been performed in both bench and solvothermal conditions, towards different metal ions (Cu^{II} , Co^{II} , Ni^{II} , Mn^{II}). On the bench, various architectures have been isolated, including Cu-based metalloligands, a mix-valence Co-based complex, and a 1D Cu-based helix. Bi- and tri-metallic chains, a 2D heterometallic compound and three 3D coordination polymers have been obtained solvothermally, a technique seldom used in oxamate chemistry. Thermal and magnetic properties were studied, temperature dependent SC to SC transition, single-ion magnet behavior or magnetic ordering were observed, supporting the potential of our approach.

Key words: oxamate ligand, molecular magnetism, solvothermal reactions, coordination polymers.

Nouvelles architectures à base d'oxamate et leurs propriétés

Résumé

La famille des ligands oxamate N-aromatiques est considérée comme idéale pour l'obtention de structures de dimensionnalité et propriétés magnétiques contrôlées. Au cours de ces travaux de thèse, nous avons incorporé au ligand phenyloxamate des groupes coordinants additionnels (hydroxyde et carboxylique), afin d'obtenir de nouveaux polymères de coordination magnétiques aux structures originales. Les études de la réactivité de ces ligands hétérotopiques ont été menées en solution et en conditions solvothermales, vis-à-vis de différents ions métalliques de transitions (Cu^{II} , Co^{II} , Ni^{II} , Mn^{II}). En solution, de nombreuses architectures ont pu être isolées, comme des metalloligands à base de Cu^{II} , un complexe à valence mixte de cobalt, et une chaîne hélicoïdale de Cu^{II} . Des chaînes bi- et tri-métalliques, un composé hétérométallique 2D et trois polymères de coordination 3D ont été obtenus par voie solvothermale, une technique rarement utilisée dans la chimie des ligand oxamate. Les propriétés thermiques et magnétiques ont été étudiées, une transition de phase, un comportement de molécule aimant et un phénomène d'ordre magnétique ont notamment pu être observés, confirmant le potentiel de notre approche.

Mots-clefs : ligand oxamate, magnétisme moléculaire, réactions solvothermale, polymères de coordination.